

# **Structure and Assembly of *Bacillus* Spore Surfaces**

**By Shuo Jiang**

**Submitted for the degree of Doctor of Philosophy**

**Department of Molecular Biology and Biotechnology  
The University of Sheffield, United Kingdom**

**June 2015**



**The  
University  
Of  
Sheffield.**

## Abstract

Endospores of *Bacilli*, and also *Clostridia*, are composed of robust structures that allow them to survive for centuries in the environment. Their remarkable resistance is conferred by the cortex and a multi-layered coat that protect a central core, containing the genetic material necessary for the production of a vegetative cell.

In the *Bacillus cereus* group, the exosporium is the outermost structure, formed from a naturally crystalline basal layer composed of a cup and crown structure and an outer surface covered in a “hairy nap” composed of the protein BclA. In *Bacillus subtilis*, the exosporium is absent; the spore coat is the outermost structure. The majority of the proteins that these ultrastructures are composed of have been identified, although many are still of unknown function. ExsY, BclA and ExsFA from the *B. cereus* exosporium and CotY, CotE and CotZ from the *B. subtilis* spore coat were studied in detail.

*B. cereus*  $\Delta bclA$  mutant endospores were shown to either lack a hairy nap or possess one that was morphologically different, indicating BclA’s major contribution to the nap. The exosporium in  $\Delta bclA$  mutant endospores was altered, possessing a cup structure with no crowns. Loss of the crown was attributed to a lack of BclA and the increased extractability of ExsFA, the nap anchor protein. An almost identical cup structure was seen in *B. thuringiensis* 4D11 that possesses no nap and low levels of ExsFA.

Expression of the cysteine-rich exosporium proteins ExsY and CotY in *Escherichia coli*, revealed the formation of novel two-dimensional crystals, driven by cooperative disulphide bonding. The structure formed is similar to that of native *B. cereus* exosporium, indicating their role as the exosporium template proteins.

The cysteine-rich *B. subtilis* spore coat proteins, CotY and CotZ, also demonstrated the capacity to self-assemble into three-dimensional stacks through cooperative disulphide bond formation. In comparison, the morphogenetic protein CotE, which is not cysteine-rich, also self-assembles, but into a net-like structure.

The ExsFA protein was overexpressed and a crystal was obtained diffracting to  $\sim 2.8$  Å, but its structure is yet to be solved.

# Table of Contents

Acknowledgements .....	i
List of Figures .....	ii
Abbreviations .....	iv
<b>Chapter 1. Introduction.....</b>	<b>1</b>
<b>1.1 The genus <i>Bacillus</i>.....</b>	<b>1</b>
<b>1.2 <i>Bacillus subtilis</i> .....</b>	<b>1</b>
<b>1.3 The <i>Bacillus cereus</i> family .....</b>	<b>1</b>
1.3.1 <i>Bacillus cereus</i> .....	2
1.3.2 <i>Bacillus anthracis</i> .....	2
1.3.3 <i>Bacillus thuringiensis</i> .....	3
<b>1.4 <i>Bacillus</i> endospores .....</b>	<b>3</b>
1.4.1 Sporulation .....	4
<b>1.4 Spore architecture.....</b>	<b>7</b>
1.4.1 The spore core .....	7
1.4.2 The inner membrane.....	7
1.4.3 The germ cell wall, cortex and outer membrane .....	9
1.4.4 The spore coat .....	9
1.4.4.1 Composition of the spore coat .....	10
1.4.4.1.1 CotY ( <i>B. subtilis</i> ) .....	12
1.4.4.1.2 CotZ .....	14
1.4.4.1.3 CotE .....	15
1.4.5 The interspace .....	15
1.4.6 The exosporium .....	17
1.4.6.1 Function of the exosporium.....	21
1.4.6.2 Formation and assembly of the exosporium .....	22
1.4.6.3 Composition of the exosporium.....	22
1.4.6.3.1 ExsFA (BxpB).....	23
1.4.6.3.2 ExsFB.....	23
1.4.6.3.3 ExsK.....	23
1.4.6.3.4 ExsY.....	24
1.4.6.3.5 CotY ( <i>B. cereus</i> ).....	24
1.4.6.3.6 BclA and other glycoproteins .....	25
1.4.6.3.7 Other exosporium proteins .....	26
<b>1.5 Architecture of the exosporium so far .....</b>	<b>27</b>
<b>1.6 Spore germination.....</b>	<b>29</b>
<b>1.7 Use of TEM in biological imaging .....</b>	<b>29</b>
<b>1.8 Aims and objectives.....</b>	<b>31</b>
<b>Chapter 2. Materials and methods .....</b>	<b>32</b>
<b>2.1 Growth media and buffers .....</b>	<b>32</b>
2.1.1 Table of growth and sporulation media .....	32
2.1.2 Table of spore buffers .....	33
2.1.3 Table of protein buffers .....	34
2.1.4 SDS-PAGE buffers and gel recipe .....	35
2.1.4.1 Table of SDS-PAGE buffers.....	35
2.1.4.2 SDS-PAGE gel recipe .....	35
2.1.4.2.1 Table of SDS-PAGE resolving gel components .....	35
2.1.4.2.1 Table of SDS-PAGE stacking gel components .....	36
<b>2.2 Bacterial strains, primers and plasmids .....</b>	<b>36</b>
2.2.1 Table of spore strains.....	36
2.2.2 Table of <i>E. coli</i> overexpression strains .....	36
2.2.3 Table of primers .....	37
2.2.4 Table of plasmids encoding endospore protein genes.....	37
<b>2.3 Isolation of exosporium .....</b>	<b>39</b>
2.3.1 Large-scale growth of <i>Bacillus</i> endospores .....	39

2.3.2 Exosporium extraction by sonication.....	39
2.3.3 Exosporium purification.....	39
2.3.4 Exosporium concentration.....	39
2.3.5 Dialysis membrane treatment .....	40
2.3.6 Exosporium washing .....	40
<b>2.4 Cloning and Expression of heterogeneously expressed endospore proteins .....</b>	<b>40</b>
2.4.1 Primer design and cloning.....	40
2.4.2 Preparation of One Shot® TOP10 Electrocomp™ <i>E. coli</i> cells .....	41
2.4.3 Preparation of <i>E. coli</i> BL21(DE3)pLysS competent cells .....	43
2.4.4 Transformation of cells with plasmids encoding spore proteins.....	43
2.4.4.1 Plasmid transformation into electrocompetent cells.....	43
2.4.4.2 Plasmid transformation into chemical competent cells .....	43
2.4.5 Glycerol stocks.....	43
2.4.6 Expression of recombinant endospore proteins.....	43
<b>2.5 Isolation and purification of recombinant endospore proteins .....</b>	<b>44</b>
2.5.1 Lysis of cells expressing recombinant proteins.....	44
2.5.1.1 Lysozyme treatment.....	44
2.5.1.2 Sonication .....	44
2.5.2 Purification of recombinant proteins.....	44
2.5.2.1 Affinity purification of soluble his-tagged endospore proteins .....	44
2.5.2.2 Batch affinity purification of his-tagged endospore protein crystals .....	45
2.5.2.3 Size exclusion chromatography .....	45
2.5.3 Protein quantification.....	45
2.5.4 Protein identification.....	45
2.5.4.1 SDS-PAGE analysis of proteins .....	45
2.5.4.2 Transfer of proteins onto polyvinylidene fluoride (PVDF) membrane.....	46
2.5.4.3 Western Blot analysis of recombinant proteins .....	46
2.5.5 Thrombin cleavage.....	47
<b>2.6 Sample preparation for TEM.....</b>	<b>47</b>
2.6.1 Coating of carbon grids .....	47
2.6.2 Preparation of uranyl formate (0.75 % w/v).....	47
2.6.3 Negative staining of samples .....	48
2.6.4 Preparation of thin sections.....	48
2.6.5 Preparation of samples for Cryo-EM.....	48
<b>2.7 Transmission electron microscopy .....</b>	<b>49</b>
2.7.1 TEM of negatively stained samples .....	49
2.7.2 Cryo-EM of ice-embedded samples.....	49
2.7.3 Film developing .....	50
2.7.4 Initial screening and scanning of films .....	50
<b>2.8 Image Processing.....</b>	<b>50</b>
2.8.1 Processing of negative stain and film images .....	50
2.8.2 Merging of processed images.....	55
2.8.3 $O, O, I$ estimation .....	56
2.8.4 Threshold estimation for three-dimensional volume maps.....	56
<b>2.9 Circular dichroism spectroscopy .....</b>	<b>57</b>
<b>2.10 X-ray crystallography .....</b>	<b>57</b>
2.10.1 Crystallisation trials .....	57
2.10.1.1 Sitting drop trials .....	57
2.10.1.2 Hanging drop vapour diffusion trials.....	58
<b>Chapter 3. Exosporium architecture in <i>Bacillus cereus</i> group strains and mutants .....</b>	<b>59</b>
<b>3.1 Introduction.....</b>	<b>59</b>
<b>3.2 Results.....</b>	<b>61</b>
3.2.1 Analysis of negatively stained endospores by transmission electron microscopy .....	61
3.2.1.1 <i>B. cereus</i> ATCC 10876 whole spores (wild type).....	61
3.2.1.2 <i>B. cereus</i> ATCC 10876 $\Delta bclA$ whole spores.....	61
3.2.1.3 <i>B. cereus</i> ATCC 10876 $\Delta exsFA$ whole spores.....	64

3.2.1.4 <i>B. thuringiensis</i> 4D11 whole spores.....	64
3.2.2 TEM analysis of isolated, negatively stained exosporium crystals in projection .....	66
3.2.2.1 2D projection maps of purified <i>B. cereus</i> ATCC 10876 $\Delta bclA$ exosporium.....	66
3.2.2.1.1 Form A crystals .....	71
3.2.2.1.2 Form B crystals .....	71
3.2.2.2 2D projection map of purified <i>B. cereus</i> ATCC 10876 $\Delta bclA$ exosporium embedded in ice.....	71
3.2.2.3 2D projection map of sonicated <i>B. cereus</i> ATCC 10876 $\Delta exsFA$ exosporium....	74
3.2.2.4 2D projection map of sonicated <i>B. thuringiensis</i> 4D11 exosporium.....	74
3.2.3 Three-dimensional reconstructions of type II exosporium crystals .....	74
3.2.3.1 3D reconstruction of <i>B. cereus</i> ATCC 10876 $\Delta bclA$ Form A exosporium.....	77
3.2.3.2 3D reconstruction of <i>B. cereus</i> ATCC 10876 $\Delta bclA$ Form B exosporium.....	77
3.2.3.3 3D reconstruction of <i>B. cereus</i> ATCC 10876 $\Delta exsFA$ exosporium .....	77
3.2.3.4 3D reconstruction of <i>B. thuringiensis</i> 4D11 exosporium .....	81
<b>3.3 Discussion.....</b>	<b>83</b>
3.3.1 Loss of BclA results in heterogeneous “hairy nap” populations .....	83
3.3.2 Architecture of $\Delta bclA$ mutant exosporium is altered through increased extractability of structural proteins.....	83
3.3.3 Analysis of the nap-less <i>B. thuringiensis</i> 4D11 strain revealed a loss of linker density.....	88
3.3.4 Mutation in ExsFA reveals contribution of redundant endospore proteins towards exosporium architecture.....	89
<b>Chapter 4. Self-assembly of ExsY and its role as the exosporium template protein .....</b>	<b>91</b>
<b>4.1 Introduction.....</b>	<b>91</b>
<b>4.2 Results.....</b>	<b>92</b>
4.2.1 Recombinant ExsY constructs .....	92
4.2.1.1 pCAexsY - ExsY Untagged.....	92
4.2.1.2 p28exsYNC - ExsY N-, C-terminal his-tagged .....	92
4.2.1.3 p28exsYN - ExsY N-terminal his-tagged.....	92
4.2.1.4 p28exsYC - ExsY C-terminal his-tagged.....	92
4.2.2 Purification of hexa-histidine-tagged ExsY.....	94
4.2.2.1 Solubilisation of ExsY for nickel column affinity purification .....	94
4.2.2.2 Isolation of ExsY macromolecular assemblies by batch affinity purification .....	94
4.2.3 TEM analysis of ExsY .....	96
4.2.3.1 Whole cell analysis of expressing cells .....	96
4.2.3.2 Analysis of affinity purified ExsY fraction .....	96
4.2.3.3 Thin sections of cells expressing ExsY .....	96
4.2.3.4 Lysis of cells expressing ExsY macro assemblies .....	101
4.2.3.5 Isolation of ExsY crystals .....	101
4.2.3.6 Crystal formation from other constructs .....	104
4.2.4 Structural analysis of ExsY crystals .....	104
4.2.4.1 Two-dimensional analysis of ExsY.....	104
4.2.4.2 ExsY reconstruction in three-dimensions.....	104
4.2.4.2.1 Threshold determination for the ExsY model .....	109
4.2.5 Secondary structure estimation using circular dichroism spectroscopy.....	109
4.2.6 Disassembly of ExsY .....	110
4.2.6.1 Analysis of ExsY disassembly by SDS-PAGE and Western blot .....	110
4.2.6.2 TEM analysis of reduced, heat and SDS treated ExsY crystals.....	112
<b>4.3 Discussion.....</b>	<b>117</b>
4.3.1 Purification and analysis of ExsY .....	117
4.3.2 ExsY as the template protein of the exosporium.....	118
4.3.2.1 Self-assembled ExsY architecture is similar to that of <i>B. cereus</i> group exosporium.....	118
4.3.3 Assembly of ExsY and exosporium template mediated by covalent disulphide bond formation .....	123
<b>Chapter 5. Assembly of other exosporium proteins and complexes .....</b>	<b>125</b>
<b>5.1 Introduction.....</b>	<b>125</b>

<b>5.2 Results</b> .....	<b>126</b>
5.2.1 Plasmid construction for expression of exosporium proteins .....	126
5.2.1.1 p28eFAC - ExsFA C-terminal his-tagged .....	126
5.2.1.2 pCAeFAY - ExsFA-ExsY duet untagged .....	126
5.2.1.3 pACbclA - BclA untagged.....	126
5.2.1.4 pACb20 - N-terminal truncated BclA untagged (Denoted: BclA <sub>m</sub> ).....	128
5.2.1.5 p28exsKC - ExsK C-terminal his-tagged.....	128
5.2.1.6 pACexsKbclA .....	128
5.2.1.7 pACexsKb20 .....	128
5.2.1.8 p28cotYBcC .....	128
5.2.2 ExsFA.....	129
5.2.2.1 Expression of recombinant ExsFA .....	129
5.2.2.2 Purification of ExsFA .....	129
5.2.2.2.1 Nickel affinity chromatography .....	129
5.2.2.2.2 Size exclusion chromatography .....	129
5.2.2.3 TEM analysis of ExsFA .....	132
5.2.2.4 Crystallisation of ExsFA .....	132
5.2.2.4.1 Sitting drop vapour diffusion screening .....	132
5.2.2.4.2 Hanging drop vapour diffusion trials.....	132
5.2.2.5 X-ray crystallography of ExsFA.....	135
5.2.3 CotY ( <i>B. cereus</i> ).....	135
5.2.3.1 Expression of CotY .....	135
5.2.3.2 TEM analysis of CotY.....	135
5.2.3.3 CotY cell thin sections .....	138
5.2.3.3 Image processing of CotY crystals.....	138
5.2.4 ExsK.....	138
5.2.4.1 Expression of ExsK.....	138
5.2.4.2 TEM analysis of ExsK .....	138
5.2.5 Co-expression of ExsY and ExsFA .....	138
5.2.5.1 Growth of ExsY-ExsFA .....	138
5.2.5.2 TEM analysis of ExsY-ExsFA .....	142
5.2.5.3 Image processing of crystals from ExsY-ExsFA co-expression.....	142
5.2.6 Co-expression of ExsY-ExsFA-BclA/BclA <sub>m</sub> .....	142
5.2.6.1 Growth of ExsY-ExsY-BclA/BclA <sub>m</sub> .....	142
5.2.6.2 TEM analysis and image processing of ExsY-ExsY-BclA .....	142
5.2.6.3 TEM analysis and image processing of ExsY-ExsY-BclA <sub>m</sub> .....	146
5.2.7 Co-expression of ExsY-ExsFA-BclA/BclA <sub>m</sub> and ExsK .....	146
5.2.7.1 Growth of ExsY-ExsY-BclA/BclA <sub>m</sub> -ExsK.....	146
5.2.7.2 TEM analysis and image processing of ExsY-ExsY-BclA/BclA <sub>m</sub> -ExsK.....	146
<b>5.3 Discussion</b> .....	<b>148</b>
5.3.1 The hairy nap exosporium anchor.....	148
5.3.2 The exosporium cap structure.....	148
5.3.3 Heterologous assembly of the exosporium .....	149
<b>Chapter 6. Self-assembly of <i>Bacillus subtilis</i> coat proteins</b> .....	<b>152</b>
<b>6.1 Introduction</b> .....	<b>152</b>
<b>6.2 Results</b> .....	<b>154</b>
6.2.1 Expression of recombinant spore coat proteins .....	154
6.2.2 CotY .....	154
6.2.2.1 Purification of CotY .....	154
6.2.2.2 TEM analysis of heterologously overexpressed CotY.....	157
6.2.2.3 Two-dimensional reconstruction of CotY .....	157
6.2.2.4 CotY thin sections .....	161
6.2.2.5 Circular dichroism spectroscopy .....	161
6.2.2.6 Stability of CotY.....	164
6.2.3 CotE .....	164
6.2.3.1 Purification of CotE .....	164
6.2.3.2 Analysis of CotE by TEM .....	166
6.2.3.3 Thrombin cleavage of CotE.....	166
6.2.3.4 CotE stability .....	170

6.2.4 CotZ .....	170
6.2.4.1 CotZ purification .....	170
6.2.4.2 TEM analysis of purified CotZ .....	170
6.2.4.3 CotZ thin sections .....	175
<b>6.3 Discussion.....</b>	<b>177</b>
6.3.1 CotY .....	177
6.3.1.1 Purification and analysis of CotY .....	177
6.3.1.2 Structure of CotY .....	178
6.3.1.3 CotY assembly .....	178
6.3.2 CotE .....	180
6.3.2.1 Purification and assembly of CotE .....	180
6.3.3 CotZ .....	181
6.3.3.1 Purification and assembly of CotZ .....	181
<b>Chapter 7. Analysis of germinating <i>B. cereus</i> spores by transmission electron microscopy .....</b>	<b>183</b>
<b>7.1 Introduction.....</b>	<b>183</b>
<b>7.2 Results.....</b>	<b>184</b>
7.2.1 Germination of <i>B. cereus</i> spores in non-outgrowing conditions .....	184
7.2.1.1 TEM analysis of non-outgrowing spores .....	184
7.2.2 Germination and outgrowth of <i>B. cereus</i> spores in BHI .....	184
7.2.2.1 TEM analysis of outgrowing spores .....	184
<b>7.3 Discussion.....</b>	<b>188</b>
7.3.1 Germination through a polar cap.....	188
<b>Chapter 8. General discussions and future investigations .....</b>	<b>189</b>
<b>8.1 Demolition of the exosporium.....</b>	<b>189</b>
<b>8.2 Building the exosporium .....</b>	<b>191</b>
<b>8.3 An extension on the exosporium.....</b>	<b>192</b>
<b>8.4 Foundations of assembly .....</b>	<b>194</b>
<b>8.5 Future developments .....</b>	<b>195</b>
8.5.1 High-resolution analysis .....	195
8.5.2 Other exosporium proteins .....	195
8.5.3 Exosporium reconstruction.....	195
<b>References.....</b>	<b>197</b>
<b>Publications .....</b>	<b>208</b>
<b>Presentation of research.....</b>	<b>208</b>
<b>Appendix.....</b>	<b>208</b>

# Acknowledgements

Day one thousand four hundred and sixty, I can see the light...

First and foremost, many thanks go out to my supervisor, Per Bullough, for giving me the opportunity to explore the unique world of spores, and science in general. His guidance has been invaluable over the past few years and has managed to get me through to today. My deepest thanks must also go out to Anne Moir for helping me along my journey, teaching me the basics of molecular biology and everything spore related.

I would like to also thank the BBSRC for funding me through this project and allowing me to progress as a scientist.

It has been a brilliant experience in the Bullough Lab over the years but special thanks must go out to Svet for keeping the microscope alive, Tham for running the lab and Dave for supplying me with the mutants necessary for my work. I would also like to thank Chris for his help with the thin sections. The images in this thesis would not have been possible, in some way or another, without these people. Huge thanks must also go out to everyone who has worked on the exosporium project in the past; none of the work presented here would have been possible without their previous efforts.

A big thanks goes out to all my friends in Sheffield over the past seven years, I'm really going to miss you lot. I owe a debt of gratitude to my best friends Lauren, Luke and Steve. Lauren, I cannot emphasise how enjoyable this PhD has been with you around and your work hard ethos has definitely rubbed off on me. I'm going to miss our 7 am starts and 11 pm takeaways to work; it's a real pity we'll have to do it all over again in Boston. Luke, I know we've not had a religion vs. science debate in a while but I would like to keep it that way, mainly because I never seen to win. Thanks to you and Sammy for always having me over if I'm hungry. And Steve, one day I hope I'll be as Yorkshire as you. It's been a great journey as a scientist around you rowdy bunch!!!

Finally, I would like to thank my family for being so persistent and keeping me on track all the way through.

## List of Figures

<b>Figure 1.1</b>	The morphological stages of sporulation in <i>B. subtilis</i> .....	5
<b>Figure 1.2</b>	A schematic diagram of a matured <i>B. cereus</i> spore.....	8
<b>Figure 1.3</b>	A schematic diagram the layers contributing to the <i>B. subtilis</i> spore coat....	11
<b>Figure 1.4</b>	A schematic diagram showing the network of proteins making up the <i>B. subtilis</i> spore coat.....	13
<b>Figure 1.5</b>	Cross-section through a <i>B. anthracis</i> spore.....	16
<b>Figure 1.6</b>	Structure of the <i>B. cereus</i> exosporium.....	20
<b>Figure 1.7</b>	Schematic diagram featuring the crystalline layers found within spore preparations.....	28
<b>Figure 2.1</b>	Maps of plasmid vectors utilised in cloning of <i>Bacillus</i> endospore proteins.	42
<b>Figure 2.2</b>	Flow diagram outlining steps for generation of three dimensional projection structures using MRC suite programs for processing two dimensional crystals.....	51
<b>Figure 2.3</b>	Schematic diagram of the MRC tilt axis conventions.....	53
<b>Figure 3.1</b>	Projection maps and three-dimensional models of <i>Bacillus cereus</i> ATCC 10876 exosporium.....	60
<b>Figure 3.2</b>	Negatively stained <i>B. cereus</i> ATCC 10876 whole spores.....	62
<b>Figure 3.3</b>	Negatively stained <i>B. cereus</i> ATCC 10876 $\Delta bclA$ whole spores.....	63
<b>Figure 3.4</b>	Negatively stained <i>B. cereus</i> ATCC 10876 $\Delta exsFA$ whole spores.....	65
<b>Figure 3.5</b>	Negatively stained <i>B. thuringiensis</i> 4D11 whole spores.....	67
<b>Figure 3.6</b>	Contour and grey level projection maps from whole spores.....	68
<b>Figure 3.7</b>	Analysis of purified Form A exosporium crystal from <i>B. cereus</i> ATCC 10876 $\Delta bclA$ .....	69
<b>Figure 3.8</b>	Analysis of purified Form B exosporium crystal from <i>B. cereus</i> ATCC 10876 $\Delta bclA$ .....	70
<b>Figure 3.9</b>	<i>B. cereus</i> ATCC 10876 $\Delta bclA$ form A crystal imaged in ice.....	72
<b>Figure 3.10</b>	Analysis of sonicated exosporium from <i>B. cereus</i> ATCC 10876 $\Delta exsFA$ ....	75
<b>Figure 3.11</b>	Analysis of exosporium from <i>B. thuringiensis</i> 4D11.....	76
<b>Figure 3.12</b>	<i>B. cereus</i> $\Delta bclA$ Form A exosporium modelled in three-dimensions.....	78
<b>Figure 3.13</b>	<i>B. cereus</i> $\Delta bclA$ Form B exosporium modelled in three-dimensions.....	79
<b>Figure 3.14</b>	<i>B. cereus</i> $\Delta exsFA$ exosporium modelled in three-dimensions.....	80
<b>Figure 3.15</b>	<i>B. thuringiensis</i> 4D11 exosporium modelled in three-dimensions.....	82
<b>Figure 3.16</b>	SDS-PAGE analysis of purified exosporium from <i>B. cereus</i> ATCC 10876 and <i>B. cereus</i> ATCC 10876 $\Delta bclA$ .....	84
<b>Figure 3.17</b>	Comparative exosporium structural overlays.....	87
<b>Figure 4.1</b>	Amino acid sequence of recombinant ExsY constructs.....	93
<b>Figure 4.2</b>	SDS-PAGE analysis of affinity purified soluble ExsY.....	95
<b>Figure 4.3</b>	Isolation of insoluble ExsY macromolecular assemblies using batch affinity purification.....	97
<b>Figure 4.4</b>	Negatively stained TEM of <i>E. coli</i> cells expressing ExsY.....	98
<b>Figure 4.5</b>	Soluble ExsY purified by nickel column affinity purification.....	99
<b>Figure 4.6</b>	Thin sections of <i>E. coli</i> cells expressing ExsY.....	100
<b>Figure 4.7</b>	Electron micrographs of lysed <i>E. coli</i> cells expressing ExsY.....	102
<b>Figure 4.8</b>	Electron micrographs of nickel affinity batch purified ExsY crystals.....	103
<b>Figure 4.9</b>	Formation of crystals by ExsY his-tagged and untagged constructs.....	105
<b>Figure 4.10</b>	Electron micrographs of isolated ExsY crystalline assemblies and two-dimensional electron crystallographic reconstruction in projection.....	106
<b>Figure 4.11</b>	ExsY self-assembled crystals modelled in three-dimensions.....	108
<b>Figure 4.12</b>	CD spectroscopy of soluble ExsY assemblies.....	111
<b>Figure 4.13</b>	SDS-PAGE and corresponding anti-His Western blot of soluble and insoluble ExsY complexes treated with DTT, heat and SDS.....	112
<b>Figure 4.14</b>	Electron micrographs of purified ExsY crystals after incubation with reducing agent, heat and SDS.....	115
<b>Figure 4.15</b>	Electron micrographs of purified ExsY crystal after treatment with combinations of 2 M DTT, 95 °C heat and 2 % SDS.....	116
<b>Figure 4.16</b>	Three-dimensional structural overlay of ExsY self-assembled crystals and <i>B. thuringiensis</i> 4D11 exosporium.....	120

<b>Figure 4.17</b>	Three-dimensional structural overlay of ExsY self-assembled crystals and <i>B. cereus</i> ATCC 10876 exosporium.....	<b>121</b>
<b>Figure 5.1</b>	Amino acid sequence of recombinant ExsFA, CotY, ExsK and BclA constructs.....	<b>127</b>
<b>Figure 5.2</b>	12 % SDS-PAGE analysis of ExsFA purified using nickel affinity chromatography.....	<b>130</b>
<b>Figure 5.3</b>	Purification of ExsFA using size exclusion chromatography.....	<b>131</b>
<b>Figure 5.4</b>	Electron micrograph of monodispersed ExsFA single particles.....	<b>133</b>
<b>Figure 5.5</b>	ExsFA crystals formed by sitting drop vapour diffusion.....	<b>134</b>
<b>Figure 5.6</b>	X-ray diffraction from ExsFA crystals formed 0.1 M sodium phosphate, 0.1 M potassium phosphate, 0.1 M MES pH 6.5 and 2 M sodium chloride by sitting drop vapour diffusion.....	<b>136</b>
<b>Figure 5.7</b>	TEM of CotY assemblies.....	<b>137</b>
<b>Figure 5.8</b>	Electron micrographs of CotY thin sections.....	<b>139</b>
<b>Figure 5.9</b>	Representative projection map of CotY ( <i>B. cereus</i> ) crystals.....	<b>140</b>
<b>Figure 5.10</b>	Electron micrograph and SDS-PAGE of cell lysate of ExsK expressing cells.....	<b>141</b>
<b>Figure 5.11</b>	SDS-PAGE analysis of cell extracts from ExsY, ExsFA and BclA/BclA <sub>m</sub> co-expression.....	<b>143</b>
<b>Figure 5.12</b>	Representative electron micrograph and projection map of crystal extracted from ExsY-ExsFA co-expression.....	<b>144</b>
<b>Figure 5.13</b>	Representative electron micrograph and projection map of crystal extracted from ExsY-ExsFA-BclA co-expression.....	<b>145</b>
<b>Figure 5.14</b>	Representative electron micrograph and projection map of crystal extracted from ExsY-ExsFA-BclA <sub>m</sub> co-expression.....	<b>147</b>
<b>Figure 6.1</b>	Heterologous expression of <i>B. subtilis</i> CotY mutant (CotY <sub>mut</sub> ) and TEM reconstructions.....	<b>153</b>
<b>Figure 6.2</b>	Amino acid sequence of recombinant <i>B. subtilis</i> spore coat protein constructs.....	<b>155</b>
<b>Figure 6.3</b>	Purification and identification of <i>B. subtilis</i> His <sub>6</sub> -CotY.....	<b>156</b>
<b>Figure 6.4</b>	Representative electron micrographs of heterologously self-assembled <i>B. subtilis</i> CotY constructs.....	<b>158</b>
<b>Figure 6.5</b>	Two-dimensional projection map of negatively stained CotY crystals.....	<b>159</b>
<b>Figure 6.6</b>	Thin sections of <i>E. coli</i> cells expressing <i>B. subtilis</i> CotY.....	<b>162</b>
<b>Figure 6.7</b>	CD spectroscopy of soluble CotY.....	<b>163</b>
<b>Figure 6.8</b>	Analysis of His <sub>6</sub> -CotY crystals and soluble fraction from <i>E. coli</i> overexpression by SDS-PAGE and Western blotting.....	<b>165</b>
<b>Figure 6.9</b>	Purification of <i>B. subtilis</i> His <sub>6</sub> -CotE.....	<b>167</b>
<b>Figure 6.10</b>	Electron micrographs of CotE net-like assemblies.....	<b>168</b>
<b>Figure 6.11</b>	Thrombin cleavage of His <sub>6</sub> -CotE.....	<b>169</b>
<b>Figure 6.12</b>	Electron micrographs of purified CotE net-like assemblies treated with 8 M urea.....	<b>171</b>
<b>Figure 6.13</b>	Stability of CotE nets under heated and reducing conditions.....	<b>172</b>
<b>Figure 6.14</b>	Purification of <i>B. subtilis</i> His <sub>6</sub> -CotZ.....	<b>173</b>
<b>Figure 6.15</b>	Electron micrograph of purified CotZ assemblies.....	<b>174</b>
<b>Figure 6.16</b>	TEM cross-sections of <i>E. coli</i> cells expressing CotZ.....	<b>176</b>
<b>Figure 7.1</b>	Electron micrograph of germinating spores in non-outgrowing conditions...	<b>185</b>
<b>Figure 7.2</b>	Electron micrograph of germinating spores in outgrowing conditions.....	<b>186</b>
<b>Figure 8.1</b>	Predicted overview of exosporium assembly in <i>B. cereus</i> .....	<b>193</b>

## Abbreviations

Å - Angstrom  
AFM - Atomic force microscopy  
ATCC - American Type Culture Collection  
BclA - *Bacillus* collagen-like protein of *anthracis*  
BCA - Bicinchoninic acid  
BDMA - Benzyl Dimethylamine  
BHI - Brain Heart Infusion  
BSA - Bovine serum albumin  
CCY - Casein-Casein Yeast  
CD - Circular dichroism  
Cryo-EM - Cryogenic-Electron microscopy  
CuPd - Copper Palladium  
DDSA - Dodecenyyl Succinic Anhydride  
dH<sub>2</sub>O - Distilled water  
DMSO – Dimethyl sulfoxide  
DNA - Deoxyribonucleic acid  
DNase - Deoxyribonuclease  
DTT - Dithiothreitol  
EDTA - Ethylenediaminetetraacetic acid  
FEG - Field emission gun  
FFT - Fast Fourier transform  
GUI - Graphical user interface  
IPTG - Isopropyl-β-galactoside  
kDa - Kilodalton  
LB - Luria-Bertani  
MCS - Multiple cloning site  
MES - 2-(N-morpholino)ethanesulfonic acid  
MRC - Medical research council  
MWCO - Molecular weight cut off  
OD - Optical density  
PCR - Polymerase chain reaction  
PEG - Polyethylene glycol  
PMSF - Phenylmethylsulphonyl fluoride  
psi - Pounds per square inch  
PVDF - Polyvinylidene fluoride  
RPM - Revolutions per minute  
SASP - Small acid soluble protein  
SDS - Sodium dodecyl sulphate  
SDS-PAGE - Sodium dodecyl sulphate polyacrylamide gel electrophoresis  
SRB - Spore resuspension buffer  
TEM - Transmission electron microscopy  
TEMED - N,N,N',N'-Tetramethylethane-1,2-diamine  
Tris - Tris(hydroxymethyl)aminomethane  
TNF - Tumour necrosis factor  
UV - Ultraviolet  
UV/Vis. - Ultraviolet-visible  
w/v, v/v - weight/volume, volume/volume

# Chapter 1. Introduction

## 1.1 The genus *Bacillus*

Members of the *Bacillus* genus consist of mesophilic Gram-positive rod shaped bacteria that are found as aerobes or facultative anaerobes, distinguishing them from the strictly anaerobic *Clostridia*. *Bacilli* commonly reside in the soil but have also been found in a variety of extreme environments (Drobniewski, 1993). For example, *Bacillus coagulans* has been found to survive in acidic conditions as low as pH 4.0 and also in temperatures exceeding 75 °C (Palop *et al.*, 1999). When *Bacilli* are exposed to unfavourable conditions, such as nutrient starvation, they differentiate into a morphologically different state- the endospore, which is exceptionally robust and metabolically dormant (Drobniewski, 1993). This process, known as sporulation, has been most extensively studied in the model Gram-positive bacteria, *Bacillus subtilis*.

## 1.2 *Bacillus subtilis*

*Bacillus subtilis* is the most widely understood prokaryote in terms of genetics, biochemistry and general physiology, except for *Escherichia coli* (Errington, 2003). The *B. subtilis* chromosome is highly amenable to genetic manipulation, promoting its use as a model organism for the study of cellular development, cell fate and in particular, sporulation (Errington, 2003). The single circular chromosome of *B. subtilis* has been sequenced in its entirety (Kunst *et al.*, 1997), and a set of mutants generated with all essential genes defined (Kobayashi *et al.*, 2003). *B. subtilis* is also important in biotechnology; one example has been its use as a cell factory for production of pharmaceutical proteins (Westers *et al.*, 2004).

## 1.3 The *Bacillus cereus* family

The *Bacillus cereus* group is composed of *B. cereus*, *B. anthracis*, *B. thuringiensis*, *B. weihenstephanensis*, *B. mycoides* and *B. pseudomycooides*, all of which are aerobic or facultative anaerobic spore formers (Anderson *et al.*, 2005, Jensen *et al.*, 2003). Genome comparisons between these *Bacilli* showed sufficient similarities that it was proposed that they could be considered the same species: *B. cereus sensu lato* (Ash *et al.*, 1991, Helgason *et al.*, 2000, Lechner *et al.*, 1998). The three major members of the *B. cereus sensu lato* group: *B. cereus*, *B. thuringiensis* and *B. anthracis*, can be differentiated by their plasmid-encoded toxin genes (Pilo and Frey, 2011, Thomas *et al.*, 2000, Tourasse *et al.*, 2011). The complete genome sequences of *B. anthracis* Ames

(Read *et al.*, 2003), *B. thuringiensis* Al Hakam (Challacombe *et al.*, 2007, Han *et al.*, 2006), *B. cereus* E33L (Han *et al.*, 2006), *B. cereus* ATCC 14579 (Ivanova *et al.*, 2003) and *B. cereus* ATCC 10987 (Rasko *et al.*, 2004) amongst others are available, along with the draft sequence of other strains of the *B. cereus* group (Priest *et al.*, 2004, Tourasse *et al.*, 2011). *B. cereus*, *B. anthracis* and *B. thuringiensis* are of particular interest due to their pathogenic properties.

### **1.3.1 *Bacillus cereus***

*Bacillus cereus* resides commonly in the soil, but many strains are also adapted for growth within the intestinal tract of insects and mammals. *B. cereus* behaves as an opportunistic pathogen whose spores are difficult to eradicate through industrial sterilisation methods. This presents a difficult challenge for the food industry in the prevention of *B. cereus*-related food poisoning (Granum and Lund, 1997), resulting in diarrhoeal and emetic syndromes (Mortimer and McCann, 1974, Taylor and Gilbert, 1975). The diarrhoeal symptoms arise from the ingestion of meat and dairy products contaminated with *B. cereus* spores, which release enterotoxins (Beecher and Wong, 1997, Lund and Granum, 1997) within the small intestine after germination (Granum, 1994). The emetic symptoms arise from ingestion of food products contaminated with emetic toxin produced by growing vegetative cells (Ehling-Schulz *et al.*, 2004, Kramer, 1989). *B. cereus* acts as an opportunistic human pathogen; systemic infections can lead to severe illnesses including meningitis (Tokieda *et al.*, 1999), septicaemia and bacterial endocarditis in immune-compromised patients (Drobniewski, 1993).

### **1.3.2 *Bacillus anthracis***

Spores of *Bacillus anthracis* are the causative agent of anthrax (Koch, 1876) and have been studied extensively due to their use as a bioterror agent (Helgason *et al.*, 2000). Anthrax predominantly affects mammals, especially herbivores, through gastrointestinal, pulmonary and cutaneous infections (Baillie and Read, 2001, Mock and Fouet, 2001, Uchida *et al.*, 1993). Macrophages from the infected host engulf the *B. anthracis* spore and transports them to the local mediastinal lymph nodes (Ross, 1957, Weiner and Glomski, 2012). *B. anthracis* spores begin to germinate into vegetative cells within the tissues or blood of mammals where the environment is rich in glucose, amino acids and nucleosides. The vegetative cells are then able to proliferate and express their virulence factors, leading ultimately to death of the host (Inglesby *et al.*, 1999).

The genes conferring virulence are found on two plasmids, designated pXO1 and pXO2, that are responsible for toxin and capsule production respectively (Green *et al.*, 1985, Mikesell *et al.*, 1983, Uchida *et al.*, 1985). The pXO1 plasmid encodes lethal and oedema factors that are both targeted through a protective antigen complex, also encoded on pXO1, for entry into the host cell (Bradley *et al.*, 2001). The pXO2 plasmid encodes enzymes required for the synthesis of the poly-D-glutamic acid capsule, responsible for protection against macrophages (Green *et al.*, 1985). A master regulator, *atxA*, governs the virulence factors found on pXO1 and has also been shown to enhance capsule production. The same level of encapsulation is seen in an *atxA* mutant and a pXO1<sup>-</sup> strain (Fouet, 2010).

### **1.3.3 *Bacillus thuringiensis***

During sporulation, *Bacillus thuringiensis* strains produce one or more proteinaceous  $\delta$ -endotoxins (Bechtel and Bulla, 1976, Scherrer and Somerville, 1977). This property of *B. thuringiensis* has allowed it to be used as a biological insecticide for the past 50 years with great success (Bravo *et al.*, 2011). The  $\delta$ -endotoxins are composed of Cytolytic (Cyt) and Crystal (Cry) toxin proteins (Koni and Ellar, 1994) that are expressed, in most cases, from plasmid-encoded genes (Bravo *et al.*, 2007).

The Cry toxins produced by *B. thuringiensis* form a naturally paracrystalline parasporal inclusion located either in the interspace region under the exosporium or more commonly separate from the spore (Aronson *et al.*, 1986, Somerville and James, 1970). The paracrystalline prototoxin is activated after ingestion by insects and binds to receptors in the epithelial cells of the mid-gut, creating membrane pores and leading eventually to cell lysis (Soberon *et al.*, 2010). Different strains of *B. thuringiensis* produce different cry toxin proteins that appear to be harmless towards humans but are active against Lepidoptera, Diptera and Coleoptera or a combination (Hofte and Whiteley, 1989). An extensive review on the use of *B. thuringiensis* can be found in (Koch *et al.*, 2015). The targeting of specific insects, such as mosquitoes, by the toxin from *B. thuringiensis* Israelensis, allows it to be potentially used in the control of malaria (Dambach *et al.*, 2014).

## **1.4 *Bacillus* endospores**

Under nutrient depletion, vegetative *Bacilli* differentiate into a metabolically dormant cell state, known as the endospore, through a process of sporulation (Errington, 1993). Endospores (spores) are highly robust structures and appear morphologically different

to that of vegetative Bacilli. In this differentiated state, endospores can remain dormant for hundreds of years (Kennedy *et al.*, 1994) whilst resisting environmental perturbations; e.g. high temperature, pH and oxidizing agents (Nicholson *et al.*, 2000, Setlow and Setlow, 1995). The longevity of the spores in these conditions is achieved by possessing a robust multilayered coat, a dehydrated core and protective agents such as: UV absorbing proteins located on the spore coat and nucleotide excision repair pathways within the spore core (Nicholson *et al.*, 2002). These features contributing to the resistance of the spore will be discussed later in this chapter.

### 1.4.1 Sporulation

Sporulation occurs over eight hours through seven defined morphological stages, termed I-VII (Fig. 1.1), which are controlled by a cascade of sigma factors (Losick and Stragier, 1992). The master regulator, Spo0A, which becomes phosphorylated by a multicomponent phosphorelay (Burbulys *et al.*, 1991), controls entry into sporulation. Once entry into sporulation begins, a cascade of compartmentalised sporulation-specific sigma factors governs the formation of the endospore (Kroos and Yu, 2000, Piggot and Hilbert, 2004).

Sporulation was famously observed by Robert Koch in 1876 on *Bacillus anthracis* (Koch, 1876) and has been studied extensively on the model organism *Bacillus subtilis* (Dawes *et al.*, 1969, Stragier and Losick, 1996) by techniques such as transmission electron microscopy (Kay and Warren, 1968). Sporulation of *B. cereus* (Ohye and Murrell, 1973, Young and Fitz-James, 1959a, Young and Fitz-James, 1959b). *B. thuringiensis* (Bechtel and Bulla, 1976) and *B. anthracis* (Liu *et al.*, 2004) have also been documented as part of the *B. cereus* group whom also possess an external exosporium layer (Desrosier and Lara, 1984).

**Stage 0-I: Axial filament formation** - After DNA replication, the two copies of the chromosome appear condensed and elongated into filaments that run along the distal axis of the cell (Hilbert and Piggot, 2004, Teleman *et al.*, 1998).

**Stage II: Asymmetric division** - Asymmetric division results from the formation of a polar septum, dividing the starved cell into a large mother cell compartment and a smaller forespore compartment. This division is mediated by the polar localisation of FtsZ as seen by fluorescence microscopy (Levin and Losick, 1996). SpoIIIE, a DNA translocase, drives the transfer of the final replicated chromosome into the forespore

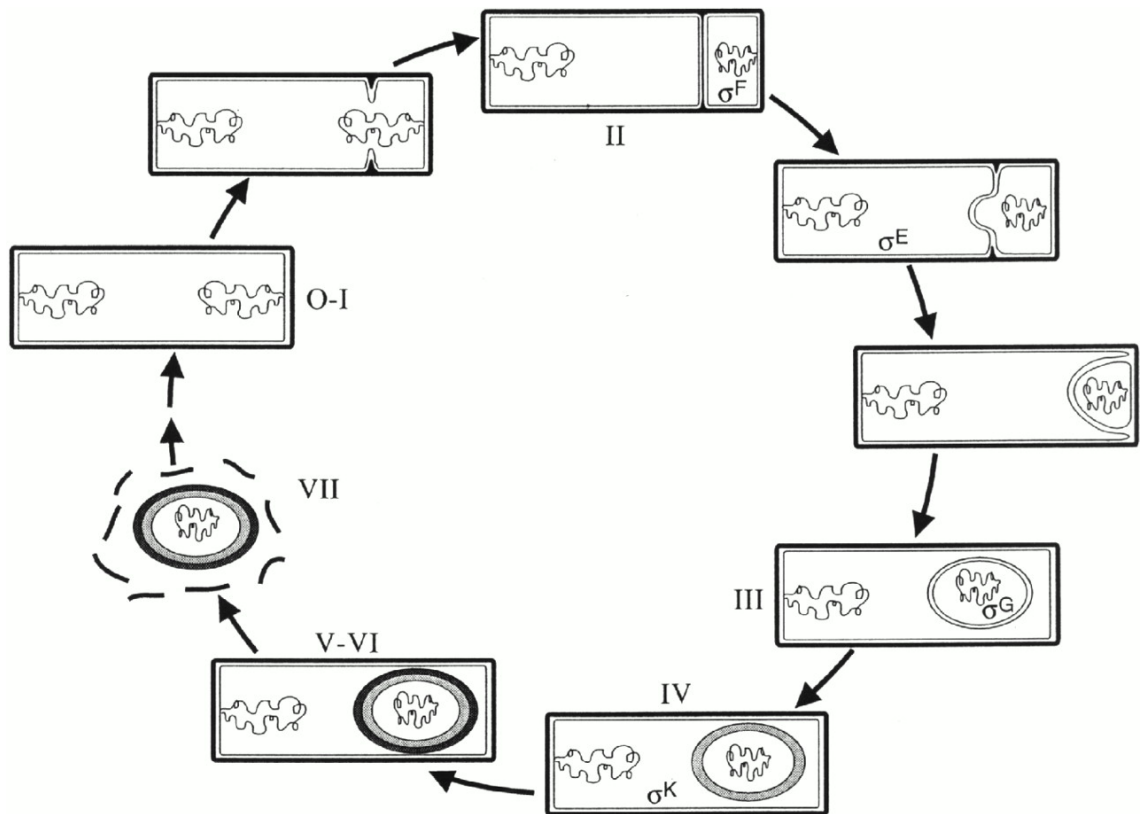


**Figure 1.1** The morphological stages of sporulation in *B. subtilis*. Stage 0-I shows the anchoring of chromosomes to the cell poles. The initiation of axial filament formation begins in stage I followed by an asymmetric division in stage II. The spore protoplast is engulfed in stage III followed by the formation of the cortex and coat in stages IV and V. Stage VI involves the maturation of the spore within the mother cell and is released in stage VII upon mother cell lysis. Figure from Stragier and Losick, 1996.

after division, followed by removal of the peptidoglycan from the asymmetric septum (Piggot and Hilbert, 2004, Wu and Errington, 1994).

**Stage III: Engulfment** - Once the genetic material is incorporated into the forespore compartment, the mother cell engulfs the forespore. The mother cell membrane migrates around the forespore towards its opposite pole until the membrane fuses around the forespore. This eventually leads to the formation of a forespore protoplast within the mother cell cytoplasm, surrounded by an inner and outer membrane of opposite polarity (Errington, 1993).

**Stage IV: Synthesis of the cortex** - A peptidoglycan cortex is formed between the inner and outer membrane of the newly developed free forespore. A peptidoglycan germ cell wall is synthesised across the forespore inner membrane (Meador-Parton and Popham, 2000) and enzymes, such as SpoVD (Bukowska-Faniband and Hederstedt, 2013), synthesize a peptidoglycan cortex across the mother cell membrane. In species that form an exosporium, visible assembly begins at this stage in the mother cell (Ohye and Murrell, 1973).

**Stage V: Synthesis of the coat** - A biochemically stable multi-layered coat is synthesized at this stage and is composed of more than seventy different proteins (Driks, 2004, Henriques and Moran, 2007). Spore coat proteins synthesized in the mother cell are deposited on the outer surface of the cortex as it continues to develop around the forespore (Driks, 1999). The spores' resistance against chemical and physical agents develop at this point (Henriques and Moran, 2007).

**Stage VI: Maturation** - The outer layers of the developing spore progressively form until completion, including those of the exosporium, within the mother cell. The complete resistance towards heat requires complete maturation of the spore (Sanchez-Salas *et al.*, 2011). As the coat and exosporium layers form, the refractivity of the spore increases in relation to its state of dehydration. Under phase contrast microscopy, this is seen as spores begin to "whiten", signifying the uptake of calcium and the synthesis of dipicolinic acid (Young and James, 1962).

**Stage VII: Mother cell lysis** - The spore core is completely dehydrated by the final stages of maturity, indicated by a fully refractile spore, and is released into the environment through the lysis of the mother cell.

## 1.4 Spore architecture

The fully mature *Bacillus* endospore is composed of multiple layers, cortex and coat, around the spore core (Fig. 1.2). This complex layered architecture provides a high degree of robustness and protection (Knaysi and Hillier, 1949) whilst also preserving the integral components required for germination.

### 1.4.1 The spore core

The innermost spore core is a metabolically dormant structure that contains the fundamental genetic material required for the propagation of a new vegetative cell. In addition to the chromosomal DNA, proteins are found within the core; including ribosomes, most vegetative cell proteins, spore enzymes and a selection of small acid soluble proteins (SASPs) - which function in protecting the DNA from damage (Connors *et al.*, 1986, Setlow, 1995). SASPs form stable nucleoprotein complexes that make up between 3-5 % of the total protein content and protect the DNA against heat, desiccation, enzymes and UV radiation (Fairhead and Setlow, 1992, Setlow, 2007, Setlow, 2006).

Pyridine-2,6-dicarboxylic acid (dipicolinic acid [DPA]) constitutes ~5-15 % of the dormant spore's dry weight and is chelated to divalent cations in the spore core, predominantly  $\text{Ca}^{2+}$ . (Gerhardt and Marquis, 1989, Huang *et al.*, 2007). During sporulation  $\text{Ca}^{2+}$ DPA is taken up by the developing spore (Li *et al.*, 2012) whilst during germination and core rehydration, some  $\text{Ca}^{2+}$ DPA leaks from the spore during the initiation of germination, followed by a rapid bulk release from the spore core as it rehydrates (Wang *et al.*, 2015).

### 1.4.2 The inner membrane

The spore core is separated from the cortex by an inner membrane that contains receptors involved in the early stages of germination (Hudson *et al.*, 2001, Paidhungat and Setlow, 2001). Germinant receptors have been proposed to be located on the outer surface of the inner membrane through observing levels of biotinylation and protease sensitivity of germinant receptor proteins in *B. subtilis* spores that have been either decoated or germinated with the coats intact (Korza and Setlow, 2013). The inner membrane has also been shown to act as a permeation barrier for many compounds, such as methylamine that penetrates germinated spores but not those that are dormant. (Cowan *et al.*, 2004).

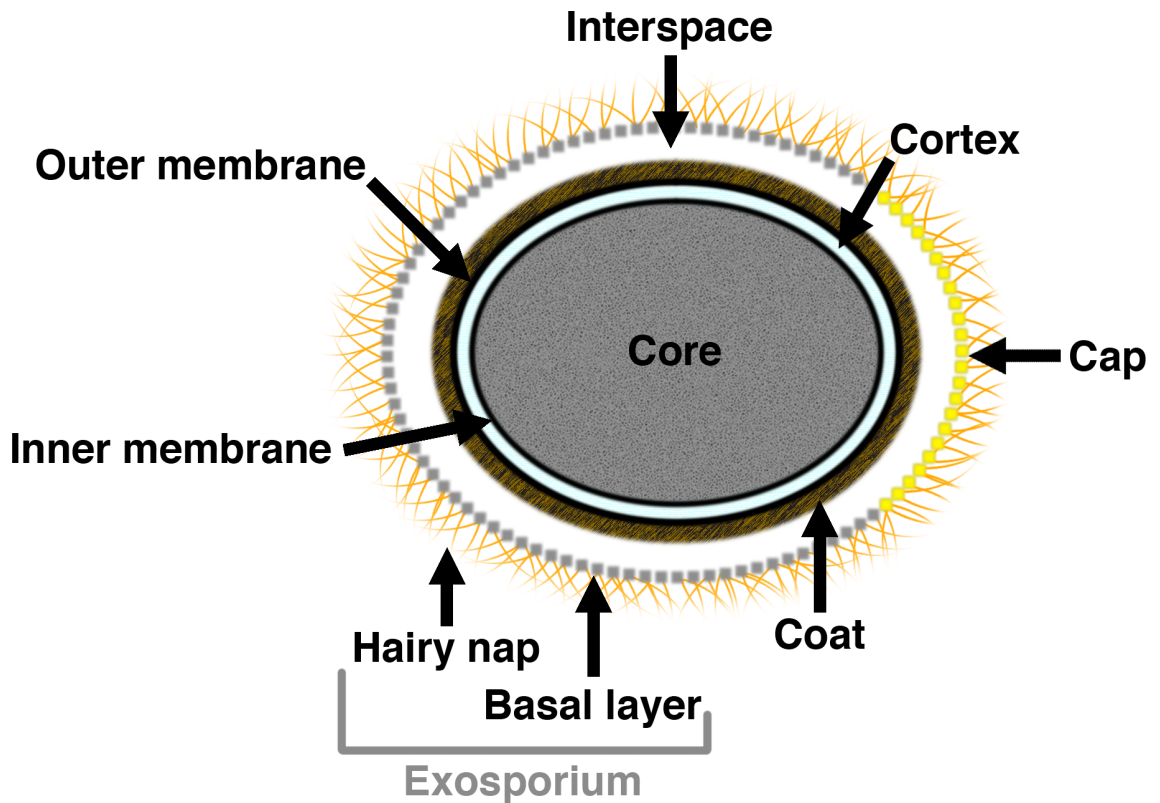


**Figure 1.2** A schematic diagram of a matured *B. cereus* spore. The architecture of the spore is composed of multiple layers of protein with a central dehydrated spore core, surrounded by a peptidoglycan cortex and proteinaceous coat. In some *Bacilli* an external balloon-like structure, the exosporium, and interspace region is also found. The exosporium can be segregated into a crystalline basal layer and an array of hairy nap-like protrusions extending into the external environment. A region of the exosporium has also been designated as the cap region composed of different exosporium proteins. The cap region is the first area of the exosporium to form during sporulation and the exit location for newly germinated cells.

### 1.4.3 The germ cell wall, cortex and outer membrane

The cortex lies between the inner and outer membrane of the spore and is composed of a spore specific peptidoglycan. The peptide side chains are removed from 50 % of the *N*-acetylmuramic acid residues making up the glycan strand, which are converted to muramic- $\delta$ -lactam, whilst another 24 % are shortened to single L-alanine residues (Meador-Parton and Popham, 2000). The resulting peptidoglycan present in the thick cortex layer is significantly less cross-linked than peptidoglycan found in vegetative cell walls (Atrih and Foster, 1999, Warth and Strominger, 1972).

A thinner germ cell wall layer sits under the cortex and is composed of a peptidoglycan identical to that found in normal vegetative cells (Atrih and Foster, 1999). The germ cell wall acts as a template for vegetative cell wall growth during germination and expands with the spore core as it rehydrates (Paidhungat and Setlow, 2002).

The outer membrane resides between the spore coat and cortex, with specific functions unknown. The removal of the outer membrane has no noticeable impact on spore resistance (Setlow, 2006) but is an essential structure in spore formation (Piggot and Hilbert, 2004). Ramamurthi *et al.*, (2006) showed a co-dependent localisation between the spore coat morphogenic protein, SpoIVA, and a 26-amino-acid peptide, SpoVM. SpoVM interacts with SpoIVA and has been modelled to show its association with the forespore outer membrane (Ramamurthi *et al.*, 2006).

### 1.4.4 The spore coat

The spore coat is a robust multi-layered structure composed of more than seventy different proteins that resides on the outside of the outer membrane (Henriques and Moran, 2007, Laaberki and Dworkin, 2008, McKenney and Eichenberger, 2012). In many *Bacilli* that lack an exosporium, such as *B. subtilis*, the spore coat forms the outermost layer of the spore, which can vary in thickness between species (Aronson and Fitz-James, 1976). The spore coats of many *Bacilli* were imaged using TEM by Holt and Leadbetter, (1969) using freeze-etched preparations, showing sections through the layers of the spore composed of many ordered ultrastructures (Holt and Leadbetter, 1969). Aronson and Fitz-James, (1976) and Wehrli *et al.*, (1980) further examined these ordered structures in *B. cereus* and *B. thuringiensis* spores, denoting a “Cross Patched” and “Pitted” layer, similar to the structures seen by Holt and Leadbetter using the same technique. Ball *et al.*, (2008) also discovered in exosporium preparations, the presence of natural crystals with periodicity similar to that of the

“pitted” layer. These “pitted” crystals, denoted as “type III”, were postulated to be from the spore coat and hence rare in exosporium preparations (Ball *et al.*, 2008).

The spore coat of *B. subtilis* has been divided into three concentric complex layers, seen in thin sections by TEM, forming a striated outer coat, lamellar inner layer and amorphous undercoat (Driks, 2004, Driks, 1999, Driks *et al.*, 1994, Henriques and Moran, 2000). More recently, *B. subtilis* spores with mutations in their spore coat proteins have been visualised by atomic force microscopy (AFM), revealing a series of structures that include features not previously seen (Plomp *et al.*, 2014). The multiple coat layers seen by Plomp *et al.* are described in Figure 1.3. Although Plomp *et al.* have shown the presence of more structural layers, it is possible that some of these could reflect aberrant coat organisation in mutants rather than natural formations. Some coat layers seen by AFM do correlate well with previous findings. An amorphous outer layer is seen by Plomp *et al.*, most likely corresponding to the amorphous glycoprotein crust visible in cross-sections of *B. subtilis* spores stained with ruthenium red (Waller *et al.*, 2004) The underlying rodlet layer, seen by AFM, contributes to the similar features seen in the previously denoted “Cross Patched layer” (Aronson and Fitz-James, 1976, Holt and Leadbetter, 1969).

The multi-layered structure of the spore coat makes it ideal in excluding large proteins, such as proteases, whilst also protecting the spore against chemical and mechanical damage (Bloomfield and Megid, 1994). The robustness and protection is proposed to be achieved by the formation of high molecular weight complexes between covalently cross-linked spore coat proteins, of which some are highly cysteine rich (Aronson and Fitz-James, 1971, Goldman and Tipper, 1978, Krajcikova *et al.*, 2009, Pandey and Aronson, 1979, Zhang *et al.*, 1993). Other covalent crosslinks such as  $\epsilon$ -( $\gamma$ -glutamyl)-lysyl isopeptide bonds have also been identified in stabilising the spore architecture (Kobayashi, 1996). Although the spore coat is fundamentally robust, it retains the capacity for nutrients to penetrate and reach receptors on the spore core. Therefore, the coat structure also acts as a molecular sieve that can both filter harmful molecules and permit access by germinants (Driks, 1999).

#### **1.4.4.1 Composition of the spore coat**

The protein composition of the spore coat has been studied, predominantly in *B. subtilis* but also in other *Bacilli* and *Clostridia*, using many different techniques. A reverse genetics approach was initially used through the N-terminal sequencing of

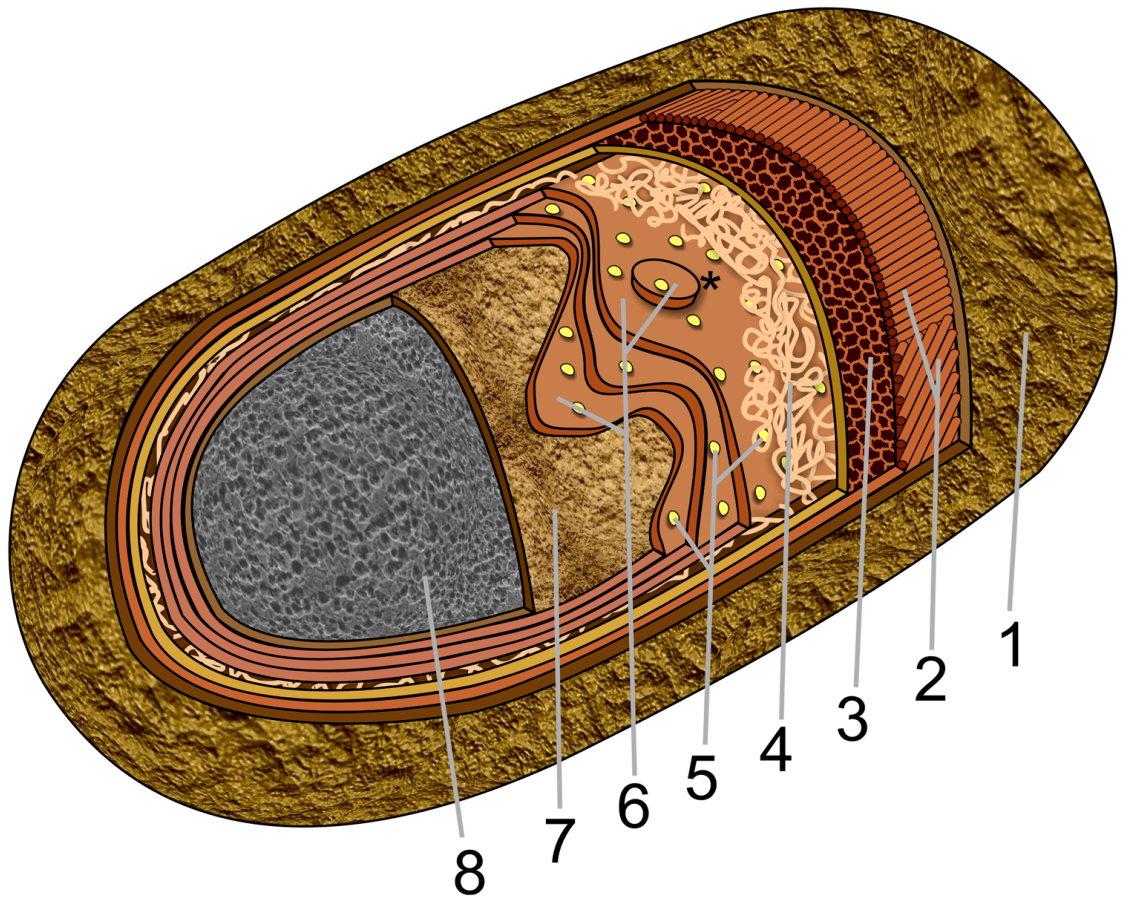


**Figure 1.3 A schematic diagram the layers contributing to the *B. subtilis* spore coat.** (1) The outermost amorphous crust; (2) the rodlet layer; (3) the honeycomb layer; (4) the fibrous granular layer; (5) the multilayer with nanodots; (6) a two-dimensional nucleus on the nanodot multilayer and (7) the basement layer. (8) Indicates the pitted surface of the cortex. Schematic diagram from: Plomp *et al*, 2014.

polypeptides separated by SDS-PAGE of spore extracts (Donovan *et al.*, 1987, Zhang *et al.*, 1993). This method isolated coat proteins such as CotY and CotZ from the spore crust, which are discussed in detail below. More recent proteomic approaches have utilised mass spectrometry (Abhyankar *et al.*, 2011, Lai *et al.*, 2003) and transcriptional profiling to identify insoluble spore coat proteins and interaction networks between proteins within the spore coat (Kim *et al.*, 2006). Proteins contributing towards the spore coat were also determined from mutant spores that displayed phenotypical changes in the spore coat structure, observed in TEM cross sections of whole spores (Zhang *et al.*, 1993), and functional properties such as lysozyme sensitivity (Riesenman and Nicholson, 2000). Mutant spores showing altered coat structures and resistance properties led to the discovery of key morphogenetic proteins, such as CotE discussed below, which are essential towards correct spore coat formation. The assembly of spore coat proteins and their respective localisation with the spore during maturation has been determined in real-time using fluorescent antibody labelling (Imamura *et al.*, 2011) and fluorescent protein fusions (Imamura *et al.*, 2010, Kim *et al.*, 2006, McKenney and Eichenberger, 2012).

The spore coat of different species of *Bacilli* (and also *Clostridia*) all form robust protective structures but vary in composition with unique proteins found in each species (Aronson, 2012). A review of the various proteins found in the spore coat of *Bacilli* can be found in Aronson, 2012, Henriques and Moran, 2007 and McKenney *et al.*, 2013. A selection of spore coat proteins found within *C. difficile* has recently been identified by Permponpattana *et al.*, (2013).

In this thesis, the coat proteins CotE, CotY and CotZ have been examined and information regarding each protein will be given below. The locations of these proteins are shown in Figure 1.4.

#### 1.4.4.1.1 CotY (*B. subtilis*)

CotY is present in the crust of the *B. subtilis* spore coat (Driks, 1999, Imamura *et al.*, 2011). The *cotY* gene is found within a cluster that contains *cotV*, *cotW*, *cotX*, *cotY* and *cotZ* which are all transcribed during the latter stages of sporulation (Zhang *et al.*, 1993, Zhang *et al.*, 1994). A *cotY* mutation does not greatly affect the properties of the spore with only subtle defects seen in germination properties (Driks, 1999). However, Zhang *et al.*, (1993) showed, through thin sections of *B. subtilis* spores, that mutation of the

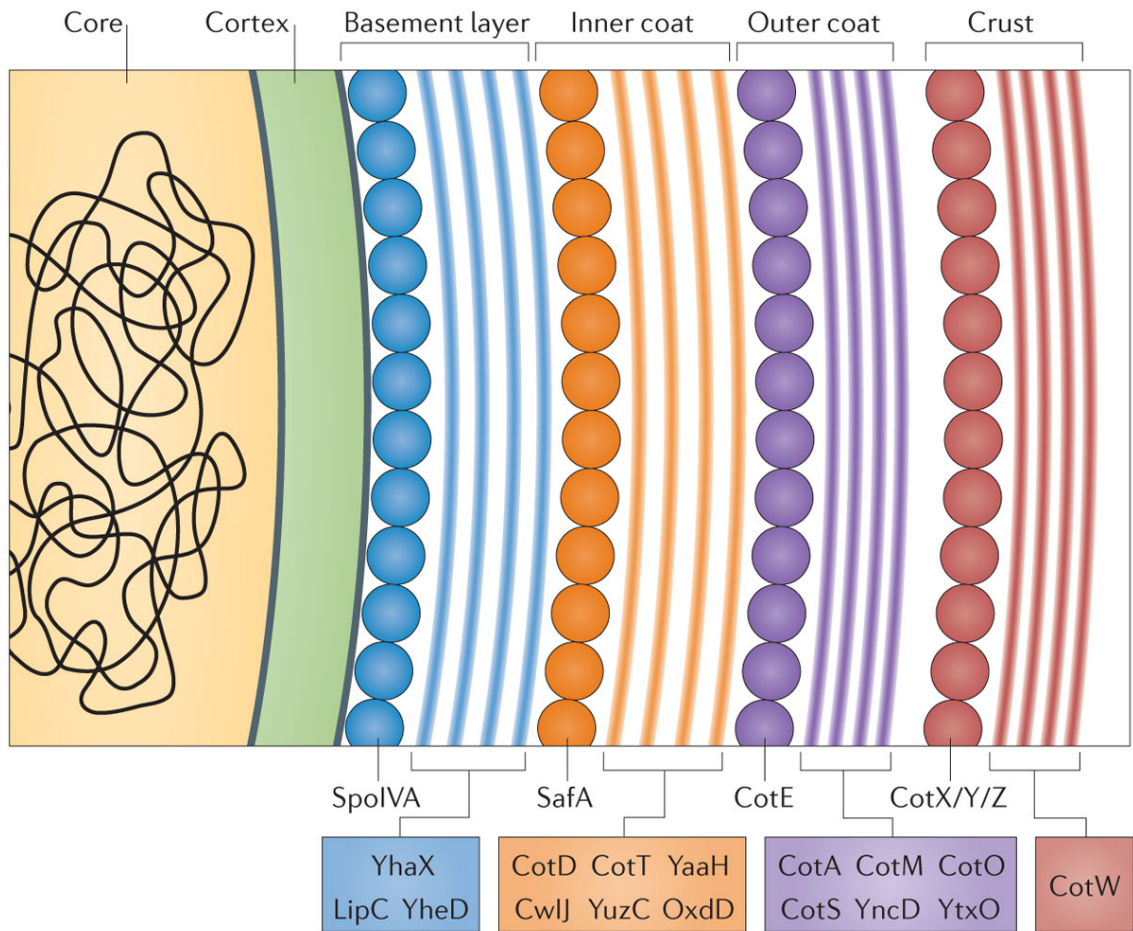


**Figure 1.4 A schematic diagram showing the network of proteins making up the *B. subtilis* spore coat.** The multiple layers of the spore coat assemble through the multimerisation of morphogenic proteins followed by the assembly of other coat proteins. CotE, CotY and CotZ are all morphogenic proteins that are related to the formation of the outer coat and crust. How each coat layer interacts with its adjoining layers is not yet known. Figure from McKenney *et al*, 2013.

*cotXYZ* genes together resulted in a spore with an incomplete outer spore coat (Zhang *et al.*, 1993).

CotY is a 161 amino acid protein that contains 15 cysteine residues. During sporulation, CotY is amongst the most highly expressed proteins along with CotE, CotV, CotW, CotX and CotZ (Mader *et al.*, 2012, Nicolas *et al.*, 2012). CotY appears as a multimeric complexes in spore extracts, detected by immunoblotting (Zhang *et al.*, 1993). Krajcikova *et al.*, (2009) also showed using yeast two-hybrid analysis that CotY has the capacity to form homotypic interactions (Krajcikova *et al.*, 2009). In the same study, CotY was also shown to interact strongly with another cysteine rich homologue, CotZ, found in the *B. subtilis* spore coat (Krajcikova *et al.*, 2009). The high cysteine content of CotY indicates the potential for multimeric assemblies through intermolecular, and also intramolecular, covalent disulphide cross-links.

In addition to *B. subtilis* CotZ, CotY also shares homology with two orthologues found in *B. anthracis*: ExsY and CotY (Redmond *et al.*, 2004). ExsY and CotY from the *B. anthracis* share ~35 % sequence identity with CotY and are part of the exosporium; a balloon-like outermost structure of the spore (Chapter 1.4.5) (Redmond *et al.*, 2004, Todd *et al.*, 2003).

#### 1.4.4.1.2 CotZ

CotZ is another cysteine rich protein found in the spore crust and is a homologue of CotY (46 % amino acid identity). CotZ is part of the *cotVWXYZ* gene cluster and plays a crucial role in formation of the spore crust but not of the spore coat (Imamura *et al.*, 2011, Zhang *et al.*, 1993). CotZ mutant spores lack a spore crust, but they remain resistant to lysozyme and heat treatment (Imamura *et al.*, 2011). Spores with a deletion in either *cotX* or *cotY* display the same phenotype as that of a *cotXYZ* triple mutant, indicating that CotZ has minor contributions towards spore resistance (Driks, 1999). Aside from providing a very insoluble structure, it is not known what other functions CotZ and the spore crust provides. Although the data is not shown, Imamura *et al* (2011) identified that the anti-GFP antibodies used in immunofluorescence assays bound non-specifically to CotZ mutant spores. These spores were also noted to clump together readily. Therefore, it was proposed from these two factors that CotZ is in part responsible for the formation of a spore crust that engulfs the spore completely and prevents clumping to allow spores to distribute within the environment (Imamura *et al.*, 2011).

#### 1.4.4.1.3 CotE

CotE is an essential morphogenic protein involved in the assembly and organisation of the layers of the spore coat (Driks *et al.*, 1994, McKenney and Eichenberger, 2012, Zheng *et al.*, 1988). During sporulation, CotE is localised to the interface between the inner and outer coat of the spore in a SpoIVA dependent manner (Bauer *et al.*, 1999, Driks *et al.*, 1994). Once localised, CotE forms a loose ring around from the forespore with a matrix region sequestered in between. The proteins involved in inner coat formation then infiltrate the CotE ring and assemble between the ring and forespore (Driks, 1999, Driks *et al.*, 1994). *cotE* mutant spores only possess an inner coat, however it was seen that material, proposed to be aggregates of outer coat proteins, were associated to the inner coat in older cultures. The correct formation of the outer coat is dependent on CotE and its association with specific outer coat proteins (Driks *et al.*, 1994, McKenney *et al.*, 2013) (Fig. 1.4).

The function of regions of CotE has been studied extensively through electron microscopy of mutant spores and molecular approaches. Bauer *et al.*, (1999) showed the C-terminal 23 amino acids to be crucial in the assembly of various spore coat proteins. An epitope added just before the C-terminal 23 amino acid region interfered with the assembly of CotS, CotB and CotG amongst others, seen by the lack of particular bands in SDS-PAGE analysis of spore coat extracts. Cross-section of the spore coat interestingly appeared like that of wild type *B. subtilis* spores. The deletion of the last 9, and up to 23, amino acids from the C-terminus resulted in a thin outer coat. Removal of the last 37 amino acids from the C-terminus resulted in no visible outer coat but did not affect the localisation of CotE to the forespore (Bauer *et al.*, 1999). An internal 35 amino acid sequence targets CotE to the forespore and in conjunction with an 18 amino acid region in the N-terminus, form CotE homooligomers (Little and Driks, 2001).

#### **1.4.5 The interspace**

In species of *Bacillus* and *Clostridium* that form an exosporium, a not well-studied region, the interspace, separates the exosporium from the rest of the spore (Fig. 1.5 [Is]). The interspace of *B. cereus* group spores appears to be devoid of visible material (Giorno *et al.*, 2007) with exceptions such as the occasional “type I” sub-exosporal crystals (Ball *et al.*, 2008) and *B. thuringiensis* toxin (Smirnova *et al.*, 1984).

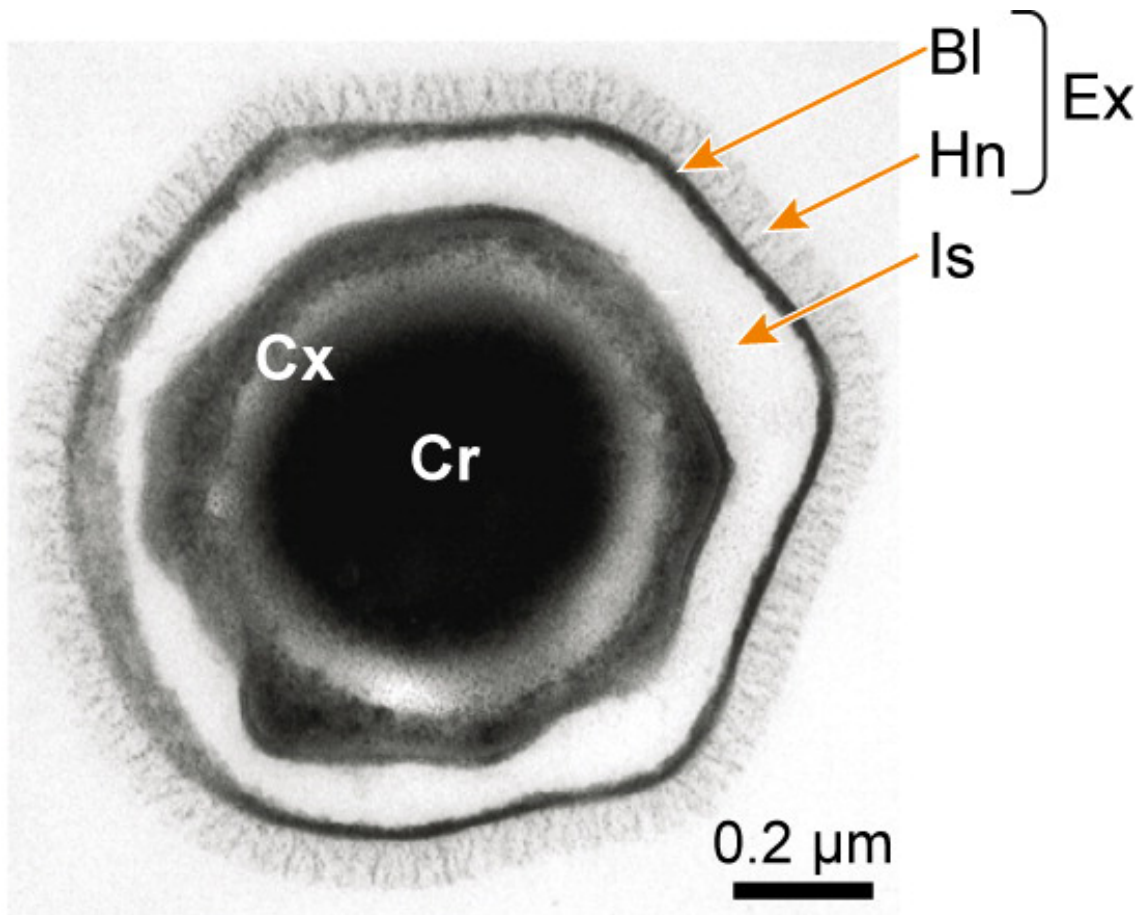


**Figure 1.5 Cross section through a *B. anthracis* spore.** The exosporium (Ex) is the outermost layer in spores of the *B. cereus* group. The exosporium forms a single layer around the spore and is divided into a crystalline basal layer (Bl) and hairy nap layer (Hn). An interspace (Is) exists between the exosporium and the rest of the spore. (Cr) and (Cx) indicate core and cortex respectively. Figure adapted from Henriques and Moran, 2007.

It was hypothesised that during the simultaneous development of the exosporium and spore coat that the two structures should be conjoined with interlinking material (Ohye and Murrell, 1973). Lamellar inclusions are found in the interspace of *B. megaterium* and some *Clostridia* linking the exosporium to the rest of the spore, which are not present in the *B. cereus* group (Beaman *et al.*, 1972, Gerhardt *et al.*, 1976, Lund *et al.*, 1978, Mackey and Morris, 1972), suggesting a possible breakdown of connective components after maturation (Ohye and Murrell, 1973).

#### 1.4.6 The exosporium

The exosporium is a balloon-like sac structure that surrounds the endospore. It forms the outermost structure of certain *Clostridia* and all spores of the *B. cereus* group (Desrosier and Lara, 1984, Gerhardt and Ribi, 1964, Mackey and Morris, 1972) (Fig. 1.5 [Ex]). All *B. cereus* group spores share a similar exosporium structure- a paracrystalline basal layer covered with hair-like projections (Beaman *et al.*, 1972, Gerhardt and Ribi, 1964, Hachisuka *et al.*, 1966). In spores of *B. anthracis*, these hair-like projections, often referred to as the “hairy nap”, are composed of the glycoprotein BclA (Sylvestre *et al.*, 2002) and can range up to 600 Å in length (Sylvestre *et al.*, 2003). The exosporium basal layer on the other hand is composed of greater than a dozen proteins that have been reviewed in Table 1.1. Two major proteins, ExsY, which is highly cysteine-rich, and ExsFA (BxpB), have been identified by SDS-PAGE to form a high molecular weight complex with the hairy nap protein BclA (Redmond *et al.*, 2004, Sylvestre *et al.*, 2002). ExsY, ExsFA and BclA are discussed in more detail in 1.4.6.3.

The basal layer of the *B. cereus* exosporium was shown to be formed from a naturally crystalline array, composed of a cup and crown structure with small pores on the surface and a unit cell of  $a = b = \sim 80 \text{ \AA}$ ,  $\gamma = \sim 120^\circ$ . (Ball *et al.*, 2008) (Fig. 1.6 A). A higher resolution Cryogenic-electron microscopy (Cryo-EM) structure of the exosporium in projection identified that the basal array appeared to be composed of an  $\alpha$ -helical structure with six strongly defined  $\alpha$ -helices per unit (Fig. 1.6 B). The presence of  $\alpha$ -helices was further supported by circular dichroism (CD) spectroscopy that suggested the exosporium contained  $\sim 75 \%$   $\alpha$ -helical content (Kailas *et al.*, 2011). The co-dependent proteins BclA and ExsFA are thought to reside at the crown structure of the exosporium model (Ball *et al.*, 2008, Kailas *et al.*, 2011). A cryo-EM projection map of a *B. anthracis bclA* mutant suggests a loss of density in the region of the crown (Rodenburg *et al.*, 2014). This however was sampled from a single cryo-EM image and hence, more iterative results are necessary for confirmation.

<b>Protein</b>	<b>Function</b>	<b>Reference</b>
<b>Alr</b>	Alanine racemase catalyses the inter-conversion of L-alanine to D-alanine. In <i>B. anthracis</i> , Alr is localised around the whole the exosporium, but devoid from the cap structure <sup>1</sup> . Alanine racemase regulates spontaneous germination by the conversion of L-Ala to D-Ala, a competitive inhibitor <sup>2</sup> .	<sup>1</sup> (Steichen <i>et al.</i> , 2007), <sup>2</sup> (Yasuda <i>et al.</i> , 1993)
<b>Arginase</b>	Arginase acts as a protective protein against macrophage-mediated killing. In <i>B. anthracis</i> , arginase functions by lowering the concentration of toxic nitric oxide species within macrophages.	(Weaver <i>et al.</i> , 2007)
<b>BetA</b>	Function unknown	Reviewed in 1.4.6.3.7
<b>BclA</b>	The hairy nap protein on the surface of <i>B. anthracis</i> .	Reviewed in 1.4.6.3.6
<b>BclB</b>	A paralogue of BclA found in the exosporium of <i>B. anthracis</i> .	Reviewed in 1.4.6.3.6
<b>CotB-1, -2</b>	CotB found in <i>B. anthracis</i> is a homologue of the <i>B. subtilis</i> CotB, which is an outer coat protein.	(Redmond <i>et al.</i> , 2004)
<b>CotE</b>	CotE was detected in the exosporium of <i>B. cereus</i> but not in <i>B. anthracis</i> . The majority of $\Delta cotE$ mutant endospores had no exosporium attached.	Reviewed in 1.4.6.3.7
<b>CotY</b>	A paralogue of ExsY found in the exosporium. Proposed to be a major component of the exosporium cap structure.	Reviewed in 1.4.6.3.5
<b>ExsA</b>	ExsA has a dramatic role in spore morphology, and in part homologous to the morphogenetic protein SafA from <i>B. subtilis</i> . $\Delta exsA$ endospores possess a thinner, loosely attached exosporium	Reviewed in 1.4.6.3.7
<b>ExsB</b>	$\Delta exsB$ mutant endospores still produce a complete exosporium, however, the exosporium is loosely attached to the spore.	Reviewed in 1.4.6.3.7
<b>ExsC</b>	Function unknown	(Todd <i>et al.</i> , 2003)
<b>ExsD</b>	Function unknown	(Todd <i>et al.</i> , 2003)
<b>ExsE</b>	Putative lipoprotein that contains three predicted transmembrane helices. Function unknown	(Todd <i>et al.</i> , 2003)
<b>ExsFA (BxpB)</b>	An exosporium protein involved in the incorporation of the hairy nap.	Reviewed in 1.4.6.3.1

<b>ExsFB</b>	A paralogue of ExsFA found in the exosporium of <i>B. anthracis</i> . ExsFB also plays a role in incorporation of the hairy nap.	Reviewed in 1.4.6.3.2
<b>ExsG</b>	Function unknown	(Todd <i>et al.</i> , 2003)
<b>ExsH</b>	Homologue of ExsJ	(Todd <i>et al.</i> , 2003)
<b>ExsI</b>	Predicted glycoprotein related to ExsJ	(Todd <i>et al.</i> , 2003)
<b>ExsJ</b>	Collagen-like glycoprotein found in <i>B. cereus</i> and <i>B. thuringiensis</i> but not in <i>B. anthracis</i> .	(Charlton <i>et al.</i> , 1999, Garcia-Patrone and Tandecarz, 1995, Todd <i>et al.</i> , 2003)
<b>ExsK</b>	Cystine-rich protein found in the exosporium of <i>B. cereus</i> group strains.	Reviewed in 1.4.6.3.3
<b>Fe/Mn-SOD</b>	Fe/Mn superoxide dismutase provides protection towards the germinating <i>Bacilli</i> from oxidative damage until full maturity.	(Baillie <i>et al.</i> , 2005)
<b>InH</b>	Inosine hydrolase plays a similar role as alanine racemase in moderating the rate of germination by levels of inosine in the environment.	(Todd <i>et al.</i> , 2003)
<b>YwdL</b>	YwdL is found on the inner surface of the <i>B. cereus</i> and <i>B. thuringiensis</i> exosporium. The exosporium in $\Delta ywdL$ mutant spores is more fragile but the crystallinity of the basal layer remains unaffected. No change is seen in the spores' resistance properties. However, $\Delta ywdL$ mutant spores cannot germinate in response to $Ca^{2+}$ DPA and possess altered germination properties.	(Terry <i>et al.</i> , 2011)

**Table 1.1. Exosporium proteins identified in *B. cereus* group strains.**

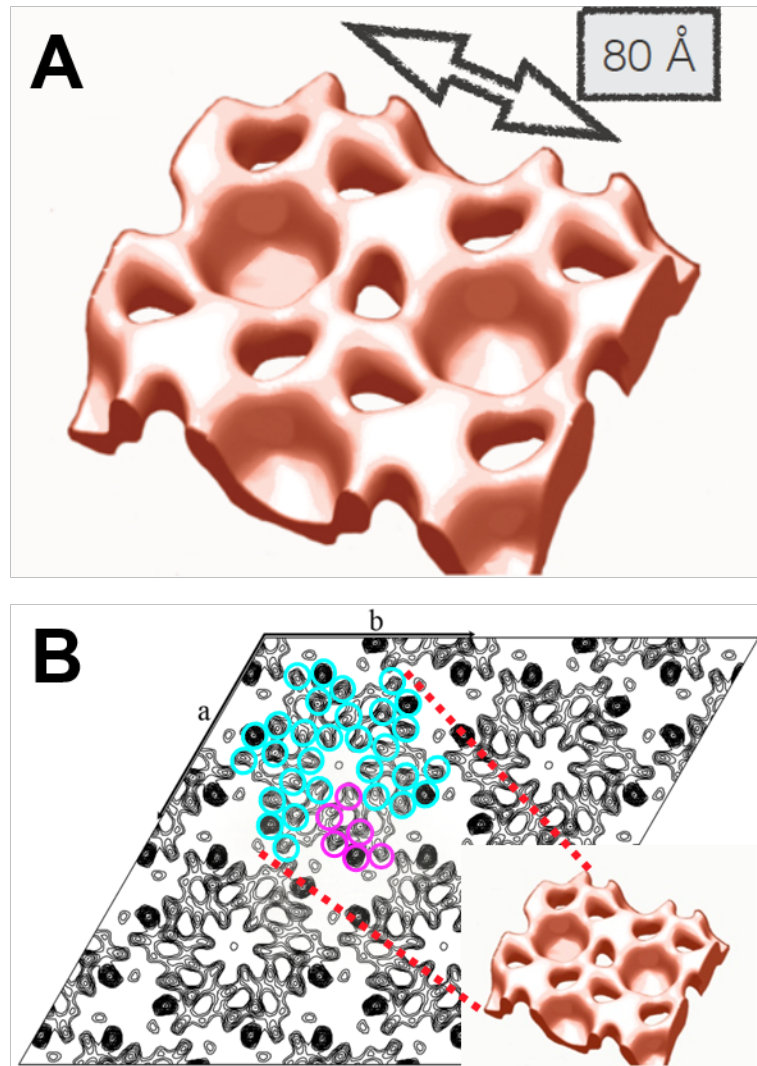


**Figure 1.6 Structure of the *B. cereus* exosporium.** (A) Low resolution negative stain reconstruction in three-dimensions showing a cup and crown structure with small pores. (B) High resolution two-dimensional cryoEM map with indications of strong  $\alpha$ -helical structure. Figure adapted from Kailas *et al.*, 2011.

The reported structures of exosporium from several strains of *Clostridia* showed that many also possessed a crystalline hexagonal lattice, much like that of the *B. cereus* exosporium (Hodgkiss *et al.*, 1967, Lund *et al.*, 1978). Recently, cysteine-rich and collagen-like proteins have been reported in the exosporium of *C. difficile* (Barra-Carrasco *et al.*, 2013, Pizarro-Guajardo *et al.*, 2014) suggesting some structural similarities to *B. cereus* exosporium proteins.

#### **1.4.6.1 Function of the exosporium**

The function of the exosporium is as yet unclear but it is known to be the initial contact surface for the spore with its external environment. The “hairy nap”, composed of the protein BclA, is the immunodominant component of the exosporium (Steichen *et al.*, 2003, Sylvestre *et al.*, 2002). Furthermore, the C-terminal head domain of BclA contains a tumour necrosis factor (TNF)-like domain that is thought to recognise hydrophobic components in the host (Rety *et al.*, 2005). The exosporium does not appear to influence the resistance properties of the spore (Boydston *et al.*, 2006, Johnson *et al.*, 2006, Thompson and Stewart, 2008) or pathogenesis in *B. anthracis* (Bozue *et al.*, 2007, Giorno *et al.*, 2007). It does however, appear to function in tissue adhesion and suppression of the innate immune system during infection (Basu *et al.*, 2007, Bozue *et al.*, 2007, Oliva *et al.*, 2009, Oliva *et al.*, 2008).

The porous structure of the exosporium is suggestive of a role as a molecular sieve, acting as a semi-permeable barrier to exclude harmful hydrolytic enzymes and antibodies whilst allowing for the passage of small germinants (Ball *et al.*, 2008, Gerhardt, 1967, Gerhardt and Black, 1961). Functional enzymes have been found adsorbed and preserved on the exosporium indicating its role as a molecular scaffold. Alanine racemase and nucleoside hydrolase are proteins that do not contribute to the integral structure of the exosporium, but are however tightly adsorbed onto the surface (Steichen *et al.*, 2003, Steichen *et al.*, 2007, Todd *et al.*, 2003). Alanine racemase at least, plays an important role in the prevention of premature germination through the modification of L-alanine to D-alanine, a germination inhibitor (Chesnokova *et al.*, 2009). Other proteins have been identified which appear to aid the spores survival during infection. SOD15 and SODA1 are two superoxide dismutase enzymes that are more loosely associated with the exosporium and protect *B. anthracis* spores against oxidative stress during infection (Cybulski *et al.*, 2008). Arginase is also present in the exosporium; it likely protects *B. anthracis* spores against macrophage-mediated killing

by lowering the concentration of toxic nitric oxide species in the macrophage (Weaver *et al.*, 2007).

#### **1.4.6.2 Formation and assembly of the exosporium**

Exosporium antigens can be detected in sporulating cells from about Stage III (Desrosier and Lara, 1984). DNA microarrays were used to monitor gene expression during sporulation (Liu *et al.*, 2004). Assembly of the exosporium, along with the cortex and coat, is dependent on SpoIVA, which is detected at 1.5 hours into the sporulation process and functions to anchor the spore coat components to the surface (Giorno *et al.*, 2007). The morphogenetic proteins ExsA and CotE are also expressed during the early stages of germination (at 2 hours) (Bailey-Smith *et al.*, 2005). Exosporium proteins, including BclA, CotY, ExsB, ExsFA/ExsFB, ExsK and ExsY (Boydston *et al.*, 2006, McPherson *et al.*, 2010, Severson *et al.*, 2009, Sylvestre *et al.*, 2002, Sylvestre *et al.*, 2005), are all expressed after engulfment of the spore core. The genes for *bclA*, *cotY*, *exsFA* and *exsY* are arranged in a cluster on the chromosome (Todd *et al.*, 2003).

The presence of exosporium proteins and formations were detected after 3 hours into sporulation using exosporium specific antibodies and electron microscopy (Desrosier and Lara, 1984, Ohye and Murrell, 1973). Exosporium assembly begins with the formation of a “cap” structure, composed of CotY, towards the middle of the mother cell (Boydston *et al.*, 2006, Steichen *et al.*, 2007, Thompson *et al.*, 2012). Subsequent extension of the exosporium completely around the spore requires the presence of ExsY (Boydston *et al.*, 2006), with *exsY* mutant endospores only displaying an exosporium cap towards one pole (Boydston *et al.*, 2006, Johnson *et al.*, 2006). Presumably, ExsFA and BclA, which are co-dependent for correct incorporation into the exosporium, (Sylvestre *et al.*, 2005, Thompson *et al.*, 2011b), associate with the template. ExsFA and BclA are only partially dissociating and have been shown to form a high molecular weight complex, observed on protein gels of purified exosporium (Redmond *et al.*, 2004, Steichen *et al.*, 2005, Sylvestre *et al.*, 2002, Sylvestre *et al.*, 2005). Although the proteins and temporal period of association between exosporium proteins is known, the intrinsic mechanism of assembly remains elusive.

#### **1.4.6.3 Composition of the exosporium**

The exosporium is composed predominantly of proteins (~50 %), lipids (~20 %), carbohydrates (~20 %) and other components, such as the filamentous appendages described by Kozuka and Tochikubo, (1985) (Kozuka and Tochikubo, 1985, Matz *et al.*,

1970). Many exosporium proteins have been identified and some have been strongly linked as possible architectural components (Bailey-Smith *et al.*, 2005, Boydston *et al.*, 2006, Fazzini *et al.*, 2010, Giorno *et al.*, 2007, Johnson *et al.*, 2006, McPherson *et al.*, 2010, Severson *et al.*, 2009, Steichen *et al.*, 2005, Sylvestre *et al.*, 2005). In this section, information regarding the proteins investigated in this thesis will be given.

#### 1.4.6.3.1 ExsFA (BxpB)

ExsFA is a 17 kDa protein identified in the exosporium of both *B. cereus* (Todd *et al.*, 2003) and *B. anthracis* (Redmond *et al.*, 2004, Steichen *et al.*, 2003) and is only present in *B. cereus* group strains. Localisation of ExsFA to the basal layer of the exosporium has been shown using both immunogold and immunofluorescence labelling techniques (Giorno *et al.*, 2009, Steichen *et al.*, 2005). SDS-PAGE analysis of purified exosporium showed that ExsFA forms a high molecular weight complex with ExsY and BclA (Redmond *et al.*, 2004, Steichen *et al.*, 2005) and is necessary for the correct localisation of BclA onto the exosporium (Sylvestre *et al.*, 2005, Thompson *et al.*, 2011b). *B. anthracis* spores lacking ExsFA display either a morphological sparse hairy nap or no hairy nap around the exosporium (Steichen *et al.*, 2005, Sylvestre *et al.*, 2005). Mutant endospores lacking ExsFA still produce a crystalline exosporium basal layer (Ball, 2006).

#### 1.4.6.3.2 ExsFB

ExsFB is a paralogue of ExsFA found in *B. anthracis* (Sylvestre *et al.*, 2005) and also *B. cereus*. ExsFB shares ~78 % sequence identity with ExsFA and differs in sequence at the N-terminal domain. The role of ExsFB in anchoring of the hairy nap within the exosporium appears minimal in the presence of ExsFA; *B. anthracis* *exsFB* mutant endospores showed little to no change in nap morphology or abundance (Sylvestre *et al.*, 2005). Removal of *exsFA* shows spores that contain a sparse hairy nap, presumably anchored by ExsFB with null mutations in both *exsFA* and *exsFB* necessary to completely devoid the spore of nap (Sylvestre *et al.*, 2005).

#### 1.4.6.3.3 ExsK

ExsK is a 12 kDa cysteine-rich protein found only in the *B. cereus* group (Liu *et al.*, 2004, Redmond *et al.*, 2004). ExsK has been detected on both the surface and underneath the exosporium by immunofluorescence microscopy and flow cytometry (Severson *et al.*, 2009). Western blots revealed that ExsK runs at the position of the high molecular weight complex that could also contain ExsY, ExsFA and BclA

(Severson *et al.*, 2009, Terry, 2010). The morphology of the spore does not appear to differ in an *exsK* mutant, but it has been shown that ExsK does indeed interact with components of the high molecular complex in a dependent manner. In *exsFA* mutant endospores, ExsK appears to only localise to the cap region of the spore whilst a *bclA* mutation results in the loss of its incorporation into the high molecular weight complex altogether (Severson *et al.*, 2009). This dependence of ExsK incorporation into the high molecular weight complex suggests a possible role in stabilisation rather than directly influencing the formation of the exosporium.

#### 1.4.6.3.4 ExsY

ExsY is a highly conserved 16 kDa cysteine-rich protein found in all *B. cereus* group strains and was first identified as part of the *B. anthracis* exosporium (Redmond *et al.*, 2004). ExsY shares >90 % sequence identity with a paralogue, CotY, found in *B. cereus* group strains. It shares ~35 % sequence identity with distant homologues CotY and CotZ in *B. subtilis* (Zhang *et al.*, 1993). ExsY, ExsFA and BclA have been shown to form a high molecular weight complex on SDS-PAGE gels and immunoblotting of the exosporium (Redmond *et al.*, 2004, Steichen *et al.*, 2005).

ExsY is required for the formation of a complete exosporium in both *B. cereus* (Johnson *et al.*, 2006) and *B. anthracis* (Boydston *et al.*, 2006). Mutants that lack the *exsY* gene display an incomplete exosporium with only a “cap-like” structure appearing at one pole of the spore (Boydston *et al.*, 2006, Johnson *et al.*, 2006). The loss of ExsY also increases the susceptibility of spores to lysozyme (Johnson *et al.*, 2006), suggesting that the spore coat is also affected.

#### 1.4.6.3.5 CotY (*B. cereus*)

CotY is a 16 kDa cysteine-rich protein and paralogue of ExsY. It shares similar homology to the *B. subtilis* coat proteins as described in 1.4.6.3.4 for ExsY. In contrast to ExsY, a mutation in the *cotY* gene results in endospores that do not appear drastically different from wild type endospores. Cross sections of *cotY* mutant endospores show a completely enclosing exosporium, although it is tighter and less “balloon-like” (Johnson *et al.*, 2006).

Endospores that lack both ExsY and CotY appear to be devoid of any exosporium around the spore; hence CotY has been deemed responsible for the template formation within the exosporium cap structure (Steichen *et al.*, 2007, Thompson *et al.*, 2012)

whilst the rest of the exosporium basal layer has been postulated to be composed of ExsY (Kailas *et al.*, 2011). The absence of ExsY, and more dramatically the absence of both ExsY and CotY, also affects coat assembly (Johnson *et al.*, 2006), suggesting they that also contribute in some way to coat structure.

#### 1.4.6.3.6 BclA and other glycoproteins

BclA (*Bacillus collagen-like protein of anthracis*) is the best-characterised glycoprotein in the exosporium and is responsible for the “hairy- nap” structure seen on the surface of the *B. anthracis* exosporium (Sylvestre *et al.*, 2002). BclA in *B. anthracis* is expressed as a 37.2-kDa monomer (Sylvestre *et al.*, 2002). It contains a variable collagen-like region composed predominately of glycine-proline-threonine repeats (Castanha *et al.*, 2006, Sylvestre *et al.*, 2003) and is highly glycosylated (Daubenspeck *et al.*, 2004, Henriques and Moran, 2007). Within the exosporium, BclA is found as part of a high molecular weight complex with ExsFA and ExsY. The genes for *bclA*, glycosyltransferases, and enzymes for rhamnose biosynthesis are all present in the same chromosomal region as *cotY*, *exsY* and *exsFA* (Redmond *et al.*, 2004, Steichen *et al.*, 2005, Todd *et al.*, 2003).

Each BclA “hairy nap” filament is composed of a BclA trimer (Boydston *et al.*, 2005) that contains a processed N-terminal attachment domain (Tan and Turnbough, 2010, Thompson and Stewart, 2008), a C-terminal TNF-like domain (Rety *et al.*, 2005) and a central collagen-like triple helix (Castanha *et al.*, 2006, Sylvestre *et al.*, 2003). In mature endospores, the N-terminal domain lacks the first 19 amino acids, which have been proteolytically processed, when incorporated into the exosporium (Steichen *et al.*, 2003, Sylvestre *et al.*, 2002, Tan and Turnbough, 2010). The structure of the C-terminal domain was solved by Rety *et al.*, (2005) and appears structurally similar to that of C1q, belonging to the TNF-like family of proteins. It is also thought that nucleation of the BclA trimer occurs at the interface of the C-terminal domain (Rety *et al.*, 2005). The central glycosylated collagen-like repeat domain is highly variable in length and has been used for the identification of different strains of *B. anthracis* (Castanha 2005, Sylvestre, 2003). Formation of a collagen triple helix requires the presence of prolyl 4-hydroxylase to catalyse the post-translational modification of proline to hydroxyproline. Prolyl 4-hydroxylase has been identified in *B. anthracis*, adding to the list of proteins most likely required for correct exosporium assembly (Culpepper *et al.*, 2010).

In *B. anthracis*, *bclA* mutant endospores either lack a visible hairy nap (Boydston *et al.*, 2005, Sylvestre *et al.*, 2002), or show a more incomplete nap (Steichen *et al.*, 2003), suggesting the possibility of other nap-related collagen-like repeat glycoproteins. One such protein, BclB, has been identified in *B. anthracis*, contributing to the residual nap (Thompson *et al.*, 2007, Waller *et al.*, 2005). Endospores lacking BclB still produce exosporium covered in nap; presumably composed of BclA. The exosporium however does appear loosely attached indicating some role for BclB in exosporium stability through the nap (Thompson *et al.*, 2007). A further protein, BetA, is found in the *B. anthracis* exosporium that shows a 15 amino acid N-terminal targeting motif, highly similar to the N-terminal motif found in BclA, and is predicted to contain a variable length collagen-like repeat region. Like BclA, the assembly of BetA is dependent on ExsFA, but no covalent interactions were detected between ExsFA and BetA though Western blots. BetA was however found as part of the high molecular weight complex containing BclA and ExsFA. Immunofluorescence assays showed that BetA was poorly accessible by antibodies. Therefore, it was proposed that BetA resides between the exosporium basal layer and hairy nap layer (Thompson *et al.*, 2011a). In *B. cereus* ATCC 10876 and *B. thuringiensis* Kurstaki, ExsJ is also detected as a major collagen-like repeat glycoprotein (Garcia-Patrone and Tandecarz, 1995, Todd *et al.*, 2003).

#### 1.4.6.3.7 Other exosporium proteins

Many of the other exosporium proteins identified (Table 1.1) are of unknown function. Of these proteins, only CotE appeared to be required for the assembly of the exosporium and was detected in Western blots of the exosporium from *B. cereus* (Todd *et al.*, 2003). CotE was not reported in the *B. anthracis* exosporium (Giorno *et al.*, 2007); however, *B. anthracis cotE* mutants possessed few endospores with their exosporium attached. Furthermore, relatively intact coats are often detached from the peptidoglycan layer (Giorno *et al.*, 2007). CotE from the *B. cereus* group shares 61 % amino acid sequence identity with CotE from *B. subtilis* (1.4.4.1.3) and also appears to function as a molecular scaffold; although the coat defect of a *cotE* mutant in *B. subtilis* is much more severe (1.4.4.1.3).

Of the other exosporium proteins with known function, ExsA and ExsB appear to contribute towards stability. ExsA has a dramatic role in spore morphology and appears to function in assembly, similar to SafA in the *B. subtilis* spore coat (Ozin *et al.*, 2000). *exsA* mutant endospores possess a loosely attached exosporium (Bailey-Smith *et al.*, 2005). ExsB, detected in both *B. cereus* (Todd *et al.*, 2003) and *B. anthracis* (Liu *et al.*,

2004), is required for the exosporium to be strongly attached to the rest of the spore (McPherson *et al.*, 2010).

## 1.5 Architecture of the exosporium so far

The architecture of the exosporium has been studied at intervals over the past half century using various techniques including transmission electron microscopy (TEM) and more recently, atomic force microscopy. Within the *B. cereus* group, multiple types of thin paracrystalline layers have been seen with differing unit cell dimensions, thought to originate from different layers of the spore (Gerhardt and Ribí, 1964, Scherrer and Somerville, 1977, Wehrli *et al.*, 1980). Up to three different types of crystals have been observed in spore preparations that are thought to be influenced, by growth conditions, strain and method of preparation (Gerhardt and Ribí, 1964, Remsen, 1966, Scherrer and Somerville, 1977, Wehrli *et al.*, 1980). A schematic of the different crystal layers described in Ball *et al.*, (2008) is shown in Figure 1.7.

The exosporium of *B. cereus* is composed of a hexagonal basal layer crystal, coined as the “type II” crystal by Ball *et al.*, (2008), with a hairy nap structure attached to the outermost surface (Ball *et al.*, 2008, Gerhardt and Ribí, 1964, Scherrer and Somerville, 1977, Wehrli *et al.*, 1980). The type II crystal, possessing a unit cell of  $a = b = \sim 80 \text{ \AA}$ ,  $\gamma = 120^\circ$ , has been found in all exosporium preparations and is composed of a cup and crown structure (Fig. 1.6 A and 1.7). The orientation of the cup and crown structure was determined by Kailas *et al.*, (2011) using AFM. The type II exosporium crystal showed two distinct surfaces. The outer surface appeared disordered due to the hairy nap whilst the inner surface displayed a hexagonal honeycomb array (Kailas *et al.*, 2011, Fig. 3) much like the underside of type II crystal seen by TEM. Furthermore, the outer surface was clearly visible in the *B. thuringiensis* 4D11 strain that lacks the outer hairy nap. This revealed the same inner surface honeycomb structure and in addition an open cup structure on the outer surface (Kailas *et al.*, 2011, Fig. 4).

A parasporal layer, which contains no hairy nap, is thought to reside between the exosporium and spore coat (Ball *et al.*, 2008, Scherrer and Somerville, 1977, Wehrli *et al.*, 1980). Crystals from the parasporal layer, termed “type I”, were found in certain exosporium preparations by Ball *et al.*, (2008) and showed unit cell dimensions of  $a = b = \sim 65 \text{ \AA}$ ,  $\gamma = 120^\circ$ . Their appearance is similar to that of type II crystals with cup like structures and an apparent linker (Ball *et al.*, 2008). The exact location of the type I crystal remains elusive, however, recent studies on *B. fusiformis* have suggested that

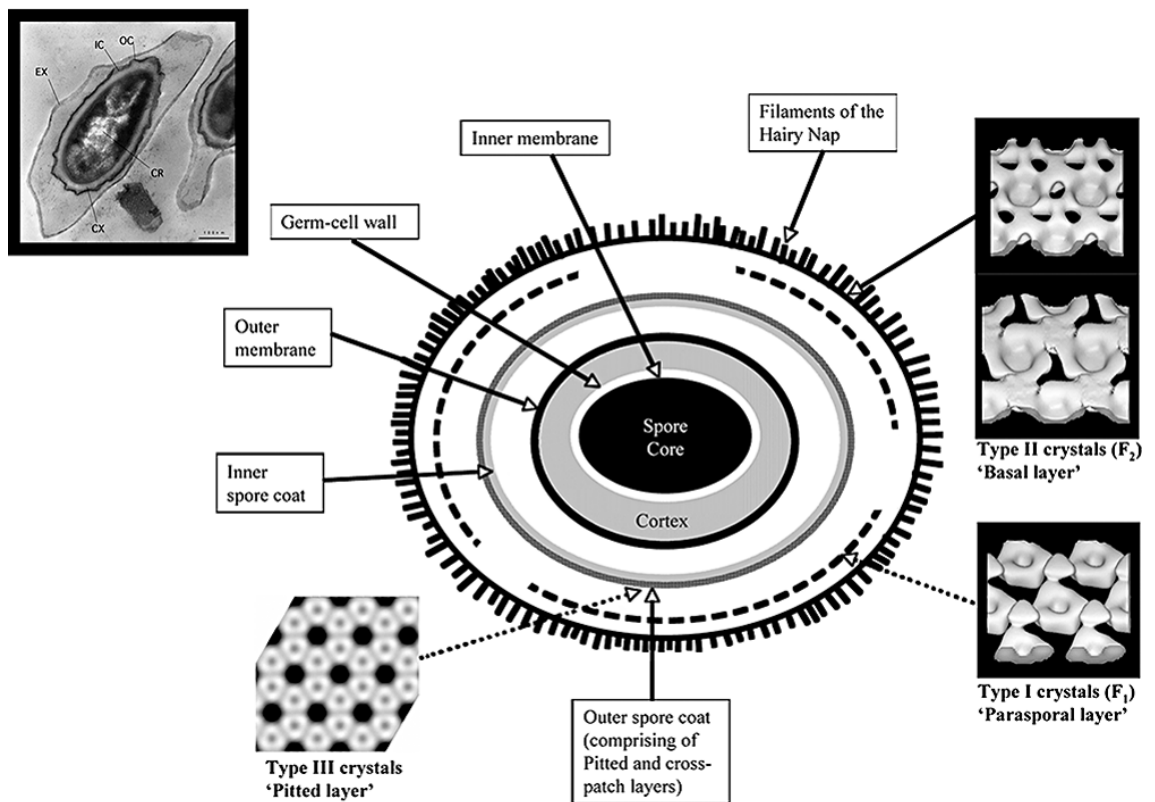


**Figure 1.7 Schematic diagram featuring the crystalline layers found within spore preparations.** Three types of crystals have been identified in exosporium preparations originating from different layers of the endospore. Type II “basal” crystals are found in the outermost exosporium, Type I “parasporal” crystals are found in the parasporal region of the spore and Type III “pitted” crystals are thought to originate from the other spore coat. Figure from Ball *et al*, 2008.

the type I crystal may in fact be a variant of the exosporium template for certain *Bacilli* (Wan, 2013).

A final pitted crystal (Aronson and Fitz-James, 1976, Holt and Leadbetter, 1969, Wehrli *et al.*, 1980), termed “type III” was observed on rare occasions in exosporium preparations (Ball *et al.*, 2008). Type III crystals possessed a much larger unit cell size at  $a = b = \sim 100 \text{ \AA}$ ,  $\gamma = 120^\circ$  (Ball *et al.*, 2008) and appeared to correspond to the “Pitted layer” of the spore coat seen by Aronson and Fitz-James (1976). The location of this layer in the complete endospore remains unclear.

## 1.6 Spore germination

Although the spore is in a metabolically dormant state, it is constantly monitoring the environment (Moir *et al.*, 2002). In response to specific germinants, spores germinate and can outgrow to form vegetative cells. Nutrient germinants included single amino acids, sugars, purine nucleosides or a combination of these. However, non-nutrient factors such as high pressure, abrasion or calcium dipicolinate can also trigger germination (Paidhungat *et al.*, 2001, Paidhungat and Setlow, 2000, Setlow, 2003, Wuytack *et al.*, 2000).

Spore germination can be distinguished as two separate phases (Setlow *et al.*, 2001). In *B. cereus*, the first phase concerns the detection of germinants such as inosine or L-alanine (Barlass *et al.*, 2002). The interaction between the germinant and germinant receptors in the inner membrane stimulates the release of monovalent cations, the calcium dipicolinic acid ( $\text{Ca}^{2+}$ -DPA) from the spore core, causing the core to become partially rehydrated (Cowan *et al.*, 2003). In the second phase, cortex lytic enzymes hydrolyse the peptidoglycan cortex; further hydrating the core. Cortex lytic enzymes; CwlJ and SleB, are essential for germination to proceed (Atrih and Foster, 1999, Blankenship *et al.*, 2015). Following these stages, the process of outgrowth begins, generating a metabolically active vegetative cell. The morphological changes to the spore during germination have been observed by TEM and appear similar in both *B. anthracis* and *B. subtilis* (Moberly *et al.*, 1966, Zaman *et al.*, 2005).

## 1.7 Use of TEM in biological imaging

Electron microscopy in the past has been used as a method for imaging biological structures that were not amenable for X-ray crystallography and other structural techniques. Membrane proteins, some of which form natural two-dimensional crystals,

are of great importance in biology but difficult to study. Electron microscopy presented a method for imaging these membrane proteins, with the first determined structure solved to a resolution of 7 Å (Henderson and Unwin, 1975, Unwin and Henderson, 1975). Since then, atomic structures of many proteins, membrane-bound and soluble, have been solved using electron microscopy. With recent advances in direct detection and image processing tools, electron microscopy remains at the forefront of structural biology (Nogales and Scheres, 2015).

To improve the contrast of biological samples when imaging by TEM, negative stains are used. This was first demonstrated with viral particles through the use of heavy metal salts that occupied hydrated areas and encased the virus in an electron dense shell (Hall, 1955). This technique allowed for gross morphological features to be seen to a resolution of ~20 Å but is not suitable for high resolution imaging due to artefacts introduced by the stain.

Cryogenic-electron microscopy is a method for imaging biological structures in their native hydrated structures. Samples are embedded in non-volatile solvents such as glucose (Henderson *et al.*, 1986, Unwin and Henderson, 1975) but more commonly in vitreous ice (Dubochet *et al.*, 1982, Taylor and Glaeser, 1974). Due to the ionising effects of accelerated electrons that bombard the specimen, biological samples are further cooled to cryogenic temperatures to minimise the change in structure through radiation damage (Glaeser, 1971, Taylor and Glaeser, 1976). New advances in direct electron detectors combined with cryogenic techniques have pushed the resolution of native biological structures to beyond the 3 Å limit (Bai *et al.*, 2015, Cheng, 2015, Grigorieff, 2013, Miyaguchi, 2014).

## 1.8 Aims and objectives

Both the gross morphological structure and protein composition of the exosporium of *B. cereus* have been identified. The specific contributions of each protein and their mode of assembly into the exosporium are yet to be solved. We hope to provide more insight into the architectural assembly of the exosporium and spore coat with the ultimate aim of reconstituting the exosporium from its major component parts. Specific proteins were chosen for study with the aim of understanding how these contribute towards the assembly of the native exosporium. The main objectives outlined for this project were:

1. To determine the effects of *bclA* and *exsFA* mutations on the *B. cereus* exosporium structure.
2. To express ExsY and CotY, the likely exosporium template proteins, in *E. coli* and explore their structure.
3. To address the mechanism of assembly of proteins within the *B. subtilis* spore coat.
4. To investigate the fate of the exosporium during germination of *B. cereus* spores using high resolution TEM.

## Chapter 2. Materials and methods

### 2.1 Growth media and buffers

All chemicals were purchased from Sigma Aldrich unless otherwise stated. All buffers and media were sterilised by autoclaving unless otherwise stated.

#### 2.1.1 Table of growth and sporulation media

Media	Ingredients	Additional comments
LB Broth (Luria-Bertani Broth)	Per litre: 950 ml of distilled water (dH <sub>2</sub> O) 10 g of Difco Bacto Tryptone 10 g NaCl 5 g Difo Bacto Yeast extract	
LB Agar	LB broth supplemented with 1.5 % (w/v) Difco Bacto agar	
Nutrient Broth	13 g l <sup>-1</sup> Oxoid Nutrient Broth CM0001	
Nutrient Agar	28 g l <sup>-1</sup> Oxoid Nutrient Agar CM0003	
TSS buffer	LB broth to 50 ml 5 g Polyethylene glycol (PEG) 8000 1.5 ml 1 M MgCl <sub>2</sub> 2.5 ml Dimethyl sulfoxide (DMSO)	Recipe from (Chung <i>et al.</i> , 1989).
Brain Heart Infusion (BHI) Broth	37 g l <sup>-1</sup> Difco Bacto Brain Heart Infusion	
CCY (1L)	10 ml of CCY Stock Buffer 10 ml of CCY Nutrient Stock 2 ml of CCY Salts 980 ml of deionised water 1 l of media added per 2 l flask	(Stewart <i>et al.</i> , 1981). CCY Salts was added just before inoculation.
CCY Stock Buffer	1.3 M KH <sub>2</sub> PO <sub>4</sub> 2.6 M K <sub>2</sub> HPO <sub>4</sub>	
CCY Nutrient Stock	0.2 % (w/v) L-glutamine 10 % (w/v) Difco Bacto Casein 10 % (w/v) Difco Bacto Yeast Extract 6 % (w/v) Glycerol 0.2 % (w/v) L-Tryptophan	

CCY Salts	0.05 M ZnCl <sub>2</sub> 0.5 M MgCl <sub>2</sub> .6H <sub>2</sub> O 0.01 M MnCl <sub>2</sub> .4H <sub>2</sub> O 0.2 M CaCl <sub>2</sub> .6H <sub>2</sub> O 0.05 M FeCl <sub>3</sub> .6H <sub>2</sub> O	1 ml of 10 M HCl is added to every 100 ml of CCY salts and sterilised by filtration.
-----------	--	--

## 2.1.2 Table of spore buffers

Buffers used in this section were all sterilised before addition.

Buffer Name	Composition	Additional comments
Spore Resuspension Buffer (SRB)	50 mM Tris-HCl, pH 7.5 0.5 mM Ethylenediaminetetraacetic acid (EDTA)	Todd <i>et al.</i> 2003. EDTA was prepared as a 0.5 M sterile stock solution and added as a 1:1000 dilution.
TEP Buffer	50 mM Tris-HCl pH 7.2 10 mM EDTA 1 mM Phenylmethylsulphonyl fluoride (PMSF)	Todd <i>et al.</i> 2003. PMSF was prepared as a 200 mM sterile stock solution in ethanol and added as a 1:200 dilution.
Wash Buffer 1	TEP buffer 0.5 M KCl 1 % (v/v) glycerol	Todd <i>et al.</i> 2003. Glycerol was prepared as a 20 % (v/v) sterile stock solution and added as a 1:20 dilution
Wash Buffer 2	1 M NaCl	Todd <i>et al.</i> 2003.
Wash Buffer 3	TEP buffer 0.1 % (w/v) SDS (BDH)	Todd <i>et al.</i> 2003. SDS was prepared as a 10 % sterile stock and added as a 1:100 dilution.
Wash Buffer 4	TEP buffer	Todd <i>et al.</i> 2003.
Germination buffer	10 mM Tris-HCl, pH 8.0 10 mM NaCl 5 mM Inosine	Barlass <i>et al.</i> , 2002. Inosine was prepared as a 50 mM sterile stock solution and added as a 1:10 dilution. Germination buffer was buffered to pH 8.0 after the addition of inosine

### 2.1.3 Table of protein buffers

Buffer Name	Composition	Additional comments
Lysis buffer	50 mM Tris-HCl, pH 7.5 50 mM NaCl 5 % glycerol 1 mM Dithiothreitol (DTT)	Glycerol was prepared as a 50 % (v/v) sterile stock solution and added as a 1:10 dilution. DTT was prepared fresh as a 0.5 M stock solution and added as a 1:500 dilution
Tris buffer	25 mM Tris-HCl, pH 8.0 150 mM NaCl	
urea buffer	8 M Urea 25 mM Tris-HCl, pH 8.0 150 mM NaCl	Add the correct mass of urea before the addition of water.
Phosphate buffer Stock 10x (0.1 M)	94 ml 1M K <sub>2</sub> HPO <sub>4</sub> 6 ml 1 M KH <sub>2</sub> PO <sub>4</sub> pH 8.0	
Wash buffer	40 mM imidazole Tris/urea buffer	
Elution buffer	0.1 M imidazole, 0.2 M imidazole, 0.3M imidazole, 1 M imidazole, all in Tris/urea buffer	
Western Blot transfer buffer	5.8 g Tris-HCl 2.9 g Glycine 0.37 g SDS 200 ml Methanol Made up to 1 l	Made fresh but no sterilising necessary.
Western Blot stock wash buffer	14.12 g K <sub>2</sub> HPO <sub>4</sub> 2.586 g KH <sub>2</sub> PO <sub>4</sub> Made up to 400 ml in dH <sub>2</sub> O	Sterilised by filtration.
Western Blot blocking buffer	4.38 g NaCl 30 ml Western Blot stock wash buffer 500 µl Tween 20 Made up to 500 ml	Made fresh but no sterilising necessary.
DTT Reducing buffer	4 M DTT added to Tris/Urea/Phosphate buffer	DTT was directly dissolved into the relevant buffer

SDS Reducing buffer	4 % SDS added to Tris/Urea/Phosphate buffer	SDS was directly dissolved into the relevant buffer
DTT SDS Reducing buffer	4 M DTT, 4 % SDS, all added to Tris/Urea/Phosphate buffer	DTT and SDS were directly dissolved into the relevant buffer

## 2.1.4 SDS-PAGE buffers and gel recipe

### 2.1.4.1 Table of SDS-PAGE buffers

Buffer Name	Composition	Additional comments
4X SDS-PAGE resolving buffer, pH 8.8	1.5 M Tris-HCl 0.4 % (w/v) SDS	Buffer pH was adjusted to 8.8 and stored at 4 °C.
4X SDS-PAGE stacking buffer, pH 6.8	0.5 M Tris-HCl 0.4 % (w/v) SDS	Buffer pH was adjusted to 6.8 and stored at 4 °C.
10X SDS-PAGE running buffer, pH 8.3	0.25 M Tris-HCl 2 M glycine 1 % (w/v) SDS	Buffer pH was adjusted to 8.3 and stored at 4 °C. Gels were run in 1X buffer, diluting in dH <sub>2</sub> O
Coomassie brilliant blue gel staining solution (1 l)	0.1 % (w/v) Coomassie® Brilliant Blue R250 30 % (v/v) Ethanol 10 % (v/v) Acetic acid	Solution made up to 1 l in dH <sub>2</sub> O.
Destain solution	10% (v/v) Ethanol 10% (v/v) Acetic acid	Solution made up to 1 l in dH <sub>2</sub> O.

### 2.1.4.2 SDS-PAGE gel recipe

SDS-PAGE was carried out using the Bio-Rad Mini-PROTEAN® Electrophoresis System.

#### 2.1.4.2.1 Table of SDS-PAGE resolving gel components

Solution	Volume
(30 %) 37.5:1 Acrylamide/Bis solution (Bio-Rad)	2.8 ml
4X SDS-PAGE resolving buffer, pH 8.8	1.75 ml
Ammonium persulfate (10 % w/v)	70 µl
TEMED (N, N, N', N'-tetramethylethylenediamine)	7 µl
dH <sub>2</sub> O	2.45 ml

### 2.1.4.2.1 Table of SDS-PAGE stacking gel components

Solution	Volume
(30 %) 37.5:1 Acrylamide/Bis solution (Bio-Rad)	0.26 ml
4X SDS-PAGE stacking buffer, pH 6.8	0.5 ml
Ammonium persulfate (10 % w/v)	30 $\mu$ l
TEMED (N, N, N', N'-tetramethylethylenediamine)	3 $\mu$ l
dH <sub>2</sub> O	1.04 ml

## 2.2 Bacterial strains, primers and plasmids

### 2.2.1 Table of spore strains

Strain	Genotype/Phenotype	Source
<i>B. cereus</i> ATCC 10876 "Wildtype"	Trp <sup>-</sup> , Str <sup>r</sup>	Clements and Moir, 1998/Laboratory Stocks
<i>B. cereus</i> ATCC 10876 $\Delta bclA$	$\Delta bclA ::spec$	David Radford, University of Sheffield
<i>B. cereus</i> ATCC 10876 $\Delta exsFA$	$\Delta exsFA ::erm$	P. Sylvestre Laboratory Stocks and Matt Johnson thesis.
<i>B. thuringiensis kurstaki</i> 4D11	cyclo <sup>r</sup> lys <sup>r</sup> cry <sup>-</sup>	(Stahly <i>et al.</i> , 1978) Laboratory Stocks

### 2.2.2 Table of *E. coli* overexpression strains

Strain	Genotype/Phenotype	Source
TOP10 <i>E. coli</i>	F <sup>-</sup> <i>mcrA</i> $\Delta$ ( <i>mrr-hsdRMS-mcrBC</i> ) $\phi$ 80 <i>lacZ</i> $\Delta$ M15 $\Delta$ <i>lac</i> X74 <i>recA1 araD139</i> $\Delta$ ( <i>ara-leu</i> ) 7697 <i>galU galK rpsL</i> (Str <sup>R</sup> ) <i>endA1 nupG</i> $\lambda$ -	Invitrogen <sup>TM</sup>
<i>E. coli</i> BL21(DE3)pLysS	F <sup>-</sup> <i>ompT hsdS<sub>B</sub></i> ( <i>r<sub>B</sub><sup>-</sup> m<sub>B</sub><sup>-</sup>) <i>gal dcm</i>, (DE3) pLysS (Cm<sup>R</sup>)</i>	Novagen

### 2.2.3 Table of primers

Primer name	Sequence 5' to 3'
CotYbc-fwd	GGT ATC ATG AGC TGC AAT TGT AAT G
CotYbc-rev	GTT AAA GCT TAA TAG AAA CAT CAC GTA AGC T
ExsFA-fwd	GCC TTA CAT GTT CTC TTC TGA TTG CGA A
ExsFA-rev-His	GTC TAA GCT TGC TAA TTT GTG CAA CTG TTA ATG C
ExsFA-rev-COLA	GTC TAA GCT TAG CTA ATT TGT GCA ACT GTT AAT GC
ExsY-fwd	GGA GGA CAT ATG AGT TGT AAC GAA AAT AAA CAC
ExsY 10876 REV ECOR1	GAG TAT GAA TTC TTA CTT TAC GAT AGA AAC GTC G
ExsY-rev-COLA	AAG TCT CGA GTT ACT TTA CGA TAG AAA CGT CG
BclAfwdfull	GCC ACA TGT CAA ATA ATA ATT ATT CAA ATG G
BclAfwd20	ACT ACC ATG GCA TTT GAC CCT AAT CTT GTA GG
BclArevall	ACA TCG AAG CTT AAG CAA TTT TTT CAA TAA TAA TGG A
ExsK-FWD-Duet	GTG AGC ATA TGG GTT CTC GAT TTA ATA ATT G
ExsK-REV-Duet	TAT CTC GAG TTA TGC CTT GTT TGC TAC ATC

### 2.2.4 Table of plasmids encoding endospore protein genes

All pET vectors were obtained from Novagen™. Plasmids encoding *B. subtilis* proteins were provided by Dr. Daniela Krajcikova, Slovak Academy of Sciences, Slovakia.

Plasmid name	Protein expressed	Vector
p28cotYBcC	<i>B. cereus</i> CotY C-terminal-His <sub>6</sub>	pET28a
pCAexsY	<i>B. cereus</i> ExsY untagged	pCOLADuet-1
p28exsYNC	<i>B. cereus</i> ExsY N&C terminal-His <sub>6</sub>	pET28a
p28exsYN	<i>B. cereus</i> ExsY N-terminal-His <sub>6</sub>	pET28a
p28eFAC	<i>B. cereus</i> ExsFA C-terminal-His <sub>6</sub>	pET28a
p21exsYC	<i>B. cereus</i> ExsY C-terminal-His <sub>6</sub>	pET21b

pCAeFAY	<i>B. cereus</i> ExsYExsFA duet untagged	pCOLADuet-1
p28cotYcBsN	<i>B. subtilis</i> CotY mutant N-terminal-His <sub>6</sub>	pET28a
p28cotYBsN	<i>B. subtilis</i> CotY N-terminal-His <sub>6</sub>	pET28a
pDUcotZBs	<i>B. subtilis</i> CotZ untagged	pETDuet-1
p28cotEBsN	<i>B. subtilis</i> CotE N-terminal-His <sub>6</sub>	pET28a
pDUcotYBS	<i>B. subtilis</i> CotY untagged	pETDuet-1
pACbclA (Bfap/Bfbp)	<i>B. cereus</i> BclA full length untagged	pACYCDuet-1
pACb20 (B202p/B203p)	<i>B. cereus</i> BclA N-term-20 untagged	pACYCDuet-1
p28exsKC (KpET)	<i>B. cereus</i> ExsK C-terminal His <sub>6</sub>	pET28a
pACexsKbclA (KBp1/KBp2)	<i>B. cereus</i> ExsKBclA-full length Untagged	pACYCDuet-1
pACexsKb20(K20 2/K203p)	<i>B. cereus</i> ExsKBclA-N-term-20aa Untagged	pACYCDuet-1

The construction of these plasmids is described in Chapters 4, 5 and 6.

## **2.3 Isolation of exosporium**

### **2.3.1 Large-scale growth of *Bacillus* endospores**

A fresh single colony grown overnight on LB agar at 37°C was inoculated into 50 ml of LB broth and grown at 37 °C, shaking at 250 revolutions per minute (rpm). At mid exponential phase ( $OD_{600} \sim 0.3$ , 4-5 h), 2 ml was used to inoculate 1 l of CCY in a 2 l conical flask and grown at 30 °C for 48 h, shaking at 200 rpm. Spores were harvested when the proportion of phase bright spores reached >95 % (determined using a Nikon Eclipse E400 microscope with an objective phase plate). Spores were harvested by centrifugation at 15,000 x g for 15 min at 4 °C. Spores were then washed 10 times in ice cold water, pelleting at 17,000 x g for 20 min at 4 °C, and resuspending until all vegetative cells were removed (checked using phase contrast microscopy, >98 % phase bright spores). The final pellet was resuspended in 50 ml of SRB and stored at -20 °C.

### **2.3.2 Exosporium extraction by sonication**

The spore suspension from 2.3.1 was pelleted and resuspended in SRB to an  $OD_{600}$  of 10 in a 1 ml eppendorf tube and placed in a beaker with ice. A MSE Soniprep 150 Ultrasonic disintegrator sonicator was used for physical disruption of the exosporium with a medium sized sonication probe immersed into a contained sample. The sample was sonicated at 15 microns for a total time of 5 min with 1 min bursts followed by 1 min breaks for cooling.

### **2.3.3 Exosporium purification**

50 ml of the spore suspension from 2.3.1 was first homogenized (Tween can be added at 0.1 % to prevent frothing) before twice passing through a pre-chilled SLM Aminco French® Pressure Cell (SLM Aminco) at 16-18 kpsi eluting at a drop rate of  $1 \text{ s}^{-1}$ . Broken spores were centrifuged at 9,000 x g for 5 min at 4 °C, and both pellet and supernatant were retained. The pellet was washed in SRB and centrifuged at 9,000 x g for 5 min at 4 °C. Supernatants from both centrifugation steps were combined and centrifuged at 10,000 x g for 15 min at 4°C to remove residual spore debris.

### **2.3.4 Exosporium concentration**

The supernatant, containing exosporium, from 2.3.3 was concentrated using a 10 kDa Molecular weight cut off (MWCO) Vivaspin centrifugal concentrator (GE healthcare – Sartorius) to a maximum volume of 1 ml. Urografin® 370 (Schering) was then added to

the sample to a final concentration of 20 % (v/v). The adjusted sample was then layered onto the surface of 10 ml of 50 % (v/v) Urografin/SRB in a Corex<sup>®</sup> centrifuge tube and centrifuged at 12,000 rpm in a JA-25.50 rotor for 30 min at 4°C to pellet all spores. The top layer (yellowish in colour) was pipetted into 12-14 kDa MWCO dialysis tubing (Medicell International Ltd) with a maximum of 2 ml in each tube. Samples were dialysed in 5 l of dH<sub>2</sub>O at 4 °C to remove Urografin with 4 changes of water every 45 min. After the final change of water, the sample was left to dialyse overnight. Dialysed samples were pooled and ultracentrifuged at 40,000 rpm in a Type 50.2 Ti rotor for 2 h. The resulting pellet was resuspended in 100 µl of SRB and stored at -20 °C. This is considered “unwashed exosporium”.

### **2.3.5 Dialysis membrane treatment**

12-14 kDa, 2 cm diameter dialysis membrane (Medicell International Ltd) was cut into 20 cm pieces and boiled for 10 min in 2 % (w/v) sodium bicarbonate, 1 mM EDTA, pH 8.0. The membrane was then rinsed in dH<sub>2</sub>O and boiled again for 10 min in 1 mM EDTA, pH 8.0. The tubing was allowed to cool, rinsed in dH<sub>2</sub>O and stored in 20 % (v/v) ethanol at 4 °C. The membrane was rinsed thoroughly before use.

### **2.3.6 Exosporium washing**

Washing of the exosporium was carried out to remove loosely associated surface proteins. The “unwashed” exosporium sample was suspended in wash buffer 1 and centrifuged at 40,000 rpm for 2 h. The supernatant was carefully discarded and pellet gently resuspended in wash buffer 2 to avoid frothing. The pellet was washed further in wash buffer 2, wash buffer 3 and wash buffer 4 in the same process. After the final wash, the pellet was resuspended in SRB (at least 300 µl) and frozen at -20 °C.

## **2.4 Cloning and Expression of heterogeneously expressed endospore proteins**

TOP10 *E. coli* (Invitrogen<sup>™</sup>) cells were transformed with the plasmids stated in 2.2.4. Proteins were overexpressed in BL21(DE3)pLysS *E. coli* (Novagen) cells unless otherwise stated.

### **2.4.1 Primer design and cloning**

The primers aforementioned in 2.2.3 were designed with restriction sites for cloning into pET28a, pCOLADuet-1 and pACYCDuet-1 (Fig. 2.1) for single and multiple protein co-expressions within *E. coli*.

Annealing temperatures and secondary structures of primers were calculated using Primer Biosoft NetPrimer ([www.premierbiosoft.com](http://www.premierbiosoft.com)). Primers were synthesised by Eurofins MWG as lyophilised and salt free at a concentration of 0.01  $\mu$ M. The polymerase chain reaction (PCR) was carried out using Phusion Master Mix HF (New England Biolabs) in a Techni PCR machine. PCR reactions were run with 5 cycles at the annealing temperature of the homologous section and then 35 cycles at the full-length annealing temperature. PCR products were analysed using Agarose gel electrophoresis in TAE buffer (0.7 % gels were usually suitable at 80 V) and cleaned using a QIAquick® PCR purification kit (Qiagen) eluting in water. Restriction enzymes were bought from New England Biolabs and DNA was digested in accordance to manufacturer protocols. All digested samples were loaded onto a 0.7 % agarose gel running at 80 V for 1 h and bands excised. Digested DNA was purified using a QIAquick® gel extraction kit eluting in water and concentrated in an Eppendorf vacuum concentrator. Digested primer and vectors were ligated using T4 DNA ligase (New England Biolabs) at 4° C overnight and 2  $\mu$ l used in transformations (2.4.4.). All final plasmid constructs were sequenced by GATC Biotech using primers for T7 forward and reverse sites or ACYCDuetUP1/2 and ACYCDuetDOWN1/2.

#### **2.4.2 Preparation of TOP10 *E. coli* cells**

TOP10 *E. coli* (electrocompetent) cells were streaked onto LB agar lacking antibiotics and grown overnight at 37 °C. A single colony was inoculated into 10 ml of LB broth and grown overnight at 37 °C at 250 rpm. 1 l of LB broth was inoculated with 10 ml of culture and grown at 37 °C until an OD<sub>600</sub> 0.35-0.4. The culture was immediately chilled on ice for 30 min before transferring to four prechilled centrifuge bottles. Cells were initially harvested by centrifugation at 1,000 x g for 20 min at 4 °C followed by resuspension in 200 ml of ice-cold dH<sub>2</sub>O and centrifuged as previous. Pellets were next resuspended into 100 ml of ice-cold dH<sub>2</sub>O and combined into two centrifuge bottles before centrifuging as previous. Pellet were resuspended in 40 ml of ice-cold 10 % glycerol in a 50 ml falcon tube and centrifuged as previous before resuspending into 1 ml of ice-cold 10 % glycerol. Cells were aliquoted into 50  $\mu$ l and stored at -80 °C.

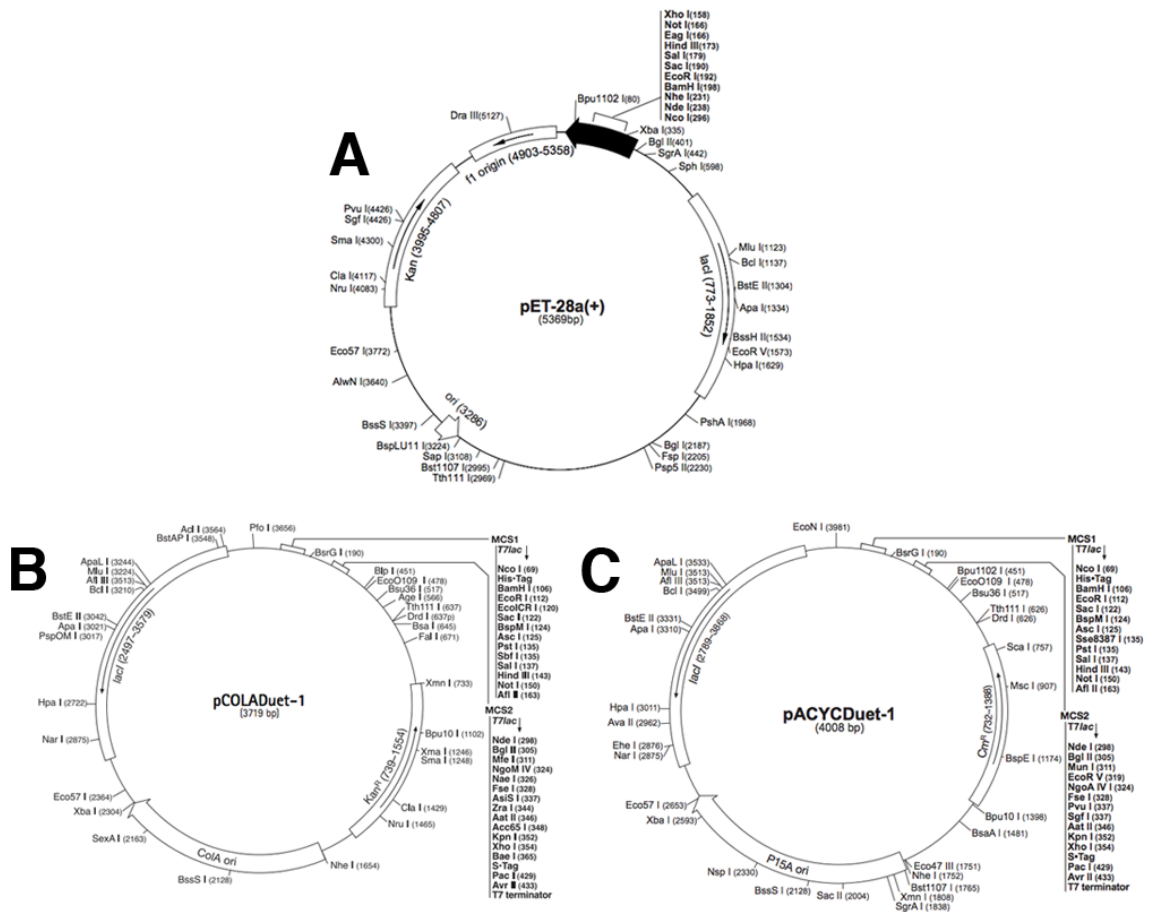


**Figure 2.1** Maps of plasmid vectors utilised in cloning of *Bacillus* endospore proteins. (A) pET28a, (B) pCOLADuet-1 and (C) pACYCDuet-1.

### **2.4.3 Preparation of *E. coli* BL21(DE3)pLysS competent cells**

*E. coli* BL21(DE3)pLysS (Novagen) was streaked onto LB agar containing chloramphenicol (34  $\mu\text{g/ml}$ ) and grown overnight at 37 °C. A single colony was inoculated into 5 ml of chloramphenicol containing LB broth and grown overnight at 37 °C at 250 rpm. Cells were diluted 1:100 into 50 ml of fresh LB broth and grown to an OD<sub>600</sub> of 0.2-0.5. Culture was chilled on ice for 10 min before centrifuging at 3,000 rpm for 10 min at 4 °C. The cell pellet was resuspended in 5 ml of chilled TSS buffer and 100  $\mu\text{l}$  aliquots were stored in Eppendorf tubes at -80 °C.

### **2.4.4 Transformation of cells with plasmids encoding spore proteins**

Electrocompetent TOP10 *E. coli* cells were transformed with plasmids encoding spore protein genes listed in 2.2.2 for amplification, before transformation into chemical competent BL21(DE3)pLysS *E. coli* for protein overexpression.

#### **2.4.4.1 Plasmid transformation into electrocompetent cells**

Plasmids were transformed into TOP10 *E. coli* cells as per manufacturers' procedures. **Word did not find any entries for your table of contents.** A Bio-Rad MicroPulser™ electroporator with 1 mm electroporation cuvettes was used for cell electroporation. 5-200  $\mu\text{l}$  of cells were plated on selective antibiotic LB agar plates and incubated overnight at 37 °C.

#### **2.4.4.2 Plasmid transformation into chemical competent cells**

BL21(DE3)pLysS *E. coli* cells were thawed on ice before addition of 2-5  $\mu\text{l}$  of DNA directly into the cells. Cells and plasmids were mixed and incubated on ice for 30 min. Cells were heat shocked at 42 °C for 45 s followed by a further 2 min incubation on ice. 900  $\mu\text{l}$  of pre-warmed LB broth was added to the cells and incubated for 1.5 h at 37 °C with shaking at 250 rpm. 20-200  $\mu\text{l}$  of cells were plated on selective antibiotic medium and grown overnight at 37 °C.

### **2.4.5 Glycerol stocks**

A single colony was grown overnight in 10 ml LB broth containing selective antibiotics and inoculated 1:1000 into 10 ml LB broth lacking antibiotic selection. Culture was grown to an OD<sub>600</sub> of 0.6 and glycerol added to a final concentration of 20 %. 1 ml aliquots of cells were frozen at -80 °C.

### **2.4.6 Expression of recombinant endospore proteins**

*E. coli* BL21(DE3)pLysS cells transformed with plasmids carrying spore protein genes were plated on selective antibiotic LB agar plates and grown overnight at 37 °C. Single colonies were selected and grown in 10 ml of antibiotic containing LB broth for 18 h at 37 °C with shaking at 250 rpm. 2 ml of culture was inoculated into 200 ml of antibiotic containing LB broth (1:100) and grown at 37 °C, 200 rpm until an OD<sub>600</sub> of 0.6 before inducing with 1 mM isopropyl-β-galactoside (IPTG) for 3.5 h. Cells were stored at 4 °C in media overnight or disrupted immediately. Overexpressing cells were pelleted by centrifugation at 5,000 x g for 10 min. Production of soluble ExsFA was carried out in volumes greater than 1 l to maximise the yield of protein.

## **2.5 Isolation and purification of recombinant endospore proteins**

### **2.5.1 Lysis of cells expressing recombinant proteins**

#### **2.5.1.1 Lysozyme treatment**

0.1 g of the cell pellet (wet weight) from 2.4.6 was resuspended in 940 μl of chilled lysis buffer (2.1.3) containing 1 mM PMSF. Lysozyme (final concentration of 300 μg ml<sup>-1</sup>) was then added to the sample in a final volume of 1 ml and incubated at 4° C for 4 h, gently shaking. MgCl<sub>2</sub> (5 μl of 1 fM) and DNase (2 μl of 500 μg ml<sup>-1</sup>) were then added and the mixture was incubated at 4° C for 30 min. Samples were loaded directly onto Copper Palladium (CuPd) grids for microscopy (2.6.3).

#### **2.5.1.2 Sonication**

The cell pellet from 2.4.6 was resuspended in 5 ml of Tris/urea buffer and disrupted by sonication in a MSE Soniprep 150 Ultrasonic disintegrator operating at 15 microns for a total of 2 min (in 20 s burst plus 40 s cooling time). Samples were loaded directly onto CuPd grids (2.6.3) or purified (2.5.2).

### **2.5.2 Purification of recombinant proteins**

#### **2.5.2.1 Affinity purification of soluble his-tagged endospore proteins**

Cells expressing hexa-histidine tagged proteins were lysed by sonication using the method stated in 2.5.1.2. Proteins were purified using 2 ml of NiNTA Agarose beads (Qiagen) packed into a 10 ml polypropylene column. Cell lysates were centrifuged for 30 min at 75,000 x g before applying the supernatant to the NiNTA Agarose column pre-equilibrated with Tris buffer. Proteins were first allowed to bind the column by

gravity flow before being washed with 20 ml of wash buffer. Proteins were then eluted in 5 ml fractions using 0.1 M, 0.2 M, 0.3 M and 1 M imidazole elution buffer.

### **2.5.2.2 Batch affinity purification of his-tagged endospore protein crystals**

Hexa-histidine tagged spore proteins from cells lysed using methods in 2.5.1.2 were batch purified using NiNTA Agarose beads (Qiagen). 1 ml of NiNTA Agarose beads was added to the cell lysate and incubated at 4 °C for 30 min with shaking. NiNTA Agarose beads were allowed to settle by gravity flow or the mix gently centrifuged at < 500 x g and unbound material removed. Beads were repeatedly washed in Tris/urea buffer and gently centrifuged for 5 repeats until samples were clear of debris. Beads were suspended into 4 ml of 1 M imidazole elution buffer to elute proteins from beads. The mixture of beads and eluted proteins was centrifuged at 500 x g for 2 min and supernatant collected. The supernatant was further ultracentrifuged at ~39,000 x g for 30 min in a Beckman Coulter TLA-100.2 ultracentrifuge rotor to pellet macro-assembled spore proteins. Pellet was resuspended in 4 ml of Tris/urea buffer.

### **2.5.2.3 Size exclusion chromatography**

Size exclusion chromatography was carried out using an Amersham Bioscience AKTA FPLC connected with a 120 ml HiLoad™ 16/600 Superdex 200 prep grade column. The column was first equilibrated with 20 mM Tris, 500 mM NaCl at pH 8.0. 4.5 ml of protein was injected into the loop and eluted at a flow rate of 0.8 ml min<sup>-1</sup>. Eluted peak fractions were analysed by SDS-PAGE.

## **2.5.3 Protein quantification**

Protein concentration of samples was determined using a BCA™ Protein Assay Kit (Pierce). The Enhanced Test Tube Protocol was followed as outlined in the protocol. Absorbance at 562 nm was measured using a Jenway 6715 UV/Vis Spectrophotometer (Bibby Scientific Ltd).

## **2.5.4 Protein identification**

### **2.5.4.1 SDS-PAGE analysis of proteins**

Proteins were separated by 12 % SDS-PAGE in 1X SDS-PAGE running buffer using a Bio-Rad Mini-PROTEAN® Electrophoresis System running at 150 V (2.1.4) or NuPAGE 4-12 % Bis-Tris gel (Invitrogen) in MES buffer running at 200 V. Samples were mixed with 4X NuPAGE® LDS Sample buffer (Invitrogen), 50 mM DTT and heated at 99 °C for 20 min before loading. Gels were stained in 0.1 % Coomassie® Brilliant Blue

(Fluka), 10 % (v/v) acetic acid and 30 % (v/v) ethanol and destained in 10 % (v/v) acetic acid, 10 % (v/v) ethanol (2.1.4.1).

#### **2.5.4.2 Transfer of proteins onto polyvinylidene fluoride (PVDF) membrane**

Affinity purified recombinant protein preparations were separated on a NuPAGE 4-12 % Bis-Tris gel at 200 V for 45 min and transferred onto a Sequi-Blot™ PVDF membrane (Bio-Rad) for Western blot analysis. The PVDF membrane was pre-wetted by incubation in 100 % methanol for 10 min, then Western blot transfer buffer for 5 min. An Invitrogen XCELL II™ Blot Module was used to transfer proteins from the gel onto the PVDF membrane using Western blot transfer buffer (2.1.3). Blotting was carried out at 175 mA for 90 min. A Novex® Sharp Pre-stained Protein Standard was included to assess the transfer, and the gel was stained following transfer to confirm that proteins had migrated to the membrane.

#### **2.5.4.3 Western Blot analysis of recombinant proteins**

PVDF membrane with transferred proteins was initially incubated in blocking buffer (2.1.3) for 5 min with gentle shaking, then washed with blocking buffer (2.1.3) supplemented with 3 % bovine serum albumin (BSA) for 1 h at room temperature. The PVDF membrane was then transferred into blocking buffer containing 1.5 % BSA and a 1:3000 dilution of Monoclonal Anti-polyHistidine antibody produced in mouse (Sigma Aldrich) for 1 h with gentle shaking. After incubation with the primary antibody in blocking buffer, the PVDF membrane was washed three times for 10 min in blocking buffer alone. Next, the PVDF membrane was incubated with blocking buffer containing 1.5 % BSA and a 1:3000 dilution of Anti-Mouse IgG-AP linked whole antibody (Sigma Aldrich). After incubation for 1 h with the secondary antibody, the PVDF membrane was washed three times again for 10 min in blocking buffer and all excess liquid was removed. 3 ml of Immun-Star™ AP Substrate (Bio-Rad) was applied to the PVDF membrane and allowed to absorb for 5 min in the dark. Excess substrate was removed and PVDF membrane was placed between two sheets of parafilm inside an Amersham™ Hypercassette™ Autoradiography Cassette (GE Healthcare). The membrane was exposed on Amersham Hyperfilm ECL™ (GE Healthcare) and developed using GBX Developer and Replenisher (Kodak) for various periods of time until bands became visible. Films were fixed using Industrex LO fixer (Kodak) and washed in water.

### **2.5.5 Thrombin cleavage**

Thrombin cleavage was used to remove the N-terminal poly-histidine tag from endospore protein expressed from a pET28a construct. 10  $\mu$ l of Thrombin protease (GE Healthcare) was incubated with purified overexpressed proteins for up to 6 h at 21 °C in 20 mM Tris-HCl, 150 mM NaCl, pH 8.0. Digested samples were analysed by SDS-PAGE with a band shift appearing in successfully digested samples.

## **2.6 Sample preparation for TEM**

### **2.6.1 Coating of carbon grids**

Using a Cressington 208 Carbon Coater, a carbon rod was evaporated onto a mica slide under vacuum. A freshly split mica slide with the exposed side up was placed on top of a filter paper (Whatman) and placed underneath a sharpened 6 mm carbon rod (Agar Scientific) in contact with a blunt carbon rod. Once the vacuum had reached  $\sim 10^4$ - $10^5$  mbar, a current was applied to the carbon rods to induce evaporation onto the surface of the mica. 5 s pulses were used and repeated until a  $\sim 150$  Å to 300 Å sheet of carbon was deposited onto the mica (determined using a Cressington Thickness Monitor). The carbon film was then left for 48 h before use at room temperature.

A Pyrex bowl filled with Milli-Q water with a piece of filter paper (Whatman) held on a tube rack was prepared for floating of the carbon film onto copper/palladium grids. 3.05 mm square CuPd grids (Agar Scientific) were placed onto the filter paper underwater and mica slowly inserted at 45° into the water so that it floated on the surface. The water was slowly drained using a syringe allowing the mica to be positioned over the placed CuPd grids guided by tweezers. The grids were dried at room temperature overnight before use.

### **2.6.2 Preparation of uranyl formate (0.75 % w/v)**

Under low light conditions 0.035 g of uranyl formate powder (Polysciences Inc.) was mixed and dissolved in 5 ml of boiling dH<sub>2</sub>O for 5 min. NaOH was added until a colour change to dark yellow occurred ( $\sim 8$   $\mu$ l per 5 ml) and mixed for a further 5 min. The solution was then filtered through a 0.2  $\mu$ m Minisart® filter unit (GE - Sartorius Stedim Biotech) and stored at 4 °C in the dark.

### **2.6.3 Negative staining of samples**

Carbon coated grids were glow discharged using a Cressington 208 Power unit for 15-60 s (dependent on age) to hydrophilically charge the carbon surface. 5-10 ml of sample was then added to the glow discharged face and left to adsorb for 1 min. Excess sample was blotted off from the edges of the grid with filter paper. The grid was then washed twice in droplets (~30  $\mu$ l) of dH<sub>2</sub>O for 2 seconds, blotting after each wash, and repeated in uranyl formate with the final wash lasting 20 s. The grid was vacuum dried and placed in a dark location.

### **2.6.4 Preparation of thin sections**

50 ml of sample was pelleted in an eppendorf tube and treated with 3 % (v/v) Glutaraldehyde in 0.1 M phosphate buffer (pH 7.0) overnight at 4 °C. The sample was washed twice further in the previous phosphate buffer for 30 min at 4 °C. 2 % (v/v) aqueous osmium tetroxide was used for secondary fixation at room temperature for 2 h and washed twice in phosphate buffer as above. The fixed sample was dehydrated through an ethanol gradient at room temperature in 15 min intervals using 75 %, 95 %, 100 %, 100 % (v/v) ethanol and dried over anhydrous copper sulphate for 15 min. Samples were placed in two changes of propylene oxide for 15 min and infiltrated using a 50:50 mix of propylene oxide and araldite resin (10 ml CY212 resin, 10 ml dodecenyl succinic anhydride (DDSA) hardener and 1 drop of benzyl dimethylamine (BDMA) accelerator per ml of resin mixture) overnight. Samples were finally left in araldite resin for 6-8 h before embedding in fresh araldite resin for 48-72 h at 60 °C. Ultrathin sections (70-90 nm) were cut using a Reichert Ultracut E ultramicrotome and stained with 3 % uranyl acetate in 50 % ethanol followed by staining with Reynold's lead citrate for 5 min.

### **2.6.5 Preparation of samples for Cryo-EM**

Copper/Molybdenum grids (Agar Scientific) were coated with carbon film and glow discharged for 20 s. The grids were then loaded into a Vitrobot plunge freezing system (FEI Company at room temperature and >80 % humidity. 10  $\mu$ l of sample was applied to the grid and allowed to adsorb for 30 seconds before blotting for 8 s with a blot offset setting of -3 mm. Grids were frozen by automatic plunging into liquid nitrogen cooled ethane and store in grid holders submerged in liquid nitrogen.

## **2.7 Transmission electron microscopy**

### **2.7.1 TEM of negatively stained samples**

Negatively stained samples were visualized on a Philips CM100 electron microscope operating at an acceleration voltage of 100 kV with a Lanthanum Hexaboride (LaB<sub>6</sub>) filament. Images were recorded as digital micrographs using a Gatan 1K x 1K Multiscan 794 CCD camera in Bright field mode and viewed using Gatan Digital Micrograph (DM, Gatan Inc.). Images for data processing were typically recorded at 52,000 x magnification with defocus at between 3,000-5,000 Å underfocus. Series of images for 3D analysis were recorded between -50° to 50° in 10° tilts. At least 5 independent tilt series were recorded for each sample.

Micrographs of thin sections and non-crystallographic samples were recorded at various levels of magnifications and underfocus.

### **2.7.2 Cryo-EM of ice-embedded samples**

Ice-embedded samples were transferred to a vacuum pumped Oxford CT3500 cryostage (Oxford Instruments) using an Oxford loading station with insulated liquid nitrogen bath prior to loading into the microscope. The Oxford CT3500 cryostage was vacuum pumped to 10<sup>-6</sup> mbar overnight using an Edwards Turbo pumping station. The cryostage was then transferred to an Oxford loading station and cooled to -180 °C using liquid nitrogen. Grids adsorbed with frozen specimens were transferred to the connecting liquid nitrogen bath housing the grid holder making sure of minimal exposure to the atmosphere to prevent ice accumulation. Grids were loaded onto the holder under liquid nitrogen and locked in place by an O-ring. A sliding cover on the cryostage was then extended to prevent ice build-up during the rapid transfer to the microscope. Once the cryostage was inserted, the cryostage dewar was refilled with liquid nitrogen and left for 1 h for thermal stabilisation.

Cryogenically frozen samples were imaged using a Philips CM200 Field emission gun (FEG) electron microscope operating at an acceleration voltage of 200 kV. Flow rate of the water-cooling to the objective lens was set to 20 l h<sup>-1</sup> prior to imaging. Room humidity was set to 20 % and temperature set to 17 °C the day before use.

TEM analysis was carried out in Low Dose Bright Field Mode and images were recorded on Kodak® electron image film SO-163 (Eastman Kodak Company). Locating samples for imaging was carried out in SEARCH mode operating at 770x magnification.

Focusing was carried out indirectly on the specimen using FOCUS mode S1 and S2. Focus positions S1 and S2 were set 2.5  $\mu\text{m}$  away from the exposure point and at 180° to each other. Defocus for imaging of crystalline material was usually set to around -700 nm. Films were exposed in EXPOSURE mode for 1 second and a nominal magnification of 50,000x.

### **2.7.3 Film developing**

Films were developed in fresh D-19 developer solution (Kodak) for 12 min at 21 °C and rinsed in water before fixing in Ilford Hypam fixer for 5 min. Films were finally rinsed for 30 min in running water before air-dried overnight at room temperature.

### **2.7.4 Initial screening and scanning of films**

Films were initially screened on a Sira laser diffractometer (Sira Technology Ltd) for diffraction from crystalline material. Selected films were digitised on a Zeiss SCAI Scanner in 8 bit grey scale at a resolution of 7  $\mu\text{m}$  pixel<sup>-1</sup>.

## **2.8 Image Processing**

Processing of these micrographs was carried out using a combination of MRC electron crystallography programs (Crowther *et al.*, 1996, Henderson *et al.*, 1986) and *2dx*, a graphical user interface (GUI) housing adapted versions of the MRC electron crystallography suite of programs (Gipson *et al.*, 2007a, Gipson *et al.*, 2007b). The processing procedure of two-dimensional crystals using the MRC software suite has been outlined in Figure 2.2. Processing of two-dimensional crystals using *2dx* utilises the same underlying programs ported onto a GUI for ease of control. A detailed procedure for two-dimensional crystal processing is explained in the text below and a manual can also be found online at:

([http://www.2dx.unibas.ch/documentation/2dx-software/2dx-user-manual-.pdf/2dx\\_manual.pdf](http://www.2dx.unibas.ch/documentation/2dx-software/2dx-user-manual-.pdf/2dx_manual.pdf))

### **2.8.1 Processing of negative stain and film images**

Micrographs collected were converted from their native .dm3 format to .tif using Digital Micrograph (Gatan) for processing with *2dx*. Converted micrographs were collated into a single directory and *2dx\_merge* was executed with this directory being the master folder. *2dx\_merge* indexed each image based on their image series and nominal tilt angle. A separate *2dx\_image* program was executed for processing of each micrograph.

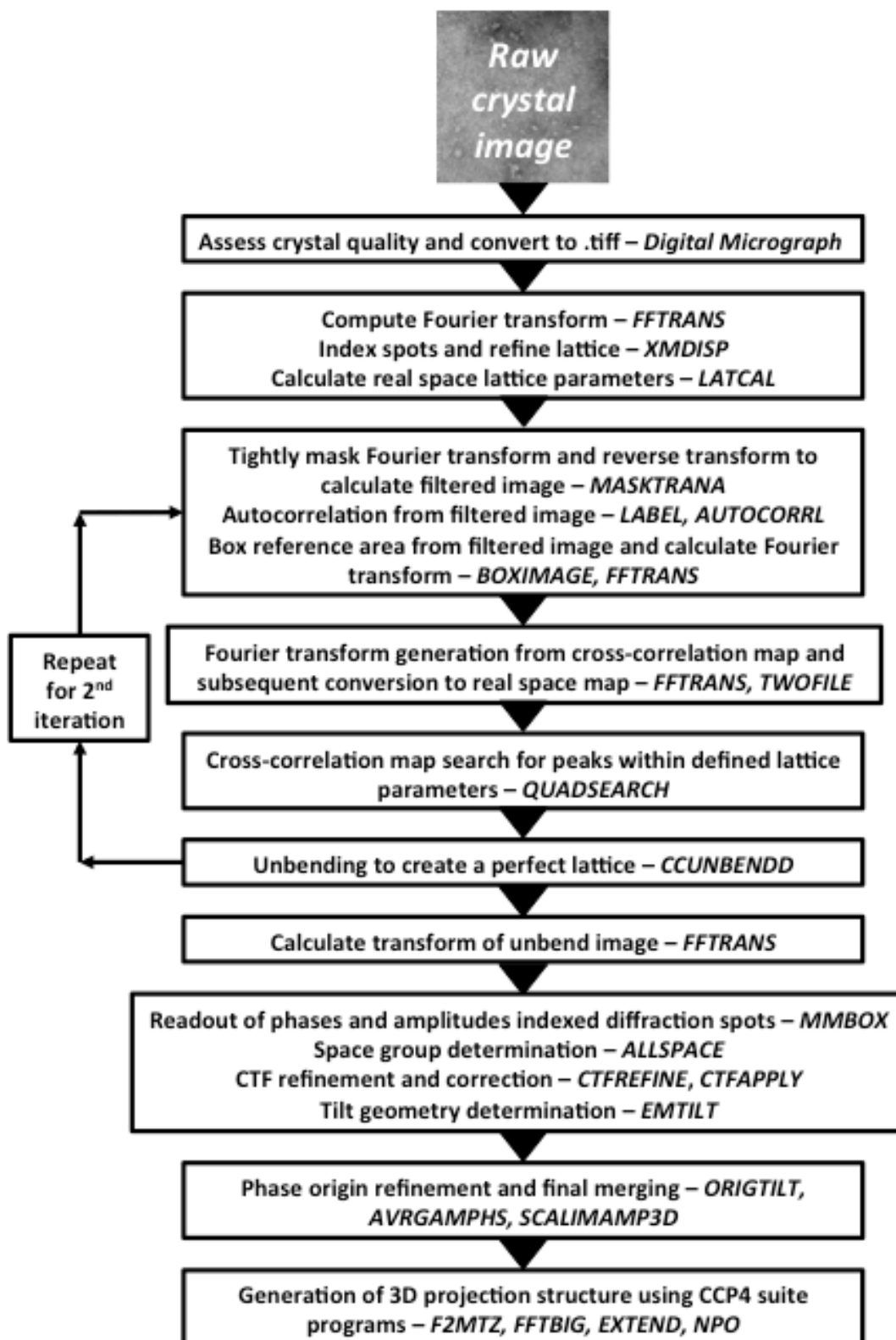
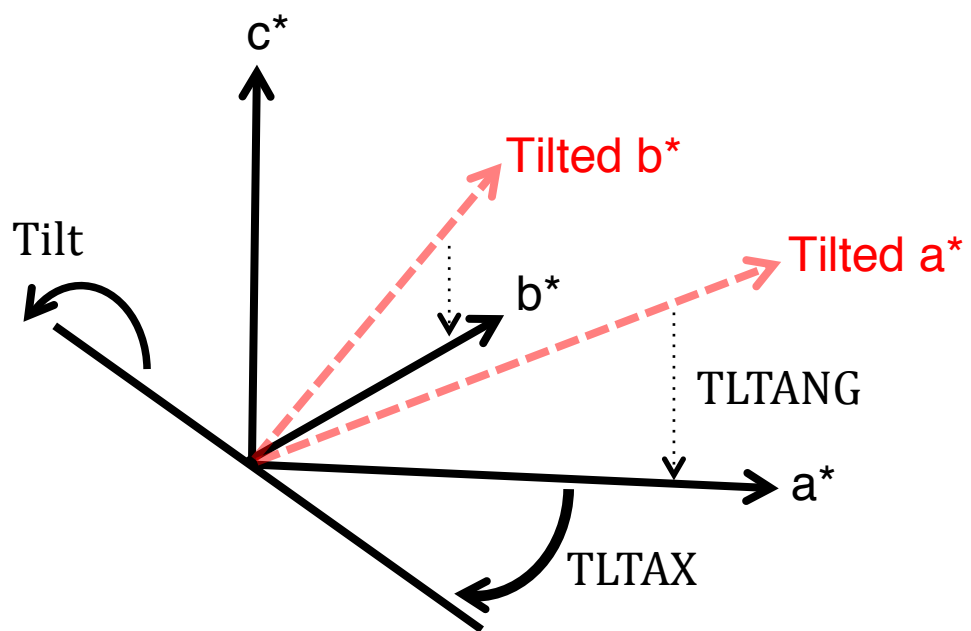


Figure 2.2 Flow diagram outlining steps for generation of three dimensional projection structures using MRC suite programs for processing two dimensional crystals (Crowther *et al.*, 1996 and Henderson *et al.*, 1986). Program names denoted in *italics*.

Upon launching of *2dx\_image*, the script *2dx\_initialize* checked the consistencies of the image directory and all external dependencies. Next the image parameters needed to be determined prior to processing. These included the magnification - nominally 52,000x but 61,005x on the actual image; the pixel size on the recording medium - 24 for negative stain and 7 for film, the spherical aberration (CS) - 3.6 on the CM 100 and 2.0 on the CM 200, the accelerating voltage - 100 kV for the CM 100 and 200 kV for the CM 200, and finally the lower resolution limit - set at 20 and 7 (Å) for negative stain and frozen film images respectively. Automatic tilt geometry determination was disabled for both untilted and tilted images. *2dx\_initialize\_files* was then executed to prepare input files for later stages of processing.

A Fast Fourier transform (FFT) of the raw image was computed using *2dx\_fftrans* to produce a diffraction pattern containing discrete diffraction spots resulting from the crystal. The defocus could be extracted from the Fourier transform along with phase, amplitude, reciprocal lattice information, etc. *2dx\_getDefTilt* was used to determine defocus, astigmatism and also tilt information by comparing defocus gradients across the image. The latter was not used as evaluations of defocus gradients were incomprehensive. Automatically detected defocus and astigmatism were checked on the computed FFT and could be manually overwritten if they did not coincide with the visible Thon rings. The crystal lattice was automatically indexed by running *2dx\_getLattice* and manually refined if necessary. Diffraction spots belonging to the Miller indices (1, 0 and 0, 1) along the *h* and *k* plane were manually selected to lay down an initial lattice and refined with higher resolution spots. Once the lattice had been refined to encompass all diffraction spots *2dx\_evaluateLattice* was used to calculate (LATCAL) the real space unit cell lattice parameters. Tilt geometry was calculated at this point, using EMTILT (Shaw and Hills, 1981), by comparison of lattice distortions in the tilted versus untilted lattice. (Option to “overwrite local tilt geometry” in *2dx\_evaluateLattice* sets EMTILT calculated values as those used for further processing). Five variables are calculated for tilt geometry. TLTAXIS, microscope axis of tilt and TLTANG, the angle between the grid and tilt axis, are independent of the crystal sample and can be measured from the defocus gradient. TLTAXA defines the tilt axis orientation of the 2D crystal on the carbon support in respect to the *a\** axis as determined by lattice distortions (Fig. 2.3). For reconstruction of three dimensional models, TAXA and TANGL are required to denote within three dimensional space the axis of tilt orientated in respect to the *a\** axis (TAXA) and the angle of tilt along that



**Figure 2.3 Schematic diagram of the MRC tilt axis conventions.** Each micrograph of a given crystal provides phase and amplitude values of a sample in Fourier space. Information sampled from one tilted image to the next can be related with given tilt angle and tilt axis values.

given axis plane (TANGL). Only TAXA and TANGL are required for construction of models in three dimensions.

Diffraction spots arising from the crystal lattice were selected using *2dx\_getspots1*. This runs a *2dx* version of MMBOX generating a spotlist for tight Fourier filtering. The Fourier-filtering was executed in *2dx\_unbend1* running MASKTRANA with a reference maskhole diameter of 6 pixels around each given diffraction spot with all other “non-zero values” in the FFT treated as noise. A reverse Fourier transform of the filtered FFT generated a filtered real space image to which a reference image was taken from the centre for use in a cross-correlation map. The central reference area from the filtered image was twenty-fold oversampled and a new reference area was taken for use as a reference autocorrelation peak (AUTOCORRL). Unbending was carried out by boxing of an area (usually the central 300 x 300 pixels) displaying the greatest crystallinity and cross correlating the Fourier transform of this area against the filtered Fourier reference. A reverse Fourier transform of the previous function produced a cross correlation map examining all relative translations within the filtered Fourier image in respect to the boxed reference. Cross correlation peaks were examined by comparison against the reference peak generated by the autocorrelation map. (The highest peak occurs at the cross correlation between the reference box and its origin on the filtered image and decrease as distortions arise throughout the crystal) (QUADSEARCH). Distortions in the lattice were corrected in the unbending by CCUNBENDD and a Fourier transform with sharper diffraction spots is generated. A second iteration of unbending using the distortion corrected Fourier transform is carried out by *2dx\_unbend2*. The previous process in the first unbend process is repeated with a tighter mask on the Fourier filtering at 1 pixel and a smaller boxed reference area (usually 200 x 200 pixels). Filtered diffraction spots were assessed with an Image Quality (IQ) at each stage of unbending and a value between 1 and 9 was given based upon peak height relative to the background. An IQ value of 7 is indicative of peaks relative to the background noise whilst a value of 1 is 7-fold higher than the noise.

Next the phase contrast transfer function (CTF) caused by the objective lens modulation on the scattered electron beam was corrected for using *2dx\_applyCTF*. The CTF results in periodical contrast reversals throughout a real space image and phase modulations of 180° in Fourier space seen as light and dark rings known as Thon rings. For negatively stained images this is non-problematic as all diffraction spots fall within the first Thon ring at the magnification and defocus used for recording images. For high

resolution images of frozen samples CTF correction was necessary to bring higher order spots beyond the first Thon ring into phase.

The symmetry and the respective phase origin of crystalline samples were determined using *2dx\_allspace* running ALLSPACE (Valpuesta *et al.*, 1994), of which seventeen two sided plane groups are possible for chiral molecules. The plane group symmetry of each crystal was determined based on the relationships between the phases of symmetry related reflections. An internal phase residual is calculated and compared to the theoretical phase residual of all possible plane groups. The symmetry group with the lowest phase residual was chosen and symmetry imposed grey level and contour map were generated using *2dx\_generateSymMap*.

### 2.8.2 Merging of processed images

Merging of images for two dimensional projection maps and three dimensional density models was carried out in both UNIX based scripts and in the new GUI based *2dx\_merge*. The procedure between the two methods is identical with UNIX based scripts requiring manual manipulation of values over *2dx\_merge*'s more autonomous interface.

The program ORGITILTK was used for merging of images. Parameters such as accelerating voltage, spherical aberration, etc. used in processing of each image was transferred into the ORGITILTK program along with the phase and amplitude information. A minimum of five image series was used in the merging of each model starting with the untilted images and moving up in 10° increments. The best untilted image, judged by its image quality value, was selected as a reference image and the starting phase origin was defined by ALLSPACE. Images were merged onto the reference by searching 361° in 1° increments in phase space for a new phase origin giving the best-merged phase residual. Alongside the phase origin search, REVHK and ROT180 parameters were refined for each image series to maximise the merging. This process was executed sequentially creating a new reference with each newly merged image. All untilted images were initially merged, followed by 10° images in both positive and negative tilt angles and so forth until the highest tilted images. For merging of tilted images, a parameter for the axis of tilt along the crystal (TAXA) and its tilt angle along that axis (TANGL) were required. A further cut off value defined as the “z\* window” was necessary to impose a limit on the vertical window in reciprocal space that reflections between new images and the reference are compared. For merging of all crystals a z\*

window of  $0.007 \text{ \AA}^{-1}$  was used. During the merging process a new phase origin was applied to the new image derived from a normalised cross-correlation between the new and reference image. An output merged phase residuals of 30 or less indicated the image was acceptable for merging into the reference. Once all images were added, a final output file containing the merged phase and amplitude information sampled at various points on the reciprocal space lattice lines was generated. The program LATLINE was then used to fit the lattice lines into the three-dimensional transform. The final output was converted to an .MTZ file and computed by programs within the CCP4 crystallographic suite to generate a three dimensional volume of the crystal. This model was viewed in UCSF Chimera (Pettersen *et al.*, 2004).

### 2.8.3 $0, 0, l$ estimation

Limitations of tilting above certain angles arise due to microscope and grid holder restrictions, causing a percentage of reciprocal space to not be sampled. This creates a “missing cone” in which no intensities are present within regions above the highest tilted sample. A solution to this was to estimate the intensities for the  $0, 0, l$  axis. For three dimensional exosporium models and self-assembling exosporium proteins from *B. cereus* ATCC 10876 values estimated by David Ball were used (Ball, 2006).

### 2.8.4 Threshold estimation for three-dimensional volume maps

The threshold volume for three-dimensional exosporium models were determined by fitting against a mass to volume calculated model of ExsY (N- and C- terminal double His<sub>6</sub> construct) self-assembling crystals. Model volumes could be displayed in UCSF Chimera and threshold-volumes set manually. The formula used was:

$$Volume = \frac{Mass}{Density} = \frac{ExsY (Da) \times Atomic\ mass\ unit}{Average\ protein\ density}$$

The volume of a single ExsY protein molecule using was estimated from its mass in Daltons converted to Kg using the constant for the atomic mass unit ( $1.66 \times 10^{-27}$  Kg) and the average protein density ( $1.35 \text{ g cm}^{-3}$ ). ExsY was determined to be a hexamer with each unit 19,419.8 Da in mass. Processing by *2dx* generates a  $2 \times 2$  unit cell model therefore the total molecules of ExsY displayed was “24”. Hence the total volume occupied was calculated to be:

$$\frac{19419.8 \text{ Da} \times 24 \text{ units} \times 1.66 \times 10^{-24} \text{ g}}{1.35 \text{ g cm}^{-3}} = 5.73 \times 10^{-19} \text{ cm}^3 = 573 \times 10^3 \text{ \AA}^3$$

At this calculated volume, features arose which were likely to be artefacts. Therefore the model was scaled to the highest volume possible at  $\sim 430 \times 10^3 \text{ \AA}^3$  before artificial features were visible. The difference in predicted and depicted volume could arise from disordered regions of the protein that have been average out and also stain impacting on the space occupied by the protein.

## 2.9 Circular dichroism spectroscopy

CD spectroscopy data was recorded on a Jasco Corp. J-810 Spectropolarimeter. Purified proteins at a concentration of greater than  $1.5 \text{ mg ml}^{-1}$  was loaded into a 0.02 cm path length quartz cuvette. Ellipticity of the protein sample was measure between wavelengths from 180 nm to 280 nm in 1 nm steps. A total of eight cycles were measured and averaged to produce the final spectrum.

Theta machine units recorded ( $\theta$ ) was converted to Ellipticity using the equation:

$$\Delta\varepsilon = \theta \times \frac{0.1 \times [\text{mean residue weight (Da)}]}{[\text{path length (cm)}] \times [\text{concentration (mg ml}^{-1}\text{)}] \times 3298}$$

Final spectra data with conversion accounted for was plotted using SigmaPlot.

## 2.10 X-ray crystallography

### 2.10.1 Crystallisation trials

#### 2.10.1.1 Sitting drop trials

Samples were screened across a variety of 96 different conditions common for the formation of protein crystals. The suites of commercial screens used, as supplied by NeXtal (Qiagen), are as follows:

- PACT Suite
- JCSG+ Suite
- Classics Suite
- PEGs Suite
- MPD Suite
- AmSO4 suite

- pHClear Suite
- Protein Complex (Proplex) Suite

A Matrix Hydra II PlusOne fully automatic robot was used for automatic dispensation of crystallisation conditions into 96 well sitting drop plates. 200 nl of each condition was deposited into the sitting drop well and 54.8  $\mu$ l deposited into the reservoir, 200 nl of protein was then deposited into the sitting drop well and trays were sealed. Each tray was centrifuged for 2 min at 2,000 rpm before storage at 16.4 °C. Trays were checked daily for the formation of crystals.

### **2.10.1.2 Hanging drop vapour diffusion trials**

Optimisation of crystallisation conditions was carried out in 24 well hanging drop plates. 1 ml of precipitant mixture, as determined from the previous robot trials, was dispensed into the reservoir. 1  $\mu$ l of protein was then mixed with 1  $\mu$ l of the precipitant before application onto a siliconised coverslip. The coverslip containing the protein precipitant mixture was placed on top of the well and sealed with oil. Trays were left at 16.4 °C and checked for formation of crystals daily.

## Chapter 3. Exosporium architecture in *Bacillus cereus* group strains and mutants

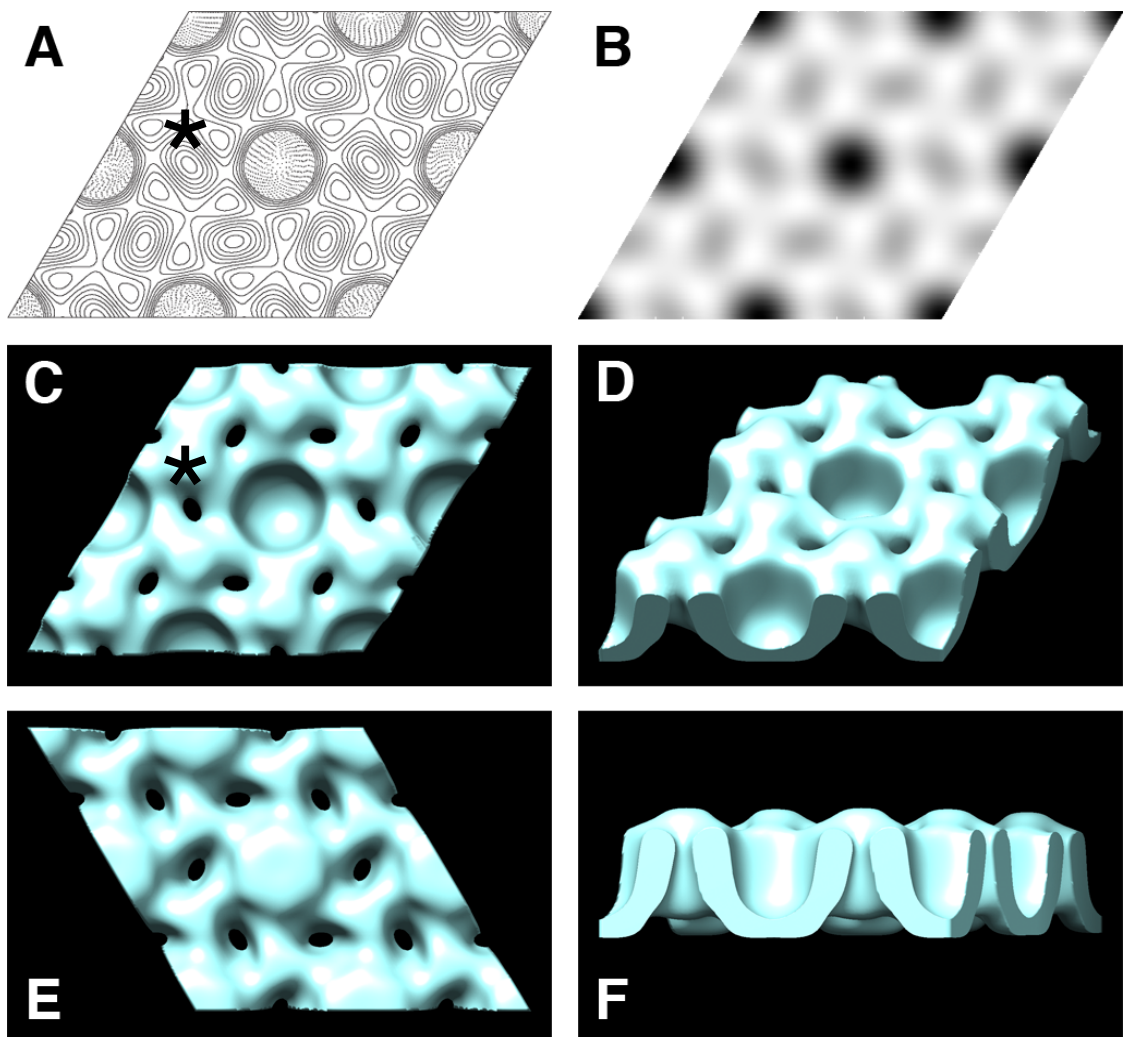
### 3.1 Introduction

Endospores of the *Bacillus cereus* family have been analysed using TEM to identify architectural features on both whole spores and purified exosporium. Comparisons were made between wild type *Bacillus cereus* ATCC 10876, *B. cereus*  $\Delta bclA$ , *B. cereus*  $\Delta exsFA$  and *B. thuringiensis* 4D11 a nap-less “wild” strain (Kailas *et al.*, 2011, Stahly *et al.*, 1978).

Analysis of negatively stained whole spores demonstrated that the “hairy nap” is composed of BclA (Boydston *et al.*, 2005, Sylvestre *et al.*, 2002) and resides upon the type II exosporium basal layer crystal (Chapter 1.4.6). The basal layer from *B. cereus* ATCC 10876 has been described in projection (Fig. 3.1 A and B) and in three-dimensions (Fig. 3.1 C to F) by Ball *et al.*, (2008) and Kailas *et al.*, (2011). *B. cereus* ATCC 10876 type II exosporium crystals display unit cell parameters of  $a = b = \sim 80 \text{ \AA}$ ,  $\gamma = \sim 120.0^\circ$  and possessed a ringed lattice structure with densely staining pits in projection (Fig. 3.1 A & B). Modelling in three-dimensions revealed a central tapering closed cup structure surrounded by a six-fold array of linkers and cavities (Ball *et al.*, 2008, Kailas *et al.*, 2011). ExsFA is required for attachment of BclA to the basal layer of the exosporium (Sylvestre *et al.*, 2005, Thompson *et al.*, 2011b) and proposed to be the contributor to the linkers sat on the three-fold symmetry axis (Kailas *et al.*, 2011).

To provide detailed information on the loci of specific proteins of interest in the basal layer, purified exosporium from each strain was studied in projection and reconstructed in three-dimensions. I aimed to identify specifically the contributions of BclA, which forms the hairy nap, and its anchor protein ExsFA, towards the architecture of the exosporium.

*The term “spore core” in this chapter refers to the spore excluding the exosporium.*



**80Å**

**Figure 3.1. Projection maps and three-dimensional models of *Bacillus cereus* ATCC 10876 exosporium.** Two-dimensional projection maps of *B. cereus* exosporium, depicted in (A) contour and (B) grey level. Three-dimensional reconstruction of *B. cereus* exosporium viewed from (C) top, (D) 40°, (E) bottom and (F) 90°. *p6* symmetry has been imposed on model and projection maps determined by Kailas *et al*, (2011). Images reconstructed from data collected by David Ball (Ball, 2006). “\*” indicates the position of the three-fold linker.

## 3.2 Results

### 3.2.1 Analysis of negatively stained endospores by transmission electron microscopy

Negatively stained, intact, endospores of *Bacillus cereus* and *B. thuringiensis* were analysed by TEM. Micrographs were collected from *B. cereus* ATCC 10876 as the wild type strain and two deletion mutants, *B. cereus* ATCC 10876  $\Delta bclA$  and *B. cereus* ATCC 10876  $\Delta exsFA$ . *Bacillus thuringiensis* kurstaki 4D11 was used as another “wild” strain belonging to the *B. cereus* group that lacks a hairy nap (Kailas *et al.*, 2011, Stahly *et al.*, 1978).

Micrographs collected were analysed using *2dx* to calculate Fourier transforms, unit cell parameters and projection maps. *2dx\_allspace* determined data collected from all *B. cereus* ATCC 10876 and *B. thuringiensis* 4D11 strains and mutants reflected  $p6$  symmetry, which was imposed onto all projection and three-dimensional models.

#### 3.2.1.1 *B. cereus* ATCC 10876 whole spores (wild type)

Micrographs of *B. cereus* ATCC 10876 endospores collected using TEM showed a dense spore core located at one pole of a balloon-like exosporium (Fig. 3.2 A). Short hair-like projections, referred to as the “hairy nap”, and long appendages are clearly visible around the periphery of the exosporium (Fig. 3.2 B). The nap appears blotchy with an average length of 30 nm; appendages varied in length. A naturally crystalline array can be seen on the exosporium surface composed of deeply staining pits (Fig. 3.2 C). Fourier analysis of the exosporium showed a diffraction pattern with discrete spots (Fig. 3.2 D). Unit cell parameters calculated from five images of whole spores showed an average lattice dimension of  $a = b = 83 \pm 3 \text{ \AA}$ ,  $\gamma = 119 \pm 4^\circ$ . A whole-spore projection map merged from these five images showed features of a central stain-accumulating pit surrounded by stain-excluding “linkers” positioned at the three-fold symmetry axis (Fig. 3.6 A).

#### 3.2.1.2 *B. cereus* ATCC 10876 $\Delta bclA$ whole spores

*B. cereus* ATCC 10876  $\Delta bclA$  mutant endospores possessed a balloon-like exosporium that appeared similar to the wild type strain; no change in robustness was seen. It was also apparently that a population of  $\Delta bclA$  mutant spores possessed a more centrally located spore core (Fig. 3.3 A). Endospores lacking BclA also appear to possess either no hairy nap around the exosporium (Fig. 3.3 B) or a sparse nap of a different morphology (Fig. 3.3 C). Populations of each were not easily quantifiable as

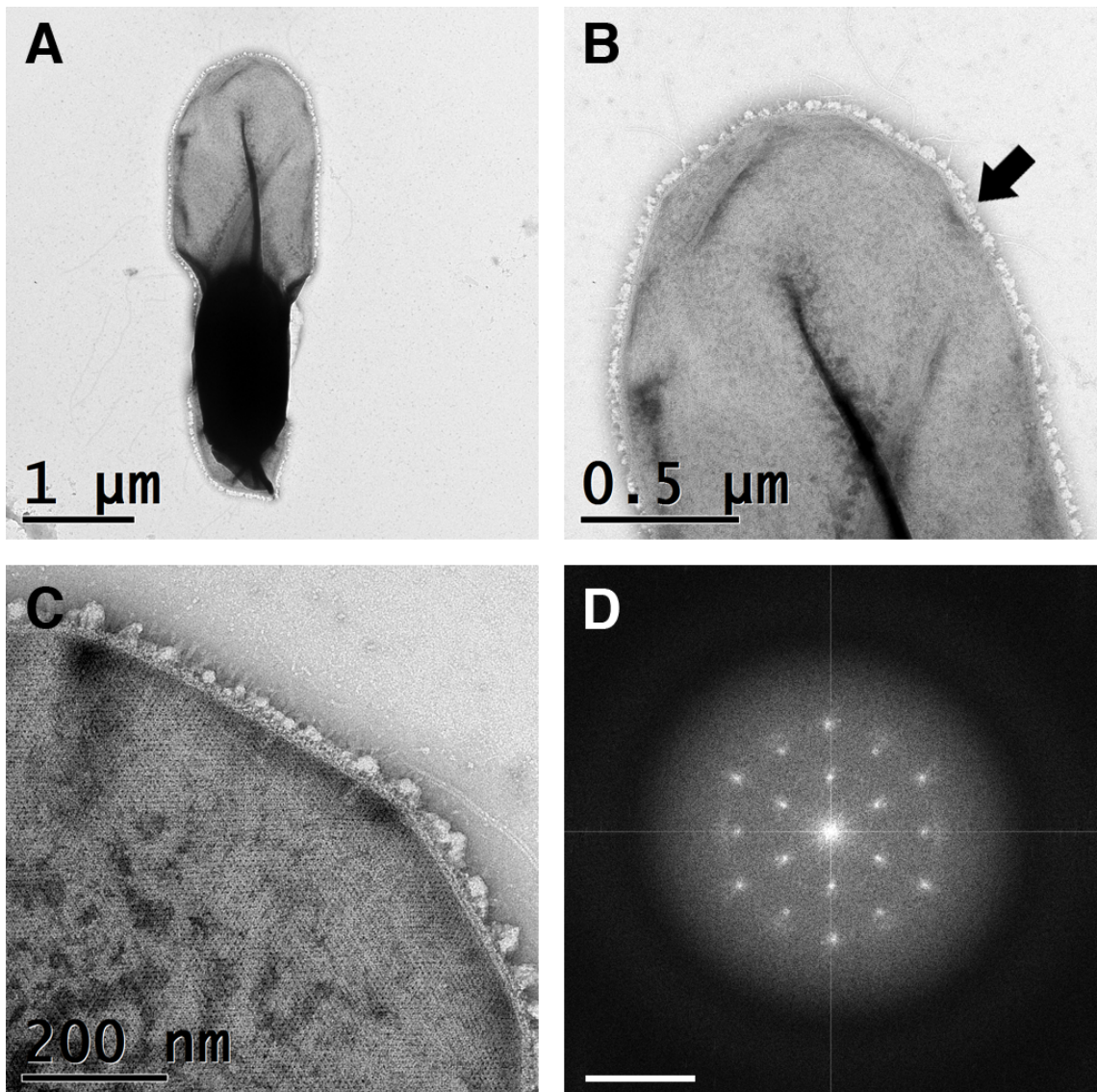


**Figure 3.2. Negatively stained *B. cereus* ATCC 10876 whole spores.** (A) Whole spore imaged using transmission electron microscopy displaying the polar localised spore core and balloon-like exosporium. (B) Highly contrasting “hairy nap” [arrow] on the surface of the exosporium. Appendages can also be seen. (C) Stain filled pits on the crystalline surface of the exosporium. (D) Computed Fourier transform from the exosporium showing diffraction from the ordered lattice. Scale bar in (D) represents  $0.025 \text{ \AA}^{-1}$ .

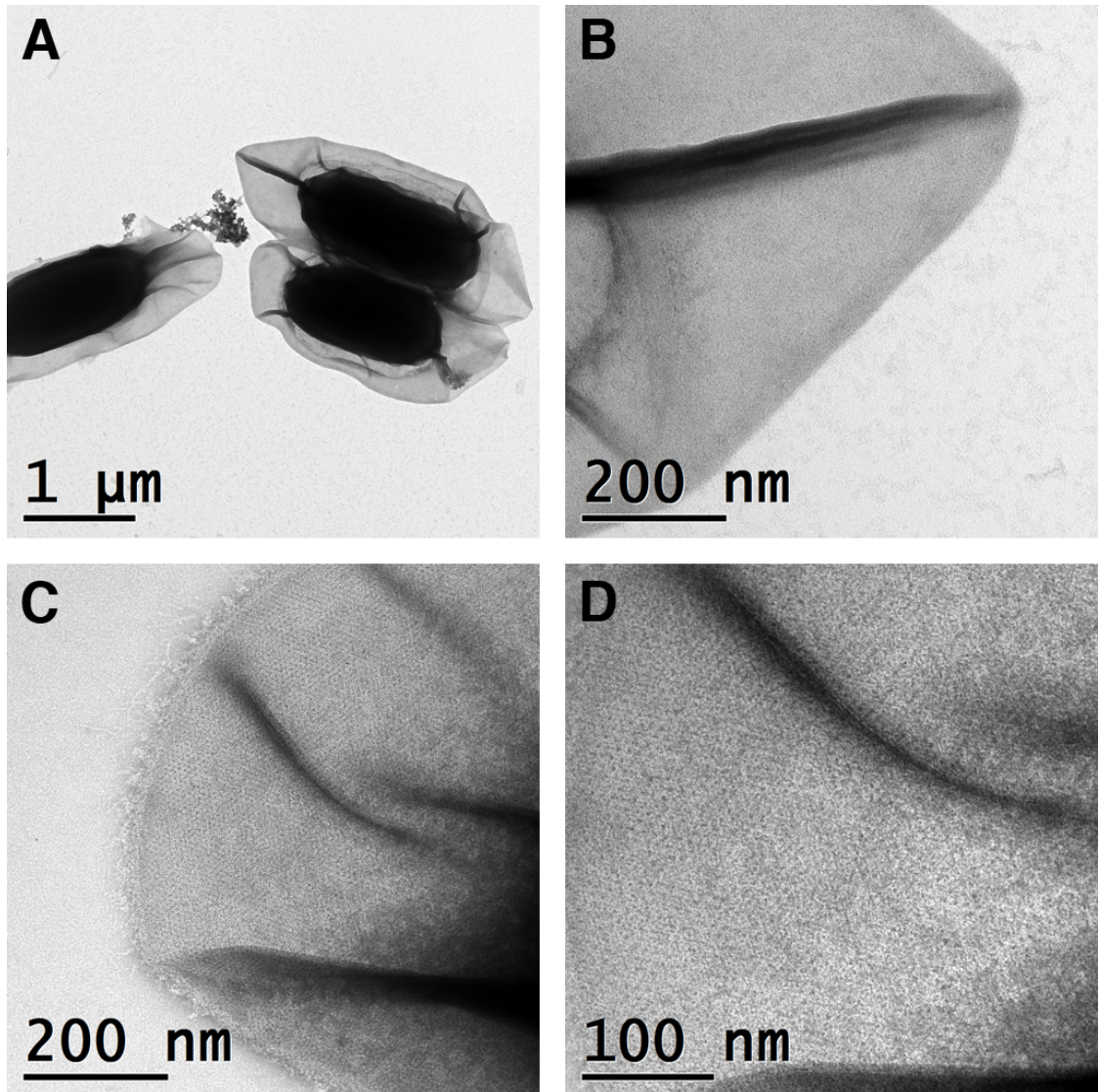


**Figure 3.3. Negatively stained *B. cereus* ATCC 10876  $\Delta bclA$  whole spores.** (A) Balloon-like exosporium attached to the dense spore core. (B) Mutated  $\Delta bclA$  endospores displaying a lack of the highly contrasting “hairy nap” on the surface of the exosporium. (C) Sparse nap of different morphology on the surface of some  $\Delta bclA$  mutant endospores. (D) Crystalline array seen on the surface of the exosporium.

morphologically similar endospores aggregated to the same location on a carbon film covered grid. The loss of the nap as a result of the  $\Delta bcIA$  mutation allows the crystallinity of the exosporium to be clearly seen on the surface (Fig. 3.3 D). This most likely arises through better penetration of the negative stain when the hairy nap is not present.

Twelve micrographs were processed showing two different projection maps, separated as Form “A” and “B”. Endospores possessing a nap showed the Form A crystal whilst endospores lacking the hairy nap showed the Form B crystal. Form A crystals showed similar features to that of the wild type whole spore exosporium at the recorded resolution, displaying a central staining pit and stain-excluding three-fold linkers (Fig. 3.6 B). Form B crystals also displayed a deeply staining central pit, but in addition, a lot of stain was present at the three-fold linker position (Fig. 3.6 C). The different crystalline arrays were never found in the same spore but always on independent spores. Unit cell parameters for Form A crystals showed dimensions of  $a = b = 83 \pm 2 \text{ \AA}$ ,  $\gamma = 120 \pm 1^\circ$  whilst Form B crystals showed  $a = b = 81 \pm 1 \text{ \AA}$ ,  $\gamma = 120 \pm 1.0^\circ$ . The almost identical unit cell dimensions made it impossible to distinguish each crystal by their lattice dimensions, hence they were differentiated using their different projection maps.

### **3.2.1.3 *B. cereus* ATCC 10876 $\Delta exsFA$ whole spores**

Endospores of *B. cereus* ATCC 10876  $\Delta exsFA$  displayed the same polar positioned spore core within a complete balloon-like exosporium seen in the wild type strain. Mutants lacking ExsFA showed no change in the robustness of their exosporium, but displayed a heterogeneous mix of nap-less (Fig. 3.4 A & B) and “wild type-like” nap-attached endospores (Fig. 3.4 C & D). Lattice dimensions of  $a = b = 84 \pm 1 \text{ \AA}$ ,  $\gamma = 120 \pm 2^\circ$  were calculated from nine images, similar to that of wild type whole spores. The exosporium from *B. cereus*  $\Delta exsFA$  endospores, both possessing and lacking the hairy nap, produced a similar projection map to that of the *B. cereus* wild type exosporium at this resolution (Fig. 3.6 D).

### **3.2.1.4 *B. thuringiensis* 4D11 whole spores**

The exosporium from endospores of *B. thuringiensis* 4D11 appeared more fragile than the previous *B. cereus* wild type and mutants examined. Under standard spore growth and preparation conditions described in 2.3.1, the spore core was rarely contained within an exosporium. Fragments of exosporium were seen attached to the intact spore

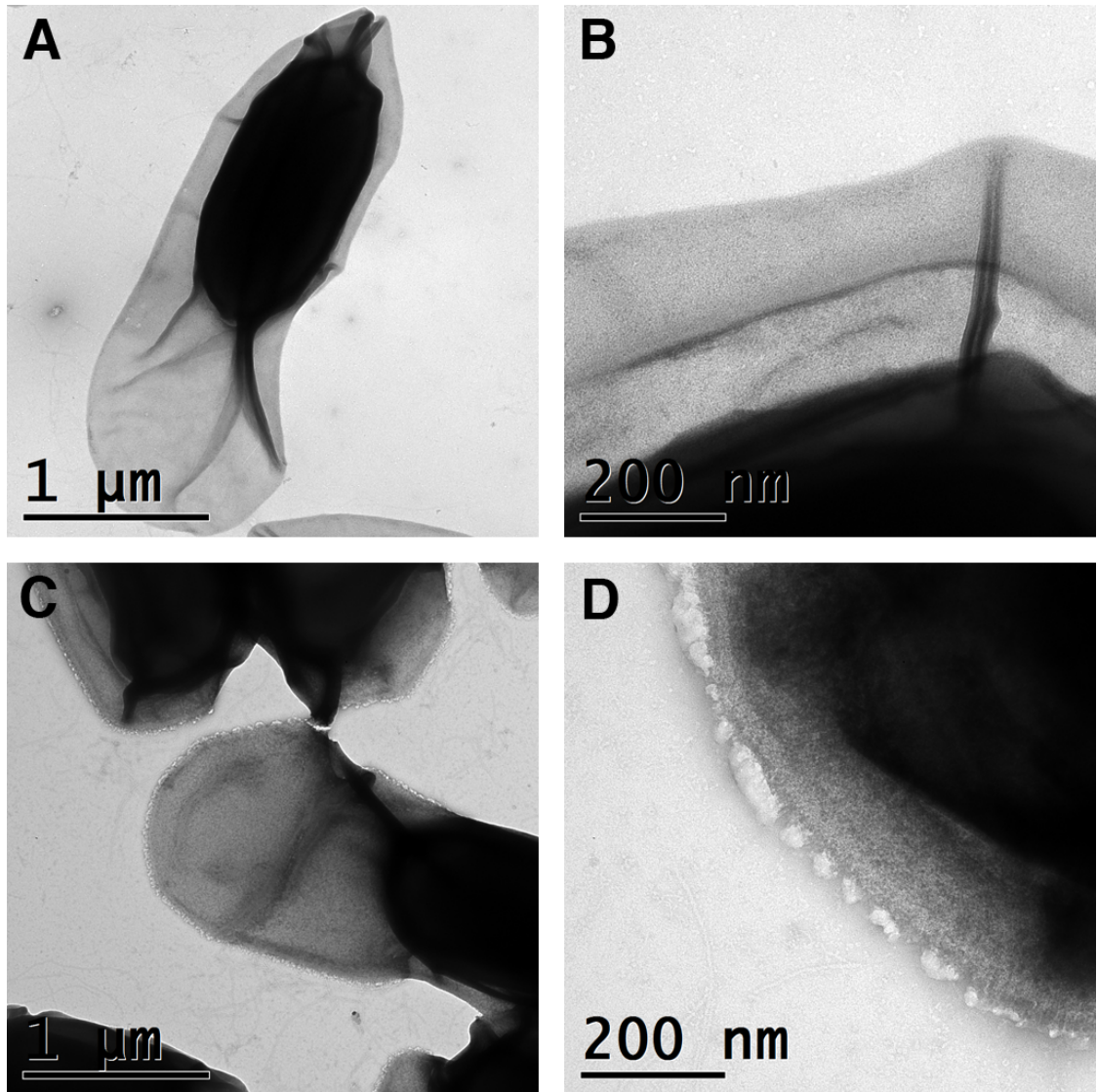


**Figure 3.4. Negatively stained *B. cereus* ATCC 10876  $\Delta$ exsFA whole spores.** (A) *B. cereus* ATCC 10876  $\Delta$ exsFA endospore displaying polar located core and balloon-like exosporium. (B) Individual  $\Delta$ exsFA endospore showing no nap on the surface of the exosporium. (C) Population of mutated  $\Delta$ exsFA endospores showing a hairy nap on the surface. (D) Highly contrasting nap on the surface of an endospore.

core, however the exosporium was more readily dissociated from the endospore completely (Fig. 3.5 A). *B. thuringiensis* 4D11 endospores were therefore grown in CCY media for 5 days at 30 °C with 60 rpm shaking to decrease the physical perturbation. Under these conditions, endospores displayed a complete exosporium, with the spore core situated at one pole (Fig. 3.5 B). The exosporium appeared similar to that in *B. cereus* with a crystalline lattice visible on the surface (Fig. 3.5 C), but no nap was seen (Fig. 3.5 D). Lattice dimensions calculated from the exosporium of ten whole spore micrographs showed parameters of  $a = b = 80 \pm 1 \text{ \AA}$ ,  $\gamma = 120 \pm 1^\circ$ . The projection map merged from these ten micrographs showed a central staining pit along with very dense staining at the three-fold linker positions (Fig. 3.6 E).

### **3.2.2 TEM analysis of isolated, negatively stained exosporium crystals in projection**

The exosporium from endospores of *B. cereus* ATCC 10876 and *B. cereus* ATCC 10876  $\Delta bclA$  was extracted using the French press method described in 2.3.3 and subsequently purified through an urografin gradient and salt washes. For purified exosporium, a concentration of  $\sim 1 \text{ mg ml}^{-1}$  was adsorbed onto a carbon coated CuPd grid as described in 2.6.3 and visualised by TEM. The exosporium from *B. cereus* ATCC 10876  $\Delta exsFA$  and *B. thuringiensis* 4D11 strains was extracted by sonication as described in 2.3.2 and imaged by TEM without purification. Exosporium fragments ranging from 10 nm to 1  $\mu\text{m}$  in diameter were found within purified preparations. Exosporium extracted by sonication yielded a greater frequency of larger fragments ( $>500 \text{ nm}$  in diameter).

#### **3.2.2.1 2D projection maps of purified *B. cereus* ATCC 10876 $\Delta bclA$ exosporium**

As already observed in whole spores, exosporium preparations from *B. cereus*  $\Delta bclA$  endospores contained two crystal variants in equal distributions. It was not possible to separate the crystals based on lattice parameters, as these were identical between the two forms. The two crystal Forms, A and B, appeared to have distinct physical appearances when visualised by negative stain TEM. Images of Form A crystals were very contrasty with rough edges (Fig. 3.7) whilst images of Form B crystals were much less contrasty but had sharp well-defined edges (Fig. 3.8).

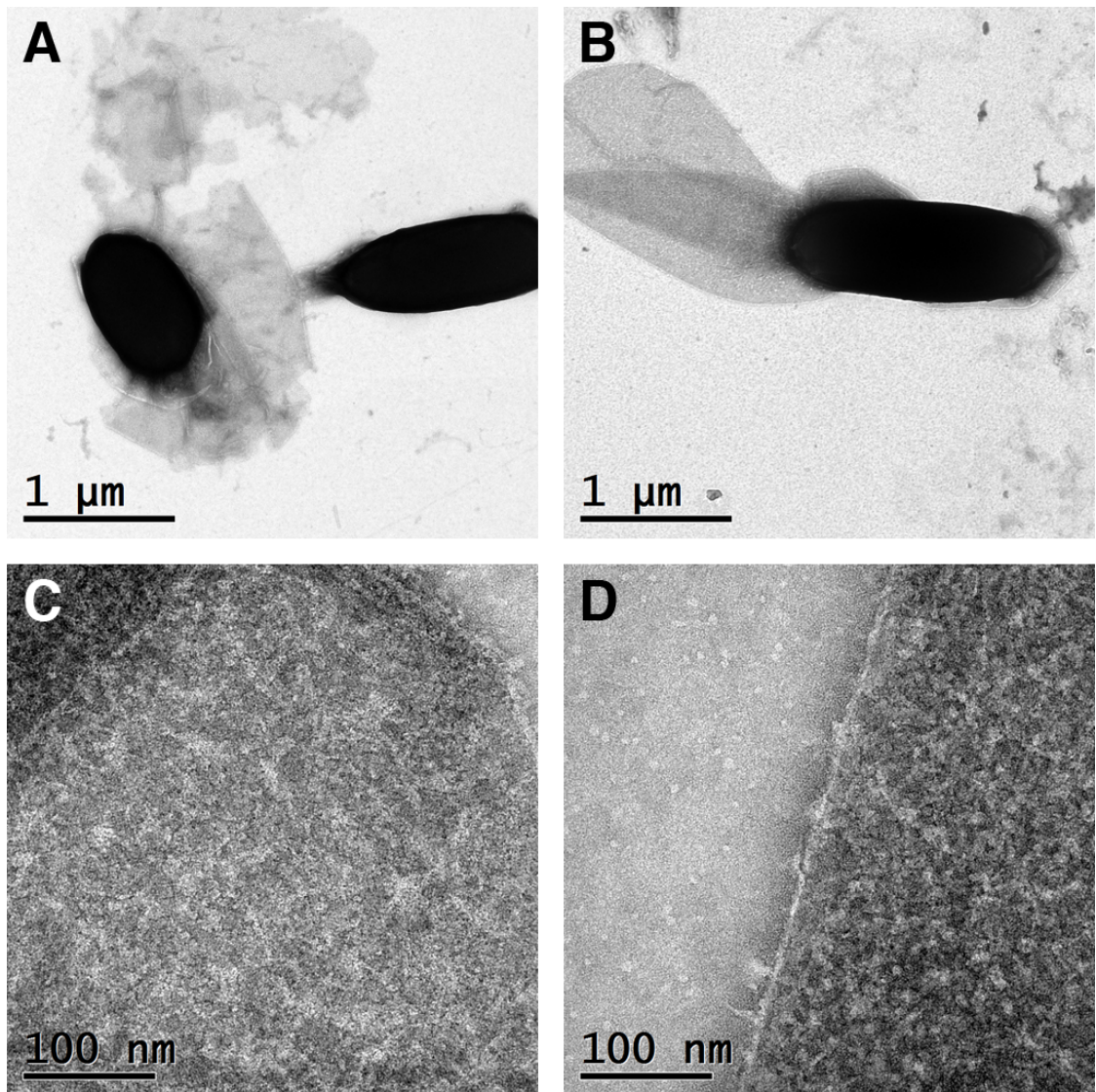


**Figure 3.5. Negatively stained *B. thuringiensis* 4D11 whole spores.** (A) Spores produced under standard conditions, showing broken exosporium. Some exosporium is completely dissociated from the spore core [top of image] and some exosporium remains spore-associated. (B) Complete exosporium attached endospores after growth using less agitation. (C) Visible hexameric lattice on the surface of the exosporium. (D) No hairy is visible on the exosporium surface of *B. thuringiensis* 4D11 endospores.

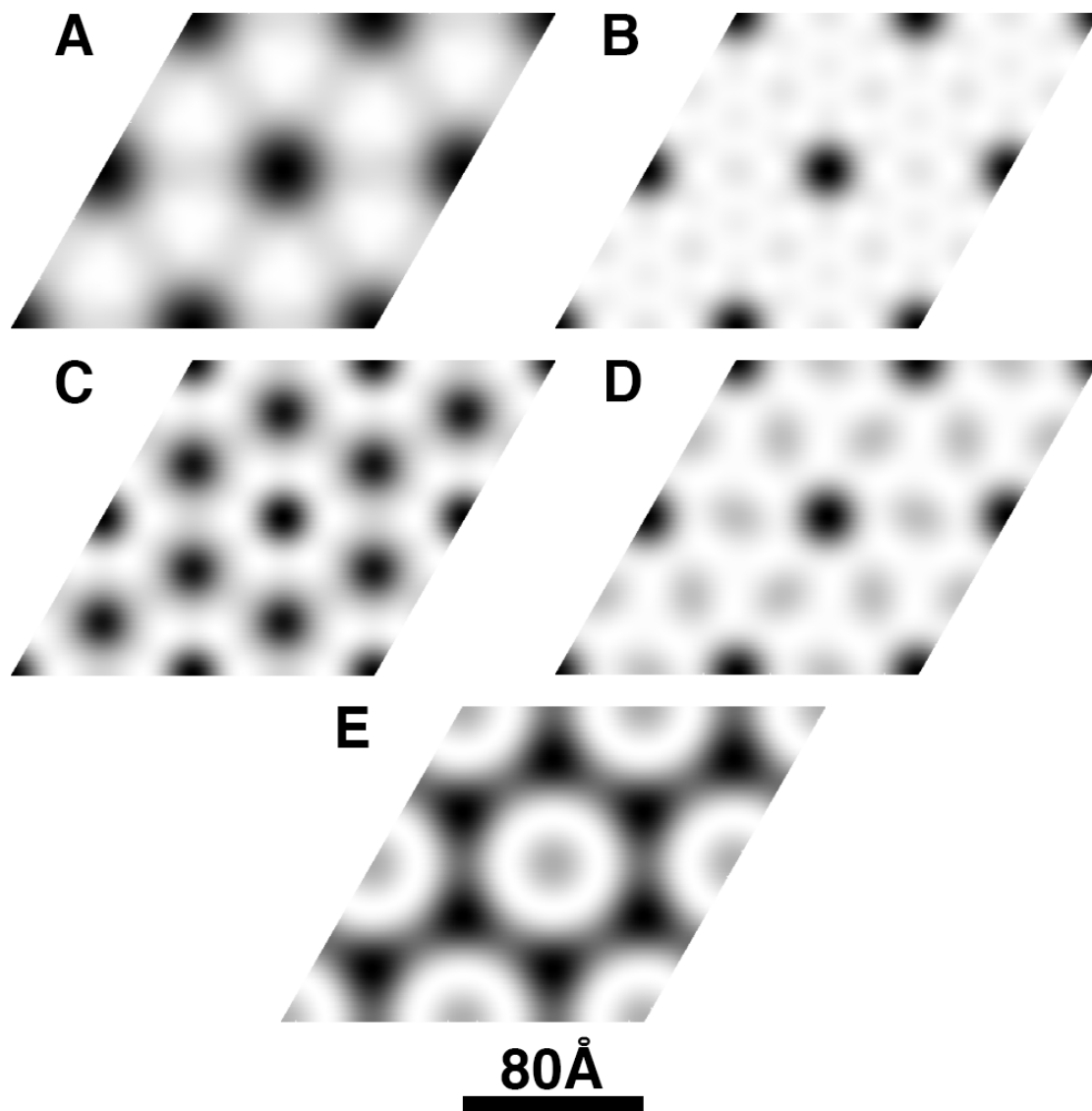


**Figure 3.6.** Grey level projection maps of exosporium from whole spores of (A) *B. cereus* ATCC 10876, (B) *B. cereus* ATCC 10876  $\Delta bclA$  Form A. (C) *B. cereus* ATCC 10876  $\Delta bclA$  Form B. (D) *B. cereus* ATCC 10876  $\Delta exsFA$ . (E) *B. thuringiensis* 4D11.

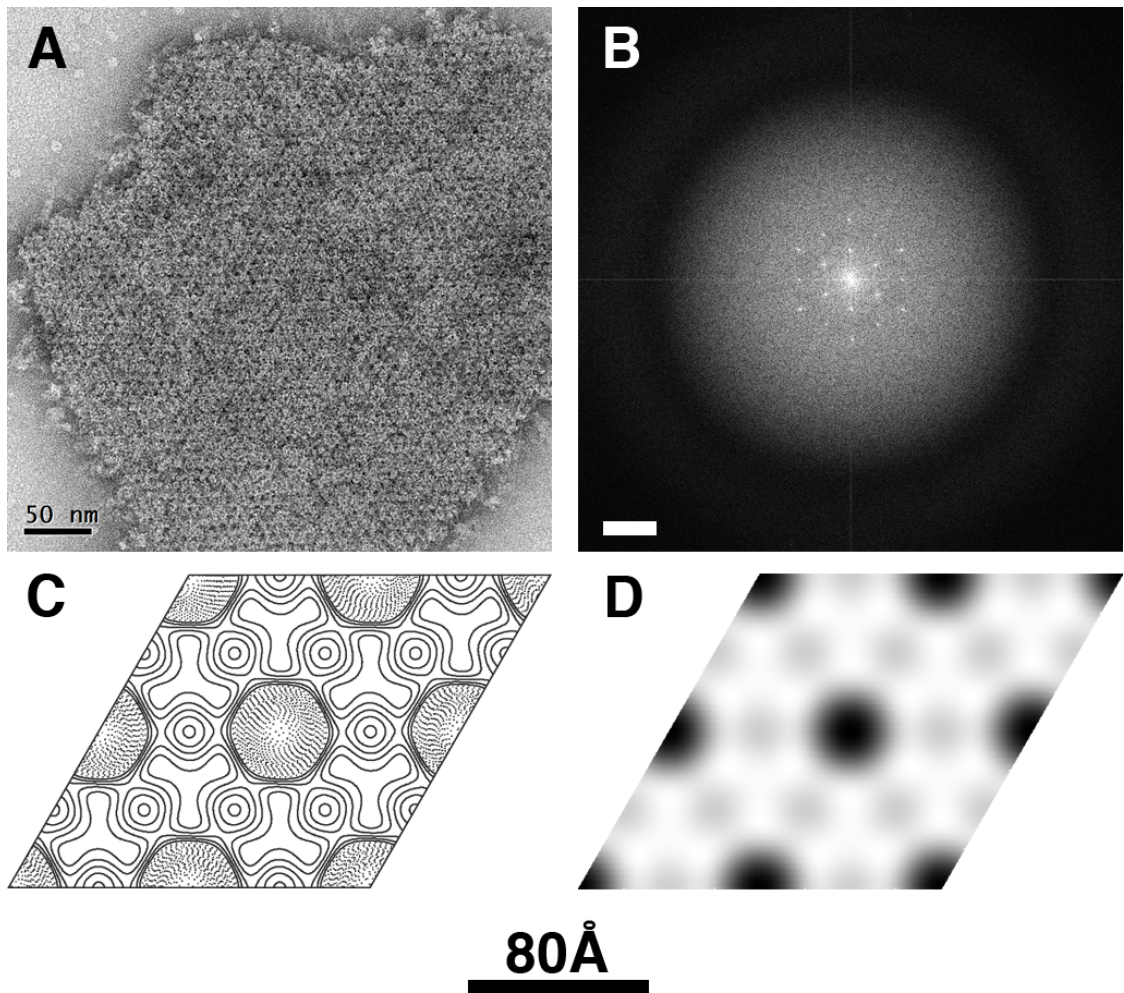
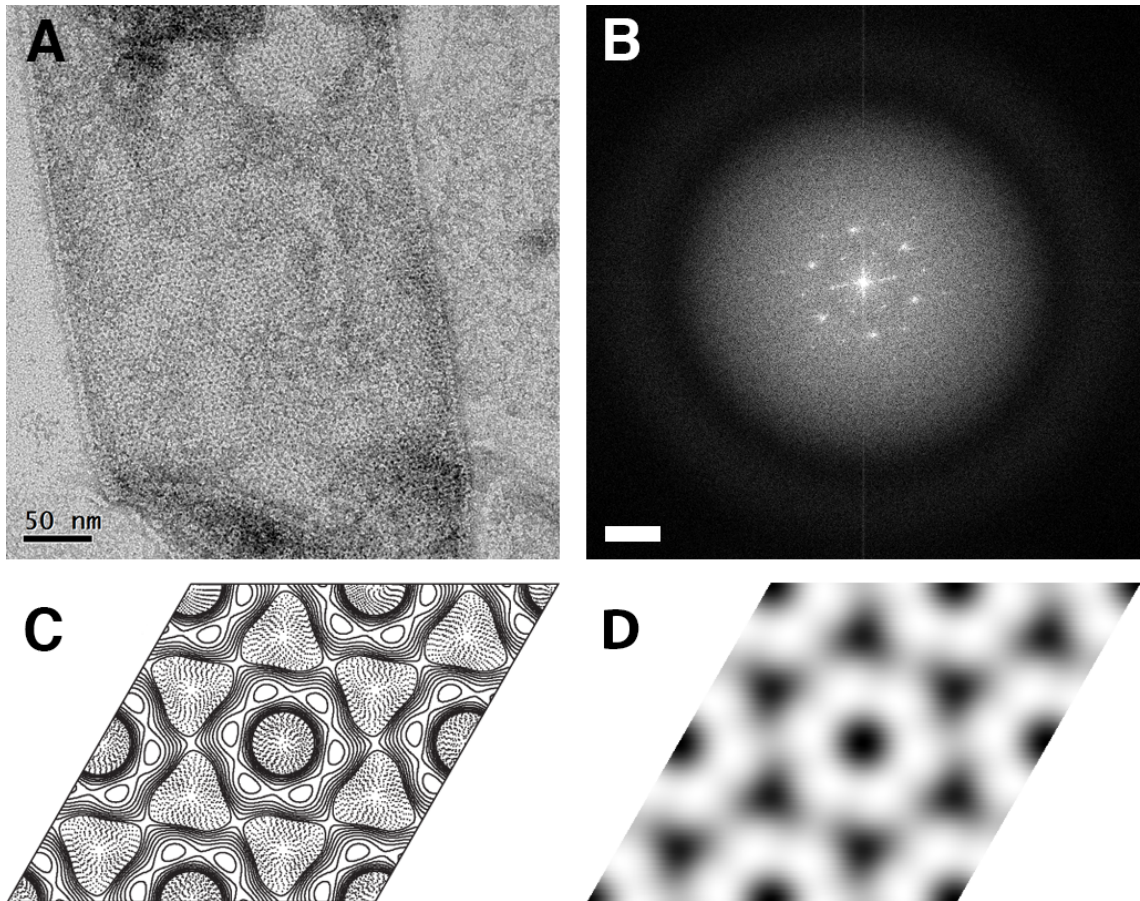


**Figure 3.7. Analysis of purified Form A exosporium crystal from *B. cereus* ATCC 10876  $\Delta bc1A$ .** (A) Form A exosporium crystal showing deeply staining pits and nap-like material around the edges. (B) Computed Fourier transform displaying diffraction from the crystalline lattice. (C) Contour and (D) grey level projection map merged from ten untilted micrographs.



**80Å**

**Figure 3.8. Analysis of purified Form B exosporium crystal from *B. cereus* ATCC 10876  $\Delta bclA$ .** (A) Form B exosporium crystal formed of clear hexamers. (B) Computed diffraction of “(A)”. Projection maps in (C) contour and (D) grey level from sixteen merged micrographs. Scale bar (B) represent  $0.025 \text{ \AA}^{-1}$ .

### 3.2.2.1.1 Form A crystals

Form A crystals imaged by negative stain TEM displayed large, deep, stain-accumulating pits, with rough edges and nap-like structures around the edges (Fig. 3.7 A). These crystals were highly contrasting and produced a diffraction pattern similar to that of wild type exosporium (Fig. 3.7 B). Ten micrographs of untilted Form A crystals were recorded and unit cell values calculated showing lattice parameters of  $a = b = 83 \pm 2 \text{ \AA}$ ,  $\gamma = 120 \pm 1^\circ$ . The images were processed using *2dx* by the method stated in 2.8 and merged to produce a projection map (Fig. 3.7 C & D). The merged Form A projection map appeared to have identical deep staining pits and a prominent stain-excluding feature at the three-fold linker position, similar to the *B. cereus* wild type exosporium and the Form A projection map seen in whole spores of *B. cereus*  $\Delta bclA$ .

### 3.2.2.1.2 Form B crystals

Negatively stained Form B crystals appeared as an array of hexameric particles with a central stain accumulating pit; no hairy nap was seen on the edges of crystals, which were instead well-defined (Fig. 3.8 A). Form B crystals produced a distinct diffraction pattern, often to the third order, with intense second order spots (Fig. 3.8 B). Sixteen micrographs were processed, producing an average unit cell parameter of  $a = b = 81 \pm 1 \text{ \AA}$ ,  $\gamma = 120 \pm 1$ . The projection map generated by Form B crystals showed a hexameric units containing a central stain accumulating region, which is further surrounded by stain accumulating regions at the location of the three-fold symmetry axis (Fig. 3.8 C & D). This also matches with the Form B projection map seen in whole spores of *B. cereus*  $\Delta bclA$ .

### **3.2.2.2 2D projection map of purified *B. cereus* ATCC 10876 $\Delta bclA$ exosporium embedded in ice**

The exosporium isolated from *B. cereus*  $\Delta bclA$  endospores was embedded in vitreous ice and imaged on a Philips CM200 at 62,800x magnification. A single film was collected showed a diffracting crystal, determined using a diffractometer. The film was scanned and imported into *2dx* for processing. The crystalline area was initially roughly masked in *2dx* for ease of processing and tightly masked after unbending (Fig. 3.9 A). A computed Fourier transform from the masked crystal displayed diffraction spots to a limit of  $15 \text{ \AA}$  (Table 3.1 A) (Fig. 3.9 B). Lattice parameters of  $a = 85.7 \text{ \AA}$ ,  $b = 85.8 \text{ \AA}$ ,  $\gamma = 120.7^\circ$  were determined from the crystal. Fourier phases suggested plane group symmetry of  $p6$  (Table 3.1 B). The projection map showed a central low density region

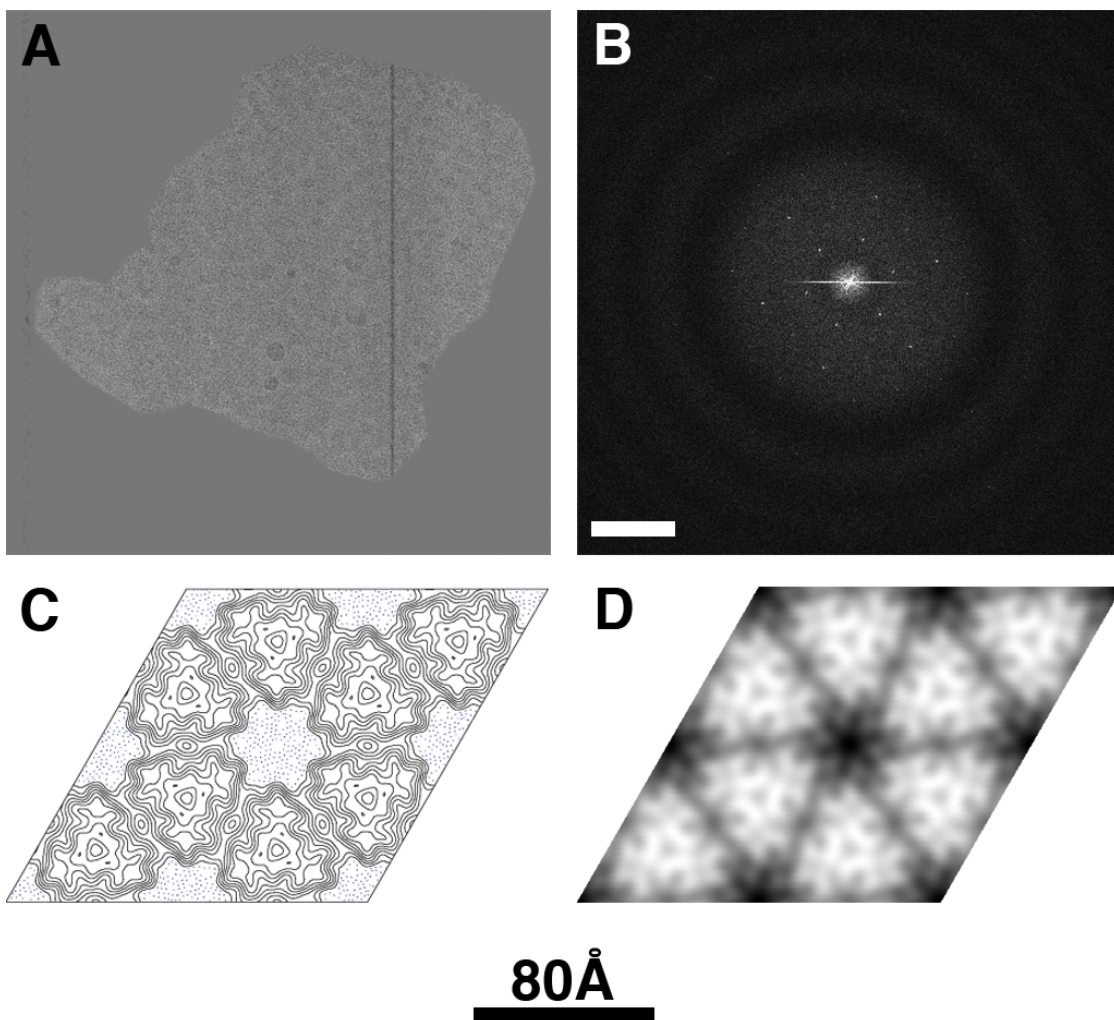


**Figure 3.9.** *B. cereus* ATCC 10876  $\Delta bclA$  form A crystal imaged in ice. (A) Masked form A crystal after scanning from film. (B) Computed Fourier transform after unbending of masked crystalline area. (C) Contour and (D) grey level projection map of crystal. Scale bar in (B) represents  $0.025 \text{ \AA}^{-1}$ .

**Table 3.1 A. Phase residuals in resolution shells for *p6* imposed *B. cereus*  $\Delta bclA$  exosporium crystal for all measured spots**

Resolution Shell (Å)	Number of unique reflections measured	Mean phase residual (°)
200 - 19	25	26.3
19 - 15	21	41.6
15 - 12	14	48.5

A mean phase residual of 90° would indicate random phases

**Table 3.1 B. The internal phase residuals determined after the imposition of all possible two-sided plane groups calculated from one cryo-EM image of a *B. cereus*  $\Delta bclA$  exosporium crystal.**

Two sided plane group	Phase residual versus with other spots (90° random)	Number of Comparisons	Target residual based on statistics taking Friedel weight into account
<i>p1</i>	20.5	38	
<i>p2</i>	22.4*	19	29.6
<i>p12_b</i>	43.4	9	23.6
<i>p12_a</i>	44.7	9	23.6
<i>p121_a</i>	61.9	9	23.6
<i>p121_b</i>	55.2	9	23.6
<i>c12_b</i>	43.4	9	23.6
<i>c12_a</i>	44.7	9	23.6
<i>p222</i>	34.1	37	25.2
<i>p2221b</i>	47.8	37	25.2
<i>p2221a</i>	58.8	37	25.2
<i>p22121</i>	60.5	37	25.2
<i>c222</i>	34.1	37	25.2
<i>p4</i>	30.2	43	24.5
<i>p422</i>	28.2	89	22.5
<i>p4212</i>	58.2	89	22.5
<i>p3</i>	13.6*	32	20.5
<i>p312</i>	13.3*	73	20.9
<i>p321</i>	14.2*	79	21.5
<i>p6</i>	14.2*	83	22.6
<i>p622</i>	14.0	171	21.5

Internal phase residuals were determined from spots of IQ1-1Q5 to 20Å resolution. The values marked with \* are good candidates for the symmetry as the experimental phase residual is close to that expected value based on the signal-to-noise ratio.

surrounded by six stain-excluding linkers lying on the three-fold symmetry axis (Fig. 3.9 C & D).

### **3.2.2.3 2D projection map of sonicated *B. cereus* ATCC 10876 $\Delta$ exsFA exosporium**

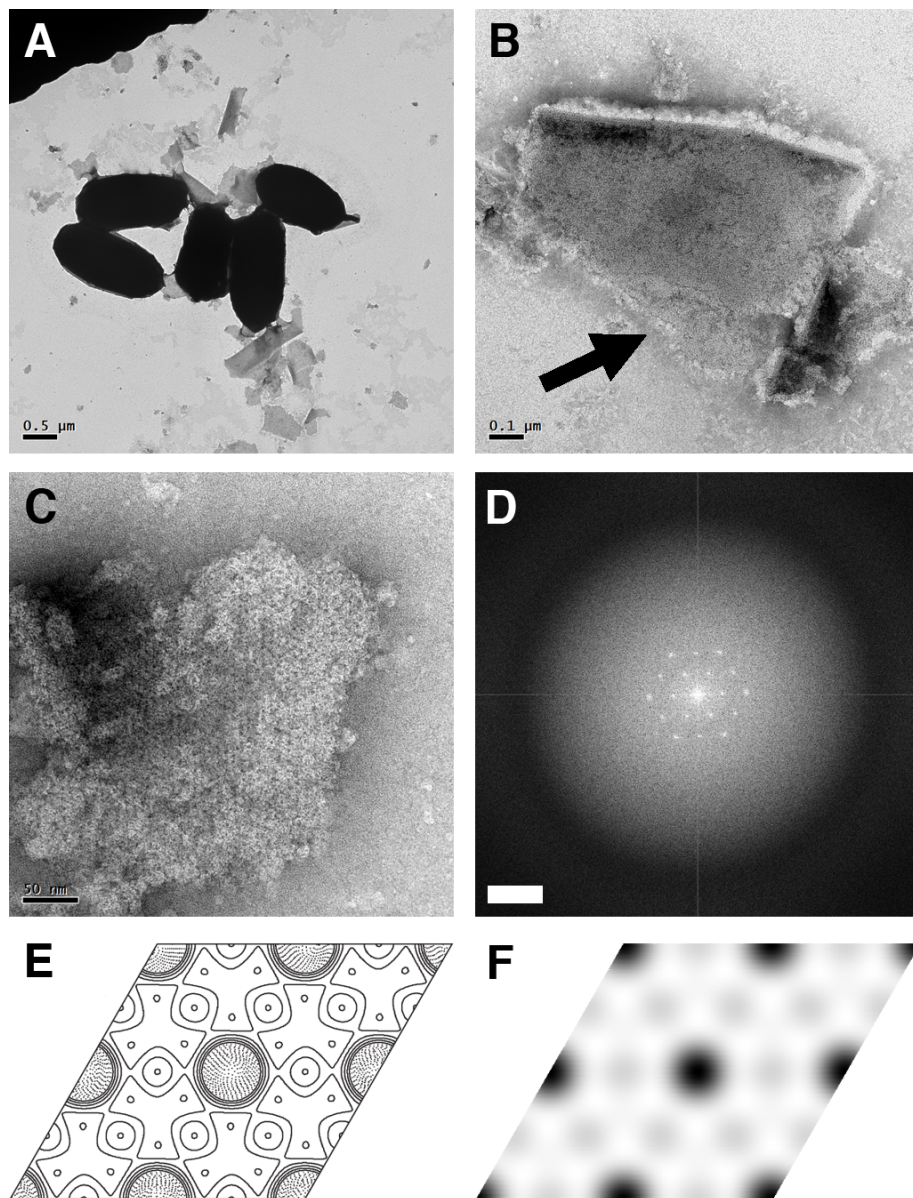
*B. cereus* ATCC 10876  $\Delta$ exsFA spores sonicated for 5 min, as described in 2.3.2, had exosporium removed with intact spore cores as visualised by TEM (Fig. 3.10 A). The exosporium fragments appeared very contrasty, much like wild type exosporium prepared by French press. Deep stain-penetrating pits were visible on the surface of the exosporium with a heterogeneous mix of nap and nap-less crystals (Fig. 3.10 B & C). The diffraction patterns from both nap and nap-less exosporium appeared identical (Fig. 3.10 D). Seven micrographs were processed and averaged showing unit cell parameters of  $a = b = 83 \pm 2 \text{ \AA}$ ,  $\gamma = 120 \pm 1^\circ$ . The projection map of the sonicated *B. cereus*  $\Delta$ exsFA exosporium was identical to that of the *B. cereus* wild type exosporium with a central staining pit and stain-excluding features at the three-fold linker position (Fig. 3.10 E & F).

### **3.2.2.4 2D projection map of sonicated *B. thuringiensis* 4D11 exosporium**

*B. thuringiensis* 4D11 spores grown with shaking at low rpm were sonicated for 5 s at 15 microns to fragment and remove exosporium attached to the spore core. The exosporium fragments were very contrasty with individual hexameric units clearly identifiable (Fig. 3.11 A). No nap was seen around the surface of the exosporium, as in *B. thuringiensis* 4D11 whole spores. A computed Fourier transform from *B. thuringiensis* 4D11 exosporium showed distinct diffraction spots similar to that of the previous *B. cereus* exosporium (Fig. 3.11 B). Eight images were processed, displaying unit cell parameters of  $a = b = 80 \pm 1 \text{ \AA}$ ,  $\gamma = 120 \pm 1^\circ$ . The *B. thuringiensis* 4D11 exosporium revealed a projection map much like that of *B. cereus*  $\Delta$ bclA Form B crystals with a central staining pit and heavy staining at the three-fold linker position (Fig. 3.11 C & D). The projection maps from sonicated *B. thuringiensis* 4D11 exosporium (Fig. 3.11 D) and whole spore exosporium (Fig. 3.6 E) were identical at this resolution.

## **3.2.3 Three-dimensional reconstructions of type II exosporium crystals**

Three-dimensional reconstructions were generated by the method described in Chapter 2.8. Images of exosporium crystals tilted between  $-50^\circ$  to  $50^\circ$  in  $10^\circ$  increments were



**80Å**

**Figure 3.10. Analysis of sonicated exosporium from *B. cereus* ATCC 10876  $\Delta$ exsFA.** (A) Sonication leaves spore cores intact with exosporium detached. (B) A possible hairy nap [arrow] can be seen on some exosporium fragments but (C) not on others. (D) Diffraction from both nap and nap-less crystals are identical. Projection maps displayed in (E) contour and (F) grey level merged from seven untilted micrographs. Scale bar in (D) represents  $0.025 \text{ \AA}^{-1}$ .

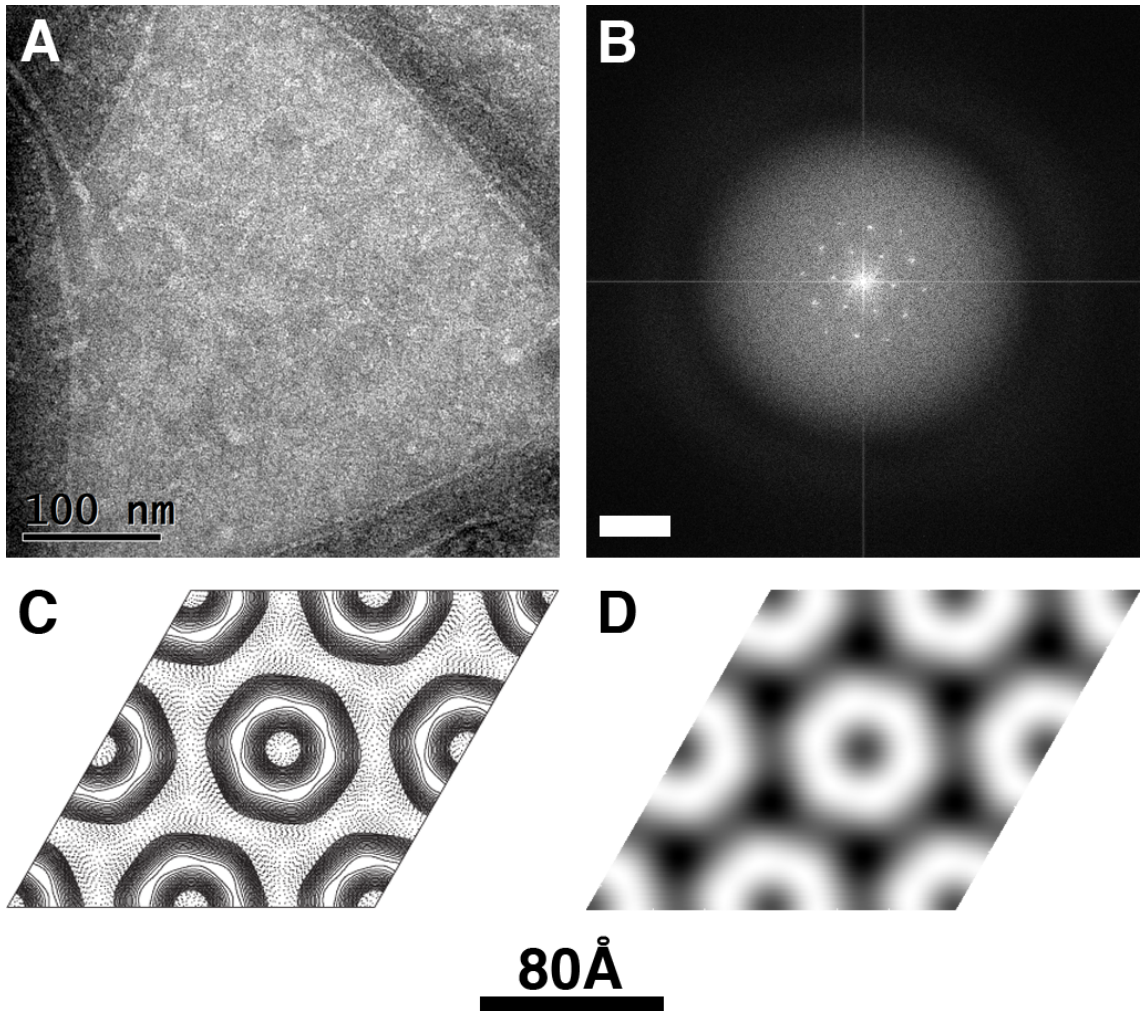


**Figure 3.11. Analysis of exosporium from *B. thuringiensis* 4D11.** (A) Crystalline array of hexameric particles. (B) Computed Fourier transform displaying clear diffraction spots. Projection maps merged from eight untilted micrographs viewed in (C) contour and (D) in grey level. Scale bar in (B) represents  $0.025 \text{ \AA}^{-1}$ .

collected in a series of micrographs. For all exosporium crystals  $p6$  symmetry was applied in the merging, determined by *2dx\_allspace*. All density models were viewed in UCSF Chimera (Pettersen *et al.*, 2004).

### **3.2.3.1 3D reconstruction of *B. cereus* ATCC 10876 $\Delta bcIA$ Form A exosporium**

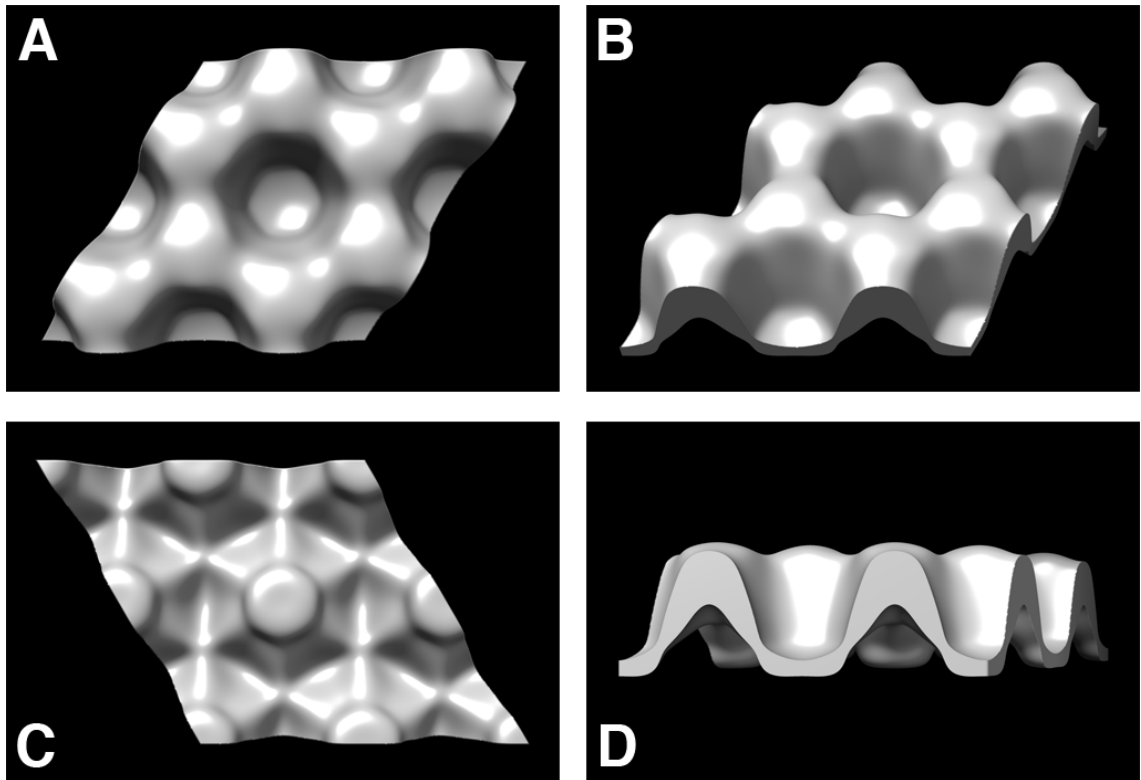
Five independent tilt series of *B. cereus* Form A exosporium crystals were collected and merged in three dimensions. A total of fifty-three micrographs were processed with two images removed due to high phase residuals during merging (Appendix 3.1). The final merged three-dimensional model (Fig. 3.12) showed a structure similar to the interlinked “crown-like” structure from *B. cereus* ATCC 10876 type II exosporium crystals (Ball *et al.*, 2008). Linkers at the three-fold symmetrical positions surround a six-fold central stain-accumulating cup. The cup structure tapers from  $\sim 60$  Å in diameter at the “top” surface to  $\sim 36$  Å at the base with a depth of  $\sim 60$  Å. The 10 Å diameter pores found in the *B. cereus* wild type reconstruction do not seem to be resolved in the Form A crystal but the density in those regions of the map appeared low.

### **3.2.3.2 3D reconstruction of *B. cereus* ATCC 10876 $\Delta bcIA$ Form B exosporium**

Fourteen tilt series were collected on Form B crystals and merged in three dimensions. A total of one hundred and thirty three images were collected with three removed in the merging due to high phase residuals (Appendix 3.2). A model in three-dimensions (Fig. 3.13) showed a six-fold cup structure  $\sim 60$  Å in diameter with a central cavity  $\sim 29$  Å in diameter and 50 Å in depth. Compared to wild type and Form A exosporium crystals, tapering of the cup structure was lost in the inner cavity and the linker was missing at the three-fold symmetry axis.

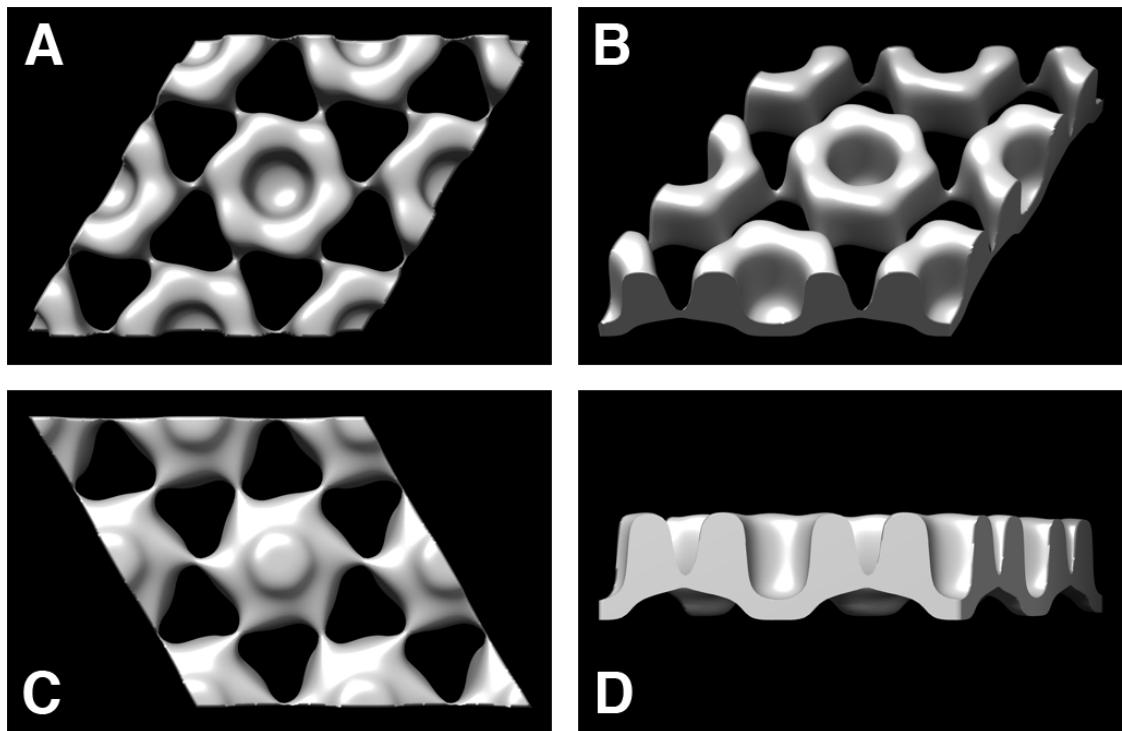
### **3.2.3.3 3D reconstruction of *B. cereus* ATCC 10876 $\Delta exsFA$ exosporium**

Five tilt series were collected on *B. cereus* ATCC 10876  $\Delta exsFA$  exosporium fragments obtained from sonicated endospores. A total of fifty-one images were processed and merged to generate a model of the mutant exosporium (Fig. 3.14) (Appendix 3.3). A central cup structure 50 Å in depth could be seen surrounded by linkers at the three-fold symmetry position. A slight tapering in the cavity of the cup could be seen with a diameter of  $\sim 55$  Å at the “top” surface and 25 Å towards the base. The predominant strain excluding regions lied at the linkers with a thickness of  $\sim 40$  Å. In comparison with



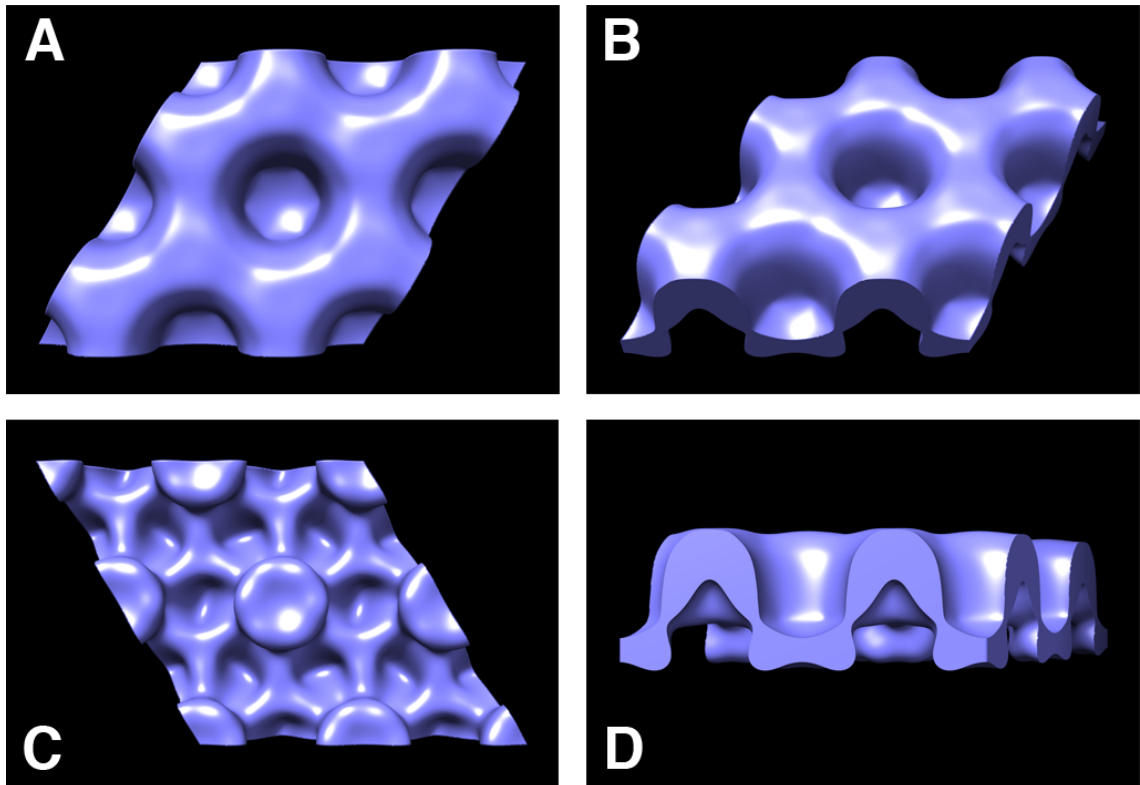
**80Å**

**Figure 3.12.** *B. cereus*  $\Delta bclA$  Form A exosporium modelled in three-dimensions. Surface representations seen from (A) above, (B) 40° tilt, (C) below and (D) 90° perpendicular to the plane of view.



**80Å**

**Figure 3.13.** *B. cereus*  $\Delta bclA$  Form B exosporium modelled in three-dimensions. Surface representations seen from (A) above, (B) 40° tilt, (C) below and (D) 90° perpendicular to the plane of view.



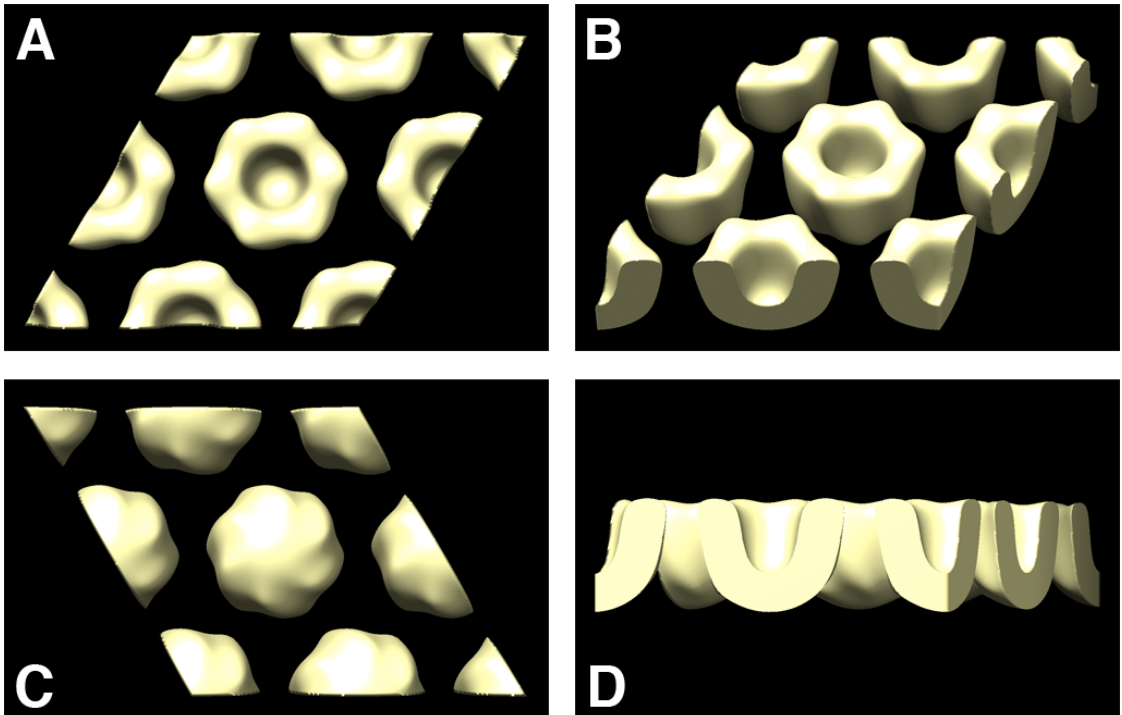
**80Å**

**Figure 3.14.** *B. cereus*  $\Delta$ *exsFA* exosporium modelled in three-dimensions. Surface representations seen from (A) above, (B) 40° tilt, (C) below and (D) 90° perpendicular to the plane of view.

the *B. cereus* type II exosporium crystal, the 10 Å cavities were not visible, but the density in those regions of the model remained very low.

#### **3.2.3.4 3D reconstruction of *B. thuringiensis* 4D11 exosporium**

Six tilt series of *B. thuringiensis* 4D11 exosporium were collected with a total of seventy images processed. One image was removed during merging due to high phase residuals (Appendix 3.4). The final three-dimensional model (Fig. 3.15) showed a six-fold cup structure ~64 Å in diameter and ~45 Å in depth. A clear tapering of the cup structure can be seen, with the diameter of the central cavity changing from ~30 Å at the surface to ~15 Å at the closed curved base. No density was present at the three-fold linker position, as was also the case for the Form B crystal found in the *B. cereus*  $\Delta bclA$  mutant.



**80Å**

**Figure 3.15.** *B. thuringiensis* 4D11 exosporium modelled in three-dimensions. Surface representations seen from (A) above, (B) 40° tilt, (C) below and (D) 90° perpendicular to the plane of view.

### 3.3 Discussion

#### 3.3.1 Loss of BclA results in heterogeneous “hairy nap” populations

*B. cereus* ATCC 10876 endospores imaged by TEM always possessed a hairy nap around the outer surface of the exosporium, presumably composed mostly of BclA. This was clearly identified in Figure 3.2 by the contrasty “blob-like” material on the edge of the exosporium. Conversely in the “wild strain” of *B. thuringiensis* 4D11, which does not possess a hairy nap (Kailas *et al.*, 2011), the exosporium was completely absent of this highly contrasting material (Fig. 3.5). Endospores of a *B. cereus*  $\Delta bclA$  mutant displayed either no hairy nap or sparse patches of nap on the exosporium surface (Fig. 3.3). This is consistent with the findings in *B. anthracis* where *bclA* mutant endospores either lacked a visible hairy nap (Boydston *et al.*, 2005, Sylvestre *et al.*, 2002) or possessed one that was morphologically shorter (Steichen *et al.*, 2003). The phenotype displaying a complete loss of nap can be attributed to the deletion of the gene and hence lack of expression of BclA on the surface. It has been reported that other glycoproteins, such as BclB in *B. anthracis* (Thompson *et al.*, 2007, Waller *et al.*, 2005) and ExsJ in *B. cereus* (Todd *et al.*, 2003) are found in the exosporium. SDS-PAGE analysis of the exosporium from *B. cereus* ATCC 10876 by Dr. D. Radford (University of Sheffield, unpublished) showed that both ExsJ and BclA were present within a high molecular weight complex (Fig. 3.16). In a *B. cereus*  $\Delta exsJ$  mutant, the band corresponding to the ExsJ high molecular weight complex is lost, whilst the band corresponding to the BclA high molecular weight complex remains. In a *B. cereus*  $\Delta bclA$  mutant, a band corresponding to the ExsJ high molecular weight complex is present but not for the BclA complex. The homologue, which may normally be redundant, or a minor population, could account for the nap-presenting population of spores and their different morphology. It was also shown using Colony PCR by myself and Dr. D. Radford that the presence of a nap did not arise through a mixed population of wild type and mutant spores (data not shown). Future investigation using mutational approaches, in particular a *B. cereus*  $\Delta bclA\Delta exsJ$  double mutant, may indicate whether these nap features result from the noted homologues. Further work is also necessary to confirm if a mutation to the *bclA* gene results in a more centrally located spore core.

#### 3.3.2 Architecture of $\Delta bclA$ mutant exosporium is altered through increased extractability of structural proteins

The robustness and crystallinity of the exosporium remained unaffected by the loss of BclA. Endospores remained intact after rigorous washing and computed Fourier transforms of the exosporium showed diffraction from the crystalline basal layer.

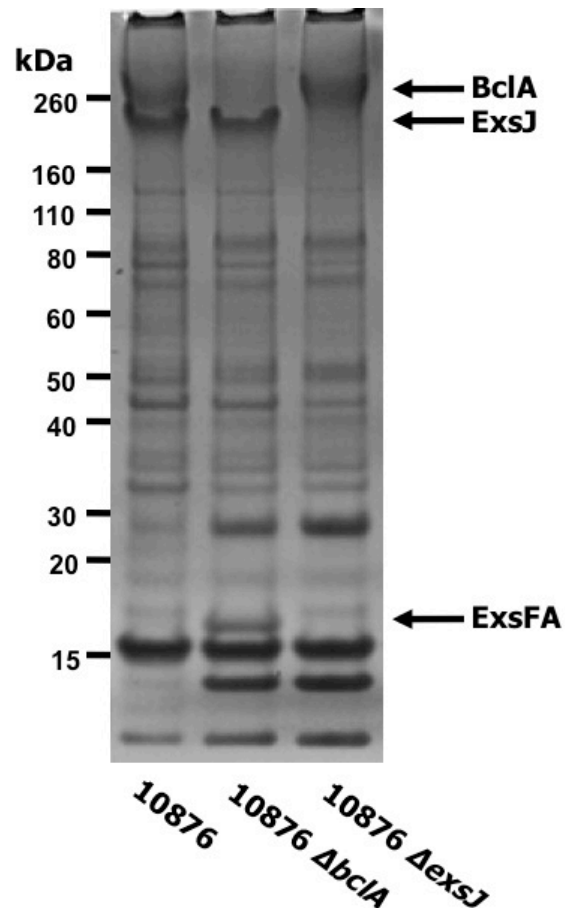


**Figure 3.16. SDS-PAGE analysis of purified exosporium from *B. cereus* ATCC 10876 and *B. cereus* ATCC 10876  $\Delta bclA$ .** 10876 lane shows presence of BclA and ExsJ as high molecular weight complexes along with no clear band for ExsFA. 10876  $\Delta bclA$  lane shows absence of BclA but retention of the ExsJ high molecular weight complex and an increase in soluble ExsFA. The 10876  $\Delta exsJ$  retains BclA. Data provided by Dr. D. Radford.

However, analysis of the exosporium from *B. cereus*  $\Delta bclA$  whole spores revealed two different projection maps with similar unit cell parameters to that of the *B. cereus* type II basal layer crystal (Ball *et al.*, 2008). The projection map from the Form A crystal appeared near identical to that of the *B. cereus* type II basal crystal, whilst in the Form B crystals, a clear loss in density could be seen at the three-fold linker. Kailas *et al.*, (2011) previously speculated that ExsFA, the hairy nap anchor protein, resides at the three-fold linker position. The loss of the three-fold linker in the Form B crystal may explain the increased intensity of a protein band corresponding to ExsFA in SDS-PAGE gels of the *B. cereus*  $\Delta bclA$  exosporium (Dr. D. Radford) (Fig. 3.16). ExsFA is known to be associated with BclA, forming a high molecular weight complex along with ExsY (Boydston *et al.*, 2006, Johnson *et al.*, 2006, Redmond *et al.*, 2004). The incorporation of ExsFA and BclA into the exosporium has also been shown to occur in a co-dependent manner, with BclA providing stability for the anchor protein for correct assembly (Sylvestre *et al.*, 2005, Thompson *et al.*, 2011b). The altered structure of the Form B crystal supports the idea that loss of BclA creates instability in the ExsFA anchor protein, leading to the loss of density from the three-fold linker domain. From this, I infer that ExsFA and BclA lie at this location within the exosporium. The structure of the Form B crystal also shows that stability of *B. cereus* exosporium once formed does not rely on either ExsFA or BclA for integrity.

Form A crystals could represent material in which ExsFA is still attached to the exosporium, producing a near identical projection map to wild type exosporium. It is also possible that the structure we see in Form A crystals arise due to the exosporium utilising other anchor protein homologues, such as ExsFB (Sylvestre *et al.*, 2005), which would also explain the wild type-like projection map seen in *B. cereus*  $\Delta exsFA$  spores.

As expected, purification of the exosporium from *B. cereus*  $\Delta bclA$  mutant endospores yielded two distinct crystal forms. The maps from each crystal form were respectively identical to the two different projection maps obtained from whole spore exosporium. Upon further inspection of individual crystals, images of Form B crystals were seen to be less contrasty in comparison that those of Form A crystals. This indicated a potential difference in surface properties, such as hydrophobicity, and interactions with the uranyl formate stain. This may be case as it was shown in *B. cereus* ATCC 14579 that loss of the C-terminal domain or collagen-like repeat from BclA increased the hydrophobicity and isoelectric point of the spore (Lequette *et al.*, 2011). The increased

hydrophobicity, as a result of the loss of BclA from the exosporium, could potentially exclude the uranyl formate stain and hence lower the contrast. Form A crystals appeared to be surrounded by a morphologically different hairy nap at the edges of the exosporium, leading to the conclusion that a different hairy nap protein was present. It was also apparent that whilst Form A crystals looked identical to the wild type basal layer crystals in their deep contrasting pitted structure, Form B crystals were comprised of visible individual hexamers much like the *B. thuringiensis* 4D11 exosporium that lacked the hairy nap. The merged projection map of the Form A crystal was identical to those of *B. cereus* wild type exosporium. The merged projection map from the Form B crystal showed however, a loss in density at the linker on the three-fold symmetry axis, proposed to be ExsFA. The Form B projection map from our *B. cereus* ATCC 10876  $\Delta bclA$  mutant appears similar to the individual *B. anthracis*  $\Delta bclA$  micrograph recorded by Rodenburg *et al.*, (2014). It is not known whether both forms exist in *B. anthracis*  $\Delta bclA$  spores but it is possible that the exosporium behaves differently resulting in only the B form.

A Form A crystal recorded under ice-embedded conditions showed a high resolution, artefact free, projection map similar to the *B. cereus* type II basal layer exosporium. The projection maps shown in Figure 3.9 clearly identify a central stain accumulating region, presumably the cup structure (Ball *et al.*, 2008), that is similar to the 7 Å exosporium map reported by Kailas *et al.*, (2011). Further stain accumulation could also be seen around the central pit, resulting from the 10 Å pores reported by Ball *et al.*, (2008). However, it was not possible to identify distinct helices due to both the insufficient resolution and number of images recorded. Future studies will hopefully reveal a high-resolution structure of both Form A and Form B crystals for comparison with each other and the wild type exosporium.

A three dimensional reconstruction of both crystal forms revealed a more detailed assessment of the structure. The Form A crystal, modelled in three-dimensions, was almost identical in comparison to the wild type *B. cereus* type II basal layer crystal in unit cell size and arrangement (Fig. 3.17 A & B). A central closed tapering cup is surrounded by a six-fold of linkers. However, the 10 Å pores found in the wild type were missing from Form A crystals that we attribute to a lack of resolution in defining these features. The micrographs used in the reconstruction of the original structure by Ball *et al.*, (2008) were taken on film and in Low Dose, resulting in images with well-ordered and higher order diffraction spots, revealing more intricate features post-processing.

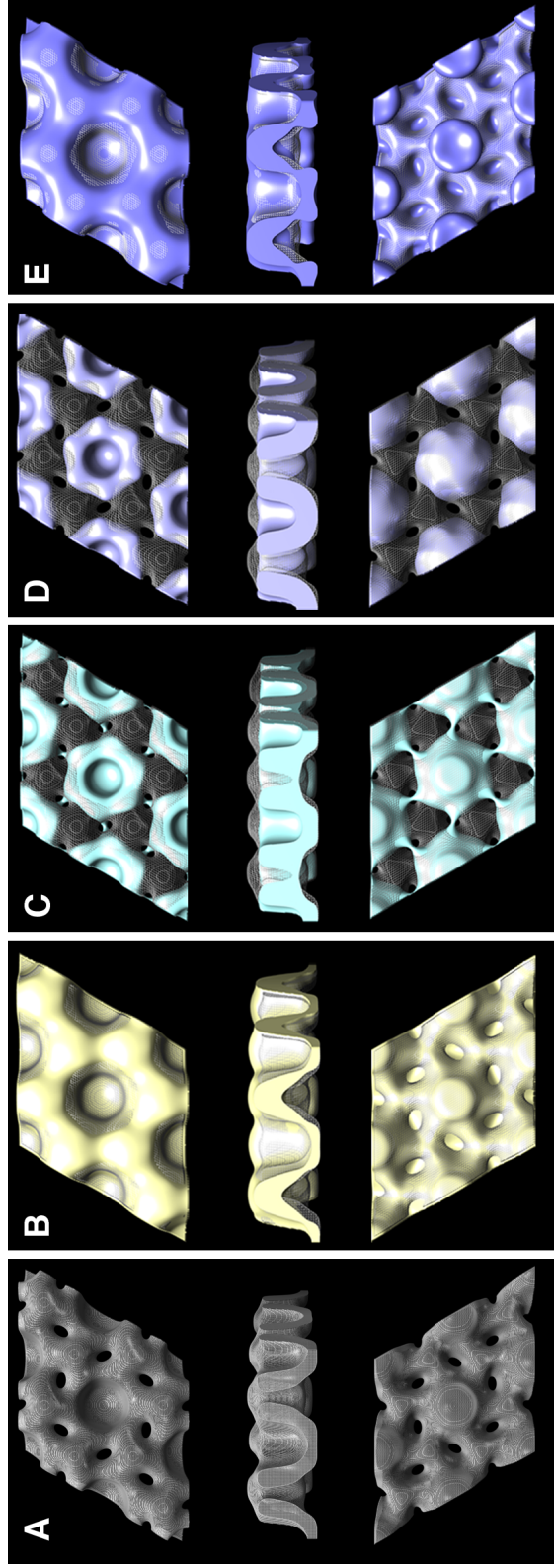


**Figure 3.17. Comparative exosporium structural overlays.** Volume comparisons between (A) *B. cereus* ATCC 10876 exosporium [density shown as see through wireframe] with: (B) *B. cereus* ATCC 10876  $\Delta bclA$  form A exosporium, (C) *B. cereus* ATCC 10876  $\Delta bclA$  form B exosporium, (D) *B. thuringiensis* 4D11 exosporium and (E) *B. cereus* ATCC 10876  $\Delta exsFA$  exosporium [density shown in solid form].

Form B crystals possessed the same unit cell size as that of *B. cereus* wild type exosporium (Fig. 3.17 C) and Form A crystals, but differed in structure. Firstly, the central closed cup was not tapered but instead perpendicular to the rest of the structure. Secondly, and more strikingly, a loss of density was seen at the three-fold linker position where ExsFA and BclA are proposed to reside. The lack of tapering in the cup structure suggests a conformation change or loss of material resulting from the loss of an architectural significant protein such as ExsFA, but the resolution limit in negative stain does not allow such speculation to be made with any confidence. It is however clear that a loss of protein has occurred at the linker loci, supporting the idea that ExsFA has become detached and accounts for the increased concentration of extractible ExsFA on SDS-PAGE gel (Fig. 3.16). The change in overall thickness of the Form B exosporium crystal, when compared to both wild type and Form A exosporium, was consistent with the loss of the linker domain (Fig. 3.17).

The Form A crystal in a  $\Delta bclA$  mutant could therefore represent a low resolution type II basal layer lacking BclA or might represent the same exosporium template with a different anchor and nap proteins. The presence of the Form B crystal may represent the basal layer structure after ExsFA has been detached, leaving the remainders of the exosporium template. There may be further changes to the proteins present on the exosporium surface; however, our electron crystallographic technique only shows the changes in the regular features. Future research into exosporium mutants by AFM may reveal the subtle changes in structure resulting from proteins that were “average out” in our crystallographic study.

### **3.3.3 Analysis of the nap-less *B. thuringiensis* 4D11 strain revealed a loss of linker density**

We further investigated the contribution of the hairy nap towards exosporium architecture through the analysis of *B. thuringiensis* 4D11, a nap-less strain belonging to the *B. cereus* sensu lato group. Endospores of this strain were grown with less agitation, as it seemed the integrity of the exosporium was compromised. Micrographs of undamaged endospores showed no nap on the exosporium surface and clear hexameric units. The projection map from whole spores revealed a unit cell near identical to the wild type *B. cereus* type II exosporium, suggesting structurally a similar template protein. The exosporium from *B. thuringiensis* 4D11 appeared to have identical features in projection to those of the *B. cereus*  $\Delta bclA$  Form B crystal, displaying a central staining cavity and heavy staining at the linker position.

A three-dimensional reconstruction revealed an array of cups, like those reported using atomic force microscopy by Kailas *et al.*, (2011). The thickness of the cup was consistent with the tapered structure of the *B. cereus* type II basal layer crystal indicative of a common protein template (3.17 D). The array appeared almost identical in size and arrangement to the  $\Delta bclA$  mutant Form B crystal, also displaying a lack of stain-excluding material at the three-fold linker, suggesting that both the nap and the anchor protein are absent. This correlates well with the absence of BclA and very low levels of ExsFA in Western blots of *B. thuringiensis* 4D11 exosporium (Terry, 2010). This evidence supports that the *B. cereus*  $\Delta bclA$  Form B crystal could arise from the loss of the hairy nap and subsequently BclA. More importantly, the *B. thuringiensis* 4D11 strain shows the nap, and most probably the anchor, is not required for complete exosporium formation. Hence, we speculate the ordered structure seen in *B. thuringiensis* 4D11 originates predominantly from the exosporium template protein.

### **3.3.4 Mutation in ExsFA reveals contribution of redundant endospore proteins towards exosporium architecture**

Analysis of *B. cereus*  $\Delta exsFA$  mutant endospores showed varying populations with and without a hairy nap on the outer exosporium surface. It was previously reported that cross-sections of *B. cereus*  $\Delta exsFA$  spores possessed a sparse and patchy hairy nap that was morphologically different from the wild type (Ball, 2006, Johnson, 2004). Sylvestre *et al.*, (2005) reported similar results in *B. anthracis* endospores where a  $\Delta exsFA$  mutant resulted in patchy sparse hairy nap. They were also able to show that the nap in a *B. anthracis*  $\Delta exsFB$  mutant was not dissimilar from the wild type and a  $\Delta exsFA\Delta exsFB$  double mutant was required for the complete loss of nap from the spore (Sylvestre *et al.*, 2005). Hence, we can attribute the presence of a nap in our  $\Delta exsFA$  strain to the homologue, ExsFB, remaining functional as an anchor protein.

Projection maps of the exosporium from *B. cereus*  $\Delta exsFA$  whole spores were identical between the nap and nap-less populations. Analysis of the exosporium in projection showed the same unit cell parameters as the wild type basal layer crystal and the same distribution of density with a central deep staining region and stain-excluding three-fold linkers. Reconstruction in three-dimensions revealed a structure similar to the wild type model (Fig. 3.17 E) but was near identical to the *B. cereus*  $\Delta bclA$  Form A crystal. The  $\Delta bclA$  Form A crystal was interpreted to be an exosporium variant in which the ExsFA anchor protein was still attached but BclA was missing. However we could also

speculate that the structure seen in the Form A crystal, which resembles the structure found in the *B. cereus*  $\Delta$ *exsFA* mutant, is possibly that of an exosporium made with a different anchor protein, such as ExsFB.

## Chapter 4. Self-assembly of ExsY and its role as the exosporium template protein

### 4.1 Introduction

The complete assembly of the exosporium during sporulation within the *B. cereus* group requires correct expression of ExsY (Boydston *et al.*, 2006, Johnson *et al.*, 2006, Redmond *et al.*, 2004). ExsY has previously been isolated as part of a high molecular weight complex with BclA, the known exosporium architectural “hairy nap” protein (Boydston *et al.*, 2005, Sylvestre *et al.*, 2002, Thompson and Stewart, 2008) and ExsFA, the hairy nap anchor protein (Sylvestre *et al.*, 2005).

To investigate the contribution of ExsY in exosporium assembly, recombinant ExsY was expressed in *Escherichia coli* as an N-, C-terminal double his-tagged protein, His<sub>6</sub>-ExsY (Provided by Dr. D Radford, University of Sheffield). Variants of ExsY protein constructed with only an N- or C-terminal his-tag and untagged were also analysed. This chapter discusses how heterologously expressed ExsY from *B. cereus* remarkably self-assembles into crystalline arrays  $\geq 1 \mu\text{m}$  within the *E. coli* host. The structural and biochemical properties of the self-assembled ExsY array was compared with that of *B. cereus* ATCC 10876 and *B. thuringiensis* 4D11 exosporium. The Identification of the exosporium template protein will allow us to advance our understanding of the formation of the *Bacillus*, and perhaps also *Clostridium*, exosporium. Appreciation of the structure and topology of the exosporium template layer will provide further insight into both the location of other exosporium associated proteins and their structural contributions.

## **4.2 Results**

### **4.2.1 Recombinant ExsY constructs**

To express and purify recombinant ExsY, the *exsY* gene from *B. cereus* ATCC 10876 was cloned into pET28a and pET21b as hexa-histidine tagged constructs and also into pCOLADuet1 as an untagged construct. Figure 4.1 shows the resulting amino acid sequence of the encoded proteins. The plasmids described below were generated following the method described in 2.4.1.

#### **4.2.1.1 pCAexsY - ExsY Untagged**

The *exsY* gene was cloned into the MCS2 site of pCOLADuet-1 as an untagged construct (Fig. 4.1 A). The *exsY* gene was amplified by PCR using primers “ExsY-fwd” and “ExsY-rev-COLA. The *exsY* PCR product and pCOLADuet-1 vector were both digested using NdeI and XhoI.

#### **4.2.1.2 p28exsYNC - ExsY N-, C-terminal his-tagged**

A N-, C-terminal double his-tagged construct of ExsY was created in pET28a by Dr. D. Radford (University of Sheffield) (Fig. 4.1 B). The construct was made as in pCAexsY except primers were replaced with “exsY-for” and “exsYC-rev”. The *exsY* insert and pET28a vector were digested with NdeI and XhoI. This construct was also designed with the last two amino acids deleted (V153 and K154) to replicate the *exsY* gene from *B. anthracis*.

#### **4.2.1.3 p28exsYN - ExsY N-terminal his-tagged**

A N-terminal his-tagged construct of the *exsY* gene was created in pET28a (Fig. 4.1 C). The construct was made as in pCAexsY except primers were replaced with “ExsY-fwd” and “ExsY 10876 REV ECOR1”. The *exsY* insert and pET28a vector were digested with NdeI and EcoR1.

#### **4.2.1.4 p28exsYC - ExsY C-terminal his-tagged**

A C-terminal his-tagged construct was made as in pCAexsY except primers were replaced with “exsY-for” and “exsYN-rev”. The *exsY* insert and pET21b vector were digested with NdeI and XhoI. This construct was also designed with the last two amino acids deleted (V153 and K154) to replicate the *exsY* gene from *B. anthracis* (Fig. 4.1 D).

**(A) ExsY untagged (pCOLA-Duet1)**

MSCNENKHHGSSHCVV DVVKFINELQDCSTTTCGSGCEIPFLGAHNTASVANTRPFILYTKT  
GEPFEAFAPSASLTSCRSPIFRVESVDDDSCAVLRVLTVVVLGDSSPVPPGDDPICTFLAVPN  
ARLISTTTCITVDLSCFCAIQCLRDVSIK

**(B) ExsY-N, -C double His-tagged (pET28a)**

MGSSHHHHHHSSGLVPRGSHMSCNENKHHGSSHCVV DVVKFINELQDCSTTTCGSGCEIPFL  
GAHNTASVANTRPFILYTKTGEPEAFAPSASLTSCRSPIFRVESVDDDSCAVLRVLTVVVLG  
DSSPVPPGDDPICTFLAVPNARLISTTTCITVDLSCFCAIQCLRDVSILEHHHHHH

**(C) ExsY-N His-tagged (pET28a)**

MGSSHHHHHHSSGLVPRGSHMSCNENKHHGSSHCVV DVVKFINELQDCSTTTCGSGCEIPFL  
GAHNTASVANTRPFILYTKTGEPEAFAPSASLTSCRSPIFRVESVDDDSCAVLRVLTVVVLG  
DSSPVPPGDDPICTFLAVPNARLISTTTCITVDLSCFCAIQCLRDVSIK

**(D) ExsY-C His-tagged (pET21b)**

MSCNENKHHGSSHCVV DVVKFINELQDCSTTTCGSGCEIPFLGAHNTASVANTRPFILYTKT  
GEPFEAFAPSASLTSCRSPIFRVESVDDDSCAVLRVLTVVVLGDSSPVPPGDDPICTFLAVPN  
ARLISTTTCITVDLSCFCAIQCLRDVSILEHHHHHH

**Figure 4.1 Amino acid sequence of recombinant ExsY constructs.** (A) Untagged ExsY, (B) ExsY hexa-histidine tagged at both N- and C-termini, (C) N-terminal hexa-histidine tagged ExsY and (D) C-terminal hexa-histidine tagged ExsY. The (B) and (D) constructs were designed to match the sequence of *B. anthracis* ExsY at the C-terminus by omitting the last two amino acids present in *B. cereus* ATCC 10876 ExsY. Amino acids that are underlined indicate additions made to the sequence and the inclusion of his-tags.

The ExsYNC double his-tagged protein (created by Dr. D. Radford, University of Sheffield) was used initially for all experiments. Once the complexity of the p28exsYNC construct was appreciated, other constructs were generated and expressed to analyse their behaviour.

## **4.2.2 Purification of hexa-histidine-tagged ExsY**

### **4.2.2.1 Solubilisation of ExsY for nickel column affinity purification**

The ExsY N-, C-terminal double his-tagged protein (predicted molecular weight of 19.4 kDa) was overexpressed in *E. coli* BL21(DE3)pLysS following the method described in 2.4.6. The cells harvested from the overexpression were resuspended in urea or Tris buffer and lysed by sonication as described in 2.5.1.2. The lysed sample was centrifuged to separate the soluble cell lysate, containing soluble ExsY, from the insoluble cell components. The soluble fraction containing ExsY was applied to a NiNTA agarose column and purified by affinity chromatography. ExsY was eluted through an imidazole gradient and each eluted fractions was analysed by SDS-PAGE under heated and reducing conditions (Fig. 4.2).

Following the procedure that lysed cells in Tris buffer without urea, there was no clear band corresponding to ExsY on SDS-PAGE of samples eluted after nickel affinity purification (Fig. 4.2 A). Lysis of cells in urea buffer was necessary to solubilize ExsY for binding onto NiNTA agarose columns. ExsY was then eluted in urea buffer containing  $\geq 0.2$  M imidazole (Fig. 4.2 B, lanes 2 -4). ExsY was seen to migrate at the predicted molecular weight of  $\sim 20$  kDa on SDS-PAGE. The detection of ExsY only after treatment with 8 M urea suggested that expression led to the formation of highly insoluble aggregates.

### **4.2.2.2 Isolation of ExsY macromolecular assemblies by batch affinity purification**

There was a risk that aggregates of ExsY, if present, might not elute from a packed column. Therefore, a batch nickel affinity purification approach was taken to isolate his-tagged ExsY assemblies. ExsY expressing cells were resuspended in urea buffer before lysis and analysed by SDS-PAGE under reduced and heated conditions for

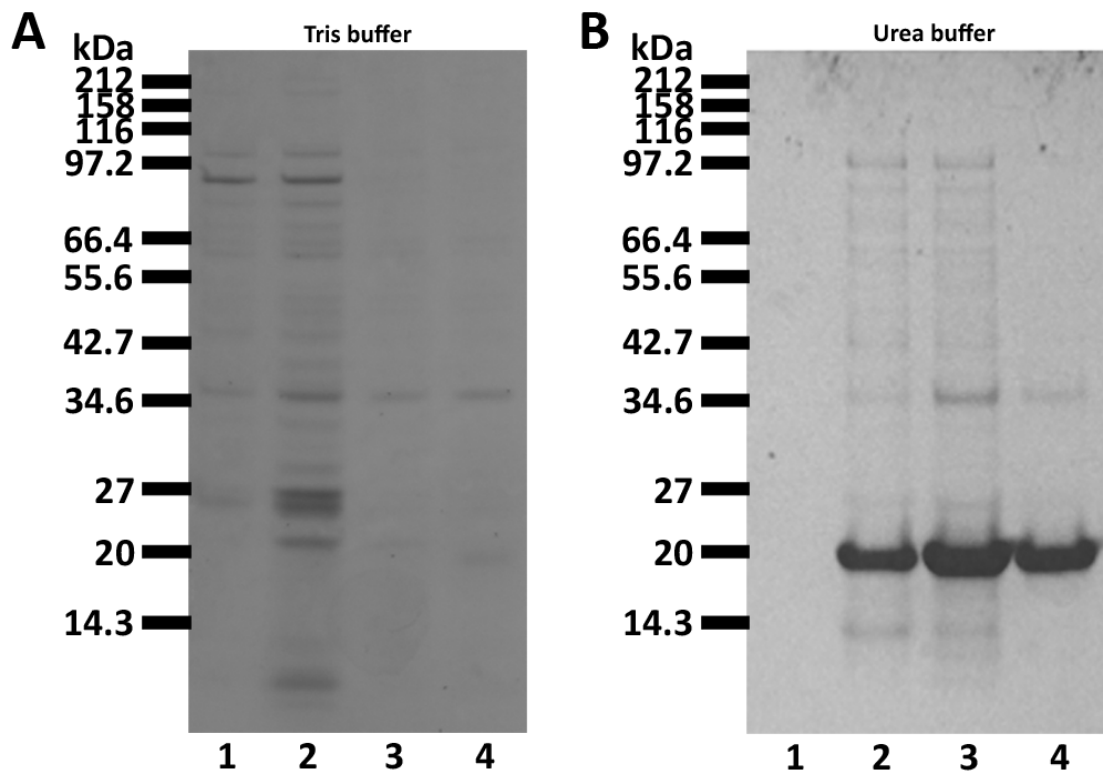


**Figure 4.2 SDS-PAGE analysis of affinity purified soluble ExsY.** (A) ExsY suspended in Tris buffer and eluted in Tris buffer containing imidazole at 0.1 M (lane 1), 0.2M (lane 2), 0.3 M (lane 3) and 1 M (lane 4). (B) ExsY suspended in Urea buffer and eluted in urea buffer containing imidazole at 0.1 M (lane 1), 0.2M (lane 2), 0.3 M (lane 3) and 1 M (lane 4). Samples were boiled by heating to 99 °C in the presence of 50 mM DTT and NuPAGE LDS loading buffer prior to SDS-PAGE analysis. Gels were stained with Coomassie brilliant blue.

presence of ExsY after each purification stage (Fig. 4.3). ExsY was detected in the cell lysate post sonication indicating correct expression (Fig. 4.3, lane 1). ExsY bound in the batch affinity purification was initially eluted using 1 M imidazole in urea buffer (Fig 4.3, lane 2) and subsequently separated into a soluble (Fig 4.3, lane 3) and insoluble fraction (Fig 4.3, lane 4) by ultracentrifugation. An equivalent amount of ExsY was loaded between the soluble and insoluble purified fractions. The amount of soluble ExsY in comparison to insoluble ExsY did vary between preparations.

### **4.2.3 TEM analysis of ExsY**

#### **4.2.3.1 Whole cell analysis of expressing cells**

*E. coli* cells expressing ExsY were negatively stained and viewed directly by TEM. The comparison of uninduced cells (Fig. 4.4 A) with cells after 3.5 h of 1 mM IPTG induction (Fig. 4.4 B) showed the accumulation of electron dense material within the *E. coli* cell. The majority of *E. coli* cells were too thick for the electron beam to penetrate, however, the edges of particular cells were thin enough for images to be collected. Micrographs collected from regions that the electron beam could penetrate (Fig. 4.4 C) revealed crystalline material within the cell, seen by the diffraction pattern on a computed Fourier transform of the area (Fig. 4.4 D).

#### **4.2.3.2 Analysis of affinity purified ExsY fraction**

Soluble ExsY purified from nickel column affinity purification was analysed by TEM for the presence of protein complexes. The ExsY sample eluted in urea buffer containing 1 M imidazole was examined as SDS-PAGE analysis showed this fraction contained the highest purity. Electron micrographs of this fraction showed small monodisperse particles no larger than ~5 nm in diameter with no discernible features (Fig. 4.5 A). Small assembled fragments of ExsY could also be seen; however these were rare and usually very small in size at ~100 nm on a side (Fig. 4.5 B).

#### **4.2.3.3 Thin sections of cells expressing ExsY**

Thin sections were cut of *E. coli* cells expressing recombinant ExsY after induction with IPTG. Thin sections were also cut of *E. coli* cells carrying the pET28a vector only after induction as a control. Both sections were analysed by TEM. Cross sections of cells containing the vector showed a regular granular cytoplasm (Fig. 4.6 A). Sections of cells expressing recombinant ExsY for 3.5 h however, appeared irregular in shape with layers of macro-assemblies forming within the cell (Fig. 4.6 B). These large assembled sheets appeared to only be restricted in size and number by the physical size of the

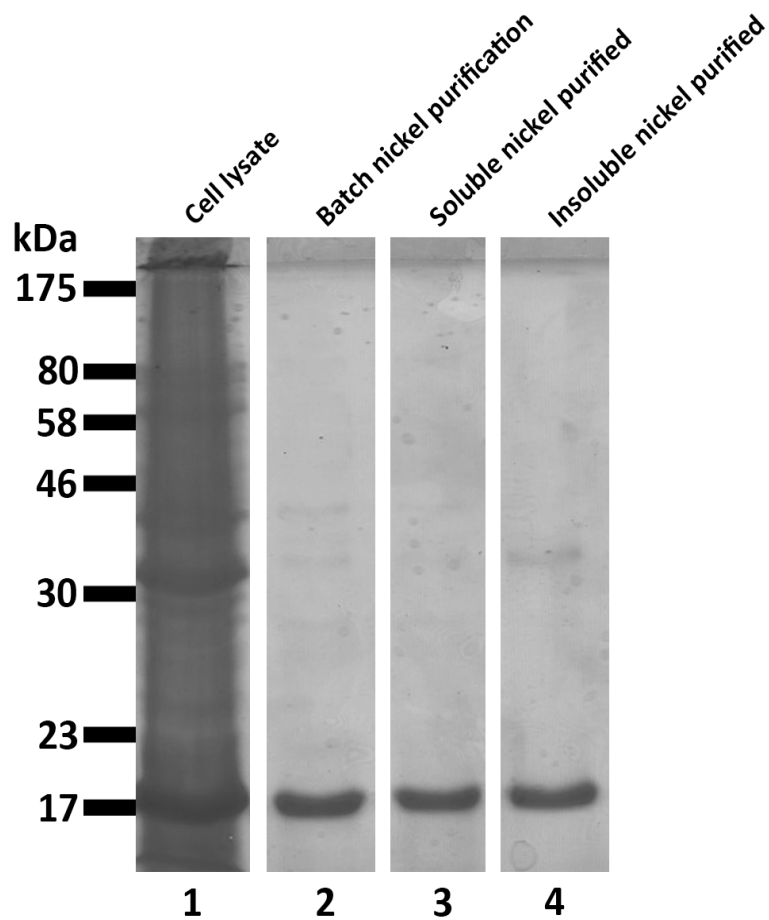


**Figure 4.3 Isolation of insoluble ExsY macromolecular assemblies using batch affinity purification.** SDS-PAGE analysis of (lane 1) cell lysate from cells overexpressing ExsY, (lane 2) total material released from batch nickel affinity purification, (lane 3) soluble ExsY fraction extracted from affinity purification and (lane 4) insoluble macromolecular assemblies from affinity purification. Samples were pretreated in 99 °C heat and 50 mM DTT prior to loading and stained with Coomassie brilliant blue.

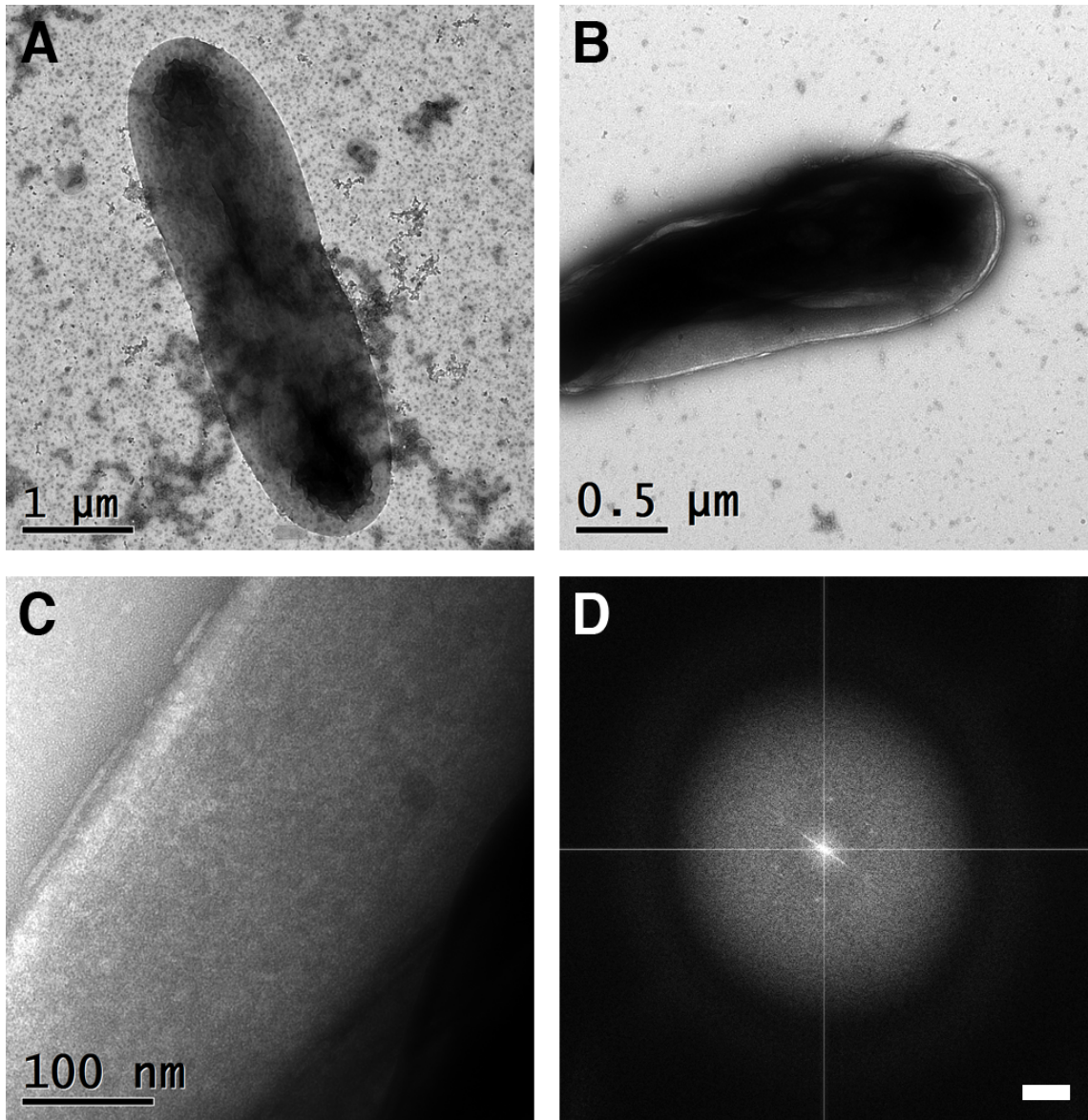


**Figure 4.4 Negatively stained TEM of *E. coli* cells expressing ExsY.** (A) Uninduced *E. coli* cell carrying recombinant ExsY gene. (B) *E. coli* cell expressing ExsY contained crystalline material after 3.5 h induction with 1 mM IPTG. (C) Magnified area of *E. coli* cell from “(B)”. (D) Computed Fourier transform of magnified area in “(C)” displaying a diffraction pattern from the contained crystal. Scale bar is  $0.125 \text{ nm}^{-1}$ .

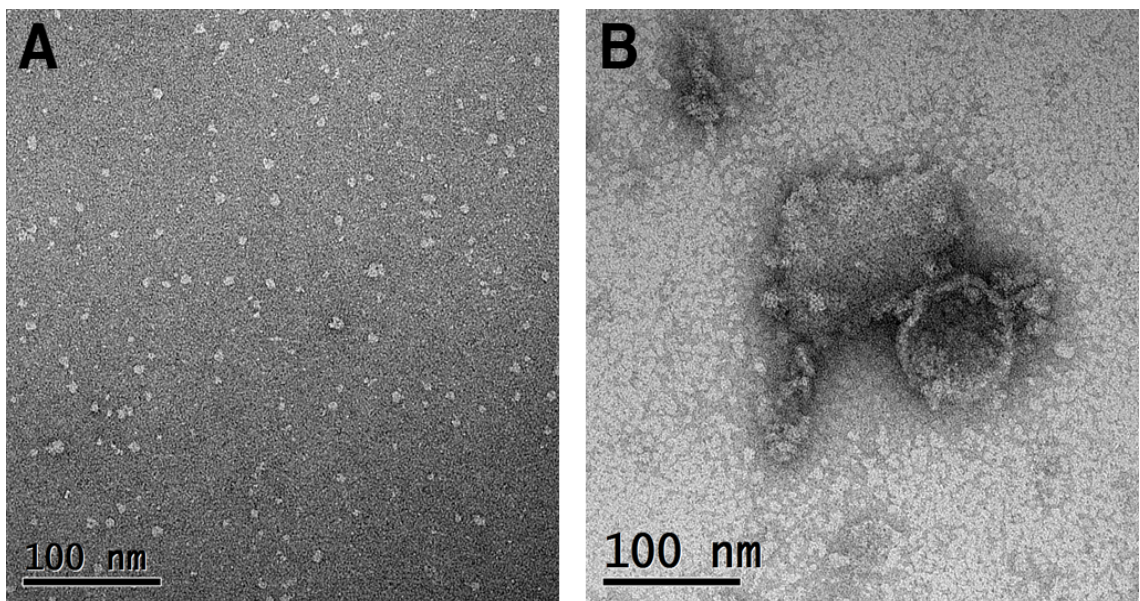


**Figure 4.5 Soluble ExsY purified by nickel column affinity purification.** (A) Representative micrograph of monodispersed single particles of soluble ExsY. (B) Representative micrograph of small ExsY complexes.

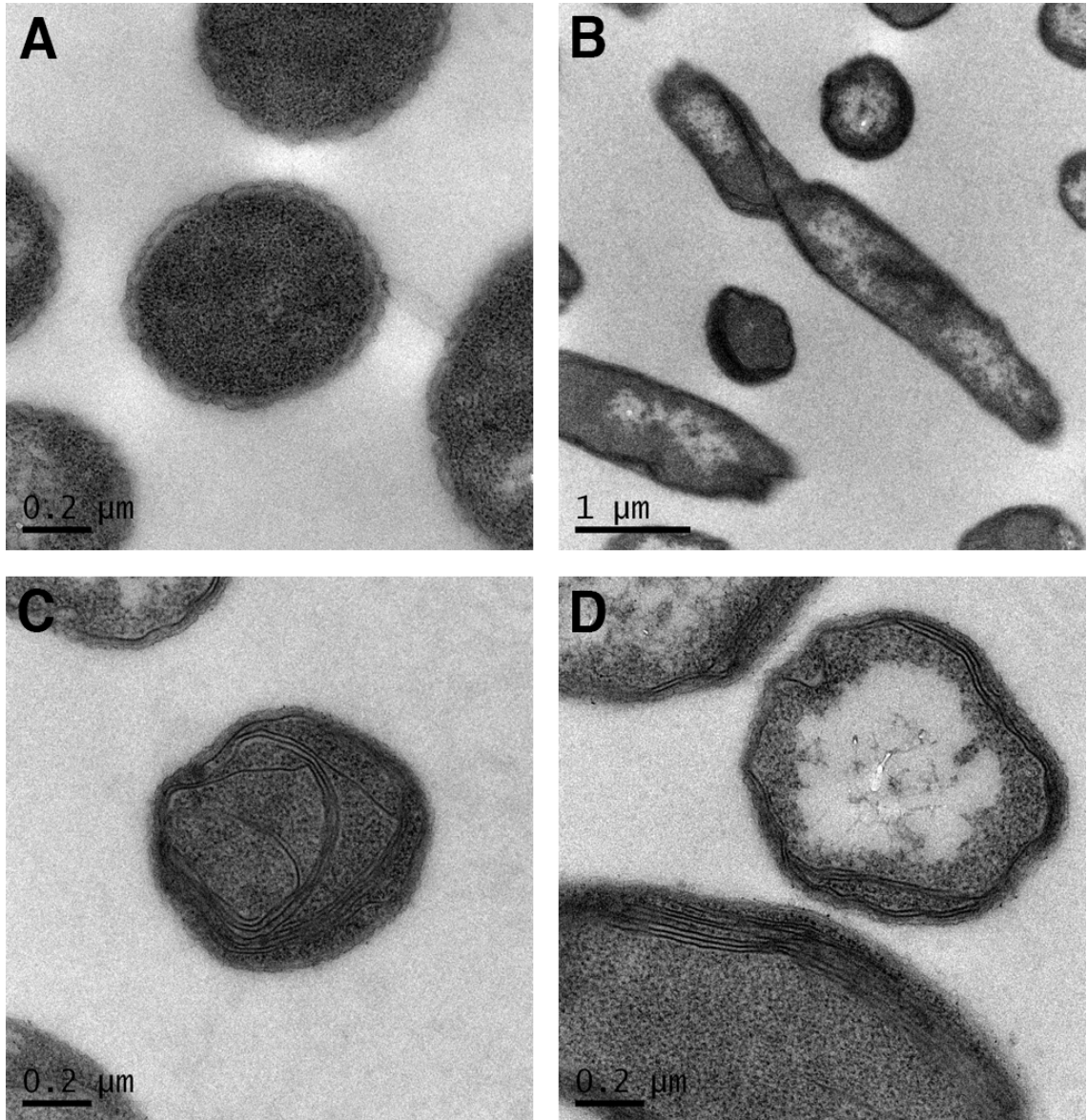


**Figure 4.6 Thin sections of *E. coli* cells expressing ExsY.** (A) Induced vector only *E. coli* cell. (B) Longitudinal and lateral cross sections of *E. coli* cell expressing recombinant ExsY after 3.5 hours. (C & D) Sheet like material forming within the cytoplasm in multiple layers.

overexpressing *E. coli* cell (Fig. 4.6 C). Each layer possessed an average thickness of ~5 nm (Fig. 4.6 D).

#### **4.2.3.4 Lysis of cells expressing ExsY macro assemblies**

Both enzymatic and physical methods of cell lysis were used in the extraction of ExsY assemblies.

Enzymatic lysis of ExsY-expressing cells was carried out using lysozyme in phosphate buffer. Lysed cells yielded large tubes of crystalline ExsY sheets  $>1\ \mu\text{m}$  on a side (Fig. 4.7 A). The ExsY sheets extracted from the cell appeared to be overlapping, resulting in a computed Fourier transform displaying diffraction from multiple lattices (Fig. 4.7 B).

Physical extraction using the sonication method described in 2.5.1.2 resulted in lysed cells containing ExsY crystals, and a mixture of cell debris and smaller ExsY fragments (Fig 4.7 C). Large ExsY macro-assemblies were seen to be overlapping other arrays, resulting in the diffraction from multiple lattices (Fig. 4.7 D).

Both extraction methods resulted in the release of large crystalline ExsY assemblies from the cell and did not appear to affect the integrity of the ordered array.

#### **4.2.3.5 Isolation of ExsY crystals**

A clean sample of pure ExsY crystals was required for electron microscopy and protein analysis. Batch purification of ExsY-expressing cells suspended in urea buffer yielded pure crystals with little to no contaminants. TEM analysis of negatively stained ExsY obtained from batch purification in urea buffer showed aggregates of large crystals greater than a few microns in size (Fig. 4.8 A). These were not suitable for image processing due to the many lattices arising from the overlapping crystals. However, fragments  $\geq 0.5\ \mu\text{m}$  on a side were readily found, which were not overlapping with other crystals (Fig. 4.8 B). These ExsY assemblies appeared stable in 8 M urea with no loss in crystallinity. Aggregates were also seen to adhere to the surface after staining (Fig. 4.8 B & C). Closer inspection of medium sized ( $\sim 0.5\ \mu\text{m}$ ) crystals showed that they were composed of hexameric ring structures and more importantly, were more ordered than their larger counterparts (Fig. 4.8 C). The computed Fourier transforms from medium sized crystals yielded discrete diffraction spots originating from a single layer of crystal (Fig. 4.8 D).

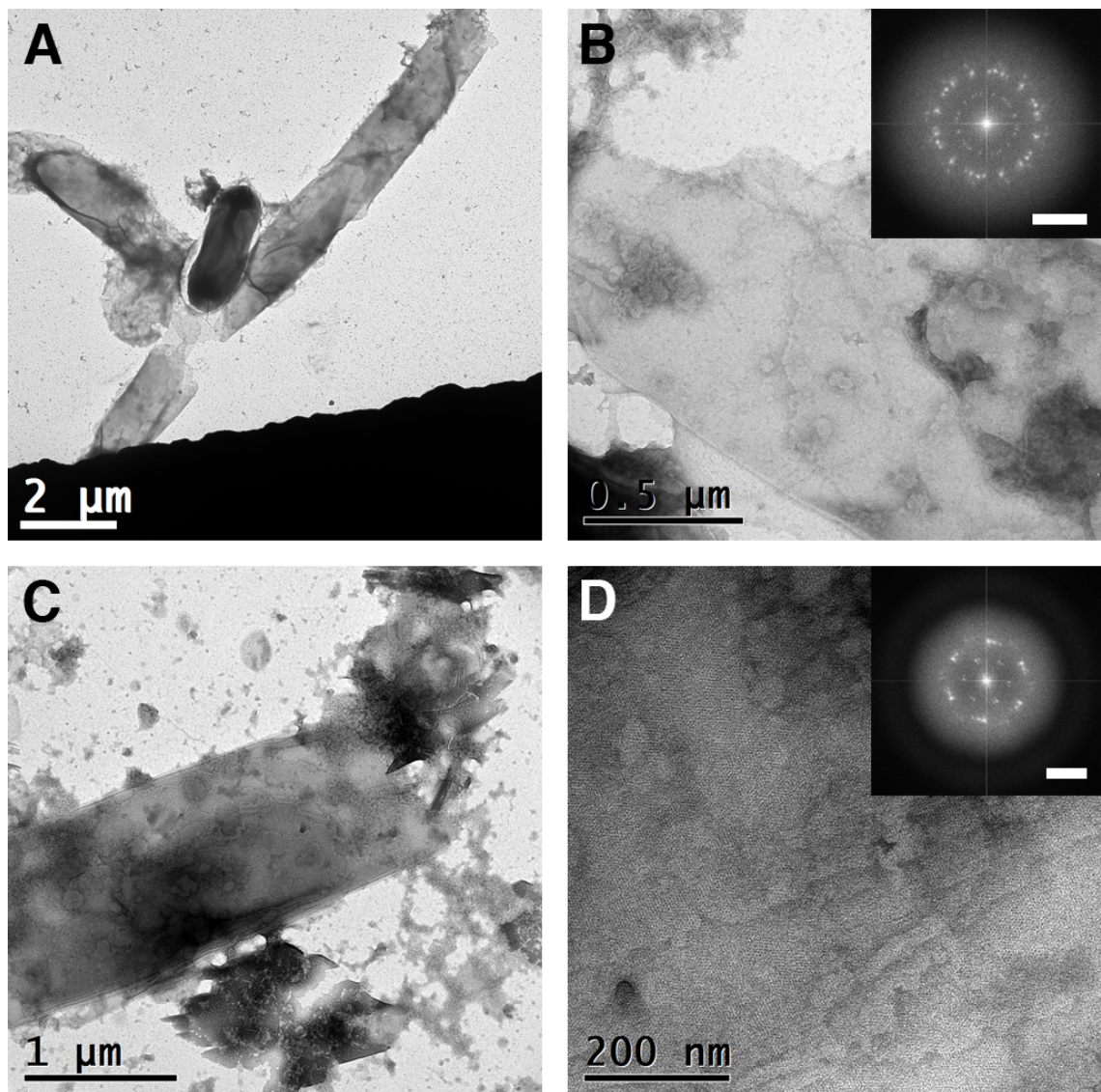


**Figure 4.7 Electron micrographs of lysed *E. coli* cells expressing ExsY** (A) Enzymatic lysis resulted in the release of large tubular sheets from expressing cells. (B) Large sheets of ExsY were crystalline and overlapping resulting in diffraction from multiple lattices seen from a computed Fourier transform (inset). (C) Physical extraction of ExsY sheets via sonication resulted in crystals trapped within partially lysed *E. coli* cells and the expulsion of smaller fragments. (D) ExsY crystals obtained from sonication remained crystalline and larger fragments were still stacked as seen through the diffraction from multiple lattices on the computed Fourier transform (inset). Scale bars in the inset of “(B)” and “(D)” represent  $0.28 \text{ nm}^{-1}$ .

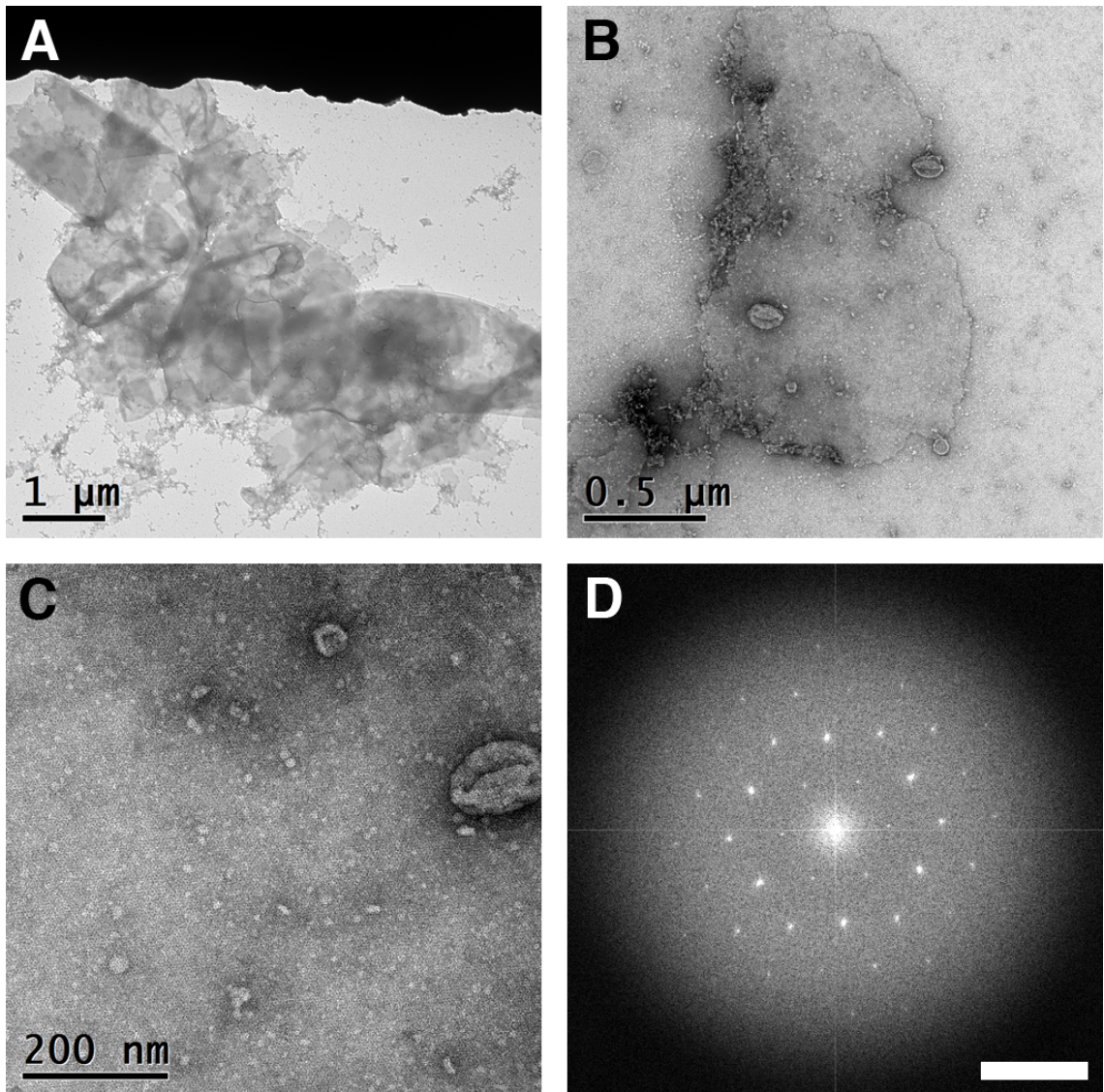


**Figure 4.8 Electron micrographs of nickel affinity batch purified ExsY crystals.** Batch purification of ExsY yielded (A) aggregations of large micron sized crystals unsuitable for data collection but also (B) smaller fragments  $\sim 1 \mu\text{m}$  in size. (C) Smaller fragments were well ordered with a clear hexamer structure visible in negative stain. (D) Computed Fourier transform with well ordered diffraction from medium sized crystals. Scale bar in “(D)” represents  $0.28 \text{ nm}^{-1}$ .

#### 4.2.3.6 Crystal formation from other constructs

N-terminal, C-terminal his-tagged and untagged ExsY constructs were analysed for crystal formation. Lysed *E. coli* cells expressing ExsY with an N-terminal his-tag (Fig. 4.9 A) or C-terminal his-tag (Fig. 4.9 C) both showed formation of crystalline assemblies (Fig. 4.9 B and D respectively). Lysed *E. coli* cells expressing recombinant untagged ExsY displayed large cellular sized ( $>1 \mu\text{m}$ ) assemblies in urea buffer (Fig. 4.9 E) that maintained their crystallinity. Crystals can be seen composed of a hexameric structure identical to his-tagged ExsY variants with similar diffraction spots from computed Fourier transforms (Fig. 4.9 F). The sizes of ExsY macro assemblies were not affected by the his-tag present on the protein.

#### 4.2.4 Structural analysis of ExsY crystals

##### 4.2.4.1 Two-dimensional analysis of ExsY

ExsY crystals were analysed by TEM and in further detail by two-dimensional electron crystallography. Images of purified ExsY crystal fragments were very contrasty and appeared to consist of hexameric particles with a central deep staining pit (Fig. 4.10 A). Computed Fourier transforms displayed a distinct hexagonal diffraction pattern with visible spots to the third order (Fig, 4.10 B). Five high-quality micrographs of untilted ExsY crystals were merged and analysed by two-dimensional electron crystallography. Crystals of ExsY displayed a unit cell parameter of  $a = b = 85 \pm 1 \text{ \AA}$ ,  $\gamma = 120 \pm 1^\circ$ . The symmetry of the molecule was determined by *2dx\_allspace* showing that ExsY crystals exhibited *p6* plane group symmetry (Table 4.1), which was applied to the merged two-dimensional projection map. A grey level (Fig. 4.10 C) projection maps revealed a hexameric ring structure with a central stain-filling cavity. Each hexameric ring was further surrounded by another six stain-accumulating cavities lying on the three-fold symmetry axis. Weak stain-excluding regions can be seen connecting each hexameric unit.

##### 4.2.4.2 ExsY reconstruction in three-dimensions

Five tilt series from  $-50^\circ$  to  $50^\circ$  in  $10^\circ$  increments were collected from independent ExsY crystals to construct a three-dimensional reconstruction from two-dimension projections. A total of fifty-one images were collected and merged to generate a three-dimensional model (Fig. 4.11). The reconstructed density showed a singled layered hexameric ring structure  $\sim 46 \text{ \AA}$  in thickness and  $\sim 68 \text{ \AA}$  in diameter. An untapered cavity with a diameter of  $\sim 27 \text{ \AA}$  runs through the centre of the hexamer. No connective density is seen between each hexameric ring unless the threshold of the model is

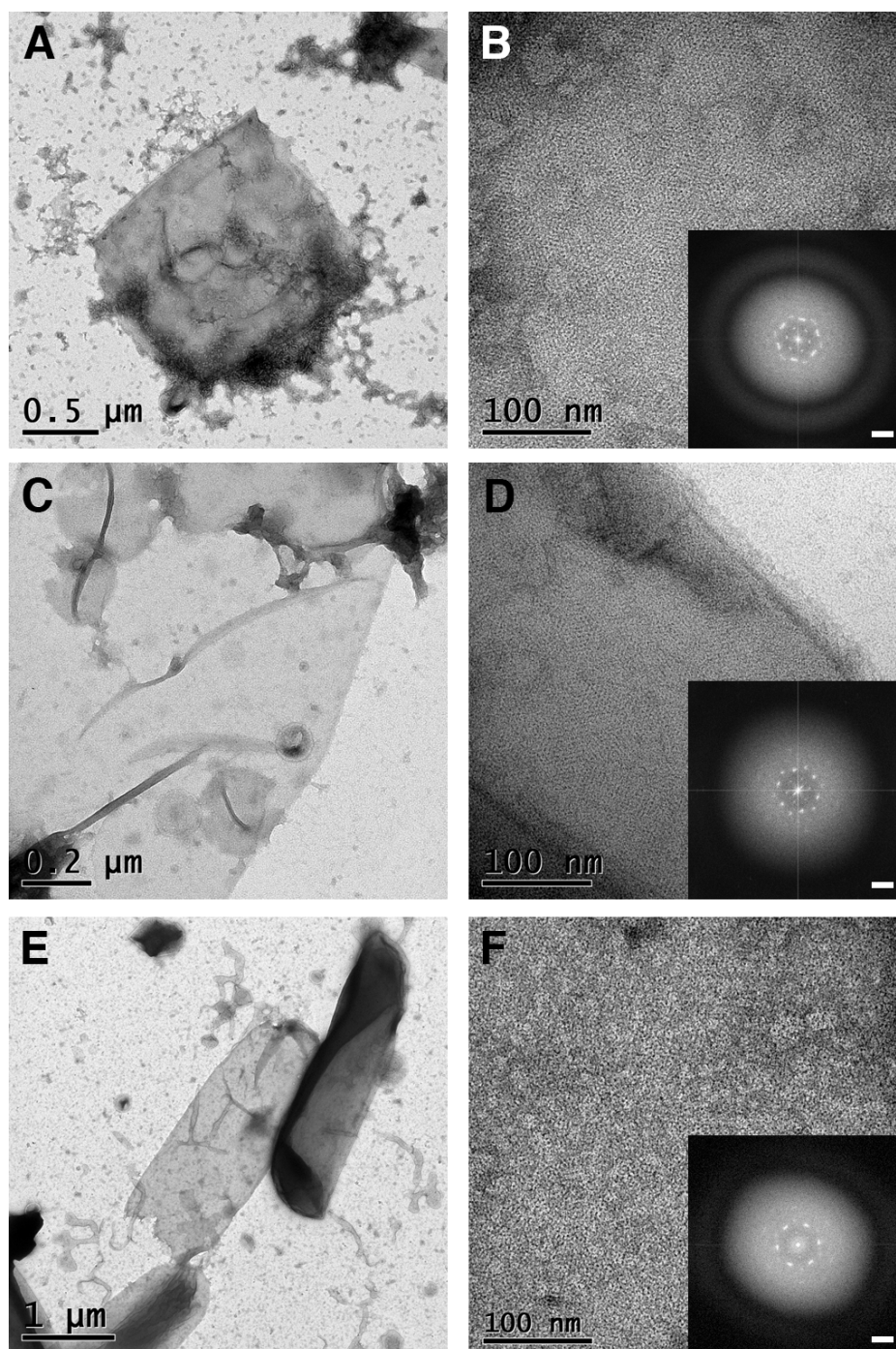


**Figure 4.9 Formation of crystals by ExsY his-tagged and untagged constructs.**

Crystalline assemblies found in cell lysates of *E. coli* expressing ExsY with (A) a N-terminal his-tag, (C) a C-terminal his-tag and (E) no tag. (B), (D) and (F) show magnified images of crystalline areas with computed Fourier transforms of “(A)”, “(C)” and “(E)” respectively. Scale bar in computed Fourier transforms “(B)”, “(D)” and “(F)” represents  $0.28 \text{ nm}^{-1}$ .

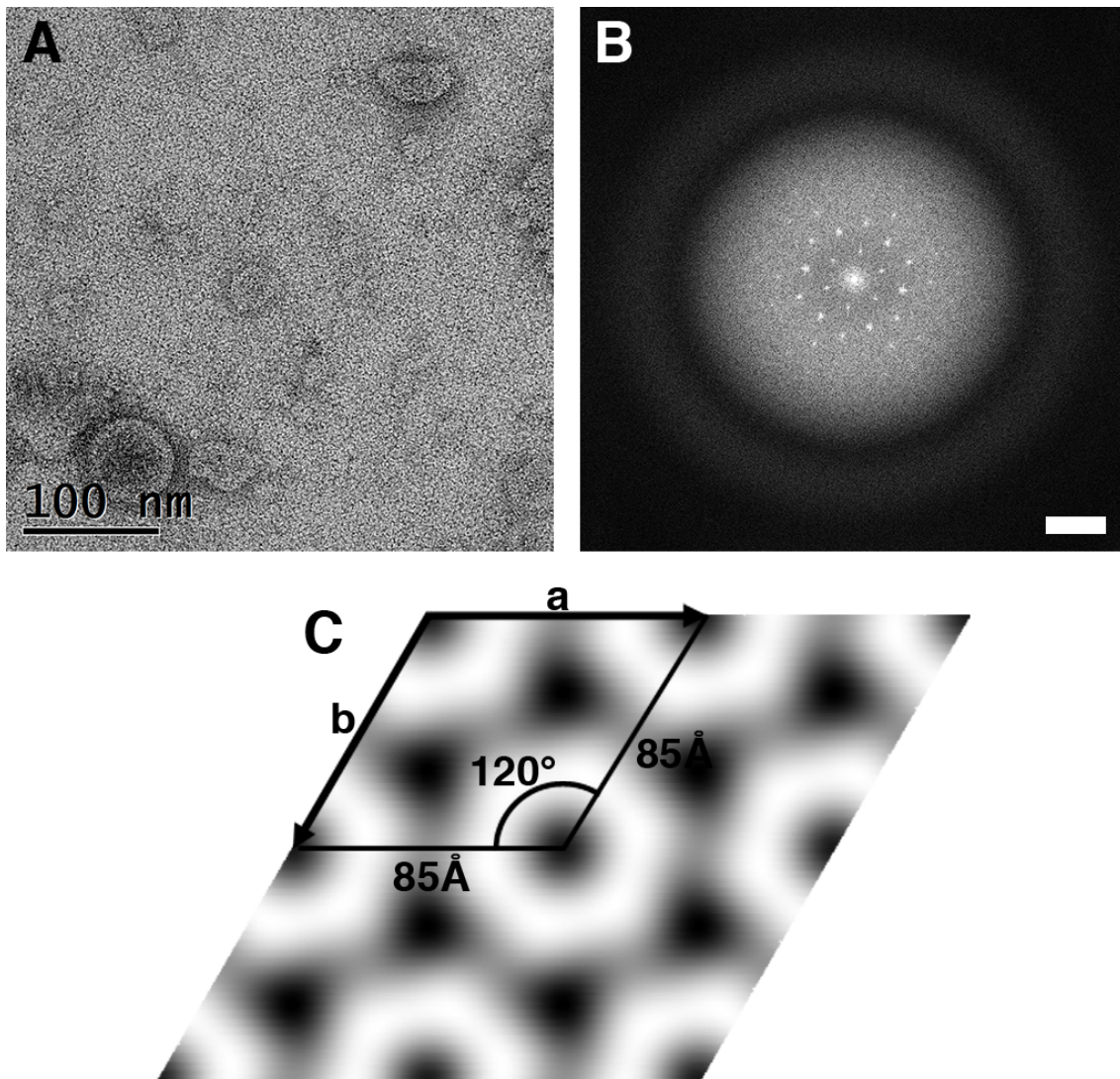
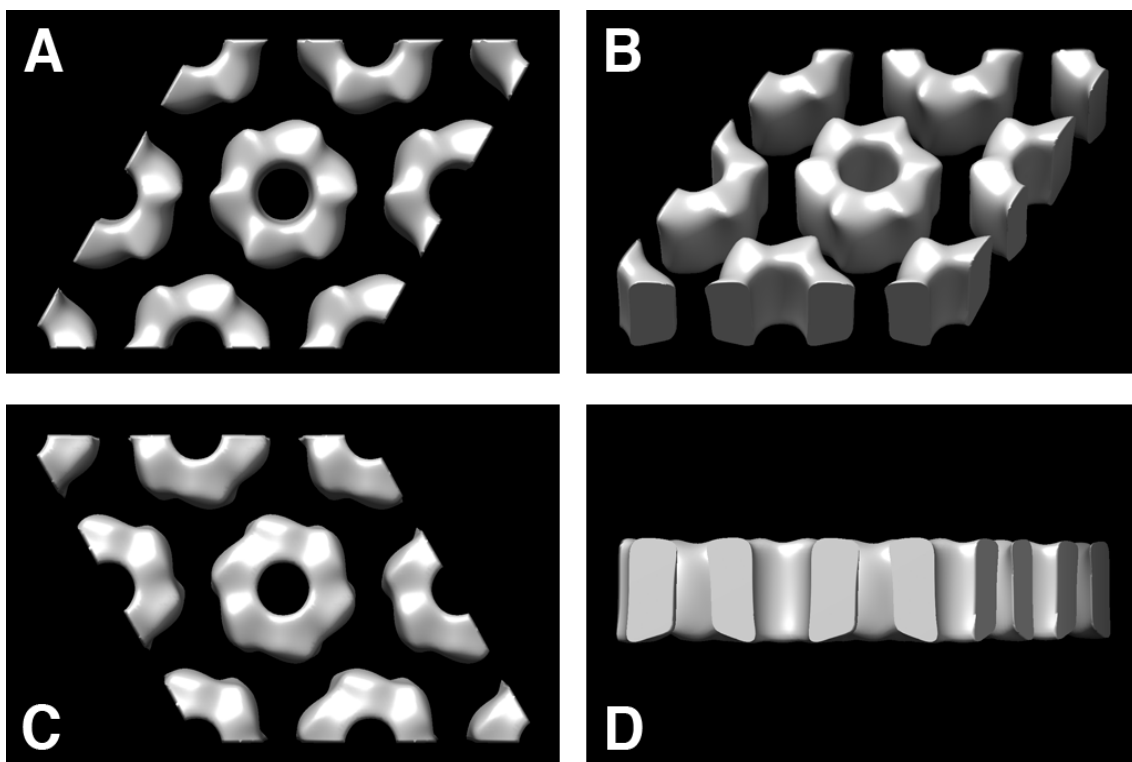


**Figure 4.10 Electron micrographs of isolated ExsY crystalline assemblies and two-dimensional electron crystallographic reconstruction in projection.** (A) Representative micrograph of ExsY crystals used for electron crystallographic studies and (B) respective Fourier transform displaying unique diffraction from the crystalline lattice. (C) Merged projection map of ExsY crystals represented in grey level with  $p6$  symmetry imposed. Scale bar in (B) represents  $0.28 \text{ nm}^{-1}$ .

**Table 4.1. The internal phase residuals determined after the imposition of all possible two-sided plane groups calculated from one of the micrographs of ExsY crystals.**

<b>Two sided plane group</b>	<b>Phase residual versus with other spots (90° random)</b>	<b>Number of Comparisons</b>	<b>Target residual based on statistics taking Friedel weight into account</b>
<i>p1</i>	14.0	48	
<i>p2</i>	21.2	24	20.0
<i>p12_b</i>	60.9	13	15.4
<i>p12_a</i>	61.7	13	15.4
<i>p121_a</i>	78.5	13	15.4
<i>p121_b</i>	39.0	13	15.4
<i>c12_b</i>	60.9	13	15.4
<i>c12_a</i>	61.7	13	15.4
<i>p222</i>	43.4	50	16.9
<i>p2221b</i>	37.2	50	16.9
<i>p2221a</i>	63.4	50	16.9
<i>p22121</i>	52.7	50	16.9
<i>c222</i>	43.4	50	16.9
<i>p4</i>	50.4	56	16.6
<i>p422</i>	56.9	119	15.2
<i>p4212</i>	67.1	119	15.2
<i>p3</i>	8.2*	48	14.0
<i>p312</i>	36.2	102	14.4
<i>p321</i>	27.3	105	14.5
<i>p6</i>	14.4*	120	15.2
<i>p622</i>	38.9	231	14.6

Internal phase residuals were determined from spots of IQ1-1Q5 to 20Å resolution. The values marked with \* are good candidates for the symmetry as the experimental phase residual is close to that expected value based on the signal-to-noise ratio.



**85Å**

**Figure 4.11 ExsY self-assembled crystals modelled in three-dimensions.** Surface representations seen from (A) above, (B) 40° tilt, (C) below and (D) 90° perpendicular to the plane of view.

increase to the level where noise becomes abundant. The lack of density is clearly observed on the position where the three-fold symmetry axis lies within the model.

#### 4.2.4.2.1 Threshold determination for the ExsY model

The volume threshold for the ExsY model was determined using a mass to volume estimation. The ExsY array exhibited six-fold symmetry with a ring structure in each unit cell composed of a hexamer of the ExsY protein. The model generated was constructed within a 2 x 2 unit cell therefore displaying 24 units of ExsY. Using the constant that proteins on average occupy a density of 1.35 g cm<sup>-3</sup> and each Dalton equated to 1.66 x 10<sup>-27</sup> Kg, a calculated estimate was made on the volume of the ExsY model:

$$Volume = \frac{Mass}{Density} = \frac{ExsY (Da) \times Atomic\ mass\ unit}{Average\ protein\ density}$$

$$\frac{19419.8\ Da \times 24\ units \times 1.66 \times 10^{-24}\ g}{1.35\ g\ cm^{-3}} = 5.73 \times 10^{-19}\ cm^3 = 573 \times 10^3\ \text{\AA}^3$$

At the maximum theoretical threshold of 573 x 10<sup>3</sup> Å<sup>3</sup>, thin linker domains were visible; however this was beyond the resolution limit to be accurately interpreted and may arise from staining artefacts or noise. Therefore, a conserved volume around ~430 x 10<sup>3</sup> Å<sup>3</sup> was used that set the threshold of the model to just below the point that noise arises.

#### **4.2.5 Secondary structure estimation using circular dichroism spectroscopy**

CD spectroscopy analysis of nickel affinity purified soluble ExsY was carried out to estimate the contributions of secondary structures. Soluble ExsY was purified by nickel column affinity chromatography and eluted in 1 M urea buffer. Purified ExsY was then buffer exchanged into 0.01 M potassium phosphate buffer. The buffer exchange was carried out to remove the Urea and imidazole from the sample, preventing any signal interference. The protein concentration was calculated using UV absorbance at 280 nm and an extinction coefficient of 2.24 determined by ProtParam (Gasteiger E., 2005). ExsY at a final concentration of 7.275 mg ml<sup>-1</sup> was used to record the spectrum. The data obtained from the ExsY sample was converted to ellipticity using the following equation:

$$\Delta\varepsilon = \theta \times \frac{0.1 \times [\text{mean residue weight (Da)}]}{[\text{path length (cm)}] \times [\text{concentration (mg ml}^{-1}\text{)}] \times 3298}$$

$$\Delta\varepsilon = \theta \times \frac{0.1 \times 107.9}{0.02 \times 7.275 \times 3298}$$

Values for  $\theta$  were collected at 1 nm intervals between the given wavelengths and averaged over eight iterations. The resulting spectrum (Fig. 4.12) is similar to that of proteins exhibiting alpha helical content. A positive peak was seen just above 190 nm and two negative peaks were visible at 208 nm and 222 nm. The spectrum was analysed on Dichroweb using the program SELCON3 and the SP175 reference dataset (Lees *et al.*, 2006, Lees *et al.*, 2004). The estimated  $\alpha$ -helical content was ~60.5 % with little to no  $\beta$ -strands detected. The rest of the protein is estimated to be composed of ~25 % random coils and ~10 % turns. A normalized root-mean-square deviation of 0.044 suggests a strong correspondence between the calculated secondary structure and the data (Miles *et al.*, 2005).

## 4.2.6 Disassembly of ExsY

SDS-PAGE analysis of purified ExsY crystals suspended in buffer containing 8 M urea, 50 mM DTT and heated to 95 °C, showed the formation of a single band indicative of an ExsY monomer (Fig. 4.3, lane 4). However, it was also noted that without any treatment no visible bands could be seen on SDS-PAGE analysis of crystals. The individual effects of urea, SDS, DTT and heat were assayed on the disassembly of ExsY crystals. Samples were analysed by SDS-PAGE, Western blotting and TEM.

### 4.2.6.1 Analysis of ExsY disassembly by SDS-PAGE and Western blot

Insoluble and soluble ExsY assemblies obtained from batch purification were analysed by NuPAGE 4-12 % Bis/Tris gels (Invitrogen™). Purified ExsY crystals (13  $\mu$ l at ~1 mg ml<sup>-1</sup>) were incubated in combinations of SDS, DTT and heating, all in the presence of urea. The soluble fraction was also analysed by SDS-PAGE without treatment. Two parallel gradient gels were run in the same tank under the same conditions with the second used for Western blot analysis. Mouse Monoclonal Anti-polyHistidine antibodies (Sigma) were used to detect the hexa-histidine tagged ExsY by Western blotting.

SDS-PAGE analysis of soluble ExsY from batch purified samples containing 8 M urea revealed the presence of very strong bands at ~20 kDa and ~45 kDa with a faint band

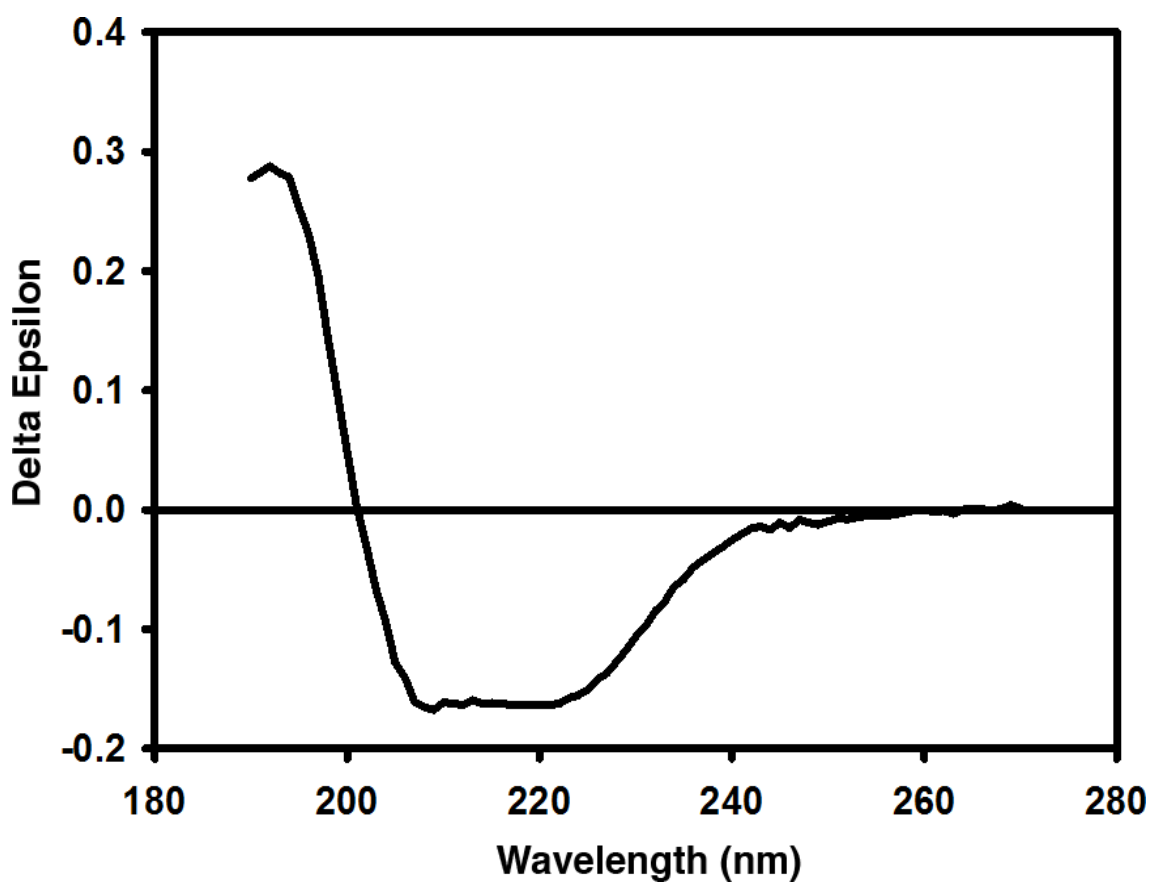


**Figure 4.12 CD spectroscopy of soluble ExsY assemblies.** Spectra collected from purified soluble ExsY. A positive peak can be seen at 193 nm and negative peaks at 208 nm and 222 nm are indicative of alpha helices.

at ~30 kDa (Fig. 4.13 A, lane 1). Western blot analysis of the same fraction showed four discernable bands at ~20, 35, 45 and 60 kDa with large oligomers found at 80 kDa and above (Fig. 4.13 B, lane 1). Purified crystals of ExsY, suspended in 8 M urea and loaded onto the SDS-PAGE gel showed an almost undetectable band at ~20 kDa with no signs of higher molecular weight oligomers in the gel (Fig. 4.13 A, lane 2). Western blot analysis however detected the presence of a monomer at ~20 kDa and also a high molecular weight complex at ~120 kDa (Fig. 4.13 B, lane 2). Separation of ExsY crystals that were incubated in 2 M DTT or heated to 95 °C showed a faint band at ~20 kDa on SDS-PAGE (Fig. 4.13 A, lanes 3 and 4). Western blot analysis of reducing or heated conditions also showed presence of a monomer at ~20 kDa and of a high molecular weight complex at ~120 kDa (Fig. 4.13 B, lanes 3 and 4). Upon addition of 2 M DTT and 95 °C heat in combination a much stronger band could be seen on SDS-PAGE of a monomer at ~20 kDa (Fig. 4.13 A, lane 5). Western blot analysis also showed a band at the position of an ExsY monomer at ~20 kDa and the loss of the high molecular weight complex (Fig. 4.13 B, lane 5). The same conditions were trialed with 2 % SDS present showing almost identical profiles. Crystals treated in 2 % SDS alone showed a faint hint of a monomer at ~20 kDa (Fig. 4.13 A, lane 6). Western blot analysis confirmed a monomer at ~20 kDa along with a possible dimer at ~35 kDa and high molecular complexes at 80 kDa and above. A combination of 2 % SDS and 2 M DTT resulted in a band at ~20 kDa visible on SDS-PAGE (Fig. 4.13 A, lane 7) that was also detected on the Western blot (Fig. 4.13 B, lane 7). Furthermore, high molecular weight complexes were also detected at ~80 kDa and above. Heating of the ExsY crystals at 95 °C in the presence of 2 % SDS resulted in a band visible at ~20 kDa on SDS-PAGE (Fig. 4.13 A, lane 8) and detected at the same point on the Western blot along with a high molecular weight complex (Fig. 4.13 B, lane 8). A combination of 2 % SDS, 2 M DTT and 95 °C resulted in a distinct band at 20 kDa on SDS-PAGE (Fig. 4.13 A, lane 9) and the corresponding band on the Western blot with no high molecular weight complex seen (Fig. 4.13 B, lane 9). The combined condition of 2 % SDS, 2 M DTT and 95 °C heating provided the optimal conditions for disassembly. Some variability was seen in the migration of ExsY monomers depending on their incubation conditions.

#### **4.2.6.2 TEM analysis of reduced, heat and SDS treated ExsY crystals**

Crystalline ExsY assemblies resuspended in 8 M urea buffer were analysed by TEM under varying conditions for signs of disassembly. Purified ExsY crystals were incubated with combinations of 2 % SDS, 2 M DTT and 95 °C heat for 20 min. Samples

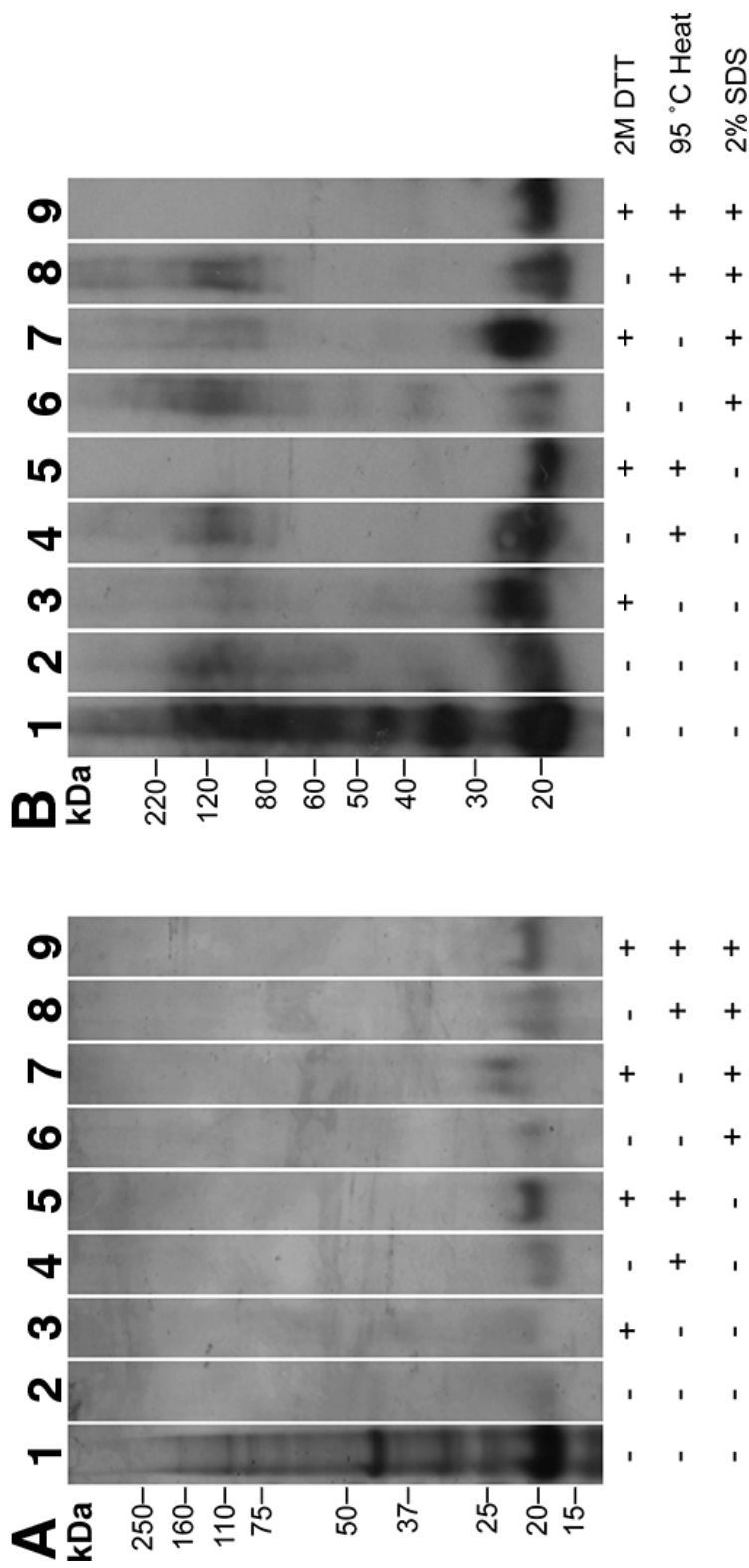


**Figure 4.13 SDS-PAGE and corresponding anti-His Western blot of soluble and insoluble ExsY complexes treated with DTT, heat and SDS. (A) SDS-PAGE and (B) Western blot of soluble ExsY from batch purification (lane 1). Batch purified ExsY crystals untreated and treated with a combination of 2 M DTT, 95 °C heat and 2% SDS. (lanes 2 – 9)**

were visualised by TEM and computed Fourier transforms of assemblies were analysed for visible diffraction.

Treatment of ExsY assemblies with 2 M DTT alone for 20 min had no effect on the crystallinity of the macromolecular assemblies. Crystals of various sizes could be found within the sample (Fig. 4.14 A) and upon closer inspection, a clear hexameric assembly was seen producing a clear diffraction pattern on the computed Fourier transform (Fig. 4.14 B). ExsY crystal samples treated with 95 °C heat for 20 min appeared dirty in appearance with aggregates covering the sample (Fig. 4.14 C). Larger crystalline assemblies were still present showing a hexagonal lattice on the surface. Diffraction spots were visible on the computed Fourier transform indicating no loss in crystallinity (Fig. 4.14 D). Incubation in 2 % SDS had little effect on ExsY crystals with large assemblies clearly visible (Fig. 4.14 E and F).

Combination treatments of 2 % SDS with either 2 M DTT (Fig. 4.15 A) or 95 °C heat (Fig. 4.15 B) still produced samples with crystals remaining and clear diffraction from the ordered lattice. However, ghosts of crystals and small aggregates could also be seen. A combination of 2 M DTT and 95 °C heating (Fig. 4.15 C) or supplemented with 2 % SDS (Fig. 4.15 D) both resulted in the loss of crystallinity from any large fragments seen within the sample. No diffraction could be seen on computed Fourier transforms in either condition (Fig. 4.15 C and D inset). These results correlate well with the results obtained from SDS-PAGE and Western blot analyses in 4.2.6.2.

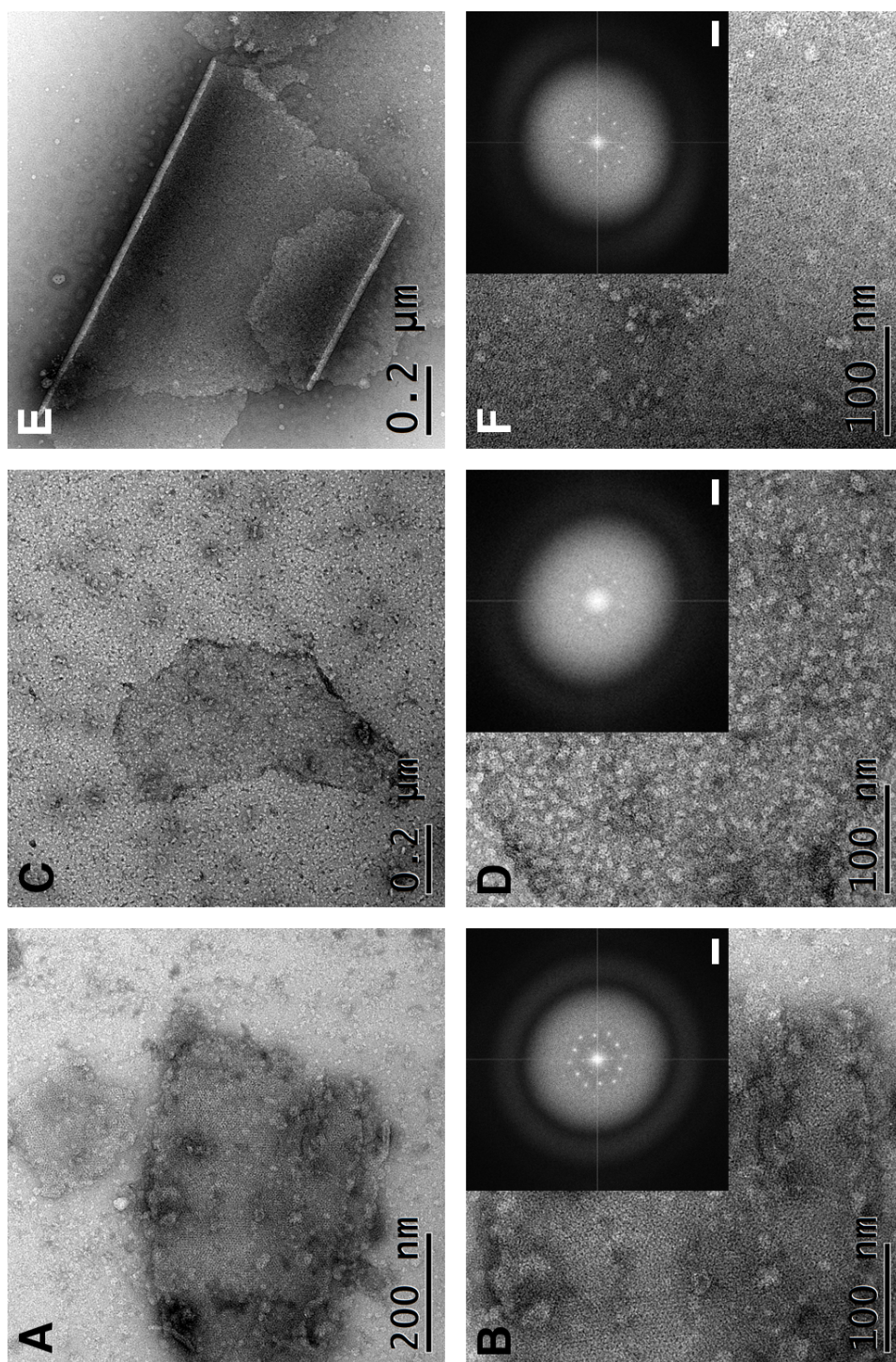


**Figure 4.14 Electron micrographs of purified ExsY crystals after incubation with reducing agent, heat and SDS.** Purified ExsY crystals incubated in (A and B) 2 M DTT, (C and D) 95 °C heat and (E and F) 2 % SDS for 20 minutes. Computed Fourier transform from magnified areas showed diffraction spots were maintained under each condition. Scale bars represent 0.28 nm<sup>-1</sup>.

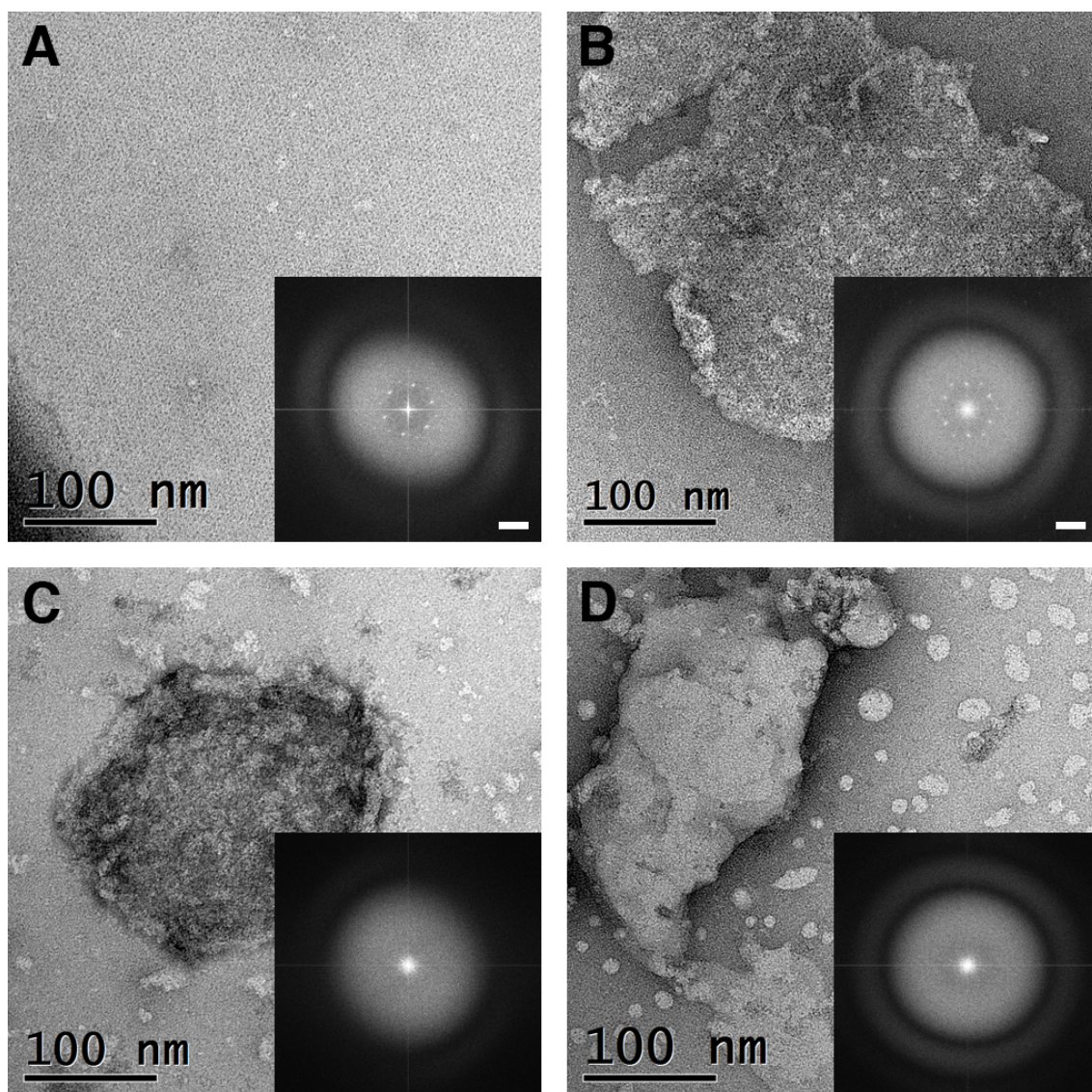


**Figure 4.15 Electron micrographs of purified ExsY crystal after treatment with combinations of 2 M DTT, 95 °C heat and 2 % SDS.** ExsY crystals remain intact in (A) 2% SDS & 2 M DTT and (B) 2% SDS & 95 °C heat with diffraction patterns seen (inset A and B). Crystallinity is lost in samples treated with (C) 2 M DTT & 95 °C heat or (D) 2% SDS, 2 M DTT & 95 °C heat with diffraction lost from all samples (inset C & D). Scale bars in inset of A and B represent  $0.28\text{nm}^{-1}$ .

## 4.3 Discussion

### 4.3.1 Purification and analysis of ExsY

It has been shown in this chapter that overexpression of ExsY within *E. coli* resulted in the formation of large crystalline arrays through a process of self-assembly within the cell cytoplasm. The ExsY arrays were insoluble in Tris buffer but showed some limited solubility in 8 M urea. This explained the appearance of a ~20 kDa band for monomeric ExsY on SDS-PAGE only in urea buffered column nickel affinity purification preparations (Fig. 4.2). Furthermore, ExsY purified from the soluble fraction tended to be of monomer size with a few small fragments composed of a small number of hexameric units (Fig. 4.5). The small fragments were not large enough to generate strong distinct diffraction patterns on computed Fourier transforms and were therefore not suitable for two-dimensional electron crystallographic studies.

The soluble fraction containing small oligomeric fragments was however suitable for CD spectroscopy. The conditions for data collection were kept as consistent as possible with those of Kalias *et al.*, (2011), deviating on the use of a 0.02 cm pathlength cuvette. The same CD spectroscopy analysis software for determination of  $\alpha$ -helical content was used along with the same reference data set. The protein concentration was determined as accurately as possible using UV absorbance, however as seen from Figure 4.1, ExsY possess no tryptophan residues, one tyrosine and eight low absorbing phenylalanine's. This produced a coefficient of extinction with an error of ~10 %. A high protein concentration (7.725 mg ml<sup>-1</sup> calculated) was used to compensate for the lack of signal and was necessary to obtain an accurate spectrum.

The large, micron sized, crystals of ExsY were highly insoluble, with diffracting fragments ~500 nm in size seen very rarely within the soluble fraction. The majority of ExsY crystals, we believe, are physically trapped within the NiNTA agarose column during purification, leading to a loss in yield of crystals seen by TEM. Therefore, a batch purification method was developed to isolate crystals directly from the cell lysate without initial separation of the soluble and insoluble fraction. This increased the yield of crystals dramatically as seen by TEM. The purity of the batch method was also confirmed by SDS-PAGE with a single band for ExsY visible in reduced and heated conditions (Fig. 4.3) showing this is a viable method for separation of large macro-assemblies.

To discount the possibility that ExsY crystals were forming due to links between his-tags, an untagged ExsY construct was tested. “Native” ExsY was shown to form large crystalline assemblies (Fig. 4.9 E and F) with the same unit cell parameters and projection maps (data not shown) as that of his-tagged constructs, therefore suggesting that the his-tag had no influence on assembly or structure.

### **4.3.2 ExsY as the template protein of the exosporium**

#### **4.3.2.1 Self-assembled ExsY architecture is similar to that of *B. cereus* group exosporium**

ExsFA, BclA and ExsY are the three known proteins to be associated in a high molecular complex in native exosporium (Boydston *et al.*, 2005, Sylvestre *et al.*, 2002, Thompson and Stewart, 2008). Exosporium formation occurs in the Kurstaki 4D11 wild strain of *B. thuringiensis* that lacks BclA and expresses low levels of ExsFA indicating that these two proteins may not contribute directly to the template assembly of the exosporium. Furthermore, spores of a *B. cereus*  $\Delta$ exsY mutant lack a complete exosporium indicating the necessity for its correct expression in construction of a complete exosporium (Boydston *et al.*, 2006, Johnson *et al.*, 2006, Redmond *et al.*, 2004). Therefore, recombinant ExsY was overexpressed as it was predicted to be the *B. cereus* group exosporium template protein. Amazingly, ExsY possessed the ability to self-assemble into a single layered crystalline sheet (Fig. 4.6), with similar architecture to that of the native *B. cereus* exosporium. The unit cell dimensions calculated from purified ExsY crystals ( $a = b = 85 \pm 1 \text{ \AA}$ ,  $\gamma = 120 \pm 1^\circ$ ) was similar to that of *B. cereus* ATCC 10876 exosporium ( $a = b = \sim 80 \text{ \AA}$ ,  $\gamma = \sim 120.0^\circ$ ) (Ball *et al.*, 2008, Kailas *et al.*, 2011) and *B. thuringiensis* 4D11 exosporium ( $a = b = 80 \pm 1 \text{ \AA}$ ,  $\gamma = 120 \pm 1^\circ$ ) within the resolution limit and shares the same  $p6$  plane group symmetry. The unit cell similarity between native *B. cereus* exosporium and self-assembled ExsY crystals points towards ExsY as the major contributor to exosporium template architecture.

Before comparisons were made between ExsY and exosporium in three dimensions, the threshold volume for ExsY was calculated using its mass to volume estimate. No estimated volumes could be assigned towards exosporium models previously as they were composed of multiple proteins to which the contribution of each was unknown. ExsY arrays however, were composed of a single protein. The calculated volume from the double his-tagged construct of ExsY was  $573 \times 10^3 \text{ \AA}^3$ , but a more conservative  $430 \times 10^3 \text{ \AA}^3$  was used in the final model to lower the potential contribution of artefacts.

The final volume used acted as an estimate as stain interactions and disordered structures could not be accounted for within the calculation. With the knowledge that ExsY may well be the exosporium template protein, all exosporium models were scaled to fit within the ExsY model.

The three-dimensional reconstruction of the ExsY assembly showed a hexameric ring structure  $\sim 68$  Å in diameter and  $\sim 45$  Å in depth with a central  $\sim 27$  Å cavity (Fig. 4. 16 A). This showed a remarkable resemblance to the exosporium of *B. thuringiensis* 4D11, a strain within the *B. cereus* group lacking the BclA “hairy nap” and ExsFA “anchor” proteins. *B. thuringiensis* 4D11 exosporium, discussed in Chapter 3.2.3.4, displayed an almost identical hexameric cup structure with a diameter of  $\sim 64$  Å and thickness at  $\sim 45$  Å (Fig. 4.16 B). An overlay between the volumes (Fig. 4.16 C) clearly shows a high degree of correlation in structure between the ExsY assembly and *B. thuringiensis* 4D11 exosporium, except that a major difference can be seen in the central cavity. The exosporium from *B. thuringiensis* 4D11 showed a closed cup structure that is clearly tapered, whilst ExsY self-assembled crystals showed a penetrating cavity that is not tapered. This extra density could arise from one or more of the more-than a dozen other proteins found on the exosporium (reviewed in Table 1.1) (Redmond *et al.*, 2004, Todd *et al.*, 2003)- excluding the contributions of BclA (Boydston *et al.*, 2005, Sylvestre *et al.*, 2002) and ExsFA (Steichen *et al.*, 2005, Sylvestre *et al.*, 2005) which have been characterised. In addition, conformational changes may occur within the exosporium structure when these additional proteins are present, hence partially contributing to the tapered structure and closed cup seen in both *B. thuringiensis* 4D11 and also native *B. cereus* ATCC 10876 exosporium (Fig. 4.17 B).

A comparison in structure between ExsY and the *B. cereus* ATCC 10876 exosporium (Fig. 3.1), discussed in Chapter 1 and 3, showed a high degree of similarity with identical unit cell parameters, within error. A tapered closed cup structure is also present along with density contributing from ExsFA and BclA making up the linkers. The width and depth of the central cup,  $\sim 67$  Å and  $\sim 50$  Å respectively, in *B. cereus* exosporium is almost identical to the hexameric ring from the ExsY assembly (Fig. 4.17 A and B). The major difference still remains within the tapered cup structure, which has a much wider diameter on the external interface. The difference between the native exosporium and self-assembled structure may arise from subtle changes in stain interactions; positive staining would lead to a wider interface due to better stain penetration. An overlay between the two structures shows the contribution of ExsY

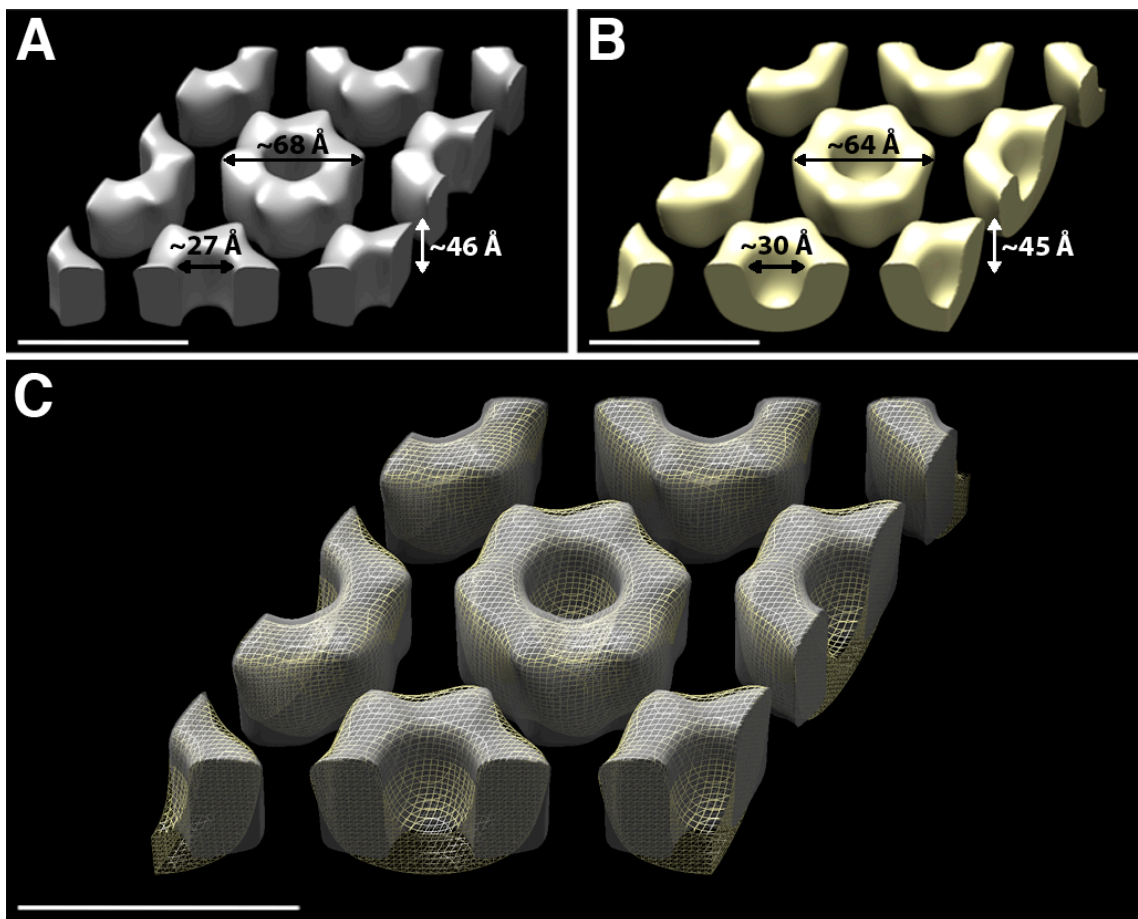


**Figure 4.16** Three-dimensional structural overlay of ExsY self-assembled crystals and *B. thuringiensis* 4D11 exosporium. (A) Heterologously self-assembled ExsY crystal, (B) *B. thuringiensis* 4D11 exosporium, (C) ExsY [solid/grey] with *B. thuringiensis* 4D11 exosporium overlaid [wireframe/yellow]. Scale bars represent  $\sim 80$  Å.

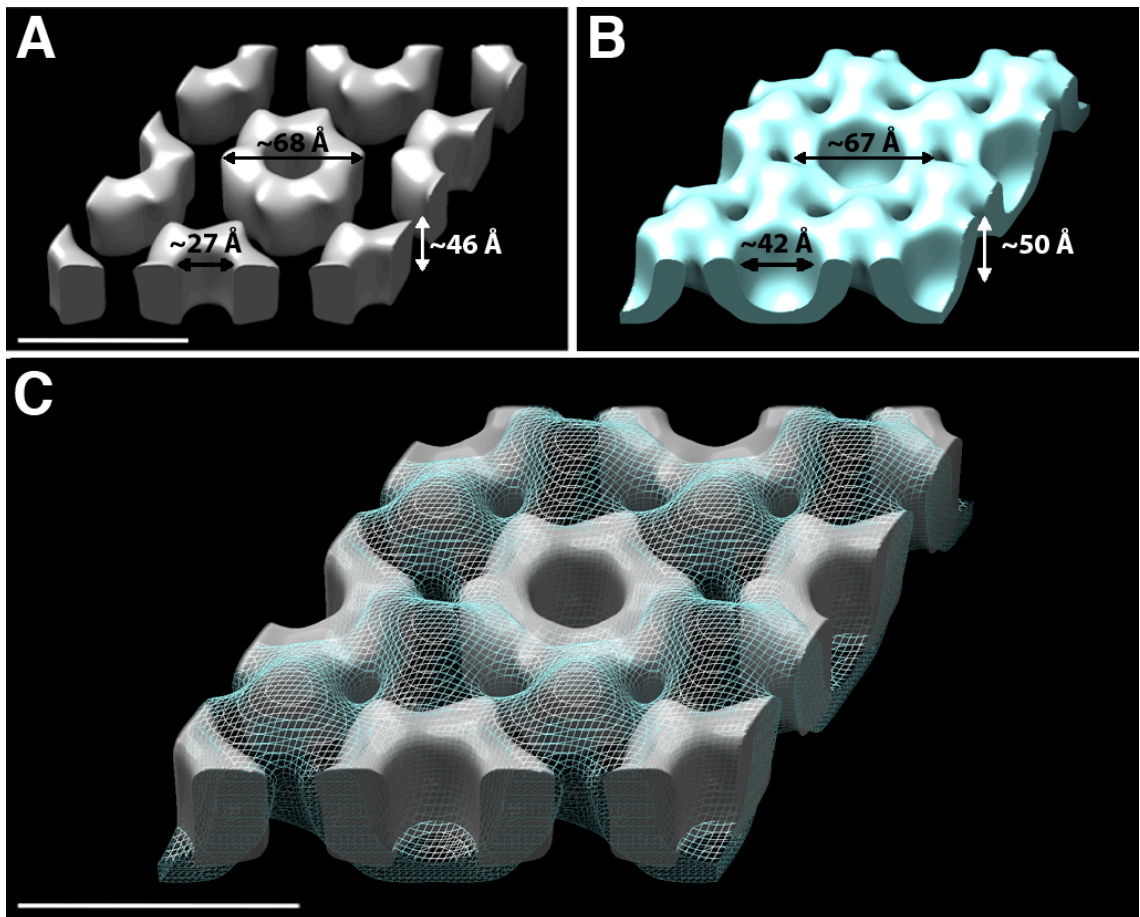


**Figure 4.17** Three-dimensional structural overlay of ExsY self-assembled crystals and *B. cereus* ATCC 10876 exosporium. (A) Heterologously self-assembled ExsY crystal, (B) *B. cereus* ATCC 10876 exosporium, (C) ExsY [solid/grey] with *B. cereus* exosporium overlaid [wireframe/blue]. Scale bars represent ~80 Å.

towards the central cup domain and further iterates the contributions of ExsFA and BclA, present at the three-fold symmetry axis, towards native exosporium architecture (Fig. 4.17 C).

Further secondary structure analysis was carried out using CD spectroscopy to estimate the  $\alpha$ -helical content present within ExsY. This was compared to the previous study in Kailas *et al.*, showing the exosporium from *B. cereus* containing an estimated 75 %  $\alpha$ -helical content. CD spectroscopy was initially carried out using large fragments obtained from batch purification, however it seemed that large ExsY fragments produced erroneous results most likely due to excess light scattering. Therefore the soluble fraction from nickel affinity purification containing a range of smaller fragments was tested. The spectra produced a positive peak at 193 nm and two negative peaks at 208 nm and 222 nm indicative of  $\alpha$ -helices (Holzwarth and Doty, 1965). This was analysed using the same program (SELCON3) and reference data set (SP175) as that for *B. cereus* exosporium giving an estimated  $\alpha$ -helical content of ~60.5 % for ExsY. The larger  $\alpha$ -helical content of ~75 % present in *B. cereus* exosporium in comparison can be attributed to the contributions of the multitude of other proteins found in the complex. The different  $\alpha$ -helical content may also be attributed to the uncertainties in the data collected from macromolecular structures and the curve fitting algorithms used for secondary structure estimation. Importantly however, the estimated  $\alpha$ -helical content between the *B. cereus* exosporium and ExsY are of comparable order. ExsY as the major exosporium template protein would be expected to reflect a high  $\alpha$ -helical content as the exosporium has been found to be predominantly helical in structure. It would however be difficult to assess the real contribution of ExsY on exosporium secondary structure without knowledge of the contributions of each protein found in purified exosporium assemblies.

Given the almost identical fit in density between crystals of ExsY with *B. thuringiensis* 4D11 and *B. cereus* exosporium, we speculate with reasonable confidence that ExsY is the predominant exosporium template protein. Western blot analysis of the exosporium by Dr. C. Terry initially showed that ExsY was a major component of the exosporium and was capable of forming multimeric assemblies (Terry *et al.*, 2010). The heterologous self-assembly of ExsY within *E. coli* shows without doubt that it alone has the capability of forming a template for the exosporium to build upon. It is however essential to note that although the unit cell parameters are identical within error between the ExsY assembly and the native exosporium found in the *B. cereus* group

strains; along with the similar structure at low resolution, we cannot conclude that the structure seen in *E. coli* is identical to the native exosporium without higher resolution information.

One further question remains with the orientation of the modelled ExsY assembly in relation to that of the exosporium. Kailas *et al* (2011) determined the orientation of the exosporium by AFM through examination of exosporium from wild type *B. cereus* and its napless counterpart *B. thuringiensis* 4D11 (Fig. 3 and 4 in Kailas *et al.*, 2011). Two surfaces could be seen on the *B. cereus* exosporium with one side disordered from the hairy nap and the other made of a honeycomb array. The same honeycomb array was seen on the *B. thuringiensis* 4D11 exosporium and a further hexagonally close-packed concave array of “cup” could be seen making up the other side (This was further confirmed with the three-dimensional model presented in Chapter 3). The ExsY model does not possess a structure where the honeycomb or cup surface could be discernible. Instead, a hexameric ring structure is seen which appears relatively similar on both surfaces. A slightly tapering of the ring is visible on one side that has been arbitrarily denoted as the underside in structural comparisons. It is possible that AFM may reveal two different surfaces if such irregular structures had been averaged out during the crystallographic processing.

### **4.3.3 Assembly of ExsY and exosporium template mediated by covalent disulphide bond formation**

ExsY is highly cysteine-rich (Fig. 4.1) (Johnson *et al.*, 2006) and has been shown to form oligomers (Fig. 4.13) that can assemble into large higher order arrays (Fig. 4.7). Although other covalent cross-links such as  $\epsilon$ -( $\gamma$ -glutamyl)-lysyl isopeptide bonds have been found to stabilise spore architecture (Driks, 1999, Kobayashi, 1996, Pandey and Aronson, 1979), disassembly of ExsY only in highly reducing and heated conditions (Fig. 4.15) suggests an essential role for disulphide bonds. Furthermore, cysteine residues found in ExsY were conserved with that of CotY, the exosporium cap protein from *B. cereus* (Boydston *et al.*, 2006, Steichen *et al.*, 2007, Thompson *et al.*, 2012). ExsY also shares ~35 % identity with *B. subtilis* CotY (discussed in Chapter 6), a cysteine rich coat protein that has also been shown to self-assemble inside *E. coli* during overexpression (Jiang *et al.*, 2015). Covalent cross-link formation within the *E. coli* cytoplasm, which is normally considered a reducing environment, may be mediated by the high degree of order and symmetry within the ExsY molecule. The ordered packing of ExsY could allow bonding partners to be held in close proximity and

contribute towards the formation of disulphide bonds in a highly cooperative process. The effect of cooperative intracellular disulphide bond formation can be seen during protein folding (Chau and Nelson, 1992) and may prove essential in providing stability towards the robust exosporium structure (Fass, 2012).

The exosporium is a known two-dimensional crystalline array, however no mechanism or machinery for its assembly has been determined as of yet. Overexpression of ExsY in *E. coli* has revealed how the crystallinity and formation of a single-layered crystal may arise through the self-assembly of a single template protein cross-linked by disulphide bridges. These disulphides appear to only permit interactions in one plane, allowing for the formation of a single layered crystal similar to that of the exosporium. To further identify ExsY as the exosporium template protein through disulphide cross-links, ExsY crystals were treated with the same conditions as that of exosporium during solubilisation assays. Fragments of exosporium crystals were only completely solubilised in combinations of 8 M urea, 2 % SDS, 0.2 M DTT and heating at 95° C for 20 min. Each condition alone did not have any effect on exosporium; crystalline assemblies were still visible (Terry, 2010) suggestive of strong disulphide cross-links mediating the robustness. These findings directly correlated to the behaviour of ExsY assemblies, which only completely disassembled under heated and reducing conditions, showing that ExsY is indeed responsible for providing the architectural robustness of the exosporium. The biological significance of possessing a remarkably stable exosporium template protein allows the structure to persist for hundreds of years, and may therefore play an important role in maintenance of other proteins with function. Examples could include alanine racemase and BclA, which are both found on the exosporium surface, that play essential roles in germination and dissemination respectively. Identification of the ExsY self-assembly mechanism through covalent disulphide interactions has provided identifiable features, such as high cysteine content, for other endospore forming organisms. This has led to the discovery of the potential exosporium template protein in *Clostridium sporogenes* (Janganan *et al.*, unpublished) and in future other related robust exosporium and coat proteins.

## Chapter 5. Assembly of other exosporium proteins and complexes

### 5.1 Introduction

Chapter 4 illustrated the formation of a *B. cereus* exosporium template structure as a result of the heterologous overexpression of ExsY. Over a dozen other proteins have been identified in the exosporium basal layer (Redmond *et al.*, 2004, Steichen *et al.*, 2005) including, the collagen-like protein BclA making up the “hairy nap” (Boydston *et al.*, 2005, Sylvestre *et al.*, 2002) and ExsFA the “hairy nap” anchor protein (Sylvestre *et al.*, 2005, Thompson *et al.*, 2011b). It is known that ExsY, ExsFA and BclA form a high molecular weight complex (Todd *et al.*, 2003), but no mechanism is known for how the multitude of exosporium proteins assemble. High-resolution structures are available for the C-terminal domain of BclA (Rety *et al.*, 2005) and exosporium in projection (Kailas *et al.*, 2011), but no atomic resolution structures are available for the rest of BclA, ExsY or ExsFA.

In this chapter the effects of ExsFA and BclA on the assembly of the exosporium template protein ExsY are discussed. I hoped to discover the proteins required for assembly of the *B. cereus* wild type exosporium cup and crown structure (Ball *et al.*, 2008, Kailas *et al.*, 2011) through the overexpression of exosporium proteins in *E. coli*. The properties of two cysteine-rich exosporium proteins CotY (*B. cereus*), an ExsY homologue and the proposed exosporium cap protein (Steichen *et al.*, 2007, Thompson *et al.*, 2012), and ExsK, a homologue of CotX (Bailey-Smith *et al.*, 2005, Redmond *et al.*, 2004, Todd *et al.*, 2003) were also analysed.

## 5.2 Results

### 5.2.1 Plasmid construction for expression of exosporium proteins

Genes for *B. cereus* *exsY*, *cotY*, *exsFA* and *bclA* were amplified by PCR using the respective forward and reverse primers listed in Table 2.2.3. Genes were cloned into pET28a for single protein expression or pCOLADuet-1 and pACYCDuet-1 for multiple protein expression. The host for primary cloning was TOP10 *E. coli* (2.4.4). Protein expression was carried out in *E. coli* BL21(DE3)pLysS chemically competent cells (2.4.6). Figure 5.1 shows the resulting amino acid sequence of the encoded proteins.

#### 5.2.1.1 p28eFAC - ExsFA C-terminal his-tagged

The *exsFA* gene was cloned into pET28a for production of a C-terminal his-tagged ExsFA protein. The *exsFA* gene was PCR amplified using primers “ExsFA-fwd” and “ExsFA-rev-His”. The purified *exsFA* PCR product was digested using PciI and HindIII; the pET28a plasmid vector was digested using NcoI and HindIII. The digested DNA vector and plasmid fragments were ligated and used in the transformation, selecting for kanamycin resistant colonies ( $30 \mu\text{g ml}^{-1}$ ).

#### 5.2.1.2 pCAeFAY - ExsFA-ExsY duet untagged

Genes for *exsFA* and *exsY* were cloned into pCOLADuet-1 for simultaneous double protein expression. The genes for *exsFA* and *exsY* were PCR amplified using the primers “ExsFA-fwd and ExsFA-rev-COLA” and “ExsY-fwd and ExsY-rev-COLA” respectively. The *exsFA* PCR product was digested using PciI and HindIII and the pCOLADuet-1 plasmid vector was digested using NcoI and HindIII. The digested *exsFA* PCR product and vector were cleaned and ligated into the MCS1 site on pCOLADuet-1 (Fig. 2.1). The gene for *exsFA* was inserted first as *exsY* naturally contained restriction sites for NcoI and PciI. The ligation mix used in the transformation and colonies exhibiting kanamycin resistance were selected. The plasmid containing the *exsFA* gene (denoted as pCAeFA) was then amplified. The *exsY* PCR product and pCAeFA plasmid were both digested with NdeI and XhoI and the *exsY* gene was ligated into the MCS2 site on the pCAeFA plasmid vector.

#### 5.2.1.3 pACbclA - BclA untagged

The gene for *bclA* was cloned into pACYCDuet-1 as part of a triple protein expression system. The methodology remains the same as for 5.2.1.1 except for a change in vector to pACYCDuet-1. The primers “BclAfwdfull” and “BclArevall” were used in the



PCR amplification. The *bclA* PCR product was digested with PciI and HindIII and the plasmid was digested with NcoI and HindIII. The digested DNA vector and plasmid were ligated and the mix used in the transformation, selecting for chloramphenicol resistant colonies ( $37 \mu\text{g ml}^{-1}$ ).

#### **5.2.1.4 pACb20 - N-terminal truncated BclA untagged (Denoted: BclA<sub>m</sub>)**

A truncated version of the *bclA* gene lacking 57 base pairs from the N-terminus was also cloned into pACYCDuet-1. The primers “BclA<sub>fwd</sub>20” and “BclA<sub>rev</sub>all” were used for PCR amplification of the truncated *bclA* gene and introduced an artificial “ATG” start codon as the native codon was removed. The PCR product and pACYCDuet-1 vector were both digested with NcoI and HindIII. The digested DNA vector and plasmid were ligated and the mix used in the transformation, selecting for chloramphenicol resistant colonies.

#### **5.2.1.5 p28exsKC - ExsK C-terminal his-tagged**

The *exsK* gene was cloned into a pET28a vector similar to that for *exsFA* in 5.2.1.1. The gene for *exsK* was PCR amplified using the primers “ExsK-FWD-Duet” and “ExsK-REV-Duet”. The PCR product and pET28a vector were both digested with NdeI and XhoI. The purified DNA vector and plasmid fragments were ligated and the mix used in the transformation, selecting for kanamycin resistant colonies.

#### **5.2.1.6 pACexsKbclA**

A plasmid containing both the *exsK* and *bclA* gene was constructed using the exact method as in 5.2.1.5, replacing the pET28a vector with pACbclA.

#### **5.2.1.7 pACexsKb20**

A plasmid containing both the *exsK* and *bclA* gene was constructed using the exact method as in 5.2.1.5, replacing the pET28a vector with pACb20

#### **5.2.1.8 p28cotYBcC**

The *cotY* gene was cloned into pET28a for production of a C-terminal his-tagged CotY protein. The *cotY* gene was PCR amplified using primers “CotYbc-fwd” and “CotYbc-rev”. The purified *cotY* PCR product was digested using BspHI and HindIII; the pET28a plasmid vector was digested using NcoI and HindIII. The purified DNA vector and plasmid fragments were ligated and the mix used in the transformation, selecting for kanamycin resistant colonies.

## 5.2.2 ExsFA

### 5.2.2.1 Expression of recombinant ExsFA

The *exsFA* gene, present on the p28eFAC vector, was expressed in *E. coli* BL21 (DE3)pLysS to produce recombinant ExsFA protein with a C-terminal hexa-histidine tag (Fig. 5.1 A). *E. coli* cells containing the p28eFAC plasmid were inoculated into 1 l of LB broth containing kanamycin selection ( $30 \mu\text{g ml}^{-1}$ ). Cells were grown and harvested as in 2.4.6. The predicted molecular weight of ExsFA is ~18.9 kDa.

### 5.2.2.2 Purification of ExsFA

The pellet harvested from 5.2.2.1 was resuspended in 20 ml of Tris buffer (table 2.1.3) and aliquoted equally into two 25 ml universal tubes. The cell suspensions were sonicated as in 2.5.1.2 and then centrifuged at  $75,000 \times g$  for 30 min to separate the soluble and insoluble fraction.

#### 5.2.2.2.1 Nickel affinity chromatography

The soluble fraction containing ExsFA was loaded onto a 3 ml NiNTA agarose column and eluted using an imidazole gradient in high salt Tris buffer (containing 500 mM NaCl). The lysed cell, supernatant and eluted fractions were analysed by SDS-PAGE (Fig. 5.2). ExsFA was detected as a strong staining band at ~18 kDa in the whole cell lysate (Fig. 5.2, lane 1) and in the soluble cell extract (Fig. 5.2, lane 2). *E. coli* proteins were washed from the column using Tris buffer (Fig. 5.2, lane 3). Other proteins bound through non-specific interactions were eluted using Tris buffer containing 50 mM imidazole (Fig. 5.2, lane 4). An initial ExsFA fraction, containing a few contaminants, was eluted in 10 ml of Tris buffer containing 0.1 M imidazole (Fig. 5.2, lane 5). The majority of ExsFA was eluted in 10 ml of Tris buffer containing 0.2 M imidazole. A large band for ExsFA can be seen with very few contaminants (Fig. 5.2, lane 6). Trace amounts of ExsFA were eluted in the fractions containing 0.3 M imidazole (Fig. 5.2, lane 7) and 1 M imidazole (Fig. 5.2, lane 8).

#### 5.2.2.2.2 Size exclusion chromatography

ExsFA eluted from 0.1 M and 0.2 M imidazole fractions in 5.2.2.2.1 were mixed and concentrated to a volume of 5 ml using a 10 kDa MWCO Vivaspin centrifugal concentrator (GE healthcare). Size exclusion chromatography was carried out for purification of ExsFA using the method described in 2.5.2.3 with three major elution peaks detected (Fig. 5.3). No protein was detected in peak 1 on SDS-PAGE gels (Fig. 5.3 B, lanes 1- 4) with trace amounts of ExsFA found in peak 2 (Fig. 5.3 B, lanes 5 and

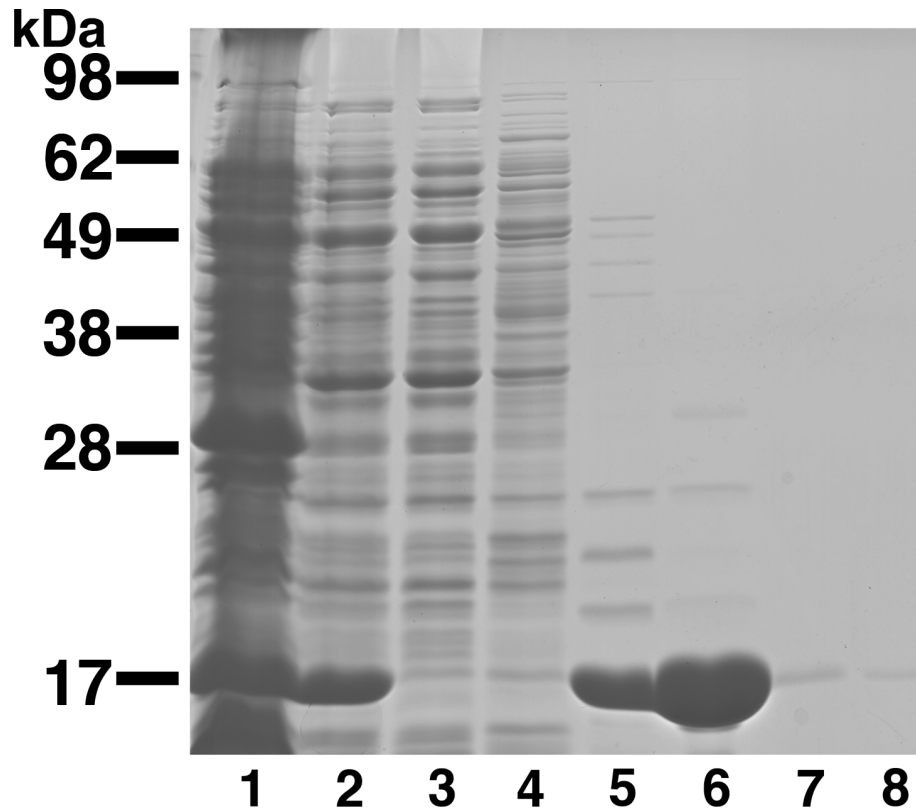


**Figure 5.2 12% SDS-PAGE analysis of ExsFA purified using nickel affinity chromatography.** Lane 1 shows the cell lysate. Lane 2 shows the soluble cell free extract. The unbound fraction and non-specifically bound proteins eluted in 50mM imidazole are shown in lanes 3 and 4 respectively. Lanes 5 – 8 show eluates from 0.1 M, 0.2 M, 0.3 M and 1 M imidazole respectively.

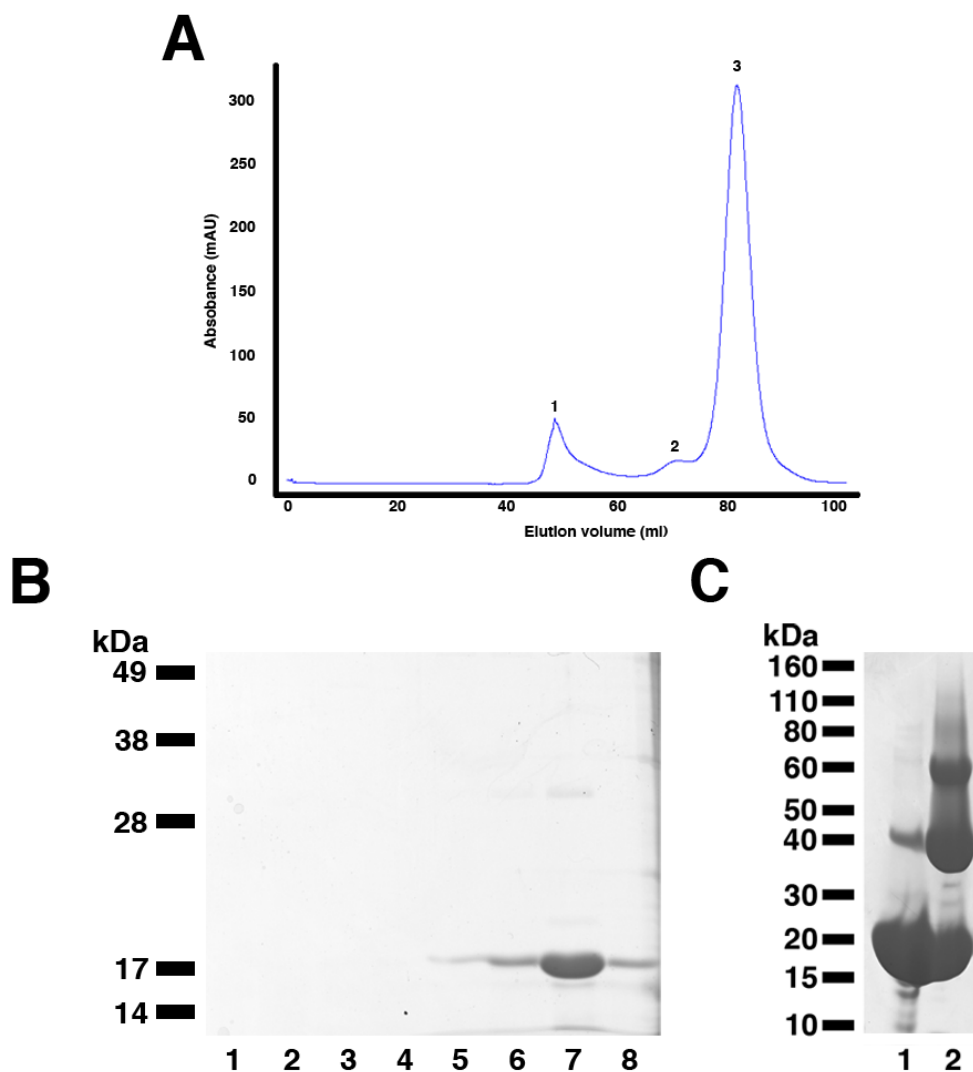


**Figure 5.3 Purification of ExsFA using size exclusion chromatography.** (A) Elution profile of ExsFA purified through gel filtration on a 120 ml HiLoad™ 16/600 Superdex 200 prep grade column with three peaks detected. (B) 12 % SDS-PAGE of elutants from “(A).” Lanes 1-4 show elution collected from peak 1. Lanes 5 and 6 show elution collected from peak 2. Lanes 7 and 8 show elution collected from peak 3. (C) 4-12 % SDS-PAGE analysis of purified ExsFA. Lane 1 shows 95 °C heat and 50 mM DTT treated sample, lane 2 shows untreated sample.

6). The majority of ExsFA was found in gel filtration peak 3 with a prominent band visible at ~18 kDa on SDS-PAGE and a faint putative dimer at ~34 kDa (Fig. 5.3 B, lane 7). The fractions corresponding to peak 3 were pooled and concentrated to a volume of 1 ml and buffer exchanged into 20 mM Tris-HCl, 25 mM NaCl pH 8.0. A final protein concentration of 35 mg ml<sup>-1</sup> was determined using a BCA assay by the method described in 2.5.3. SDS-PAGE analysis of purified ExsFA without 50 mM DTT or heat treatment showed the presence of ~18 kDa, 38 kDa and 60 kDa species presumably originating from the mild denaturation of a native trimer (Fig. 5.3 C, lane 2).

### **5.2.2.3 TEM analysis of ExsFA**

Purified ExsFA was analysed under TEM for the presence of monodispersed single particles. ExsFA, at a concentration of 35 µg ml<sup>-1</sup>, was loaded onto a carbon grid and negatively stained in uranyl formate following the method described in 2.6. TEM analysis showed small monodisperse particles around ~7 nm in negative stain which appear to be in various orientations (Fig. 5.4). Particles were too small for single particle reconstructions.

### **5.2.2.4 Crystallisation of ExsFA**

#### 5.2.2.4.1 Sitting drop vapour diffusion screening

ExsFA was screened for crystallisation conditions using the method described in 2.10.1. 200 nl of ExsFA at a concentration of 35 mg ml<sup>-1</sup> was applied to each well and stored at 16.4 °C. After 8 weeks, crystals were found in two separate conditions. Flat plate-like crystals were found in 0.8 M sodium/potassium phosphate buffer pH 7.5 (NeXtal Protein complex suite, 80) (Fig. 5.5 A) and triangular prism shaped crystals formed in 0.1 M sodium phosphate, 0.1 M potassium phosphate, 0.1 M MES pH 6.5, 2 M sodium chloride (Classics suite, 42) (Fig. 5.5 B).

#### 5.2.2.4.2 Hanging drop vapour diffusion trials

Attempts were made to optimise crystals of ExsFA through hanging drop vapour diffusion trials with slightly altered crystallisation conditions. The flat plate-like crystals grown in 0.8 M sodium/potassium phosphate buffer pH 7.5 were found to be poorly diffracting and therefore not optimised. The triangular prism shaped crystals formed in 0.1 M sodium phosphate, 0.1 M potassium phosphate, 0.1 M MES pH 6.5, 2 M sodium chloride were optimised in hanging drop trays with varying concentrations of NaCl from no salt to 3.5 M in 0.175 M intervals. ExsFA precipitated immediately when mixed with buffer containing higher than 1.8 M NaCl. Precipitate formation occurred throughout all

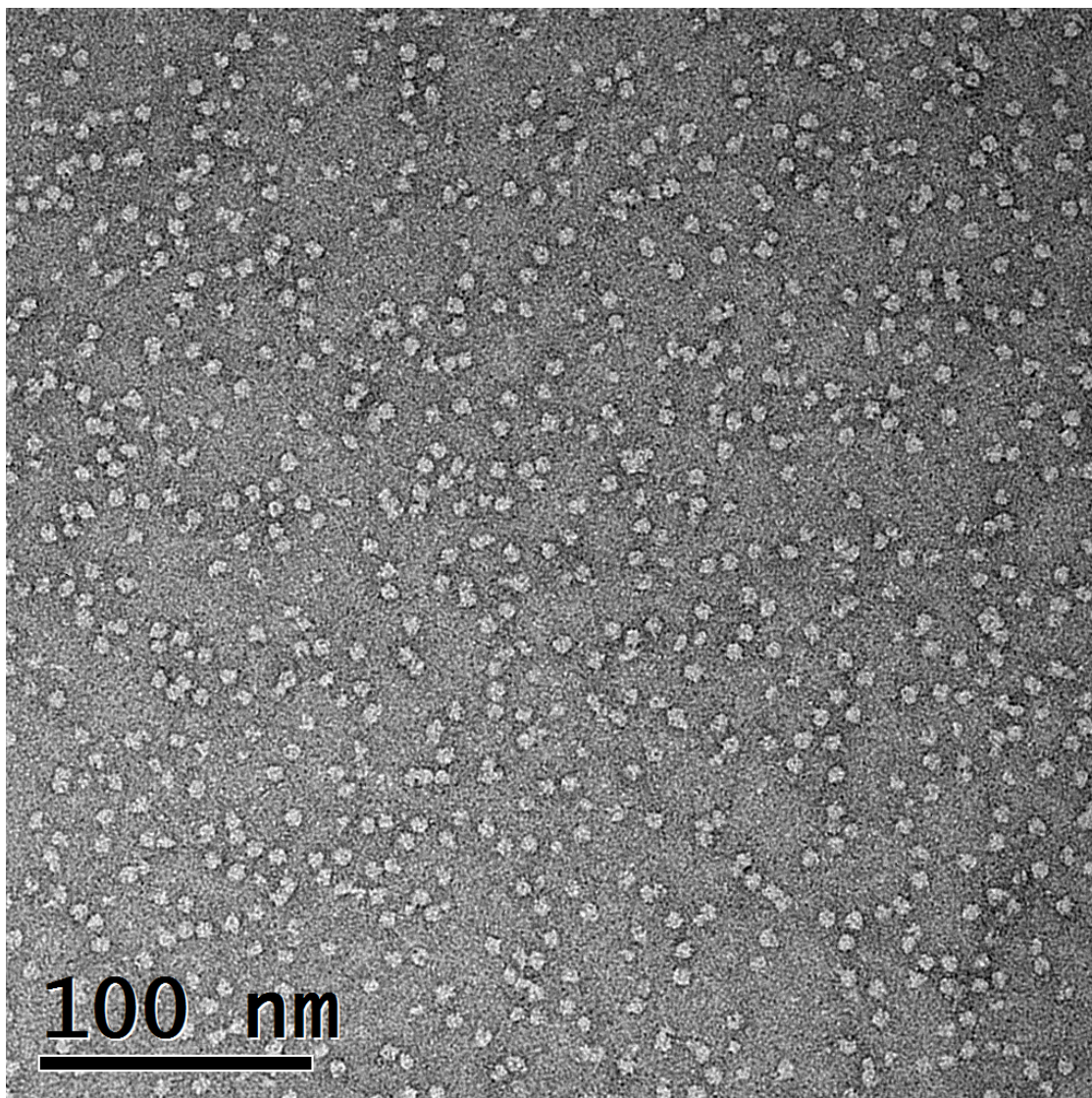


**Figure 5.4 Electron micrograph of monodispersed ExsFA single particles.**  
ExsFA appears as small lighter coloured particles.

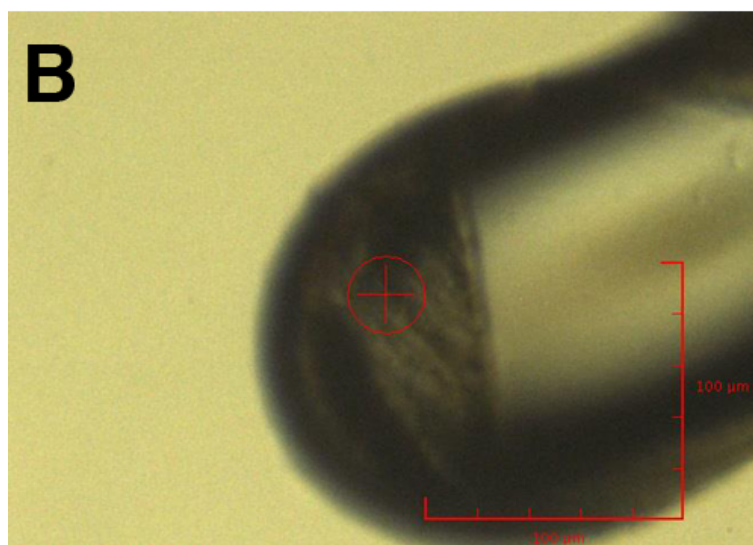
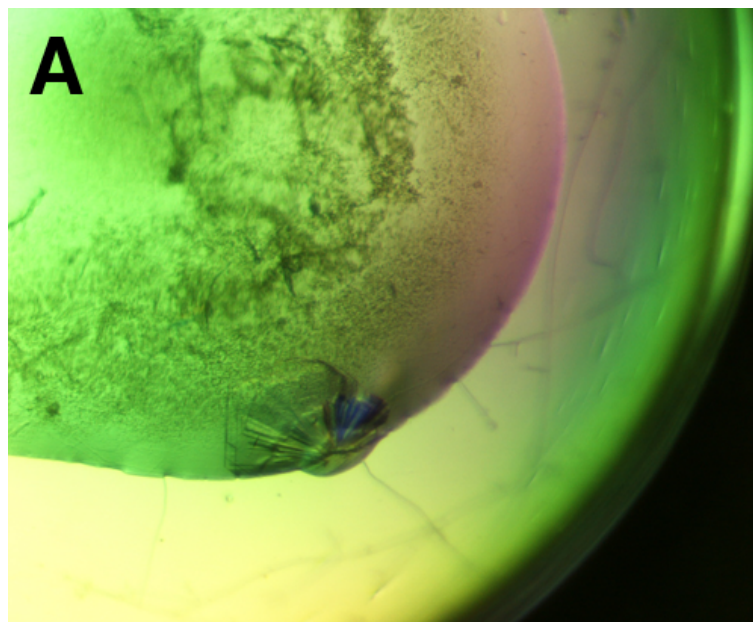


**Figure 5.5 ExsFA crystals formed by sitting drop vapour diffusion.** (A) Plate like crystals formed in 0.8 M sodium/potassium phosphate buffer pH 7.5 and (B) triangular prism shaped crystals formed in 0.1 M sodium phosphate, 0.1 M potassium phosphate, 0.1 M MES pH 6.5, 2 M sodium chloride.

concentrations of NaCl after 7 days. Precipitant was also seen to form a film on the surface of the hanging drop after 7 days in conditions with >2.2 M NaCl. No crystals were found in hanging drop trials after 8 weeks, including in the original sitting drop trial crystallisation condition.

#### **5.2.2.5 X-ray crystallography of ExsFA**

Crystals obtained from sitting drop vapour diffusion trials in 0.1 M sodium phosphate, 0.1 M potassium phosphate, 0.1 M MES pH 6.5 and 2 M sodium chloride were tested on the IO4-1 beamline at the Diamond Light Source, UK by Dr. P. Baker, Dr. C. Bisson, H. Owen and J. Wilson from the University of Sheffield. Crystals were exposed with a single fixed wavelength (0.92 Å) beamline around 360° rotation. ExsFA crystals diffracted to a resolution of 2.43 Å. Diffraction spots appeared sharp in one plane but smeared in the perpendicular plane (Fig. 5.6). The crystallographic symmetry determined from the diffraction of the crystal showed a space group of *p121*. A self-rotation function, carried out by Dr. P. Baker and J. Wilson, indicated a non-crystallographic three-fold symmetry was present in the asymmetric unit, suggesting that ExsFA was present as a trimer (data not shown).

### **5.2.3 CotY (*B. cereus*)**

#### **5.2.3.1 Expression of CotY**

The *cotY* gene from *B. cereus*, present on the p28cotYBcC vector, was expressed in *E. coli* BL21 (DE3)pLysS to produce recombinant CotY protein with a C-terminal hexahistidine tag (Fig. 5.1 B). *E. coli* cells containing the p28cotYBcC plasmid were grown and harvested as in 2.4.6 with kanamycin selection (30 µg ml<sup>-1</sup>).

#### **5.2.3.2 TEM analysis of CotY**

*E. coli* cells expressing *B. cereus* CotY were lysed by sonication using the method described in 2.5.1.2. The cell lysate was examined by TEM for the formation of macro-assemblies. CotY was seen to form sheets and sacs >1 µm in size (Fig. 5.7 A). Single layers of CotY sheets appeared to be crystalline, composed of small hexameric particles with a central stain filled cavity (Fig 5.7 B). Images of CotY crystals appear to be poorly diffracting with faint smeared diffraction spots (Fig. 5.7 C). CotY crystals appeared highly disordered with patchy crystallinity, shown by the incoherent vector distortion distribution plot (Fig. 5.7 D).

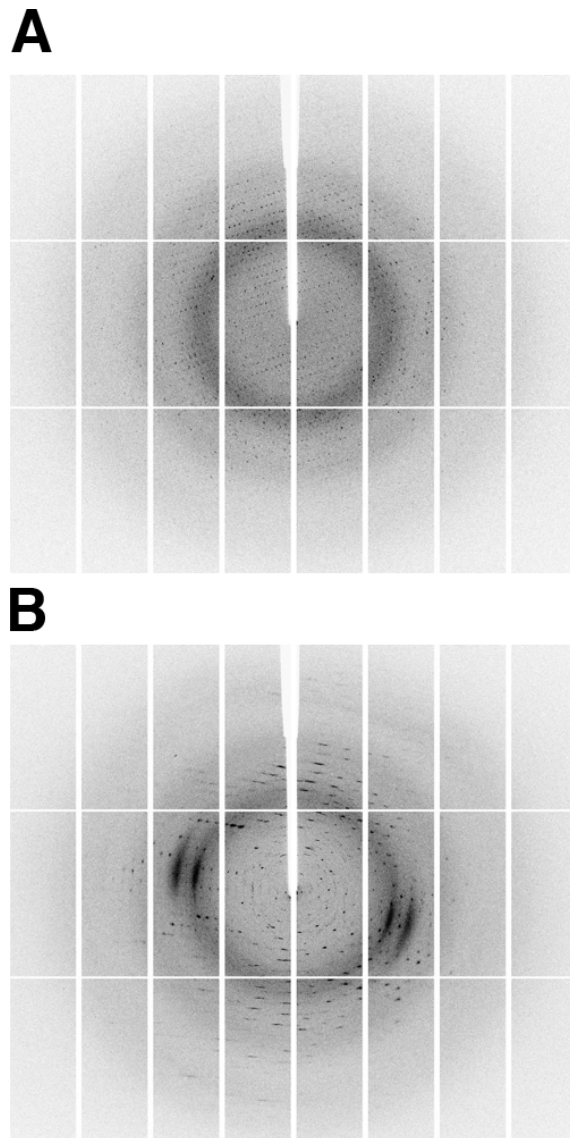


**Figure 5.6** X-ray diffraction from ExsFA crystals formed 0.1 M sodium phosphate, 0.1 M potassium phosphate, 0.1 M MES pH 6.5 and 2 M sodium chloride by sitting drop vapour diffusion. Diffraction patterns recorded at (A) perpendicular to the face of the crystal and (B) after 90° rotation of the crystal.

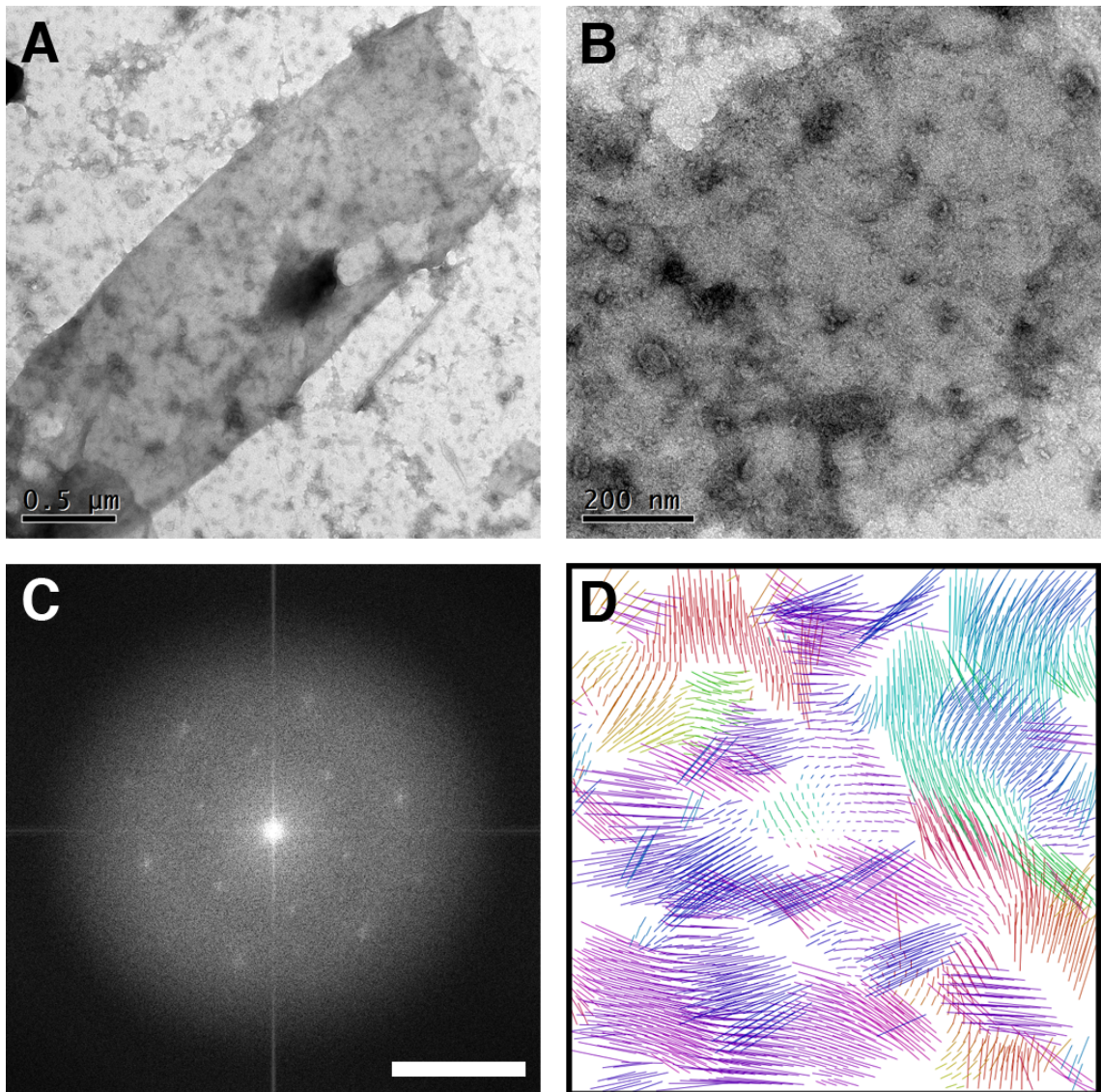


**Figure 5.7 TEM of CotY assemblies.** (A) Large  $>1 \mu\text{m}$  sheets formed by heterologously expressed CotY. (B) Single layer of CotY composed of hexameric particles and (C) computed Fourier transform of “(B)” with poorly defined diffraction. (D) Vector plot of distortion of a representative CotY crystal. Lines indicate continuity of crystals. In the case of CotY, Non-continuous lines indicate multiple patches of small crystals within one large crystalline lattice.

Scale bar in “(C)” indicates  $0.3 \text{ nm}^{-1}$ .

### 5.2.3.3 CotY cell thin sections

Thin sections of *E. coli* cells expressing CotY were prepared through the method described in 2.6.4 and samples analysed using TEM. Cross sections through *E. coli* cells expressing CotY revealed the formation of large sheets of CotY within the cytoplasm of the cell, often near the perimeter of the cytoplasm (Fig. 5.8). Each single layer of CotY measured ~10 nm in thickness.

### 5.2.3.3 Image processing of CotY crystals

Electron micrographs of CotY crystals were processed using *2dx* by the method described in 2.8. The majority of CotY crystals were poorly diffracting with blurred diffraction spots. Six images were processed showing an average unit cell parameter of  $a = b = 79 \pm 2 \text{ \AA}$ ,  $\gamma = 119^\circ \pm 1 \text{ \AA}$ . In projection, CotY crystals appear to be composed of a hexameric ring structure with a central deep stain-accumulating pit (Fig. 5.9 A and B). *2dx\_allspace* determined that *p6* plane group symmetry was suitable for diffracting crystals. A *p6* symmetry imposed map can be seen in Figure 5.9 C and D.

## 5.2.4 ExsK

### 5.2.4.1 Expression of ExsK

The *exsK* gene, present on the p28exsKC plasmid, was expressed in *E. coli* to produce recombinant ExsK with a C-terminal his-tag (Fig. 5.1 C). *E. coli* cells containing the p28exsKC plasmid were grown and harvested as in 2.4.6 with kanamycin selection ( $30 \mu\text{g ml}^{-1}$ ). An overexpressed band could be seen in the *E. coli* cell lysate at ~18 kDa (Fig. 5.10 B).

### 5.2.4.2 TEM analysis of ExsK

*E. coli* cells expressing *B. cereus* ExsK were lysed by sonication using the method described in 2.5.1.2. The cell lysate was examined by TEM for the formation of macro-assemblies. ExsK was seen to form large spherical electron dense aggregates of varying sizes (Fig. 5.10 A). No diffraction could be seen originating from these aggregates.

## 5.2.5 Co-expression of ExsY and ExsFA

### 5.2.5.1 Growth of ExsY-ExsFA

*E. coli* cells containing the pCAeFAY plasmid, carrying genes for both *exsY* and *exsFA*, were induced for co-expression of both ExsY and ExsFA. Cells were grown and harvested as in 2.4.6 with kanamycin selection ( $30 \mu\text{g ml}^{-1}$ ). Both ExsY and ExsFA

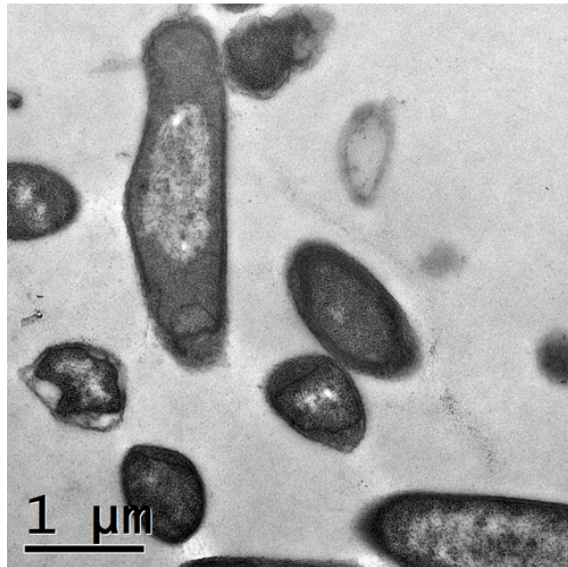
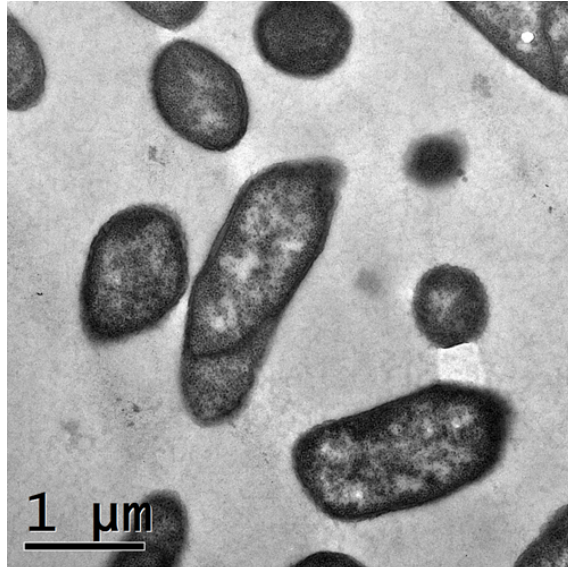


**Figure 5.8 Electron micrographs of CotY thin sections.** Sheet like material composed of CotY was seen forming in the *E. coli* cytoplasm.

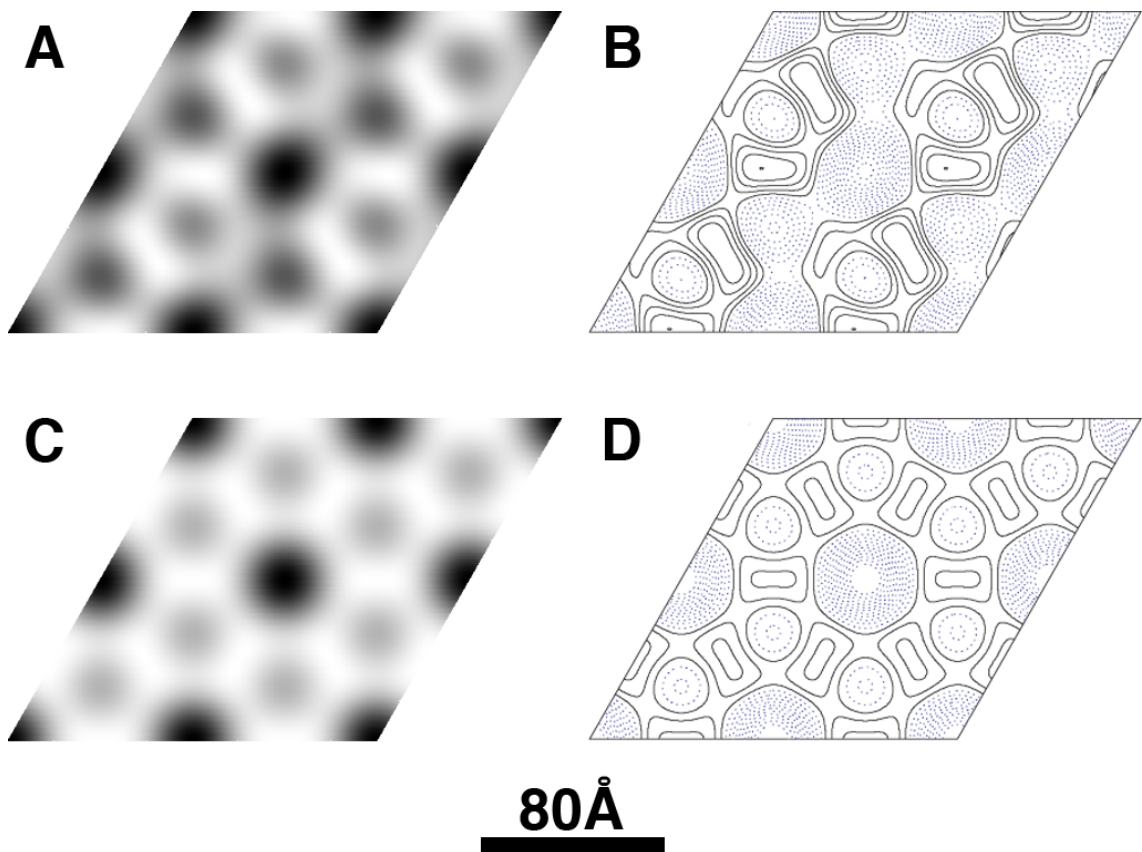


**Figure 5.9** Representative projection map of *B. cereus* CotY crystals. Projection map of CotY in (A) grey level and (B) contour with no symmetry imposed. Projection map of CotY in (C) grey level and (D) contour with  $p6$  plane group symmetry imposed.

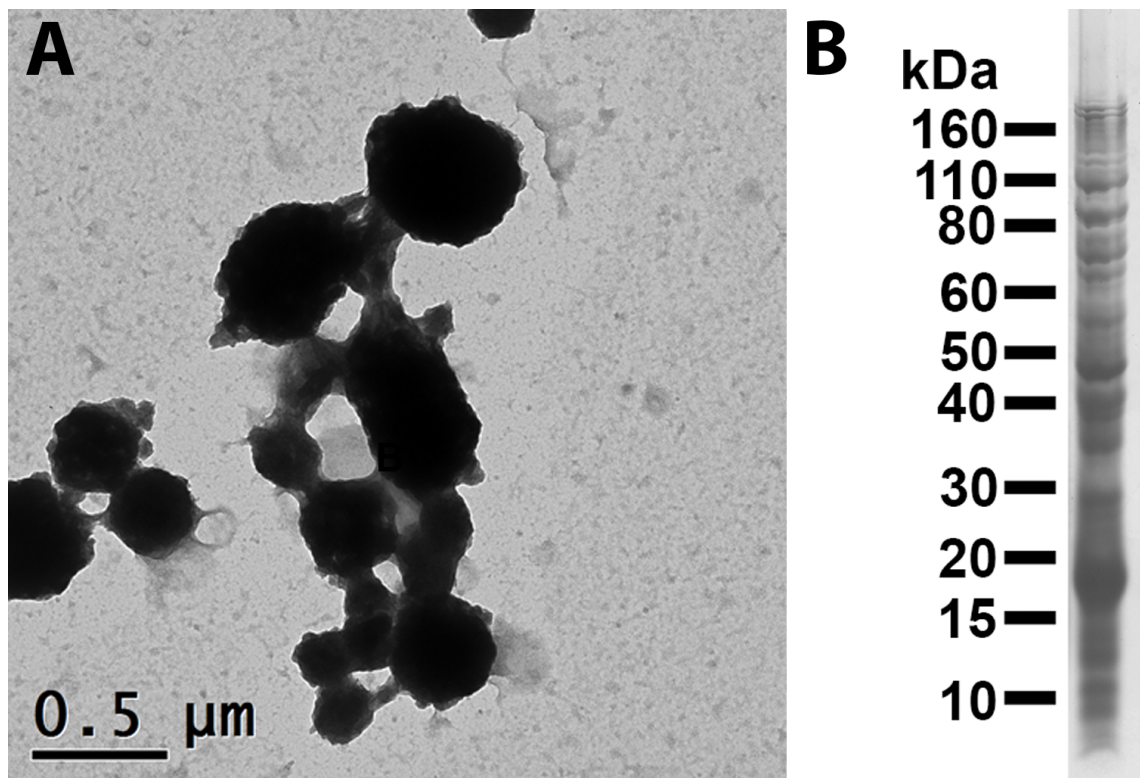


**Figure 5.10 Electron micrograph and SDS-PAGE of cell lysate of ExsK expressing cells.** (A) Large electron dense aggregates seen in the cell lysate of *E. coli* cells expressing ExsK. (B) A band at ~18 kDa corresponding to ExsK can be seen on SDS-PAGE after treatment with 50 mM DTT and heating at 99 °C for 20 minutes.

were untagged to prevent artificial interactions. SDS-PAGE analysis showed the presence of two possible ~17 kDa species (Fig. 5.11, lane 1) in cell extracts.

### 5.2.5.2 TEM analysis of ExsY-ExsFA

*E. coli* cells expressing both ExsY and ExsFA were lysed by sonication using the method described in 2.5.1.2 and analysed by TEM. Large assemblies, >500  $\mu\text{m}$  in size, could be seen within the cell lysate (Fig. 5.12 A). The macro assemblies were composed of hexameric particles with a deep central staining cavity (Fig. 5.12 B). Fourier analysis showed discrete diffraction spots with stronger second order (Fig. 5.12 B [inset]). Crystals often appeared well diffracting although usually overlapped producing multiple lattices.

### 5.2.5.3 Image processing of crystals from ExsY-ExsFA co-expression

Seven images of crystals extracted from ExsY-ExsFA expressing cells were processed using *2dx* by the method described in 2.8. The extracted crystals showed an average unit cell parameter of  $a = b = 83 \pm 2 \text{ \AA}$ ,  $\gamma = 120^\circ \pm 1 \text{ \AA}$  and displayed  $p6$  plane group symmetry. The projection map merged from seven images showed a hexameric ring structure with a central stain accumulating cavity (Fig. 5.12 C and D). Furthermore, six deep stain filling cavities, lying on the three-fold symmetry axis, can be seen surrounding each hexameric ring.

## 5.2.6 Co-expression of ExsY-ExsFA-BclA/BclA<sub>m</sub>

### 5.2.6.1 Growth of ExsY-ExsY-BclA/BclA<sub>m</sub>

*E. coli* cells containing the pCAeFAY and pACbclA/pACb20 plasmids, carrying genes for *exsY*, *exsFA* and *bclA/bclA<sub>m</sub>* were induced for co-expression of ExsY, ExsFA and BclA/BclA<sub>m</sub> (Fig. 5.1 D and E). Cells were grown and harvested as in 2.4.6 with kanamycin (30  $\mu\text{g ml}^{-1}$ ) and chloramphenicol (34  $\mu\text{g ml}^{-1}$ ) selection. All proteins expressed were untagged to prevent artificial interactions. SDS-PAGE analysis showed the presence of a smeared double band at ~17 kDa, however no additional bands corresponding to either BclA or BclA<sub>m</sub> could be seen (Fig. 5.11 B and C).

### 5.2.6.2 TEM analysis and image processing of ExsY-ExsY-BclA

*E. coli* cells expressing ExsY, ExsFA and BclA were lysed by sonication using the method described in 2.5.1.2 and analysed by TEM. Large macro-assemblies were visible in the cell lysate (Fig. 5.13 A), composed of a crystalline array of hexameric units (Fig. 5.13 B). Each hexamer appeared to contain a central deep staining cavity.

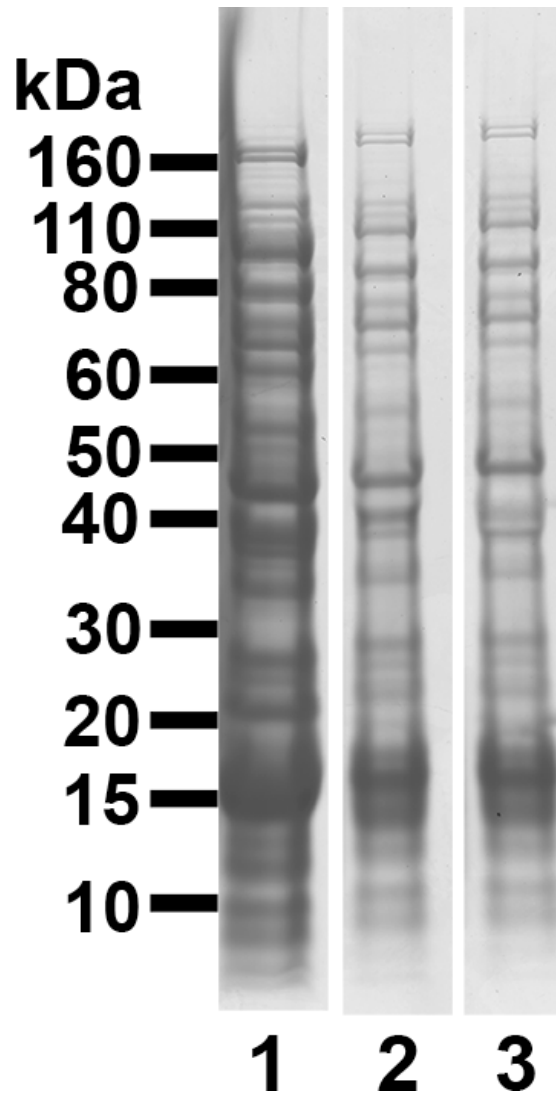
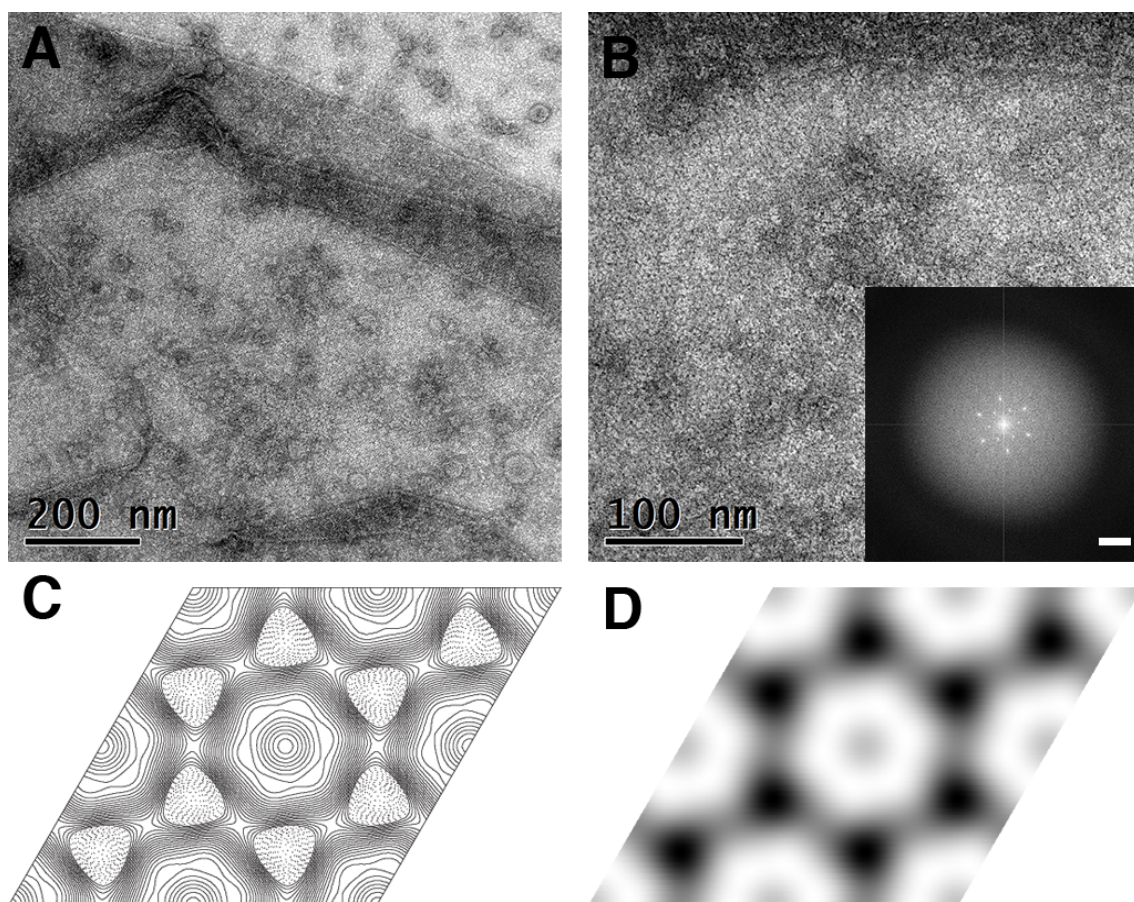
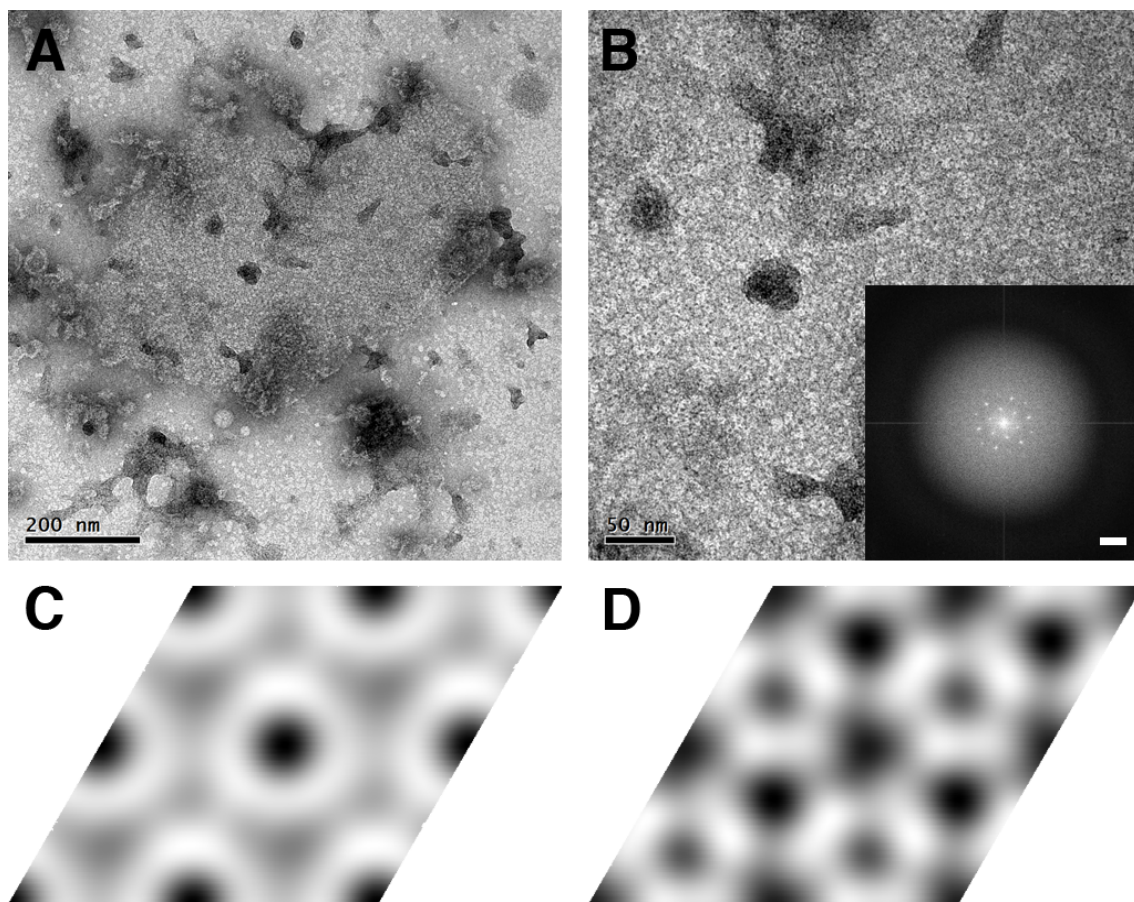


**Figure 5.11 SDS-PAGE analysis of cell extracts from ExsY, ExsFA and BclA/BclA<sub>m</sub> co-expression. Co-expression of; ExsFA and ExsY (lane 1); ExsFA, ExsY and BclA (lane 2) and ExsFA, ExsY, and BclA<sub>m</sub> (lane 3)**



**83Å**

**Figure 5.12 Representative electron micrograph and projection map of crystal extracted from ExsY-ExsFA co-expression.** (A) Large assembly composed of hexameric units. (B) Crystalline surface of the macro-assembly with computed Fourier transform [inset] showing clear diffraction. Projection map from seven merged crystals with  $p6$  plane group symmetry imposed viewed in (C) grey level and (D) contour. Scale bar in “(B) [inset]” indicates  $0.3 \text{ nm}^{-1}$ .



**85Å**

**Figure 5.13 Representative electron micrograph and projection map of crystal extracted from ExsY-ExsFA-BclA co-expression.** (A) Large assembly composed of hexameric units. (B) Crystalline surface of the macro-assembly with computed Fourier transform [inset] showing clear diffraction. (C) and (D) show representative projection maps processed from crystals with no symmetry imposed. Scale bar in “(B) [inset]” indicates  $0.3 \text{ nm}^{-1}$ .

Crystals processed using *2dx* showed unit cell parameters of  $a = b = \sim 85 \text{ \AA}$ ,  $\gamma = \sim 120^\circ$ . Various projection maps calculated from the crystalline assemblies showed an apparent hexameric ring structure with a central deep staining core (Fig. 5.13 C and D).

### **5.2.6.3 TEM analysis and image processing of ExsY-ExsY-BclA<sub>m</sub>**

*E. coli* cells expressing ExsY, ExsFA and the mutated BclA appeared identical to that of the wild type BclA with identical results as that of 5.2.6.2. Large crystalline assemblies were visible in the cell lysate (Fig. 5.14 A), composed of clear hexameric units (Fig. 5.14 B). Crystals showed unit cell parameters of  $a = b = \sim 85 \text{ \AA}$ ,  $\gamma = \sim 120^\circ$  and produced identical projection maps to those seen for ExsY-ExsFA-BclA co-expressions in 5.2.6.2.

## **5.2.7 Co-expression of ExsY-ExsFA-BclA/BclA<sub>m</sub> and ExsK**

### **5.2.7.1 Growth of ExsY-ExsY-BclA/BclA<sub>m</sub>-ExsK**

*E. coli* cells containing the pCAeFAY and pACexsKbclA/pACexsKb20 plasmids, carrying genes for *exsY*, *exsFA*, *exsK* and *bclA/bclA<sub>m</sub>*, were induced for co-expression of ExsY, ExsFA, ExsK and BclA/BclA<sub>m</sub>. Cells were grown and harvested as in 2.4.6 with kanamycin ( $30 \mu\text{g ml}^{-1}$ ) and chloramphenicol ( $34 \mu\text{g ml}^{-1}$ ) selection. All proteins expressed were untagged to prevent artificial interactions.

### **5.2.7.2 TEM analysis and image processing of ExsY-ExsY-BclA/BclA<sub>m</sub>-ExsK**

Addition of ExsK did not influence the crystalline formations during co-expression of ExsY, ExsFA and BclA. Crystals found within the sample appeared identical to those seen in the co-expression experiments described in 5.2.5 and 5.2.6. Aggregates of ExsK, identical to those seen in Figure 5.10 A, were found within the co-expressed samples.

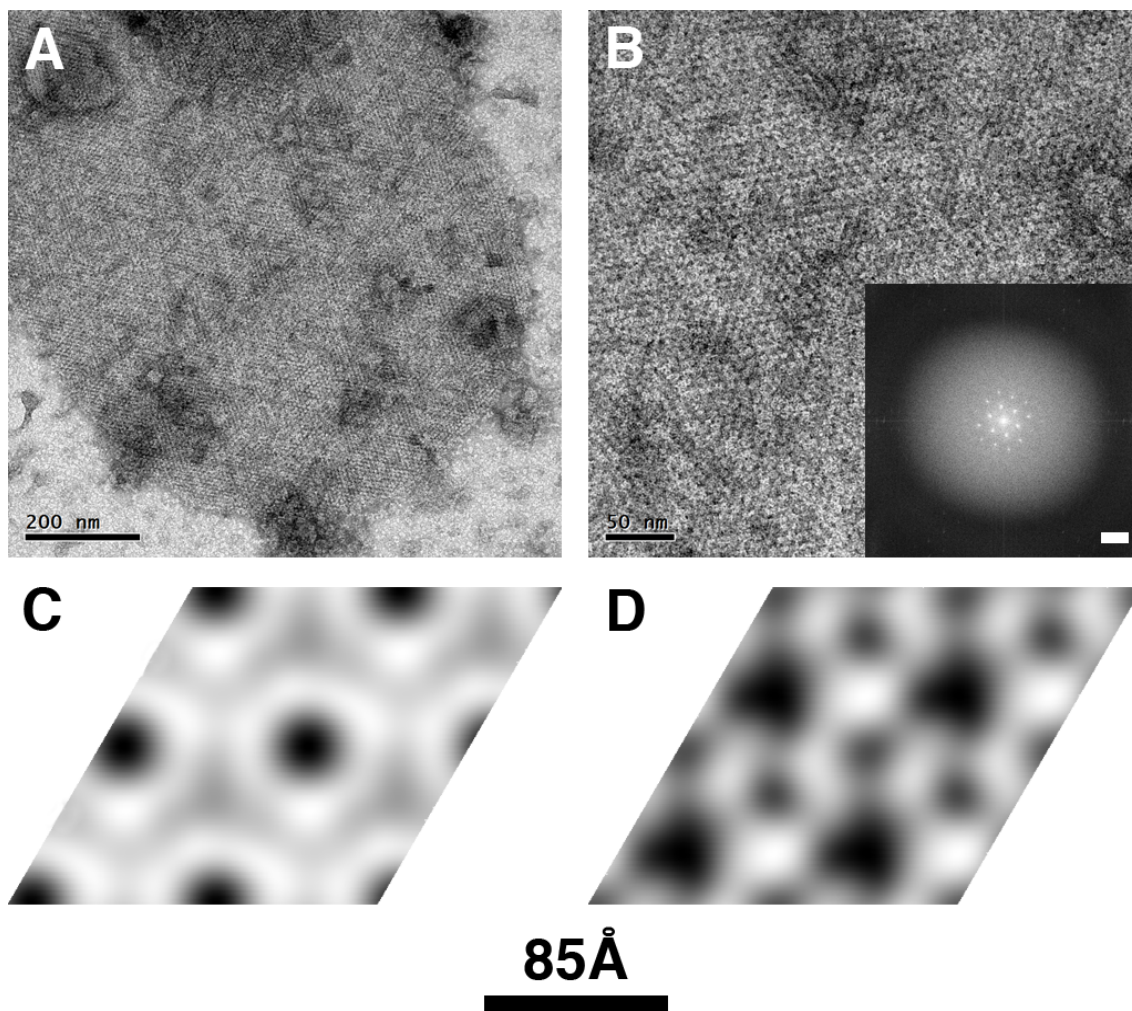


**Figure 5.14 Representative electron micrograph and projection map of crystal extracted from ExsY-ExsFA-BclA<sub>m</sub> co-expression.** (A) Large assembly composed of hexameric units. (B) Crystalline surface of the macro-assembly with computed Fourier transform [inset] showing clear diffraction. (C) and (D) show representative projection maps processed from crystals with no symmetry imposed viewed. Scale bar in “(B) [inset]” indicates 0.3 nm<sup>-1</sup>.

## 5.3 Discussion

### 5.3.1 The hairy nap exosporium anchor

It has been shown in this chapter that ExsFA exists as a trimeric complex by SDS-PAGE (Fig. 5.3). The presence of a trimer was also supported by the determination of non-crystallographic three-fold symmetry within the asymmetric unit in X-ray crystallographic studies. A calculated estimate of the diameter of ExsFA as a trimer, assuming ExsFA as a spherical globular protein, suggested a particle diameter of ~5 nm, similar to the size of ExsFA seen by TEM (Fig. 5.4). The significance of ExsFA forming a homotrimer agrees with the hypothesis that ExsFA is the major contributor to the *B. cereus* exosporium linker structure lying on the three-fold symmetry axis (Ball *et al.*, 2008, Kailas *et al.*, 2011). In addition, BclA itself contains a trimeric C-terminal domain and a collagen-like triple helix (Rety *et al.*, 2005) following a short N-terminal domain, which ideally could dock to a trimeric anchor without a symmetry mismatch.

ExsFA formed a thin film around the drop in hanging drop vapour diffusional trials, preventing the exchange of precipitant from the reservoir with the hanging drop. This prevented the hanging drop from reaching a condition suitable for ExsFA to crystallise. This phenomenon however did show the preference of ExsFA in forming two-dimensional lateral interactions, such as those found at the surface of a droplet. This was further supported by X-ray crystallographic data showing crystals of ExsFA appearing to be well-diffracting in one plane and poorly-diffracting in the perpendicular plane (Fig. 5.6). It may be likely that ExsFA prefers forming interactions in the two-dimensional lateral plane if it is to interact with a two-dimensional array, like that of the exosporium template.

### 5.3.2 The exosporium cap structure

*B. cereus* CotY has been shown in this chapter to self-assemble into large monolayer crystalline sheets within the *E. coli* cytoplasm (Fig. 5.7) to form a similar structure to that of the native exosporium. The unit cell parameters calculated from CotY crystals ( $a = b = 79 \pm 2 \text{ \AA}$ ,  $\gamma = 119^\circ \pm 1 \text{ \AA}$ ) were also similar to those of native *B. cereus* exosporium and hinted at a similar plane group symmetry of  $p6$  (Ball *et al.*, 2008, Kailas *et al.*, 2011). ExsY, a homologue of CotY with ~90 % amino acid identity (Johnson *et al.*, 2006) has already been shown in Chapter 4 to be the major exosporium template protein. CotY on the other hand, is known to be involved in the formation of the exosporium cap structure – a polar region of the exosporium from which the germinating cell escapes (Steichen *et al.*, 2007). In an *exsY* mutant, the polar

cap region is the only area that forms during sporulation (Boydston *et al.*, 2006, Johnson *et al.*, 2006). The formation of CotY assemblies are thought to occur through cooperative disulphide bonds, much like ExsY, due to the natural crystallinity of the protein. CotY crystals differed however in that they were much less well-ordered in comparison to ExsY crystals. This feature of CotY may provide an explanation for the small difference in structure and unit cell parameters calculated, however more work is necessary to confirm this. The less ordered nature of CotY presumably arises from the small difference in amino acid sequence with ExsY. It may however be indicative of its function as an exosporium cap during germination by providing an architectural weak point in the exosporium. This would allow germinating cells to escape in due course but still provide exosporium stability in the dormant spore.

A mechanism is not yet known for controlling the size of the exosporium during sporulation. However, the less well-ordered packing of CotY might also shed light on this matter. Large CotY crystals were less well-ordered as they appeared to be composed of smaller adjoining patches of CotY (Fig. 5.7 D). This suggests CotY intrinsically possesses a limit to the size that a single well-ordered array can reach. The homology in sequence and similarity in assembly between CotY and ExsY would indicate that both proteins could be incorporated into the same array (Johnson *et al.*, 2006, Redmond *et al.*, 2004). Therefore during sporulation, it is possible that the CotY cap structure, although produced first, interacts with the rest of the exosporium through the ExsY template protein and in some manner limits the growth of the final exosporium.

### **5.3.3 Heterologous assembly of the exosporium**

ExsY, ExsFA, BclA and ExsK were all co-expressed with the aim to assemble a complete exosporium from its known major component proteins. ExsY was shown in Chapter 4 to be the exosporium template protein, however features such as the BclA “hairy nap” and ExsFA “linkers” from the native *B. cereus* exosporium model (Ball *et al.*, 2008, Kailas *et al.*, 2011) were missing. Therefore the proteins BclA and ExsFA, thought to be responsible for these features, were co-expressed along with ExsY to see if these integrated *in vivo* and altered the structure formed by ExsY.

TEM analysis of ExsY and ExsFA co-expression showed crystals that did not differ from that of ExsY alone (Fig. 5.12); this is not surprising. It has previously been shown that a co-dependence exists between ExsFA and BclA for correct incorporation into the

exosporium in *B. anthracis* (Thompson *et al.*, 2011b, Thompson and Stewart, 2008). It was also noted that BclA incorporated into the exosporium contained a processed N-terminal region lacking 19 amino acids (Sylvestre *et al.*, 2002, Tan and Turnbough, 2010, Thompson and Stewart, 2008). Therefore, a triple construct containing ExsY, ExsFA along with the native or processed BclA was analysed by TEM. However no change to the self-assembling template structure could be seen (Fig 5.13 and 5.14).

A final protein, ExsK, was added to the co-expression, as it was shown to be found in the high molecular weight complex along with ExsY, ExsFA and BclA through Western blotting and fluorescence localisation (Severson *et al.*, 2009, Terry, 2010). ExsK failed to localise to the exosporium when ExsFA and BclA were not present, indicating a potential role in the complex (Severson *et al.*, 2009). The high cysteine content present in ExsK also indicated a possible function and role in self-assembly. Expression of ExsK resulted in the formation of large electron dense aggregates, which also appeared to migrate much larger on SDS-PAGE than the predicted protein size of 13.5 kDa (Fig. 5.10 B). Co-expression of all four proteins did not yield any change in the self-assembling structure, with ExsK still forming large aggregates much like those seen in Figure 5.10 A. It appeared that although the exosporium template protein, ExsY, is able to self-assemble, the other accessory proteins required to complete the exosporium may require other factors for correct incorporation. Factors including: expression level, timing of expression and other proteins all may impact on the correct assembly of the exosporium.

The lack of spontaneous assembly between the exosporium proteins expressed is not surprising. In the case of BclA, SDS-PAGE analysis showed a lack of any band corresponding to protein (Fig. 5.11, Lanes 2 and 3) suggesting that BclA may be incorrectly formed during attempts at *E. coli* overexpression. BclA is glycosylated in the native *Bacillus* cell during sporulation (Daubenspeck *et al.*, 2004) and is most likely unable to fold correctly in *E. coli*. In this case, BclA will most likely have been degraded and therefore played no part in the assembly of ExsFA into ExsY. A Western blot analysis may have revealed if BclA was indeed present, absent, or mis-folded. If BclA was however expressed correctly but not visible on the SDS-PAGE, other factors may also play a major role in the lack of assembly. It has already been shown that the N-terminal domain is processed for correct incorporation, which we have tried to artificially remove before *E. coli* overexpression. This truncation however did not appear to influence the assembly suggesting that other *Bacillus* proteins may play a

key role in the assembly too. More than a dozen proteins are found in the exosporium (Boydston *et al.*, 2006, Henriques and Moran, 2007, Redmond *et al.*, 2004, Steichen *et al.*, 2005, Todd *et al.*, 2003), some of which may interact with the aforementioned complex of ExsY, ExsFA and BclA but are more readily dissociated. These therefore would not be present in the high molecular weight complex. We may also therefore need to look at proteins which are not directly associated with the high molecular weight complex in attempts to reconstruct a complete exosporium in *E. coli* cells. Once such protein found in *B. anthracis* that is not present in *E. coli*, is prolyl 4-hydroxylase, which catalyses the formation the collagen triple helix (Chapter 1.4.6.3.6). This protein may be required for BclA to fold correctly and function in the co-dependent assembly of the other higher molecular weight components.

## Chapter 6. Self-assembly of *Bacillus subtilis* coat proteins

### 6.1 Introduction

Endospores of the *Bacillus* family possess a robust multilayered coat (Henriques and Moran, 2007, Klobutcher *et al.*, 2006, Laaberki and Dworkin, 2008, Nicholson *et al.*, 2000, Setlow, 2006). *Bacillus subtilis* is the best-studied spore former with a coat composed of greater than 70 different proteins (Henriques and Moran, 2007, McKenney and Eichenberger, 2012).

We identify in this chapter the assembly of coat proteins: CotE, a major morphogenetic protein, and CotY and CotZ, found in the insoluble fraction of the outer coat and crust (Krajcikova *et al.*, 2009, Zhang *et al.*, 1993).

*B. subtilis* CotY and CotZ, orthologues of *B. cereus* ExsY, show ~35 % sequence identity and conservation of nine cysteine residues in both cases (An amino acid sequence alignment can be found in Supplementary Figure 6.1). A mutant of CotY, with an additional 19 amino acids at the C-terminus, (denoted CotY<sub>mut</sub>) has been shown by Dr. Qiang Wan to self-assemble inside *E. coli* (Fig. 6.1 A) into a crystalline lattice with dimensions of  $a = b = \sim 87 \text{ \AA}$ ,  $\gamma = \sim 120^\circ$  (Wan, 2013). Projection maps of CotY<sub>mut</sub> showed a trimeric structure with high-density regions around the three-fold symmetry axis both above and below the contour threshold (Fig. 6.1 B). A three-dimensional model showed that CotY<sub>mut</sub> was formed from a stacked hexameric ring structure made up of two-layers offset by  $\frac{a}{2} + \frac{b}{2}$  with a total thickness of  $\sim 60 \text{ \AA}$  (Fig. 6.1 C & D) (Wan, 2013). It was important to explore whether the native CotY protein would behave in a similar fashion.

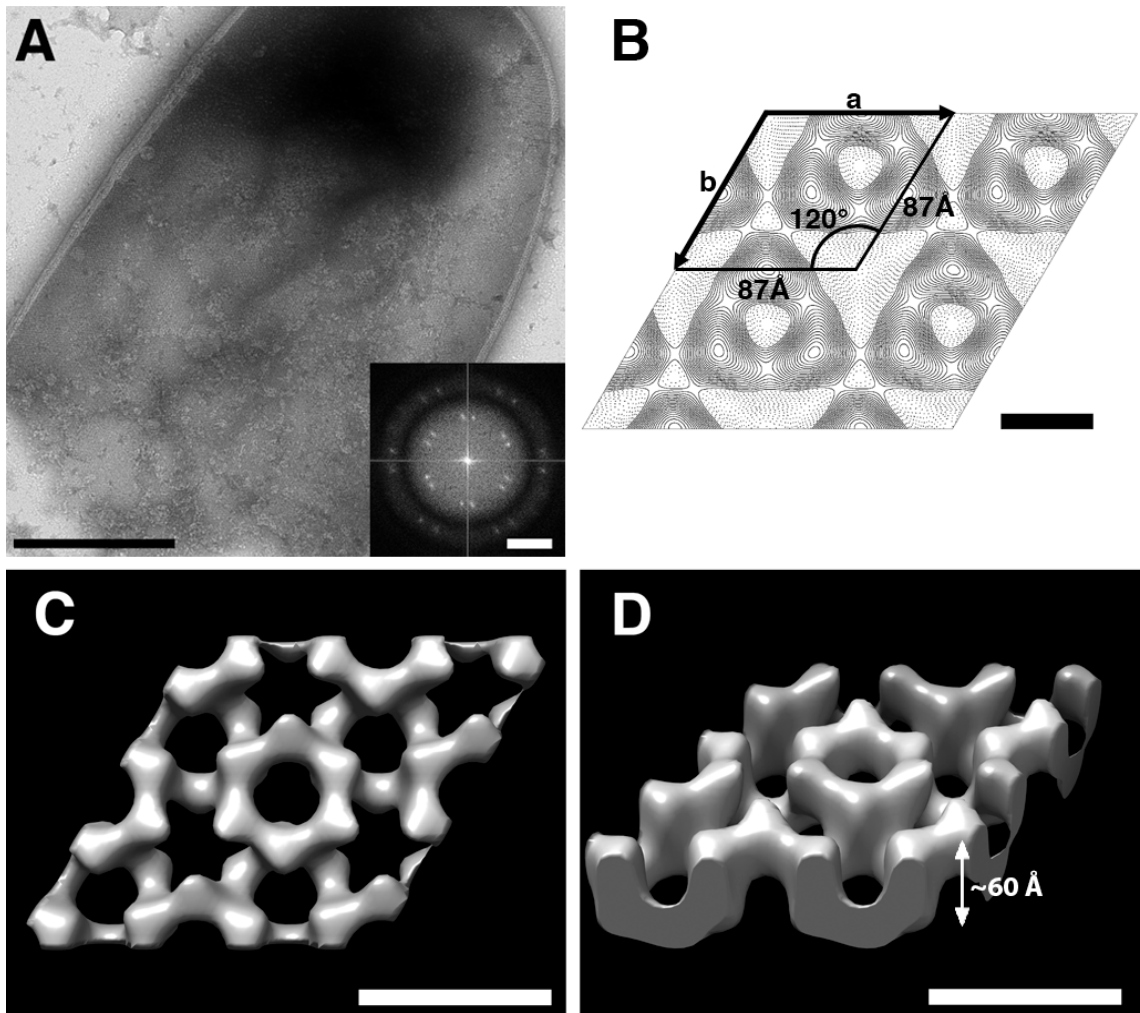


**Figure 6.1 Heterologous expression of *B. subtilis* CotY mutant ( $CotY_{mut}$ ) and TEM reconstruction.** (A) Formation of crystalline arrays inside *E. coli* and inset showing diffraction. (B) Two-dimensional contour projection map with  $p3$  symmetry imposed. (C) Three-dimensional reconstruction of stacked  $CotY_{mut}$  crystals viewed from above and at (D)  $40^\circ$  to the plane. Scale bars in (A) indicate 500 nm and  $0.14 \text{ nm}^{-1}$  inset, (B), (C) and (D) all indicate  $\sim 43.5 \text{ \AA}$ . Images adapted from Wan, 2010.

## 6.2 Results

### 6.2.1 Expression of recombinant spore coat proteins

All plasmids described in this chapter were constructed and provided by Dr. Daniela Krajcikova, Slovak Academy of Sciences, Bratislava. The genes of *B. subtilis* spore coat proteins were cloned into pET28a to encode an N-terminal hexa-histidine tag or into pETDuet-1 as an untagged construct. CotY was cloned as an untagged construct in pETDuet-1 (Fig. 6.2 A) and an N-terminal his-tagged construct in pET28a (Fig. 6.2 B). Both CotE (Fig. 6.2 C) and CotZ (6.2 D) were cloned as N-terminal his-tagged construct in pET28a.

Plasmids encoding spore coat proteins were introduced into *E. coli* BL21(DE3)pLysS cells by transformation, following the method described in 2.4.4.2, with antibiotic selection for plasmid-containing colonies. Protein expression was induced with 1 mM IPTG for 3.5 h following the method described in 2.4.6. Cells were lysed by physical extraction methods described in 2.5.1.2 and proteins batch purified as in 2.5.2.2.

### 6.2.2 CotY

#### 6.2.2.1 Purification of CotY

N-terminal his-tagged CotY (denoted as His<sub>6</sub>-CotY, MW 20.0 kDa) was purified using both column and batch nickel affinity purification.

For affinity purification, soluble cell lysate from His<sub>6</sub>-CotY overexpressing cells was applied to a 1 ml NiNTA agarose column. Bound His<sub>6</sub>-CotY was eluted using an imidazole concentration gradient in urea buffer. His<sub>6</sub>-CotY was eluted at imidazole concentrations of 0.3 M and higher (Fig. 6.3 A, lanes 3 and 4). A visible band was observed with an apparent molecular weight of ~25 kDa following separation by SDS-PAGE.

For batch purification, 1 ml of NiNTA agarose beads was mixed with the whole cell lysate from 200 ml of *E. coli* cells expressing His<sub>6</sub>-CotY. CotY was eluted from the beads in urea buffer containing 1 M imidazole and further separated into a soluble fraction and crystalline insoluble fraction by ultracentrifugation. The soluble and crystalline fractions were analysed on 4-12 % NuPAGE gradient precast gels (Novagen) and bands corresponding to CotY confirmed by Western blotting (Fig. 6.3 B & C). From the soluble fraction, multiple bands could be seen on the gel. A strong band was visible at ~20 kDa, corresponding to a His<sub>6</sub>-CotY monomer with visible oligomers

**(A) CotY untagged (pETDuet-1)**

MSCGKTHGRHENCVCDAVEKILAEQEAVEEQCPTGCVTNLLNPTIAGKDTIPFLVFDKKG  
GLFSTFGNVGGFVDDMQCFESIFFRVEKLCDCCATLSILRPVDVKGDTLSVCHPCDPDFFG  
LEKDFCIEVDLGCFCAIQCLSPELVDRTSPHKDKKHHHG

**(B) CotY N-terminal His-tagged (pET28a)**

MGSSHHHHHHSSGLVPRGSHMSCGKTHGRHENCVCDAVEKILAEQEAVEEQCPTGCVTN  
LLNPTIAGKDTIPFLVFDKKGGLFSTFGNVGGFVDDMQCFESIFFRVEKLCDCCATLSILRP  
VDVKGDTLSVCHPCDPDFFGLEKDFCIEVDLGCFCAIQCLSPELVDRTSPHKDKKHHN  
G

**(C) CotE N-terminal His-tagged (pET28a)**

MGSSHHHHHHSSGLVPRGSHMSEYREIITKAVVAKGRKFTQCTNTISPEKKPSSILGGWIIN  
HKYDAEKIGKTVEIEGYDINWYSYADNTKTEVVTERVKYVDVIKLRDNNYLDDEHEVI  
AKVLQQPNCLEVTISPNGNKIVVQAEREFLAEVVGETKVVVEVNPDWEEDDEEDWEDEL  
EELEDINPEFLVGDPEE

**(D) CotZ N-terminal His-tagged (pET28a)**

MGSSHHHHHHSSGLVPRGSHMSQKTSSCVREAVENIEDLQNAVEEDCPTGCHSKLLSVS  
HSLGDTVPF AIFTSKSTPLVAFGNVGELDNGPCFNTVFFRVERVHGSCATLSLLIAFDEHK  
HILDFTDKDTVCEVFRLEKTNVICIEVDLDCFCAINCLNPRLINRTHH

**Figure 6.2 Amino acid sequence of recombinant *B. subtilis* spore coat protein constructs.** (A) Untagged CotY, (B) CotY hexa-histidine tagged at the N-terminus, (C) N-terminal hexa-histidine tagged CotE and (D) N-terminal hexa-histidine tagged CotZ. Underlined amino acids indicate the additional region containing the his-tag.

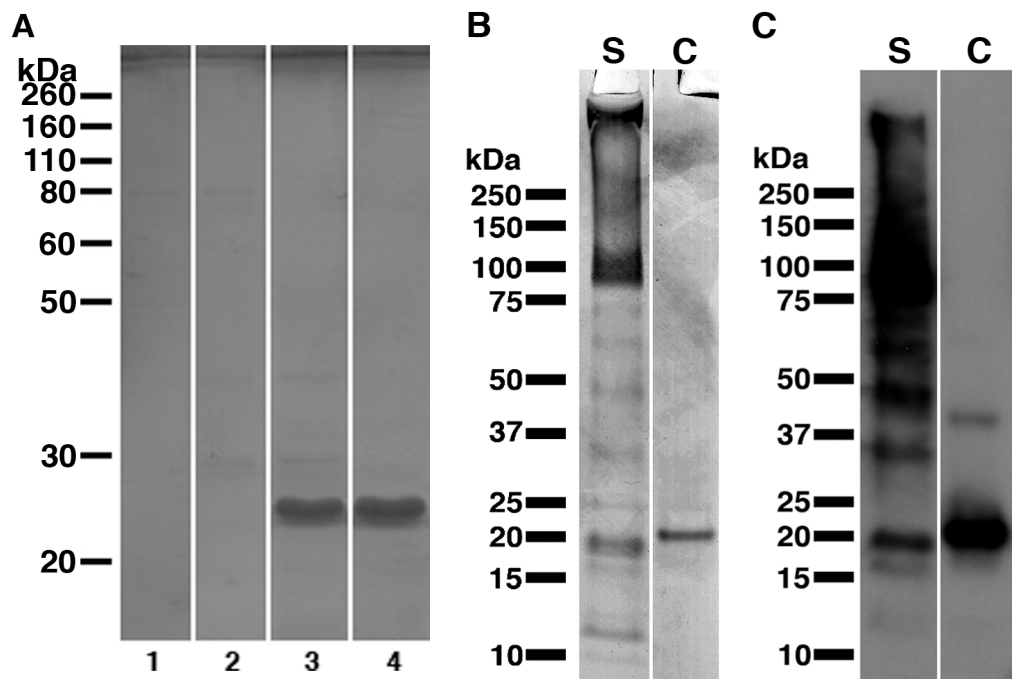


**Figure 6.3 Purification and identification of *B. subtilis* His<sub>6</sub>-CotY.** (A) SDS-PAGE analysis of nickel column affinity purified CotY eluted in imidazole at concentrations of 0.1 M (lane 1), 0.2 M (lane 2), 0.3 M (lane 3) and 1 M (lane 4). All samples were incubated in 50 mM DTT and heated at 99 °C for 20 mins before loading. Batch nickel affinity purified CotY separated into soluble [s] and crystalline [c] fractions and analyzed using (B) SDS-PAGE and (C) Western blotting. Only the crystalline sample [c] was incubated in 50 mM DTT and heated at 99 °C for 20 mins before loading. .

ranging up to 250 kDa and above. Western blot analysis confirmed the presence of a strong ~20 kDa band and other high molecular oligomers. The crystalline fraction displayed a single strong band at ~20 kDa with a putative dimer at ~40 kDa.

The untagged CotY construct could not be purified as no affinity tags were present on the construct. However, overexpression and analysis by SDS-PAGE shows a strong band at ~20 kDa indicating correct protein expression (data not shown).

### 6.2.2.2 TEM analysis of heterologously overexpressed CotY

It was shown by Dr. Q. Wan that CotY<sub>mut</sub> overexpressed in *E. coli* was able to form single layered crystalline sheets (Fig. 6.4 A). To further observe the assembly effects of a natural CotY, untagged and his-tagged CotY was overexpressed in *E. coli*.

Lysed cells expressing untagged CotY and His<sub>6</sub>-CotY constructs were able to form large, >1  $\mu\text{m}$  sized crystals which appeared stacked within the cell (Fig. 6.4 B). The crystals were packed in a tremendously ordered fashion with clearly interlinked hexameric particles (Fig. 6.4 C). A well ordered diffraction pattern could be seen on the computed Fourier transform originating from the crystalline lattice with information up to the 4<sup>th</sup> order spot visible (~12 Å). The variable thickness of CotY and His<sub>6</sub>-CotY crystals prevented the processing of a three-dimensional reconstruction.

### 6.2.2.3 Two-dimensional reconstruction of CotY

Electron micrographs of negatively stained CotY and His<sub>6</sub>-CotY crystals were analysed using *2dx* for structural comparisons. His<sub>6</sub>-CotY crystals were isolated as the crystal fraction from batch purification stated in 2.5.2.2. Untagged CotY was analysed as a sonicate from overexpressing cells, in the presence of urea, loaded directly onto EM grids. His-tagged and untagged CotY crystals both form a hexameric ring structure (Fig. 6.5 A & B) that displays *p6* plane group symmetry determined by *2dx\_allspace* (Table 6.1). Each hexameric unit possesses a ring structure ~65 Å in diameter with a ~25 Å central stain accumulating cavity. A further lower density-linking region can be seen between each hexamer. Both CotY constructs form crystals with identical unit cell parameters of  $a = b = \sim 87 \text{ \AA}$ ,  $\gamma = \sim 120^\circ$  similar to that of the CotY<sub>mut</sub> construct. No differences in structure could be discerned between constructs possessing or lacking a hexa-histidine tag.

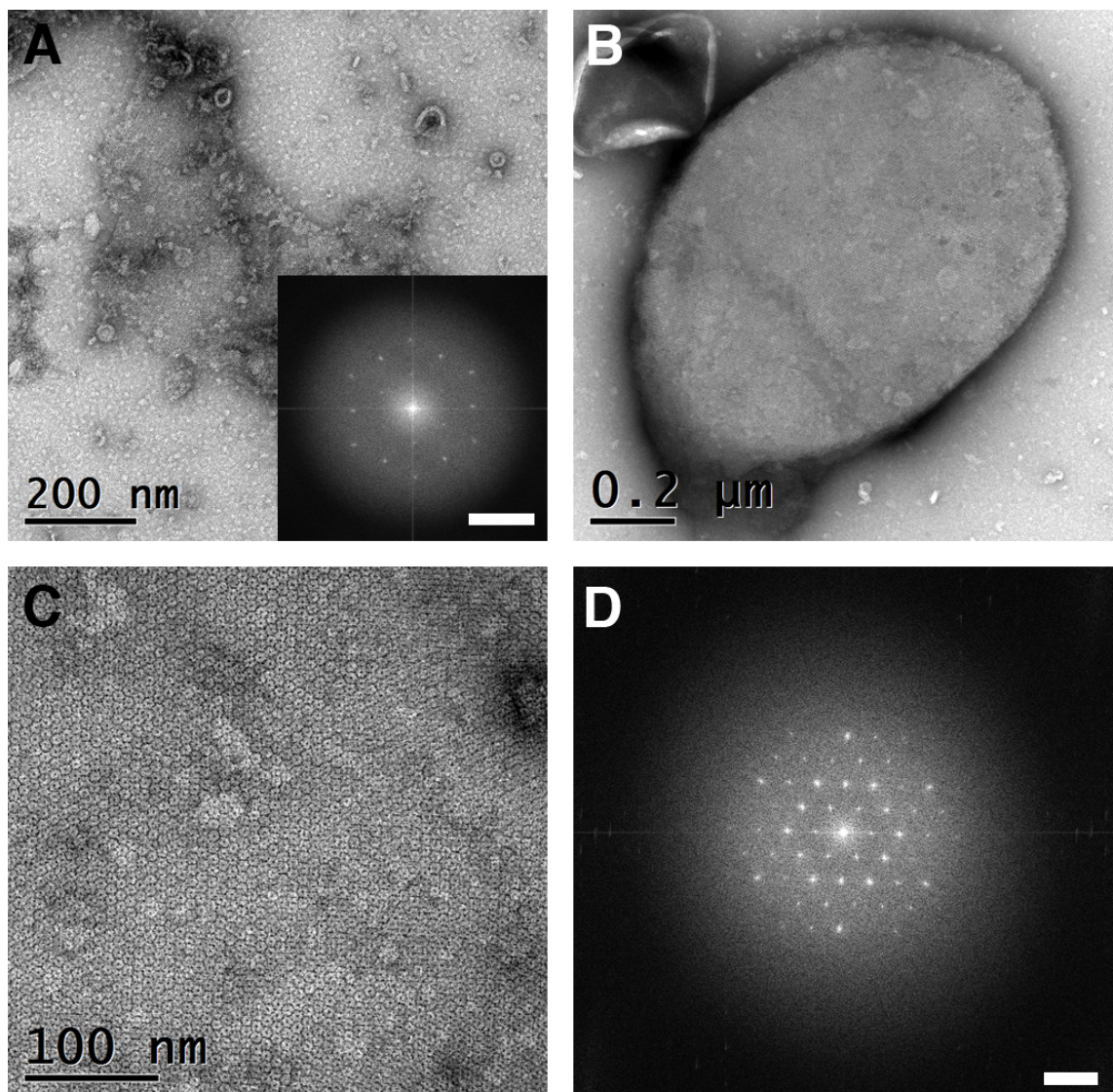


**Figure 6.4 Representative electron micrographs of heterologously self-assembled *B. subtilis* CotY constructs.** (A) CotY<sub>mut</sub> single layered crystals and computed diffraction inset. (B) Multilayered crystal from by untagged CotY. His<sub>6</sub>-CotY crystals were identical to those in “(B)”. (C) Magnified area from untagged CotY showing near perfect array of hexameric particles. (D) Computed Fourier transform from “(C)” showing a clear well ordered diffraction pattern. Scale bar in (A inset) and (D) represent  $0.28 \text{ nm}^{-1}$ .

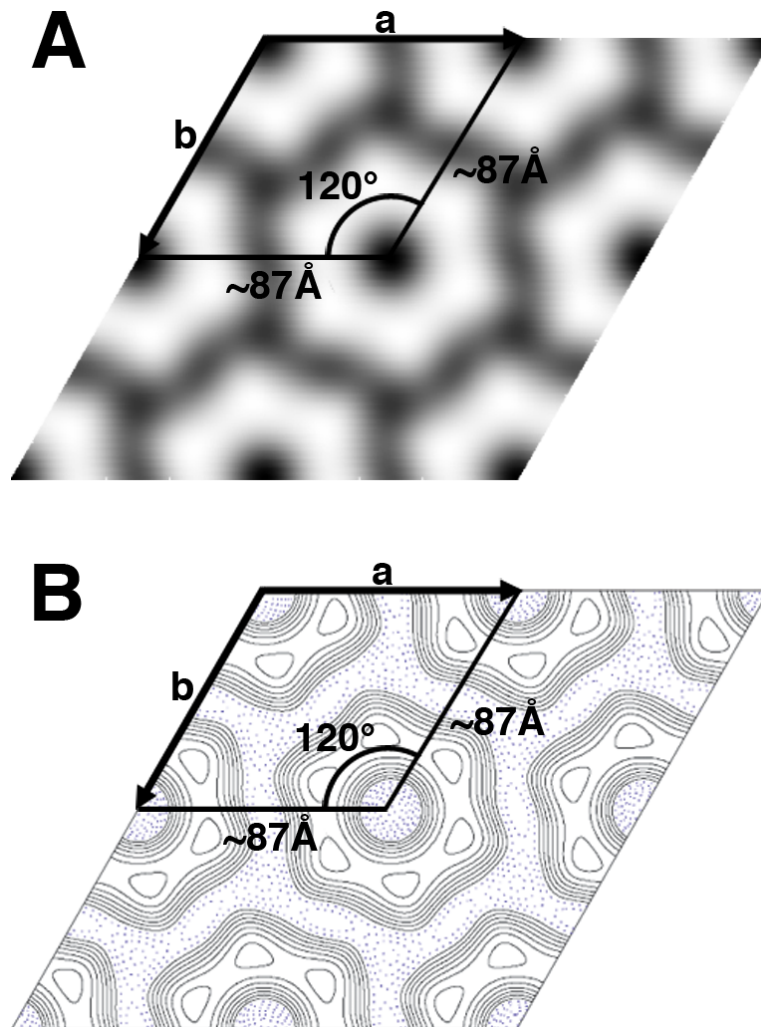


**Figure 6.5 Two-dimensional projection map of negatively stained CotY crystals.** (A) Grey level map showing a hexameric ring structure. Dark areas in indicate stain accumulating regions. (B) Contour map showing the hexameric ring structure with an arbitrary threshold set.  $p6$  symmetry was imposed and unit cells are labeled with parameters of  $a = b = \sim 87 \text{ \AA}$ ,  $\gamma = 120^\circ$ .

**Table 6.1. The internal phase residuals determined after the imposition of all possible two-sided plane groups calculated from one of the micrographs of *B. subtilis* CotY crystals.**

Two sided plane group	Phase residual versus with other spots (90° random)	Number of Comparisons	Target residual based on statistics taking Friedel weight into account
<i>p</i> 1	18.5	86	
<i>p</i> 2	17.4*	43	26.6
<i>p</i> 12_b	46.1	21	20.4
<i>p</i> 12_a	46.4	20	20.1
<i>p</i> 121_b	28.8	21	20.4
<i>p</i> 121_a	66.3	20	20.1
<i>c</i> 12_b	46.1	21	20.4
<i>c</i> 12_a	46.4	20	20.1
<i>p</i> 222	32.4	84	22.7
<i>p</i> 2221b	62.1	84	22.7
<i>p</i> 2221a	27.7	84	22.7
<i>p</i> 22121	57.3	84	22.7
<i>c</i> 222	32.4	84	22.7
<i>p</i> 4	45.9	91	22.3
<i>p</i> 422	52.4	195	20.3
<i>p</i> 4212	64.1	195	20.3
<i>p</i> 3	11.7*	74	18.5
<i>p</i> 312	42.6	166	18.8
<i>p</i> 321	42.4	174	19.2
<i>p</i> 6	13.1*	191	20.3
<i>p</i> 622	39.7	383	19.4

Internal phase residuals were determined from spots of IQ1-1Q5 to 12Å resolution. The values marked with \* are good candidates for the symmetry as the experimental phase residual is close to that expected value based on the signal-to-noise ratio.

#### 6.2.2.4 CotY thin sections

The extent of the stacking between layers of CotY was seen in thin sections of *E. coli* cells expressing his-tagged and untagged CotY. CotY macro-assemblies were seen within the *E. coli* cytoplasm and reached sizes only limited by the dimensions of the expressing cell (Fig. 6.6 A). These cross sections provided a view perpendicular to the side seen by negative stain TEM, showing the formation of stacked layers of CotY crystals (Fig. 6.6 B). Analyses of the perpendicular thin sections showed an ordered stacking array (Fig. 6.6 C) producing intense diffraction spots on a computed Fourier transform (Fig. 6.6 D). Diffraction spots were seen up to the second order with a reciprocal space distance of  $0.16 \text{ nm}^{-1}$  in the first order (Fig. 6.6 D,  $x_i$ ) and  $0.32 \text{ nm}^{-1}$  for the second (Fig. 6.6 D,  $x_{ii}$ ). The weaker first order spots showed a fundamental  $\sim 63 \text{ \AA}$  spacing between each layer and stronger second order spots indicated the presence of sublayers with  $\sim 32 \text{ \AA}$  spacing.

#### 6.2.2.5 Circular dichroism spectroscopy

Nickel affinity purified soluble His<sub>6</sub>-CotY was analysed using CD spectroscopy to estimate the contribution of secondary structures using the method described in 2.9. UV absorbance at 280 nm was used to calculate the protein concentration with an extinction coefficient of 2.37 determined by ProtParam (Gasteiger E., 2005). A final volume of 150  $\mu\text{L}$  of CotY at  $12.6 \text{ mg ml}^{-1}$  was applied to a 0.02 cm path length cuvette and the spectrum was recorded on a Jasco Corp. J-810 Spectropolarimeter. Readings were collected as Theta Machine Units ( $\theta$ ) between 180 nm and 300 nm and converted to Ellipticity.

$$\Delta\varepsilon = \theta \times \frac{0.1 \times 110.2}{0.02 \times 12.6 \times 3298}$$

Theta values ( $\theta$ ) were collected at 1 nm intervals between 180 nm and 300 nm and averaged over eight iterations. The final spectrum (Fig. 6.7) showed characteristics of a protein exhibiting high alpha helical content. The spectra was analysed on Dichroweb using the program SELCON3 and the SP175 reference dataset (Lees *et al.*, 2006, Lees *et al.*, 2004). CotY was estimated to contain  $\sim 70 \%$   $\alpha$ -helical content with little to no  $\beta$ -strands detected. The rest of the protein was estimated to be composed of 9 % random coils and 19 % turns. A normalized root-mean-square deviation of 0.035 suggests a strong correspondence between the calculated secondary structure and the data (Miles *et al.*, 2005).

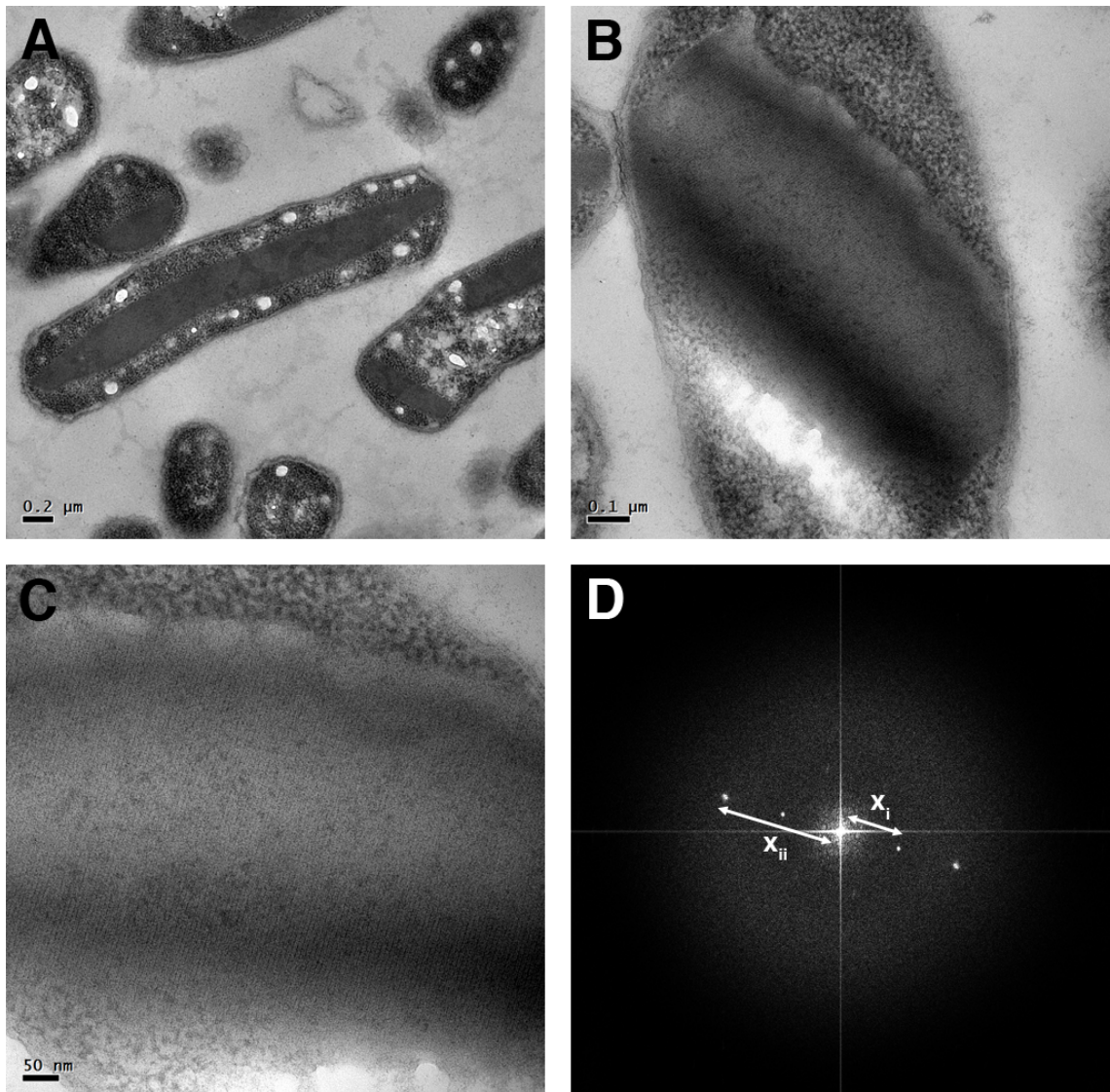


**Figure 6.6** Thin sections of *E. coli* cells expressing *B. subtilis* CotY. (A) Formation of CotY macro assemblies within *E. coli* cells under overexpressing conditions. (B) CotY assemblies formed from continuously stacked layers. (C) Magnified cross section through a crystal showing ordered stacks. (D) Computed diffraction of “(C)” showing diffraction pattern originating from the ordered packing. Reciprocal space distance to the first order spot [ $x_i$ ] and second order spot [ $x_{ii}$ ] are  $0.16 \text{ nm}^{-1}$  and  $0.32 \text{ nm}^{-1}$  respectively.

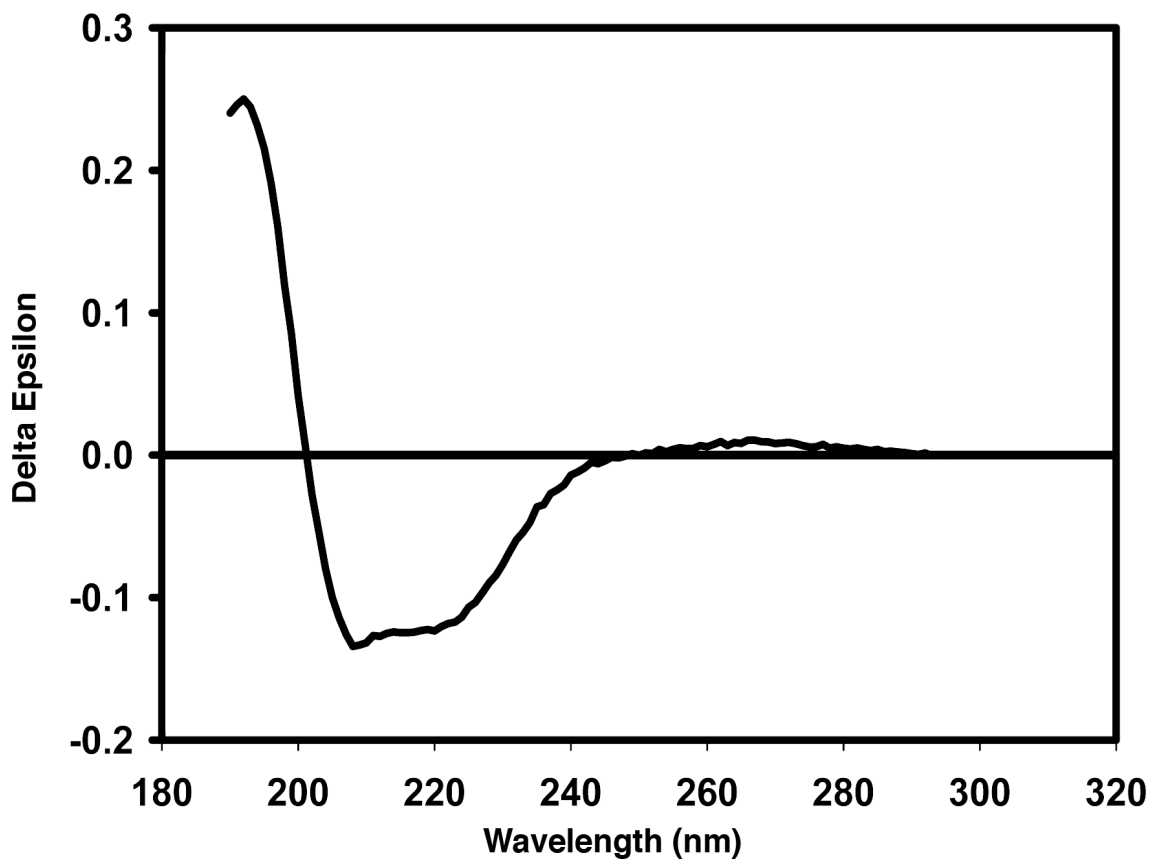


**Figure 6.7 CD spectroscopy of soluble CotY.** Spectra collected from purified soluble CotY. A positive peak can be seen at 193 nm and negative peaks at 208 nm and 222 nm indicative of alpha helices.

### 6.2.2.6 Stability of CotY

Purified His<sub>6</sub>-CotY protein was assayed for stability under combinations of detergent, heat and reducing conditions in 8 M urea buffer, and then loaded directly onto SDS-PAGE gels. Crystalline and soluble samples of His<sub>6</sub>-CotY, obtained from batch purification, were analysed using 4-12 % gradient NuPAGE gels (Novagen) with subsequent identification of bands using an anti-His Western blot. Soluble CotY obtained after batch purification was shown to form faint oligomers in 1 % SDS with a predominant band ~19 kDa, a predicted monomer, and large amounts of protein retained in high molecular weight complexes (Fig. 6.8 A & B, lane 1). In comparison, crystals of His<sub>6</sub>-CotY were highly insoluble in 1 % SDS with only a faint band of material visible at >80 kDa. Western blotting confirmed the >80 kDa band to be His<sub>6</sub>-CotY and showed the presence of higher molecular weight oligomers. (Fig. 6.8 A & B, lane 2). Heating of His<sub>6</sub>-CotY crystals to 99 °C for 20 min resulted in a minor disruption to the crystal with a monomer species ~19 kDa faintly visible on SDS-PAGE and a band shift of the high molecular weight species to ~75 kDa (Fig. 6.8 A, lane 3). Western blotting confirmed the presence of CotY at ~19 kDa and two further smeared oligomer bands at ~75 kDa and ~140 kDa (Fig. 6.8 B, lane 3). Incubation in 50 mM DTT at room temperature for 20 min had little effect on stability with a faint band visible at ~80 kDa on the SDS-PAGE (Fig. 6.8 A, lane 4). This band was confirmed by Western blotting that further showed the presence of high molecular weight oligomers (Fig. 6.8 B, lane 4). His<sub>6</sub>-CotY crystals incubated in 50 mM DTT at 99 °C for 20 min showed the disruption of the higher molecular weight oligomer and a strong band visible on SDS-PAGE at ~19 kDa (Fig. 6.8 A, lane 5). Western blot analysis confirmed the presence of a strong monomeric band at ~19 kDa and faint putative dimer at ~40 kDa (Fig. 6.8 B, lane 5). Only under heat and reducing conditions did the high molecular weight complexes, which were present also in the wells of the SDS-PAGE, completely disappear (bands at the top of Fig. 6.8 B lanes 2-5). Therefore, the disassembly of stable His<sub>6</sub>-CotY complexes monitored by EM can be related with the appearance of a monomeric species and disappearance of the oligomeric species, as seen by SDS-PAGE and Western blotting.

## 6.2.3 CotE

### 6.2.3.1 Purification of CotE

N-terminal hexa-histidine tagged CotE (His<sub>6</sub>-CotE, MW 23.1 kDa) was isolated using the batch nickel affinity purification method described in 2.5.2.2. His<sub>6</sub>-CotE was eluted from the beads using Tris buffer containing 1 M imidazole. The final eluted sample was

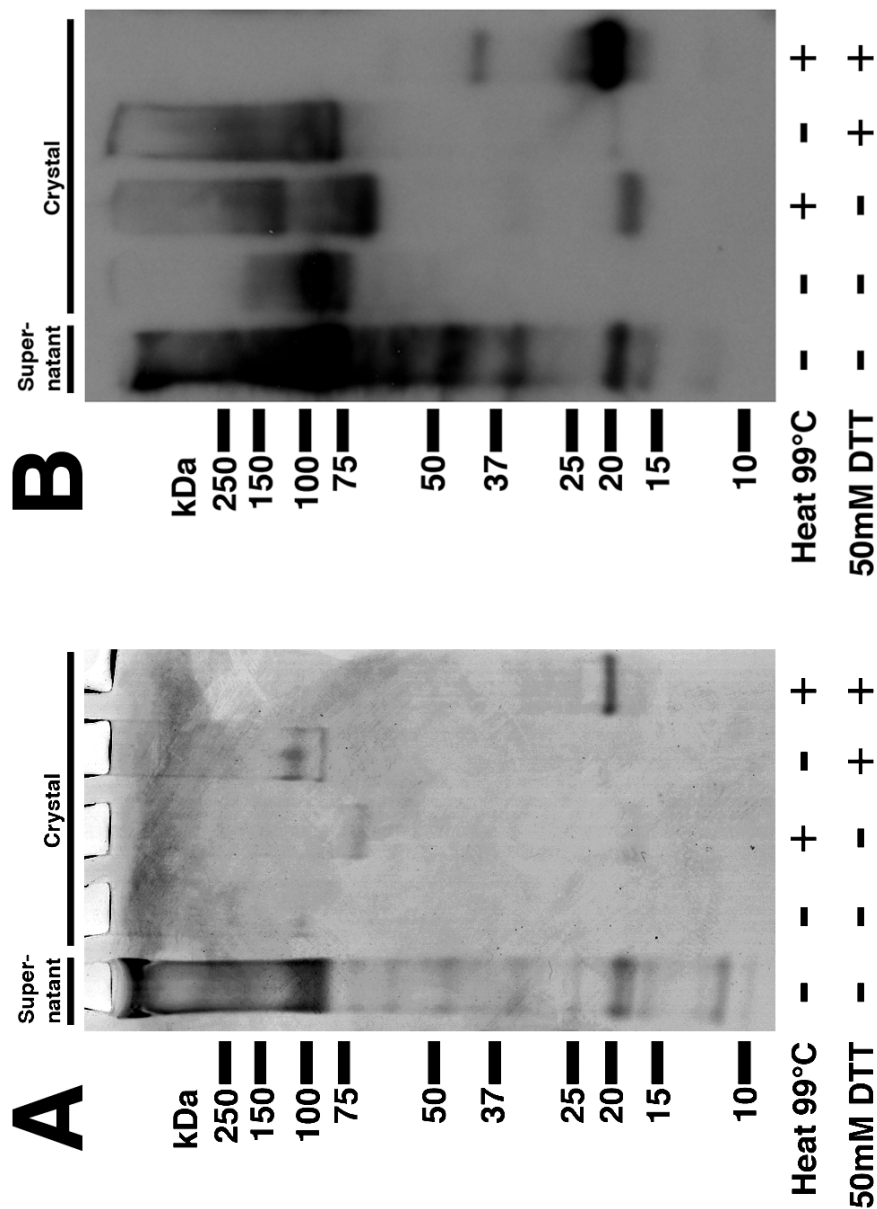


**Figure 6.8 Analysis of His<sub>6</sub>-CotY- crystals and soluble fraction from *E. coli* overexpression by (A) SDS-PAGE and (B) Western blotting.** Lane 1 contains untreated supernatant fraction from nickel affinity purification. Lanes 2 – 5 show nickel affinity purified CotY crystals treated with combinations of heating and DTT for 20 minutes.

ultracentrifuged to separate soluble and insoluble material. SDS-PAGE analysis showed an abundance of a ~25 kDa band corresponding to the His<sub>6</sub>-CotE protein from the cell lysate (Fig. 6.9, lane 1) along with native *E. coli* proteins. After batch purification and ultracentrifugation, purified His<sub>6</sub>-CotE remained in both the soluble fraction (Fig. 6.9, lane 2) and the insoluble fraction (Fig. 6.9, lane 3) with a band at ~25 kDa for both.

### 6.2.3.2 Analysis of CotE by TEM

*E. coli* cells overexpressing His<sub>6</sub>-CotE were lysed by sonication using the method described in 2.5.1.2. Negatively stained whole cell lysates showed large insoluble net-like assemblies visible under TEM (Fig. 6.10 A). These large net-like assemblies were recovered after batch purification using NiNTA agarose beads and eluted in Tris buffer containing 1 M imidazole as described in 2.5.2.2. Purified His<sub>6</sub>-CotE displayed the same net-like aggregates with each fibre measuring ~45 Å in width (Fig. 6.10 B). The net-like aggregates were found to be pseudo crystalline with highly variable spacings in the sizes of the nets (Fig. 6.10 C). A computed Fourier transform showed that the spacings in the net ranged from ~110 Å to ~170 Å in diameter (Fig. 6.10 D).

### 6.2.3.3 Thrombin cleavage of CotE

To eliminate the possibility that formation of His<sub>6</sub>-CotE net assemblies occurred through artificial interactions between N-terminal his-tags, a thrombin cleavage was carried out using the method stated in 2.5.5. Purified His<sub>6</sub>-CotE was incubated for up to 6 h at room temperature with 10 µl of thrombin (GE Healthcare) with agitation. The thrombin protein recognises the “Leu-Val-Pro-Arg-Gly-Ser” site between the N-terminal his-tag and the CotE protein, cleaving after the Serine residue. SDS-PAGE analysis of batch purified His<sub>6</sub>-CotE showed a single band at ~25 kDa (Fig. 6.11 A, lane 1). This fraction under TEM showed an abundance of His<sub>6</sub>-CotE net-like assemblies with no disruption in structure. After incubation with thrombin for 1 hr, the CotE band was shifted to ~23 kDa on SDS-PAGE (Fig. 6.11 A, lane 2) corresponding to the loss of 19 amino acids with traces of the ~25 kDa species remaining. After 6 h incubation with thrombin, SDS-PAGE analysis showed similar results to that of incubation for 1 h with a band at ~23 kDa and a faint ~25 kDa band (Fig. 6.11 A, lane 3). TEM analysis of CotE after digestion for 1 h and 6 h both show the presence of net-like assemblies (Fig. 6.11 C & D).

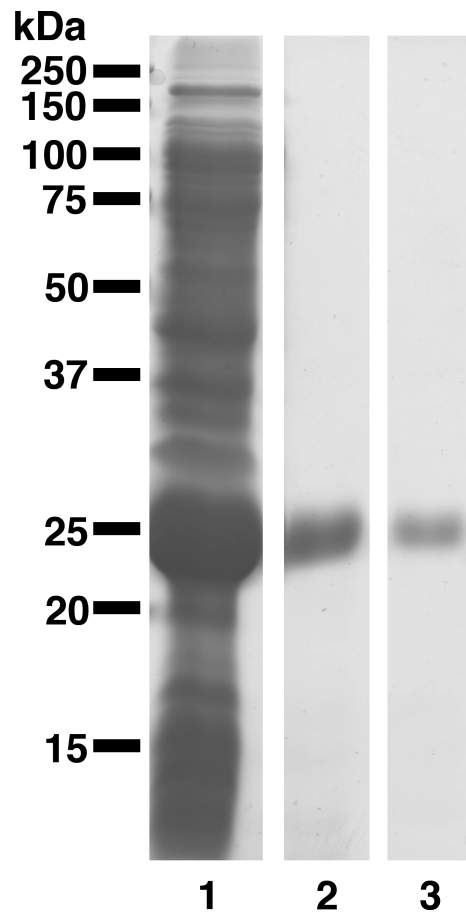


**Figure 6.9 Purification of *B. subtilis* His<sub>6</sub>-CotE.** SDS-PAGE analysis of batch nickel affinity purified CotE. Lane 1 shows the whole cell lysate. Lane 2 shows the soluble fraction and lane 3 shows the insoluble fraction after ultracentrifugation.

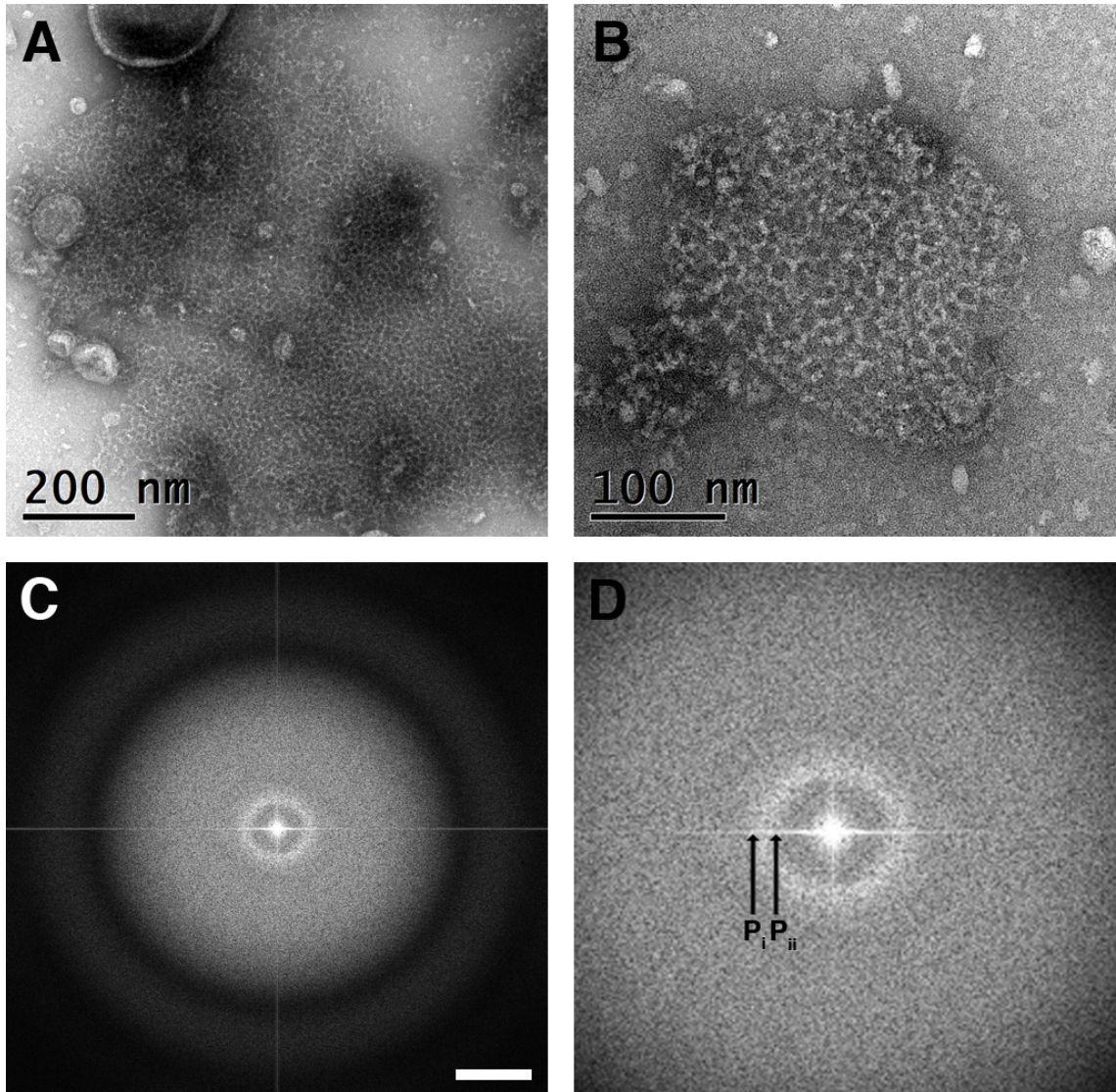


**Figure 6.10 Electron micrographs of CotE net-like assemblies.** (A) CotE macro assembly extracted from whole *E. coli* whole cell lysate. (B) Batch purified CotE displaying a net-like assembly. (C) CotE nets display pseudo crystalline diffraction on a computed Fourier transform. (D) Spacing within the nets reach a minima [ $P_i$ ] of  $\sim 0.09 \text{ nm}^{-1}$  and a maxima [ $P_{ii}$ ] of  $\sim 0.06 \text{ nm}^{-1}$ .

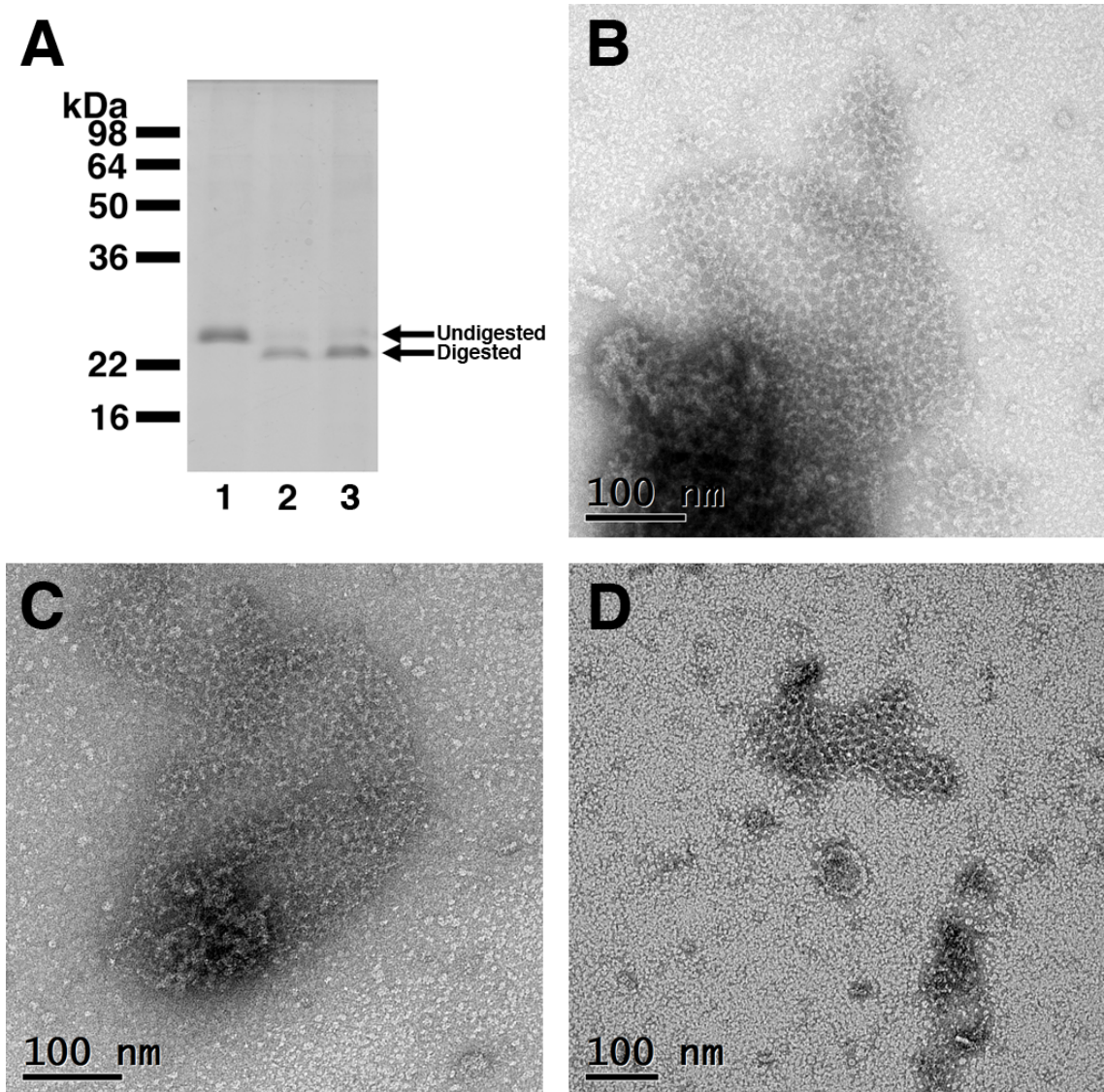


**Figure 6.11 Thrombin cleavage of His<sub>6</sub>-CotE.** (A) SDS-PAGE analysis of CotE before [lane 1] and after 1 hour [lane 2] & 6 hour [lane 3] incubation with thrombin at room temperature. Representative electron micrographs of CotE net assemblies found in (B) untreated, (C) after 1 hour thrombin incubation and (D) after 6 hour thrombin incubation.

#### **6.2.3.4 CotE stability**

Stability of His<sub>6</sub>-CotE was tested in denaturing and reducing conditions. Batch purified His<sub>6</sub>-CotE was resuspended in Urea or Tris buffer and incubated in urea, DTT and also heated. His<sub>6</sub>-CotE was susceptible to denaturation by 8 M urea with a small population of net-like structures remaining (Fig. 6.12 A). Samples however were largely composed of fibrous aggregate-like material (Fig. 6.12 B). Batch purified His<sub>6</sub>-CotE suspended in Tris buffer was treated with 50 mM DTT or 95 °C heating. SDS-PAGE analysis of CotE treated with 50 mM DTT (Fig. 6.13 A, lane 2) or 95 °C heat (Fig. 6.13 A, lane 3) showed a single band ~25 kDa corresponding to a monomer much like treatment in 1 % SDS (Fig. 6.13 A, lane 1). TEM of CotE macro assemblies treated with 50 mM DTT show denaturation and a loss in any net-like structures (Fig. 6.13 B). Under 95 °C heating, denaturation of net-like structures can be seen with filamentous aggregates remaining (Fig. 6.13 C).

#### **6.2.4 CotZ**

##### **6.2.4.1 CotZ purification**

His<sub>6</sub>-CotZ (predicted MW ~18.7 kDa) was batch affinity purified in either Tris or urea buffer using NiNTA agarose beads using the method stated in 2.5.2.2. A band at ~17 kDa is seen in both soluble and insoluble fraction from Tris and urea buffered purifications. The ~17 kDa band from the soluble urea buffered fraction appears more abundant with more contaminant bands (Fig. 6.14, lane 3) whilst the Tris buffered soluble fraction contains a weak band with less contaminants (Fig. 6.14, lane 1). Only a faint ~17 kDa band could be seen in the insoluble fraction for both Tris and Urea purified samples, despite pre-treatment with heat and reducing agent.

##### **6.2.4.2 TEM analysis of purified CotZ**

Batch purified CotZ obtained from 6.2.4.1 was resuspended in both 8 M urea buffer and Tris buffer for analysis of large macro assemblies. CotZ samples were negatively stained in uranyl formate as in 2.6.3 and analysed by TEM. Large single layered assemblies, ranging from 100 nm to >500 nm in size, were seen in purified CotZ samples (Fig. 6.15 A). No ordered lattice was visible on the surface of the assembly, confirmed by the lack of diffraction spots on the computed Fourier transform (Fig. 6.15 A, inset). Resuspension of CotZ in 8 M urea buffer still produced large macro-assemblies with sheet-like material, >500 nm, readily visible (Fig. 6.15 B). No ordered structure was visible on the electron micrograph and no diffraction spots were visible on the computed Fourier transform (Fig. 6.15 B, inset).

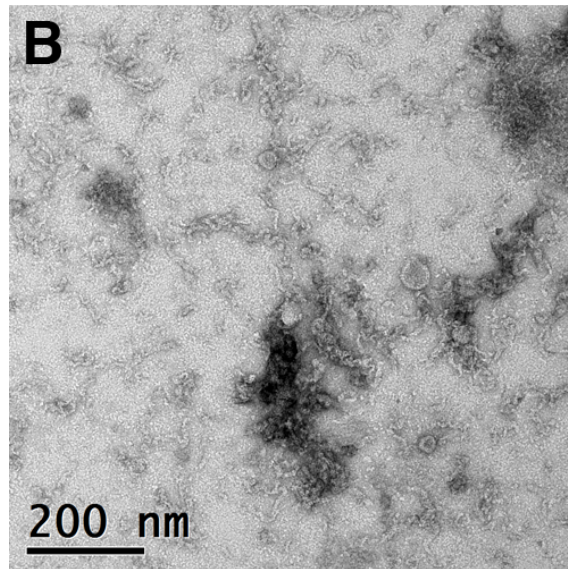
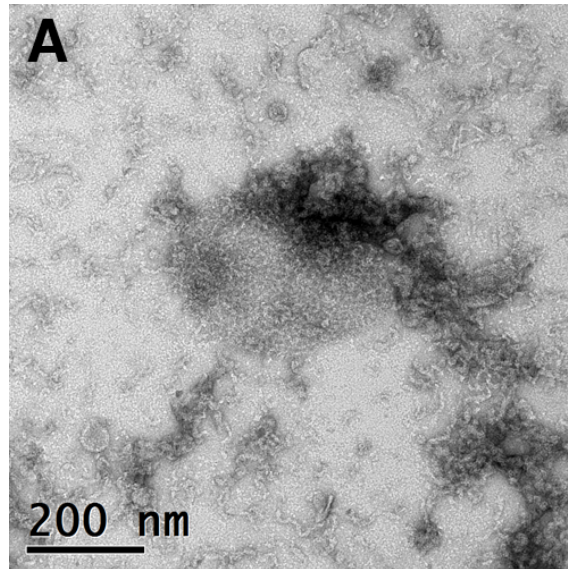


**Figure 6.12 Electron micrographs of purified CotE net-like assemblies treated with 8 M urea.** (A) Low frequency of net-like assemblies still present. (B) Majority of treated CotE samples display thick fibrous aggregates.

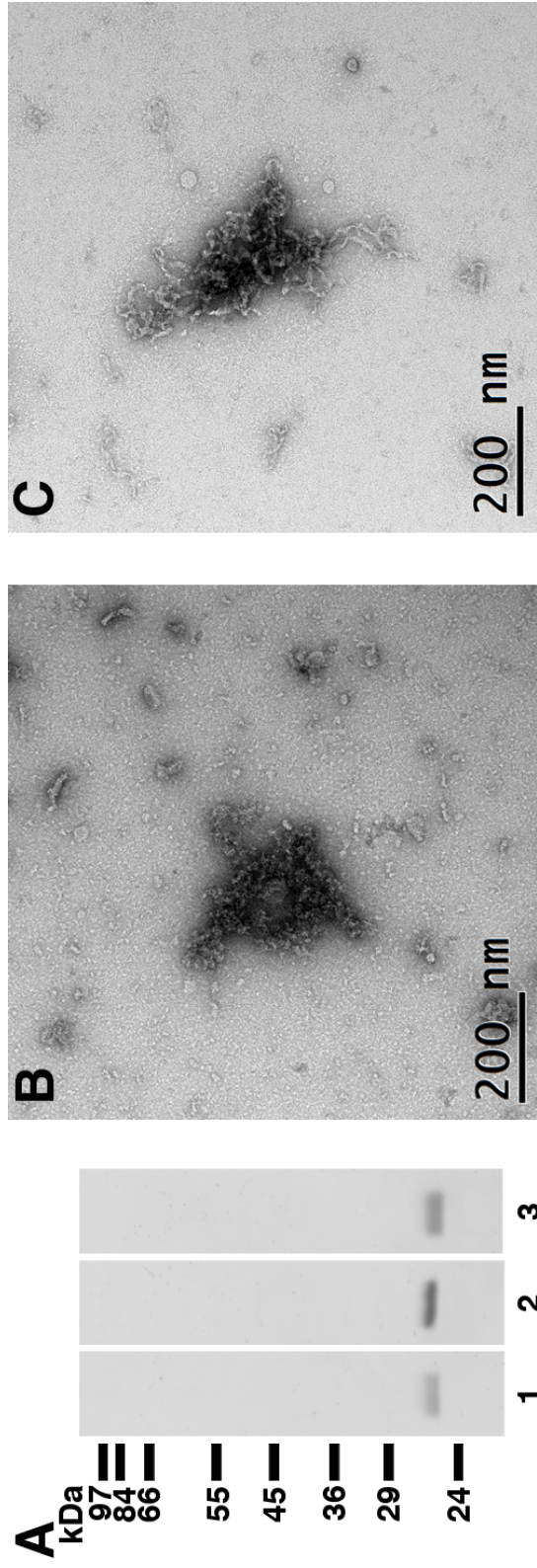


**Figure 6.13 Stability of CotE nets under heated and reducing conditions.** (A) SDS-PAGE analysis of CotE untreated (lane 1), 50 mM DTT treated (lane 2) and 95 °C heat treated (lane 3) for 20 minutes. Electron micrograph of purified CotE nets treated with (B) 50 mM DTT and (C) 95 °C heat for 20 minutes.

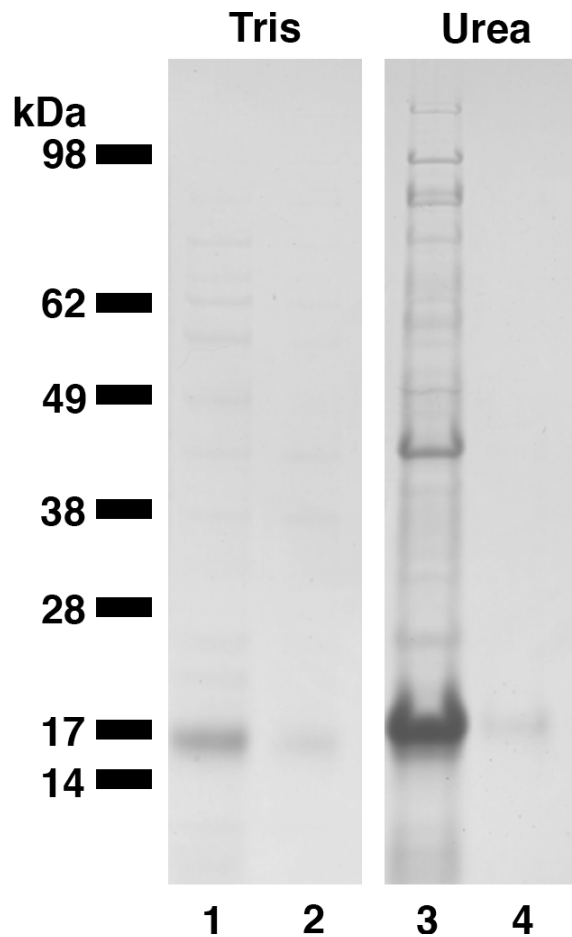


**Figure 6.14 Purification of *B. subtilis* His<sub>6</sub>-CotZ.** SDS-PAGE analysis of batch nickel affinity purified CotZ. Lane 1 shows the soluble fraction and lane 2 shows the insoluble fraction after batch affinity purification and subsequent ultracentrifugation in Tris buffer. Lane 3 and 4 show the soluble and insoluble fraction respectively after batch affinity purification and subsequent ultracentrifugation in Urea buffer. All samples were treated with 50 mM DTT and 95 °C heating for 20 minutes before loading onto the gel.

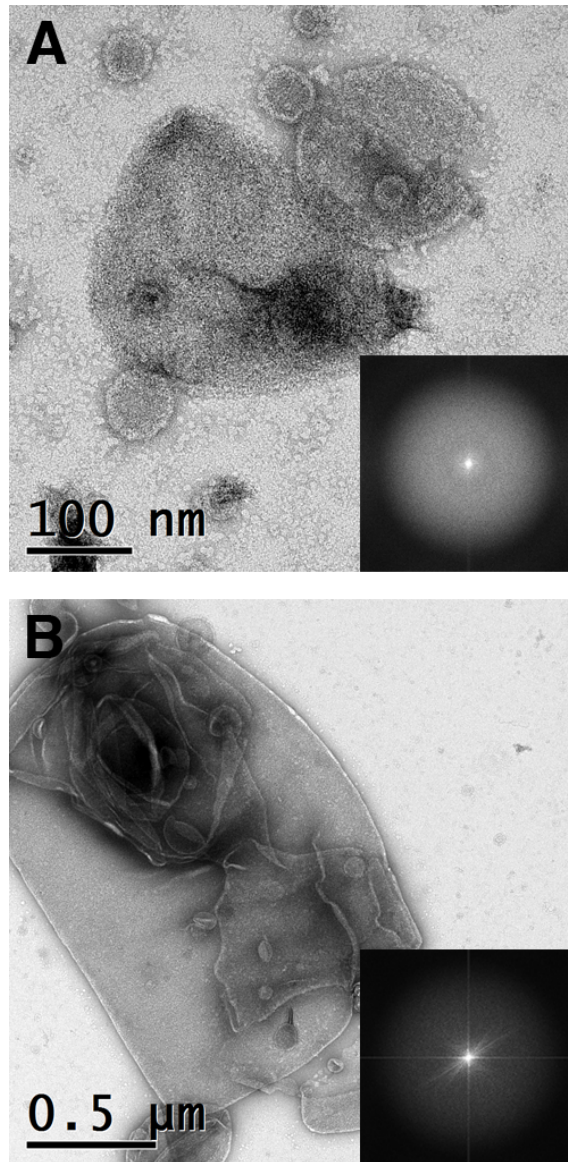


**Figure 6.15 Electron micrograph of purified CotZ assemblies.** Large assemblies are found in CotZ samples purified in (A) Tris buffer and (B) 8 M urea buffer. No diffraction arises from CotZ assemblies (A and B inset).

#### **6.2.4.3 CotZ thin sections**

*E. coli* cells expressing CotZ were grown as in 6.2.1 and subsequent thin sectioning was carried out by the method stated in 2.6.4. Cross sections of *E. coli* cells expressing CotZ showed the formation of stacked multi-layered lattices within the cytoplasm of the cell (Fig. 6.16 A). Each lattice can be clearly seen composed of ordered layers of CotZ with uniform thickness of ~7 nm.

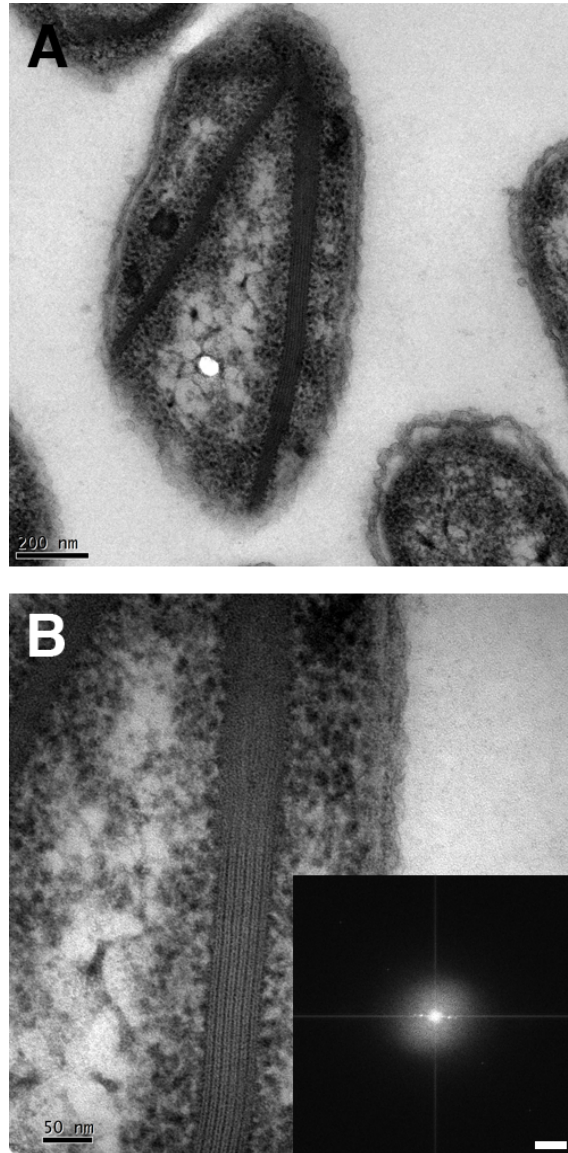


**Figure 6.16 TEM cross sections of *E. coli* cells expressing CotZ.** (A) Large lattices are seen in the cytoplasm of the *E. coli* host. (B) Lattices appear composed of uniformly stacked layers  $\sim 7$  nm in thickness giving rise to an ordered diffraction [inset]. Scale bar in “(B) [inset]” represents  $0.4 \text{ nm}^{-1}$ .

## 6.3 Discussion

### 6.3.1 CotY

#### 6.3.1.1 Purification and analysis of CotY

It has been shown in this chapter that overexpression of CotY and His<sub>6</sub>-CotY within *E. coli* resulted in the formation of large multi-layered crystalline arrays within the cytoplasm through a process of self-assembly. Figure 6.3 A showed that column nickel affinity purification allowed isolation of soluble CotY which appeared around ~25 kDa in size on SDS-PAGE gels after incubation in 50 mM DTT and heating before loading. Figure 6.3 B and C however showed that batch purification isolated a species ~20 kDa in both the soluble and insoluble fractions. The ~25 kDa species is always seen on 12 % SDS-PAGE gels made using the Bio-Rad Mini-PROTEAN<sup>®</sup> system whilst the ~20 kDa is present on Novagen 4-12 % gradient precast SDS-PAGE gels. A ~25 kDa species has however been recorded on Novagen precast gels when extremes of heating and reducing treatment have not been met. This band shift is likely to be explained by the robust nature of CotY and its incomplete denaturation without extremes of conditions. As shown in Section 6.2.2.6 of this chapter, complete denaturation of CotY requires the presence of 50 mM DTT and 99 °C heat treatment to complete disassembly of the high molecular weight species.

The soluble fraction from column nickel affinity purification was suitable for use in CD spectroscopy. The conditions for data collection for His<sub>6</sub>-CotY were kept consistent with that for ExsY in Chapter 4.2.5 for comparison between the two homologues. The concentration of CotY was determined as accurately as possible using UV absorbance, however CotY possess no tryptophan residues, one tyrosine and twelve low absorbing phenylalanine's (Figure 6.2 B). The lack of highly absorbing aromatic residues, much like ExsY, produced a coefficient of extinction with a ~10 % error.

Crystals of CotY and His<sub>6</sub>-CotY, shown in Figure 6.4, could reach sizes of >1  $\mu\text{m}$  causing them to become highly insoluble. Crystals of this size were rare in column nickel affinity purified samples, as they would become trapped in the mesh of the NiNTA agarose column during purification, leading to a decrease in total protein yield. Therefore a batch purification method was developed, allowing for the isolation of large crystals for TEM analysis. The purity of the batch method can be seen in Figure 6.3 B by the single band for His<sub>6</sub>-CotY on SDS-PAGE in reduced and heated conditions.

### 6.3.1.2 Structure of CotY

The elongated mutant CotY<sub>mut</sub> construct was examined by Dr. Q. Wan and shown to form not only hexameric particles, but also large crystalline arrays two molecules in thickness (Wan, 2013). Both the native CotY and His<sub>6</sub>-CotY display the same self-assembling nature but instead formed large, robust, multilayered crystals (Fig. 6.4 B). This observation was consistent with predictions that CotY would form homotypic multimers in the coat (Krajcikova *et al.*, 2009, Zhang *et al.*, 1993). The additional amino acid residues in the CotY<sub>mut</sub> protein prevented CotY from multi-layered stacking whilst an addition of a hexa-histidine tag did not inhibit the propensity of stacking. Cross sections of *E. coli* cells expressing CotY showed multi-layered crystals within the cytoplasm cut along the vertical plane (Fig. 6.6). The fundamental spacing of ~63 Å corresponds to the thickness of two stacked CotY rings. The stronger diffraction from the spacing at ~63/2 Å indicated that each CotY layer is composed of two single CotY sub-layers, much like the structure derived from the CotY<sub>mut</sub> construct (Fig. 6.1 C and D). A subset of CotY crystals displayed *p321* symmetry (Wan, 2013), indicating a head-to-head packing of each layer. This may limit the maximum thickness of each crystal and hence provide a mechanism for restricting the thickness of individual layers in the native *Bacillus* spore coat. All CotY self-assembled crystals showed similar unit cells, at  $a = b = \sim 87 \text{ \AA}$ ,  $\gamma = 120^\circ$ , with the same symmetry suggesting CotY is assembling into the same arrangement on the two-dimensional plane in each case. Furthermore, projection maps obtained from stained CotY and His<sub>6</sub>-CotY multi-layered crystals (Fig. 6.5) appear identical to the hexagonal crystal found in CotY<sub>mut</sub>. This work has been published in Jiang *et al.*, 2015.

### 6.3.1.3 CotY assembly

The ability of CotY, a *B. subtilis* coat protein, to self-assemble into a naturally crystalline lattice resembles the mode of formation of ExsY (Chapter 4), the *B. cereus* group exosporium protein (Ball *et al.*, 2008, Kailas *et al.*, 2011), shown to be the template protein of the basal layer. A relationship between the *B. subtilis* spore crust (McKenney *et al.*, 2010) and *B. cereus* exosporium has previously been hypothesised (Imamura *et al.*, 2011). CotY is a component in the spore crust (Imamura *et al.*, 2011, McKenney *et al.*, 2010). Comparisons between the sequences of *B. subtilis* CotY and its two orthologues in *B. cereus*, ExsY and CotY, show not only ~35 % identity but also a conservation of many of the cysteine residues. A three-dimensional reconstruction of the CotY<sub>mut</sub> and ExsY crystals showed some resemblance in structure with both forming hexameric rings and similar unit cell parameters. CD spectroscopy further

identified similarities in secondary structure with comparable  $\alpha$ -helical content between CotY (70 %) and ExsY (60 %).

Although other covalent cross-links, such as  $\epsilon$ -( $\gamma$ -glutamyl)-lysyl isopeptide bonds, have been found to stabilise spore architecture (Kobayashi, 1996), it has been shown previously in Chapter 4 that formation of two-dimensional crystalline arrays is mediated through cooperative disulphide bonding. In the case of *B. cereus* ExsY, the natural crystallinity of the protein and cysteine residues promotes formation of disulphide bonds, even within the reducing environment of the *E. coli* cytoplasm. *B. subtilis* CotY appears to utilise the same mechanism of assembly through cooperative disulphide bonding, but the self-assembly mechanism has extended into the third dimension to form ordered stacked structures. Zhang *et al.*, 1993 previously reported the formation of disulphide-linked multimers in the spore coat. Such multimers could be seen in the supernatant fraction from batch purification of CotY, with a distinct banding pattern produced by the various assembly states (Fig. 6.8 B, lane 1). The larger insoluble macro-assemblies obtained from batch purification of CotY appeared exceptionally strong with a combination of heat and reducing agent necessary for disassembly of high molecular weight complexes (Fig. 6.8). Heat alone had minimal effects on disassembly whilst reducing agent alone had no effect on CotY stability. CotY migrates as 26 kDa monomer on some SDS-PAGE gels (Figure 6.3), as previously reported by Zhang *et al.*, 1993. It has however been shown in this chapter that complete denaturation results in migration at its predicted molecular weight of  $\sim$ 19 kDa. This further suggests disulphide bonds are involved in both intramolecular bonding and intra-subunit folding.

The question still remains if the heterologously expressed CotY structure resembles its native formation within the *B. subtilis* spore coat and provides the same function. During sporulation, other spore coat proteins may regulate the size of CotY arrays formed with less total protein necessary to cover a smaller surface. CotY however has been noted to be the most abundantly expressed *B. subtilis* coat protein in the later stages of sporulation, indicative of its role in an essential structural feature (Mader *et al.*, 2012, Nicolas *et al.*, 2012). Previous studies have reported the formation of hexagonal arrays from unidentified coat proteins *in situ* with an organised spacing of  $\sim$ 90 Å similar to the CotY assembly (Aronson and Fitz-James, 1976, Ebersold *et al.*, 1981, Holt and Leadbetter, 1969, Plomp *et al.*, 2007, Plomp *et al.*, 2005a, Plomp *et al.*, 2005b). Furthermore, a recent AFM study by Plomp *et al* showed a hexagonal honeycomb

layer present within the *B. subtilis* spore coat (Plomp *et al.*, 2014). The honeycomb matrix possessed an almost identical periodic spacing, at  $\sim 85$  Å, and symmetry as that of the self-assembled CotY structure. This further strengthens the proposal that the heterologously self-assembled CotY structure is representative of a specific coat layer within the *B. subtilis* spore coat. To address the question of functionality, the structure formed by the *B. subtilis* spore coat protein, CotY, can be compared to the native *B. cereus* exosporium. The exosporium is composed of an array of cups and open-channels, acting as a molecular sieve with the function of allowing free passage of germinants whilst excluding unwanted molecules such as proteases (Ball *et al.*, 2008). The similar porous architecture formed by *B. subtilis* CotY would suggest a similar role as a molecular sieve as germinants must penetrate the coat and into the spore core to initiate germination.

## 6.3.2 CotE

### 6.3.2.1 Purification and assembly of CotE

CotE has been shown in this chapter to form large self-assembling two-dimensional pseudo crystalline net-like arrays (Fig. 6.10). Native net-like arrays have been observed on *B. subtilis* spore coats that are absent in *cotE* mutant spores (Aronson *et al.*, 1992). Furthermore, homotypic interactions have previously been predicted to occur between molecules of CotE (Krajcikova *et al.*, 2009, Little and Driks, 2001), reflected in the formation of self-assembling pseudo crystalline nets in this work. The possible assembly through artificial interactions originating from the his-tag were removed through a thrombin cleavage (Fig. 6.11), leaving the native CotE protein sequence. Net-like arrays were clearly visible after cleavage indicating the his-tag had no effect on assembly.

CotE was however shown to be more fragile than its spore coat counterpart CotY. CotE nets were not stable in urea with the majority of nets disassembling into fibrous aggregates (Fig. 6.12). Treatments with 50 mM DTT and heating to 95 °C alone yielded similar results with a loss in net-like arrays and the formation of fibrous aggregates (Fig. 6.13). Furthermore, a large amount of CotE, running on SDS-PAGE denaturing gels as a monomer under standard conditions without denaturants, could be obtained from both the soluble and insoluble fractions during batch purification (Fig. 6.9). CotE is not cysteine-rich, unlike CotY, showing that the disulphide bonds involved in intermolecular interactions, and also intra-subunit folding play a key role in stability and resistance of the CotY complex.

CotE has a known role in the formation of the outer coat, positioning itself between the inner and outer coat interface (Driks *et al.*, 1994, Zheng *et al.*, 1988), and mediates the assembly of other coat proteins such as CotX, CotZ and CotW (Kim *et al.*, 2006) (Fig. 1.4). The flexible net structure could provide an interface for subsequent coat proteins to assemble onto, acting as a two-dimensional molecular scaffold for the ultimate formation of a shell-like native spore coat (Driks, 1999). Furthermore the large mesh structure formed by the CotE net would permit the passage of inner coat proteins (Driks, 1999) that closed packed structures, such as the CotY assembly, would not.

### 6.3.3 CotZ

#### 6.3.3.1 Purification and assembly of CotZ

CotZ has been shown to form large macro-assemblies within the *E. coli* cytoplasm. *B. subtilis* CotZ shares ~46 % identity with *B. subtilis* CotY and ~34 % identity with *B. cereus* ExsY along with a conservation of key cysteine residues. CotY and ExsY proved difficult to solubilise due to the cooperative disulphide bonding present within the macro-assembled structure. This is likely the same case for CotZ explaining the lack of visible protein found in the insoluble fraction from batch purification.

The large CotZ assemblies seen in Figures 6.15 and 6.16 again show the unique ability for spore coat proteins to self-assemble. The assembly that CotZ forms however does not appear to be crystalline like that of the CotY and ExsY orthologues. It was speculated that the natural crystallinity of proteins such as CotY and ExsY promoted the formation of cooperative disulphide bonds, however as seen with CotZ assemblies, the lack of crystallinity does not appear to hinder the formation of large assemblies (Fig. 6.15). Cross-sections through *E. coli* cells expressing CotZ showed the formation of a multi-layered lattice that appears to show some signs of crystalline nature (Fig. 6.16). It is also possible that CotZ indeed forms crystalline arrays within the *E. coli* cell that becomes disordered under our extraction mechanisms.

CotZ is known to localise to the spore crust and only correctly assembles in the presence of CotY (Imamura *et al.*, 2011). Furthermore, the phenotype of spores lacking *cotXYZ* appears similar to those only lacking *cotXY* indicating that CotZ may not function correctly without CotX and CotY (Driks, 1999). Imamura *et al* proposed that CotZ is required for the spore crust to assemble around the spore (Imamura *et al.*, 2011), which could explain the role of our two-dimensional self-assembled CotZ sheets.

It was seen by phase contrast and fluorescence microscopy that crust like material was formed in *cotZ* mutants spores, but failed to assemble around the spore. Furthermore, the dependency of CotZ on CotY may provide a mechanism for limiting the uncontrolled expansion of CotY arrays, seen in *E. coli* in this chapter, allowing for correct encasing of the endospore by the spore coat.

## **Chapter 7. Analysis of germinating *B. cereus* spores by transmission electron microscopy**

### **7.1 Introduction**

The assembly of the exosporium during sporulation begins at the pole of the spore facing the mother cell centre, forming a region in the exosporium known structurally as the cap (Gerhardt and Ribi, 1964, Steichen *et al.*, 2007, Thompson *et al.*, 2012, Thompson and Stewart, 2008). During outgrowth, the cap structure appears to rupture, as observed by low-resolution immunofluorescence (Steichen *et al.*, 2007), and releases the outgrowing cell into the environment. Details of release through the cap region remain relatively unknown at higher resolution. In this chapter, germinating spores were examined using TEM for the detection of a “cap” region through which the germinating cell protrudes, and to see if this structure possesses any special features.

## 7.2 Results

### 7.2.1 Germination of *B. cereus* spores in non-outgrowing conditions

*B. cereus* spores grown using the method stated in 2.3.1 were resuspended into 20 ml of 10 mM Tris-HCl, 10 mM NaCl pH 8.0 buffer to an OD<sub>580</sub> of 10 and germinants, inosine and alanine, were added to concentrations of 5 mM and 50 mM respectively. 20  $\mu$ l of the suspension was removed before and directly after the addition of germinants. The sample was incubated at ~20 °C and a suspension was removed 1, 5 and 10 min after germinant addition.

#### 7.2.1.1 TEM analysis of non-outgrowing spores

A suspension of germinating spores from 7.2.1 was negatively stained and analysed by TEM. An initial image of spores suspended in buffer was taken as a control showing the buffer alone did not induce germination and that the spores had not germinated before germinant addition. Spores in buffer appeared to show an electron dense core with a loose balloon-like exosporium (Fig. 7.1 A). After addition of germinants, the spore did not visible change immediately (Fig. 7.1 B) or after 1 min (Fig. 7.1 C). After 5 min, a large number of spore cores can be seen to become more penetrable by electrons (Fig. 7.1 D) presumably indicating rehydration. After 10 min, all spore cores appear hydrated (Fig. 7.1 E). It was not possible to follow a single spore using this approach, but spores present in each sample appeared to be reflective of the general state of the population.

### 7.2.2 Germination and outgrowth of *B. cereus* spores in BHI

*B. cereus* spores grown using the method described in 2.3.1 were resuspended in 20 ml of BHI broth containing 10 mM Tris-HCl, 10 mM NaCl pH 8.0 and 5 mM inosine to an OD<sub>580</sub> of 10. The sample was incubated at ~20 °C and 20  $\mu$ l of suspension was removed directly after spores were added to the BHI broth and subsequently at 10, 60, 120, 180, 240 and 300 min after addition.

#### 7.2.2.1 TEM analysis of outgrowing spores

Germinating spores from 7.2.2 were negatively stained and analysed by TEM. Upon the initial addition to spores into BHI broth supplemented with 5 mM inosine, each spore appeared with an electron dense core and exosporium (Fig. 7.2 A). After 10 min, slight hydration of the core could be seen occurring by the core becoming less electron-dense (Fig. 7.2 B). After 60 min, the spore core appeared completely penetrable by electrons (Fig. 7.2 C) and had swelled. After 120 min, the outgrowing spore appeared

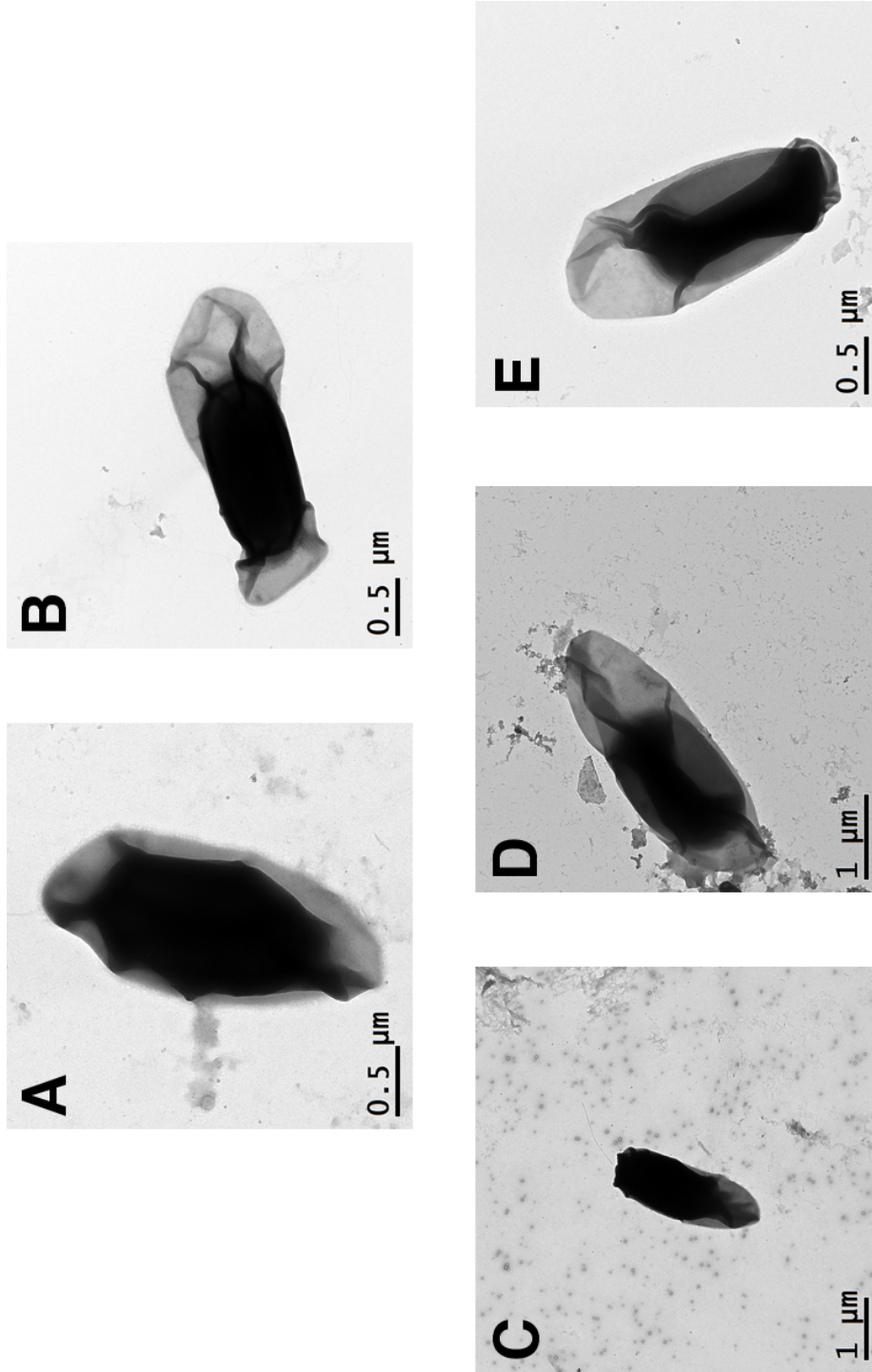


**Figure 7.1 Electron micrograph of *B. cereus* spores germinating in non-outgrowing conditions.** Endospore (A) in buffer before addition of germinant, (B) directly after addition of germinant, (C) after 1 minute, (D) after 5 minutes and (E) after 10 minutes.

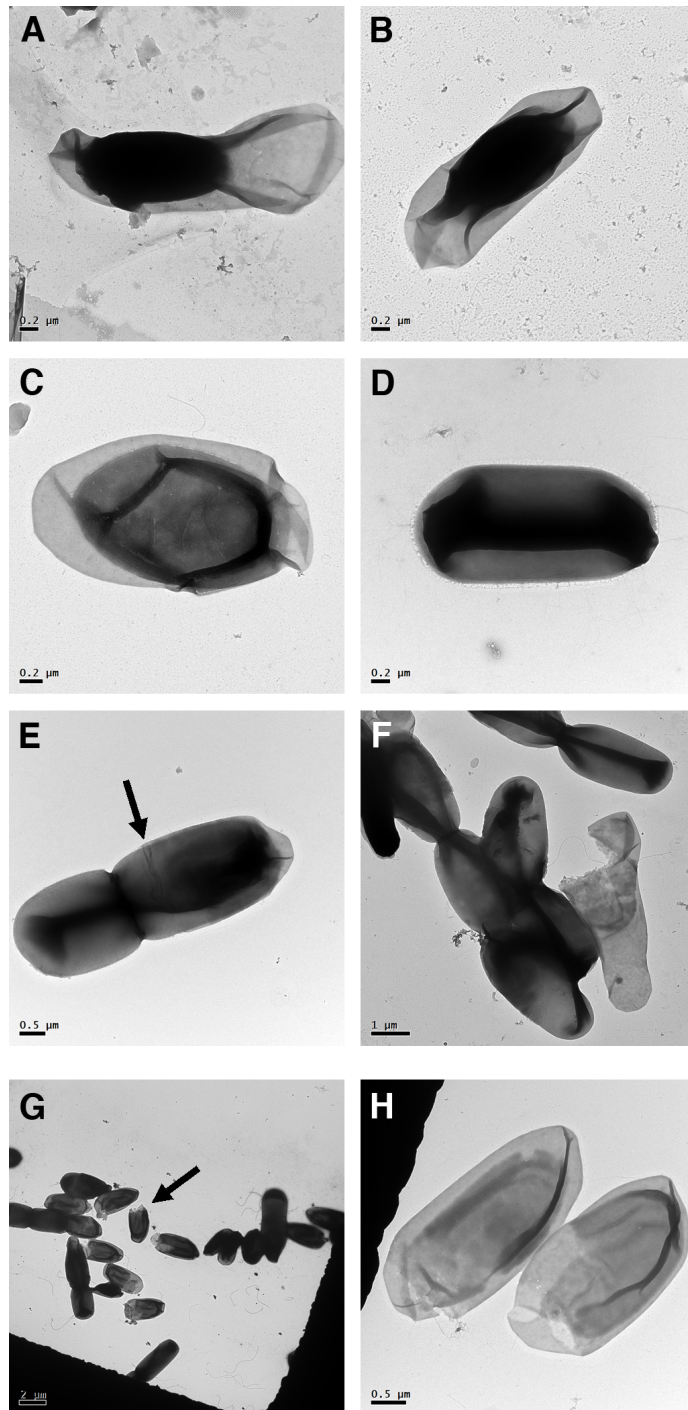


**Figure 7.2 Electron micrograph of *B. cereus* spores germinating in outgrowing conditions.** Endospore (A) in buffer immediately after addition of germinant, (B) after 10 min, (C) after 60 min, (D) after 120 min, (E) after 180 min, (F) empty shells of exosporium and coat material after 240 min and (G & H) after 300 min. Arrow “(E)” indicates the boundary between the “popped” exosporium and outgrowing cell. Arrow in “(G)” indicates an empty exosporium.

to have filled the exosporium sac, but is still contained within. A hairy-nap is still visible surrounding the spore. The core appears to be penetrable by electrons and the outgrowing cell was elongated (Fig. 7.2 D). At 180 min, cells can be seen dividing and popping out, from one end, of their once encasing exosporium (Fig. 7.2 E). After 240 min, spores appeared to have fully outgrown into vegetative cells, leaving behind their exosporium along with what appears to be a coat layer within (Fig. 7.2 F). The same exosporium sacks are visible at 300 min along with dividing cells (Fig. 7.2 G and H). Empty exosporium sacks appear with openings at one end, originating from where the outgrowing cell emerged, and an overhanging cap (Fig. 7.2 F and H).

## 7.3 Discussion

### 7.3.1 Germination through a polar cap

TEM analysis of germinating spores under outgrowing conditions does indeed show the exit of a vegetative cell through a polar region in the exosporium (Fig. 7.2 E), leaving behind an empty exosporium sack with a rupture at one end (Fig. 7.2 H). This confirms the results of germination through a cap region in the exosporium “bottle-cap” model, reported by Steichen *et al.*, (2007) using immunofluorescence microscopy. The TEM analysis of spores during germination show an increase in the size of the spore core during hydration and it appears to be a physical “popping” of the cap region as the cell expands. This evidence suggests that mechanical force drives the escape of the outgrowing cell from the exosporium with the cap providing a region of “easy” escape. The cap region is known to contain CotY, ExsFB and BxpB (ExsFA) (Thompson *et al.*, 2012). Structural comparison between ExsY, the major protein responsible for the exosporium, and CotY showed the latter formed *in vivo* crystals that were much less ordered (Chapter 5.2.3). This increased disorder in CotY formations may provide the mechanical instability necessary to function as a weak spot for the “popping” out of the cap.

The work carried out here is preliminary with many avenues to explore. Ideally, we would like to monitor a single spore continuously during germination. This is not possible with negative stain TEM but may be possible with video AFM.

## Chapter 8. General discussions and future investigations

Endospores of *Bacilli*, and also *Clostridia*, form fascinating differentiated coat and exosporium structures whose roles are derived from their unique architecture. Understanding the assembly of these diverse supramolecular structures is of great importance towards appreciating how spores can persist as stable entities for long periods of time. With such information, new strategies may be developed for decontamination. It may also extend the possible use of spores as surface display platforms.

The investigation outlined by this thesis relates to the basic components of the two-dimensional exosporium and three-dimensional spore coat. The exosporium template protein was identified and showed a novel mechanism of self-assembly in *E. coli*, which most likely reflects the same mechanism of basal layer formation in the native spore. The self-assembled minimal structure was further confirmed through a top-down mutational study of exosporium lacking particular components such as the hairy nap and its corresponding anchor. We attempted a bottom-up approach in reassembling the exosporium from its component parts in *E. coli* although to no avail. It was however informative towards understanding the behaviour of other exosporium proteins, such as ExsFA, and reminded us that assembly of the exosporium still requires a higher order of complexity. Finally, the trend of self-assembly was further identified in several proteins constituting the spore coat. Much like the case of assembly in the exosporium, uncontrolled growth of spore coat components in *E. coli* indicated that multiple factors are necessary in the assembly of a native spore, of which our knowledge is only just scratching the surface.

### 8.1 Demolition of the exosporium

The deletion of key proteins found in the ExsY, ExsFA, BclA high molecular weight complex of the exosporium (Redmond *et al.*, 2004, Steichen *et al.*, 2005) revealed the loss of particular topological features. Most strikingly, inactivation of the *bclA* gene resulted in a mixed population of spores which either possessed a morphologically different nap or were completely devoid of the nap altogether (Fig. 3.3). We concluded that the lack of BclA resulted in the nap-less population whilst presence of other glycoproteins, such as ExsJ (Fig. 3.16) (Todd *et al.*, 2003), accounted for the

morphologically different nap-presenting population. Future investigations may include constructing a *B. cereus*  $\Delta bclA\Delta exsJ$  double mutant to see if all spores of such a mutant are devoid of the hairy nap, to confirm the expectation that ExsJ is the major residual nap protein.

Purification of the exosporium from *B. cereus*  $\Delta bclA$  spores revealed two different crystal forms arising from the nap-presenting and nap-less populations (Fig. 3.7 and 3.8). Both crystal forms displayed identical unit cells suggestive of a common template protein, however as their structures were visibly different, they were designated as Form “A” and “B”.

Form A crystals displayed a nap and showed a similar structure to wild type exosporium (Fig. 3.17 B). The simplest explanation for this crystal form would be that ExsFA has not been dissociated from the exosporium and has a different nap protein, most likely to be ExsJ, on its surface.

In contrast, the Form B crystal lacked any nap and any density corresponding to the linkers at the three-fold symmetrical axis of the model (Fig. 3.17 C). I speculate that the change in structure is a result of destabilisation of ExsFA due to the absence of BclA (a destabilisation is shown by SDS-PAGE in Fig. 3.16). It is known ExsFA and BclA are co-dependent for localisation (Thompson *et al.*, 2011b); hence it is not surprising that the loss of BclA prevents correct attachment of its respective ExsFA anchor resulting in the Form B crystal. A “wild strain” of *B. thuringiensis* 4D11 within the *B. cereus* group, which was also devoid of a hairy nap, showed an almost identical structure and unit cell to the Form B crystal (Figs. 3.5 and 3.15). The genomic sequence of the *B. thuringiensis* 4D11 strain is not known but their exosporium structure possessed near identical unit cell and structure (Fig. 3.17 C and D). I suspect there is a high degree of similarity between the exosporium template protein found in *B. cereus* ATCC 10876 and *B. thuringiensis* 4D11. More importantly, *B. thuringiensis* 4D11 did confirm that the density found at the three-fold linker is somewhat dependent on the presence of a hairy nap (Fig. 3.17 D). Previous anti-ExsFA Western blots, carried out by Dr. C. Terry, also showed that ExsFA was detected but not abundant in *B. thuringiensis* 4D11 (Terry, 2010).

The exosporium of a *B. cereus*  $\Delta exsFA$  mutant was also inspected which showed a mixed population of nap-less and nap-presenting spores (Fig. 3.4). The structure of the

exosporium purified from these spores however, all displayed a similar structure to that of the *B. cereus* wild type exosporium. The ExsFA homologue ExsFB, is most likely responsible for the redundancy in structure, but more proteomic analysis is necessary to confirm this. Sylvestre *et al.*, (2005) reported the presence of a hairy nap on *B. anthracis*  $\Delta$ exsFA mutant endospores consistent with our observations. More work is necessary to demonstrate whether ExsFA resides at the loci of the three-fold linker, possibly by using a *B. cereus*  $\Delta$ exsFA $\Delta$ exsFB double mutant to remove any effects from redundant proteins.

## 8.2 Building the exosporium

Serendipity showed us that overexpression of ExsY, one of the proteins found within a high molecular weight exosporium complex, in *E. coli* resulted in the formation of large two-dimensional crystalline arrays (Fig. 4.7 and 4.8) with the same unit cell parameters as that of native exosporium (Fig. 4.10). The structure derived from these crystals appeared as a hexameric ring, which when compared to the native *B. thuringiensis* 4D11 exosporium structure (Fig. 4.16) showed an almost perfect resemblance. This informed us that the exosporium template is in fact composed of a single protein upon which other exosporium proteins can assemble.

Comparison of the ExsY template structure with the *B. cereus* native exosporium revealed two major features that were missing: the base of the cup structure and the three-fold symmetrical linker (Fig. 4.17). We have speculated that BclA and ExsFA are unlikely to reside at the bottom of the cup due to the lack of electron density visible in this region that could correlate to these proteins. Kailas *et al.*, (2011) proposed that the stain-excluding linker was the location of ExsFA and the docking site for BclA. BclA is a trimeric protein that is known to be composed of a trimeric C-terminal domain along with a collagen triple helix (Boydston *et al.*, 2005, Rety *et al.*, 2005) and a short N-terminal domain. One may therefore assume that ideally, it docks into a trimeric domain on the exosporium such as the linker lying at the three-fold symmetry axis. ExsFA was shown by SDS-PAGE to migrate as a ~58 kDa species that would correspond to a trimer (Fig. 5.3). The particles visible by TEM also showed a faint outline of a protein assembly that a molecule smaller than 50 kDa would not exhibit (Fig. 5.4). Furthermore, preliminary X-ray diffraction data suggested a non-crystallographic three-fold symmetry axis was present (Chapter 5.2.2.5). It would have been ideal to confirm this using a calibrated gel filtration column. Nonetheless, the data here suggests that ExsFA is indeed trimeric, fitting with the previous assumptions that it is: (i) most likely the anchor

for the trimeric BclA protein and (ii) the protein which resides in the three-fold symmetrical region of the crown.

A proposed model of exosporium assembly is shown in Figure 8.1. In an attempt to reconstitute the exosporium *in vivo* inside an *E. coli* cell, no assemblies aside from the ExsY template was formed (Chapter 5). The possible reasons for a lack of assembly were discussed in Chapter 5.3.3 but overall the minimalist approach we took overlooked the vast number of other exosporium and chaperone proteins present in the exosporium. It may be of interest in future to express the ExsY, BclA and ExsFA complex in *B. subtilis* during sporulation to see if an artificial exosporium could be generated in a strain closer to the native host. It could be the case however, that we are missing one key protein that holds the whole complex together.

### 8.3 An extension on the exosporium

Amongst the other exosporium proteins examined, CotY from *B. cereus* was of particular interest. CotY (Chapter 5) and ExsY (Chapter 4) are homologues that show ~90 % amino acid sequence identity and are both known components of the exosporium. ExsY appears to be responsible for the bulk of the exosporium template structure (Johnson *et al.*, 2006), whilst CotY has been shown to be part of the exosporium cap (Steichen *et al.*, 2007, Thompson *et al.*, 2012). Similar to ExsY, CotY possesses the ability to self-assemble in the cytoplasm of the *E. coli* cell into a crystalline array (Fig. 5.7). Furthermore, crystals of CotY possessed a near identical unit cell and hexameric ring structure to that of ExsY (Fig. 5.9). The similarities between the two proteins could allow heterogeneous interactions much like the ones necessary at the exosporium and cap interface. More strikingly, CotY maintained the ability to assemble into large arrays, but appeared to be less well ordered with patches of crystallinity (Fig. 5.7). The CotY cap structure is known to be (i) the first structure assembled during exosporium formation and (ii) the point at which germinating cells escape from. The patchy crystallinity of CotY would contribute to both these properties.

No mechanism is yet known for how the exosporium limits its size, however CotY may play a role as an exosporium cap. The seeding of a region that is composed of a template protein that does not preferentially aggregate into a large sheet, i.e. CotY, limits the expansion of the exosporium from this position and hence creates a structural “bottle cap”. Furthermore, a region of instability created by the CotY protein cap allows for newly germinating cells to “pop” from a less resistant area of the exosporium (Fig.

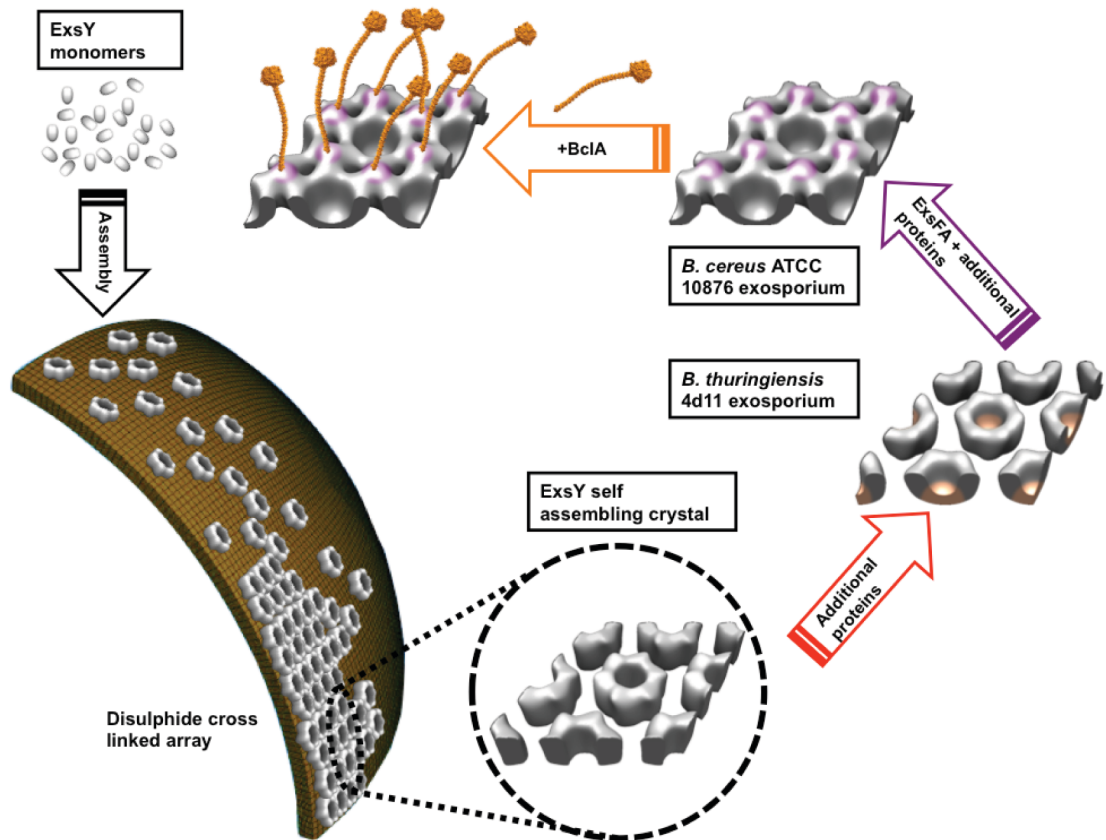


**Figure 8.1 Predicted overview of exosporium assembly in *B. cereus*.** The initial step in exosporium formation requires the self-assembly of ExsY monomers (top left) into a disulphide cross-linked array. Accessory proteins, which are yet to be identified, form the base of the cup in the basal layer. Finally incorporation of ExsFA, BclA and other addition proteins complete the structure seen from purified exosporium.

7.2). It would be interesting in future to see if Duet expression of both ExsY and CotY together results in formation of complete exosporium balloons in *E. coli*.

## 8.4 Foundations of assembly

It has been shown in this thesis that *B. cereus* ExsY (Chapter 4) and CotY (Chapter 5), as well as *B. subtilis* CotY (Chapter 6), naturally self-assemble into crystalline arrays when overexpressed in *E. coli*. In the case of *B. cereus* ExsY (Fig. 4.7) and CotY (Fig. 5.7), two-dimensional crystals are formed; whilst *B. subtilis* CotY forms three-dimensional crystals (Figs. 6.4 and 6.6). The crystalline formations of *B. cereus* ExsY and *B. subtilis* CotY showed remarkable resistance against 8 M urea, heating at 99 °C or DTT treatment; a combination of heat and DTT was necessary for disassembly (Figs 4.13 and 6.8). Although *B. cereus* CotY was not tested in these conditions, one would hypothesise that the same properties may be seen in a protein that shows 90 % sequence identify with ExsY. The common feature amongst ExsY and the two different CotY proteins is their high cysteine content that which points towards a highly likelihood of disulphide bonding. The presence of disulphide bonds has previous been noted in the spore coat (Gould *et al.*, 1970, Hitchins *et al.*, 1966, Zhang *et al.*, 1993) and suggested in the exosporium (Steichen *et al.*, 2005, Terry, 2010).

The persistence of *B. cereus* ExsY and *B. subtilis* CotY crystalline assemblies after heating for 20 min at 99 °C indicate that covalent cross-links may stabilise the assembly, similar to cysteine-rich thermophilic proteins found in Archaea that can withstand temperatures greater than 100 °C (Mallick *et al.*, 2002, Toth *et al.*, 2000). Interestingly, treatment with the reducing agent DTT appeared to have no effect on the stability of the crystal (Fig. 4.14 A and B; Fig. 6.8), indicating that the disulphide covalent cross-links are buried within the structure and are inaccessible. A combination of both heating and DTT treatment was necessary to destabilise the crystal lattice (Figs. 4.15 and 6.8); heating may be necessary to expose the bonds for reducing agents to act upon.

It is unusual for disulphide bond formation to occur in the reducing environment of the *E. coli* cytoplasm, but there may be several explanations for this phenomenon. Firstly, the crystalline assemblies may form through cooperative disulphide bonds mediated by the natural crystallinity of the molecule. The highly ordered and symmetrical structure formed by ExsY and CotY promotes a process in which molecules are positioned precisely within a growing lattice. The effect of such ordered packing would mediate the

positioning of specific cysteine residues during folding of the molecule and lead to disulphide bond formation in a cooperative manner. Such effects have previously been noted during the folding of the apamin protein (Chau and Nelson, 1992). Secondly, although the cytoplasm is normally reducing, we cannot discount the effect protein overexpression has on intracellular conditions. Cells under induced overexpression already appear “unhealthy” in morphology, which might also be the case for their intracellular conditions. This may therefore influence the redox potential within a cell, leading to a more oxidising environment that allows disulphide bonds to form.

## **8.5 Future developments**

### **8.5.1 High-resolution analysis**

Kailas *et al.*, (2011) presented a high-resolution cryo-EM projection map of the *B. cereus* exosporium, however no three-dimensional structure has yet been solved. With the current advances in cryo-EM, it would be of great interest to reconstruct a three-dimensional structure of the exosporium to atomic resolution. A high-resolution comparison can then also be made between the ExsY self-assembled crystal and that of native *B. cereus* exosporium. We could confirm, from a structural point of view, whether the structure of the natural exosporium and the self-assembled crystal are indeed homologous. The same structural analysis could be applied to the various exosporium mutants and self-assembled crystals and allow us to isolate the specific contributions of each exosporium protein. High-resolution analysis of both the exosporium and ExsY crystals would also reveal the sites of disulphide bond formation between each monomeric unit and strengthen our proposed cooperative disulphide bonding argument.

### **8.5.2 Other exosporium proteins**

ExsFA has been shown to form protein crystals, but further optimizations are necessary for the growth of crystals that are better ordered. It will also be necessary to phase these crystals, which may be achieved through soaking in iodine, bromine or heavy metals. However, it may also be necessary to introduce methionine residues for selenomethionine substitutions. Solving the structure of ExsFA would provide a great deal of information on how the anchor protein interacts with both the hairy nap and exosporium.

### **8.5.3 Exosporium reconstruction**

Inroads have been made towards reconstructing the exosporium from its component parts in this thesis, however parts of the system are still missing. If reassembly of the

exosporium is possible in an *E. coli* host, this could open the doors to a wealth of biotechnological applications with the use of the exosporium as a surface display interface. Although ExsY could already be used as a biological display interface, the exosporium possesses a much more unusual property. The exosporium is able to maintain functional proteins, such as alanine racemase, for hundreds of years. Understanding how this is achieved would create an interface for displaying proteins that could be resistant to external perturbations and ultimately function for an indefinite period of time.

## References

- Abhyankar, W., Beek, A. T., Dekker, H., Kort, R., Brul, S. & De Koster, C. G. 2011. Gel-free proteomic identification of the *Bacillus subtilis* insoluble spore coat protein fraction. *Proteomics*, 11, 4541-50.
- Anderson, I., Sorokin, A., Kapatral, V., Reznik, G., Bhattacharya, A., Mikhailova, N., Burd, H., Joukov, V., Kaznadzey, D., Walunas, T., Markd'souza, Larsen, N., Pusch, G., Liolios, K., Grechkin, Y., Lapidus, A., Goltsman, E., Chu, L., Fonstein, M., Ehrlich, S. D., Overbeek, R., Kyrpides, N. & Ivanova, N. 2005. Comparative genome analysis of *Bacillus cereus* group genomes with *Bacillus subtilis*. *FEMS Microbiol Lett*, 250, 175-84.
- Aronson, A. I. 2012. The structure and composition of the outer layers of the bacterial spore. *Bacterial Spores: current research and applications*, 57-71.
- Aronson, A. I., Beckman, W. & Dunn, P. 1986. *Bacillus thuringiensis* and related insect pathogens. *Microbiol Rev*, 50, 1-24.
- Aronson, A. I., Ekanayake, L. & Fitz-James, P. C. 1992. Protein filaments may initiate the assembly of the *Bacillus subtilis* spore coat. *Biochimie*, 74, 661-7.
- Aronson, A. I. & Fitz-James, P. 1976. Structure and morphogenesis of the bacterial spore coat. *Bacteriol Rev*, 40, 360-402.
- Aronson, A. I. & Fitz-James, P. C. 1971. Reconstitution of bacterial spore coat layers *in vitro*. *J Bacteriol*, 108, 571-8.
- Ash, C., Farrow, J. A., Dorsch, M., Stackebrandt, E. & Collins, M. D. 1991. Comparative analysis of *Bacillus anthracis*, *Bacillus cereus*, and related species on the basis of reverse transcriptase sequencing of 16S rRNA. *Int J Syst Bacteriol*, 41, 343-6.
- Atrih, A. & Foster, S. J. 1999. The role of peptidoglycan structure and structural dynamics during endospore dormancy and germination. *Antonie Van Leeuwenhoek*, 75, 299-307.
- Bai, X. C., McMullan, G. & Scheres, S. H. 2015. How cryo-EM is revolutionizing structural biology. *Trends Biochem Sci*, 40, 49-57.
- Bailey-Smith, K., Todd, S. J., Southworth, T. W., Proctor, J. & Moir, A. 2005. The ExsA protein of *Bacillus cereus* is required for assembly of coat and exosporium onto the spore surface. *J Bacteriol*, 187, 3800-6.
- Baillie, L., Hibbs, S., Tsai, P., Cao, G. L. & Rosen, G. M. 2005. Role of superoxide in the germination of *Bacillus anthracis* endospores. *FEMS Microbiol Lett*, 245, 33-8.
- Baillie, L. & Read, T. D. 2001. *Bacillus anthracis*, a bug with attitude! *Curr Opin Microbiol*, 4, 78-81.
- Ball, D. A. 2006. *3D Structure and Mutational Studies on the Exosporium of the Bacillus cereus Family*. University of Sheffield, U.K.
- Ball, D. A., Taylor, R., Todd, S. J., Redmond, C., Couture-Tosi, E., Sylvestre, P., Moir, A. & Bullough, P. A. 2008. Structure of the exosporium and sublayers of spores of the *Bacillus cereus* family revealed by electron crystallography. *Mol Microbiol*, 68, 947-58.
- Barlass, P. J., Houston, C. W., Clements, M. O. & Moir, A. 2002. Germination of *Bacillus cereus* spores in response to L-alanine and to inosine: the roles of gerL and gerQ operons. *Microbiology*, 148, 2089-95.
- Barra-Carrasco, J., Olguin-Araneda, V., Plaza-Garrido, A., Miranda-Cardenas, C., Cofre-Araneda, G., Pizarro-Guajardo, M., Sarker, M. R. & Paredes-Sabja, D. 2013. The *Clostridium difficile* exosporium cysteine (CdeC)-rich protein is required for exosporium morphogenesis and coat assembly. *J Bacteriol*, 195, 3863-75.
- Basu, S., Kang, T. J., Chen, W. H., Fenton, M. J., Baillie, L., Hibbs, S. & Cross, A. S. 2007. Role of *Bacillus anthracis* spore structures in macrophage cytokine responses. *Infect Immun*, 75, 2351-8.
- Bauer, T., Little, S., Stover, A. G. & Driks, A. 1999. Functional regions of the *Bacillus subtilis* spore coat morphogenetic protein CotE. *J Bacteriol*, 181, 7043-51.
- Beaman, T. C., Pankratz, H. S. & Gerhardt, P. 1972. Ultrastructure of the exosporium and underlying inclusions in spores of *Bacillus megaterium* strains. *J Bacteriol*, 109, 1198-209.
- Bechtel, D. B. & Bulla, L. A., Jr. 1976. Electron microscope study of sporulation and parasporal crystal formation in *Bacillus thuringiensis*. *J Bacteriol*, 127, 1472-81.
- Beecher, D. J. & Wong, A. C. 1997. Tripartite hemolysin BL from *Bacillus cereus*. Hemolytic analysis of component interactions and a model for its characteristic paradoxical zone phenomenon. *J Biol Chem*, 272, 233-9.
- Blankenship, B. G., Heffron, J. D. & Popham, D. L. 2015. Lytic enzyme-assisted germination of *Bacillus anthracis* and *Bacillus subtilis* spores. *J Appl Microbiol*. doi: 10.1111/jam.12839.

- Bloomfield, S. F. & Megid, R. 1994. Interaction of iodine with *Bacillus subtilis* spores and spore forms. *J Appl Bacteriol*, 76, 492-9.
- Boydston, J. A., Chen, P., Steichen, C. T. & Turnbough, C. L., Jr. 2005. Orientation within the exosporium and structural stability of the collagen-like glycoprotein BclA of *Bacillus anthracis*. *J Bacteriol*, 187, 5310-7.
- Boydston, J. A., Yue, L., Kearney, J. F. & Turnbough, C. L., Jr. 2006. The ExsY protein is required for complete formation of the exosporium of *Bacillus anthracis*. *J Bacteriol*, 188, 7440-8.
- Bozue, J., Cote, C. K., Moody, K. L. & Welkos, S. L. 2007. Fully virulent *Bacillus anthracis* does not require the immunodominant protein BclA for pathogenesis. *Infect Immun*, 75, 508-11.
- Bradley, K. A., Mogridge, J., Mourez, M., Collier, R. J. & Young, J. A. T. 2001. Identification of the cellular receptor for anthrax toxin. *Nature*, 414, 225-229.
- Bravo, A., Gill, S. S. & Soberon, M. 2007. Mode of action of *Bacillus thuringiensis* Cry and Cyt toxins and their potential for insect control. *Toxicon*, 49, 423-435.
- Bravo, A., Likitvivanavong, S., Gill, S. S. & Soberon, M. 2011. *Bacillus thuringiensis*: A story of a successful bioinsecticide. *Insect Biochem Mol Biol*, 41, 423-31.
- Bukowska-Faniband, E. & Hederstedt, L. 2013. Cortex synthesis during *Bacillus subtilis* sporulation depends on the transpeptidase activity of SpoVD. *FEMS Microbiol Lett*, 346, 65-72.
- Burbulys, D., Trach, K. A. & Hoch, J. A. 1991. Initiation of sporulation in *B. subtilis* is controlled by a multicomponent phosphorelay. *Cell*, 64, 545-52.
- Castanha, E. R., Swiger, R. R., Senior, B., Fox, A., Waller, L. N. & Fox, K. F. 2006. Strain discrimination among *B. anthracis* and related organisms by characterization of bclA polymorphisms using PCR coupled with agarose gel or microchannel fluidics electrophoresis. *J Microbiol Methods*, 64, 27-45.
- Challacombe, J. F., Altherr, M. R., Xie, G., Bhotika, S. S., Brown, N., Bruce, D., Campbell, C. S., Campbell, M. L., Chen, J., Chertkov, O., Cleland, C., Dimitrijevic, M., Doggett, N. A., Fawcett, J. J., Glavina, T., Goodwin, L. A., Green, L. D., Han, C. S., Hill, K. K., Hitchcock, P., Jackson, P. J., Keim, P., Kewalramani, A. R., Longmire, J., Lucas, S., Malfatti, S., Martinez, D., Mcmurry, K., Meincke, L. J., Misra, M., Moseman, B. L., Mundt, M., Munk, A. C., Okinaka, R. T., Parson-Quintana, B., Reilly, L. P., Richardson, P., Robinson, D. L., Saunders, E., Tapia, R., Tesmer, J. G., Thayer, N., Thompson, L. S., Tice, H., Ticknor, L. O., Wills, P. L., Gilna, P. & Brettin, T. S. 2007. The complete genome sequence of *Bacillus thuringiensis* AI Hakam. *J Bacteriol*, 189, 3680-1.
- Charlton, S., Moir, A. J., Baillie, L. & Moir, A. 1999. Characterization of the exosporium of *Bacillus cereus*. *J Appl Microbiol*, 87, 241-5.
- Chau, M. H. & Nelson, J. W. 1992. Cooperative disulfide bond formation in apamin. *Biochemistry*, 31, 4445-50.
- Cheng, Y. 2015. Single-particle cryo-EM at crystallographic resolution. *Cell*, 161, 450-457.
- Chesnokova, O. N., Mcpherson, S. A., Steichen, C. T. & Turnbough, C. L., Jr. 2009. The spore-specific alanine racemase of *Bacillus anthracis* and its role in suppressing germination during spore development. *J Bacteriol*, 191, 1303-10.
- Chung, C. T., Niemela, S. L. & Miller, R. H. 1989. One-step preparation of competent *Escherichia coli*: transformation and storage of bacterial cells in the same solution. *Proc Natl Acad Sci U S A*, 86, 2172-5.
- Connors, M. J., Mason, J. M. & Setlow, P. 1986. Cloning and nucleotide sequencing of genes for three small, acid-soluble proteins from *Bacillus subtilis* spores. *J Bacteriol*, 166, 417-25.
- Cowan, A. E., Koppel, D. E., Setlow, B. & Setlow, P. 2003. A soluble protein is immobile in dormant spores of *Bacillus subtilis* but is mobile in germinated spores: implications for spore dormancy. *Proc Natl Acad Sci U S A*, 100, 4209-14.
- Cowan, A. E., Olivastro, E. M., Koppel, D. E., Loshon, C. A., Setlow, B. & Setlow, P. 2004. Lipids in the inner membrane of dormant spores of *Bacillus* species are largely immobile. *Proc Natl Acad Sci U S A*, 101, 7733-8.
- Crowther, R. A., Henderson, R. & Smith, J. M. 1996. MRC image processing programs. *J Struct Biol*, 116, 9-16.
- Culpepper, M. A., Scott, E. E. & Limburg, J. 2010. Crystal structure of prolyl 4-hydroxylase from *Bacillus anthracis*. *Biochemistry*, 49, 124-33.
- Cybulski, R. J., Jr., Sanz, P., Mcdaniel, D., Darnell, S., Bull, R. L. & O'brien, A. D. 2008. Recombinant *Bacillus anthracis* spore proteins enhance protection of mice primed with suboptimal amounts of protective antigen. *Vaccine*, 26, 4927-39.

- Dambach, P., Louis, V. R., Kaiser, A., Ouedraogo, S., Sie, A., Sauerborn, R. & Becker, N. 2014. Efficacy of *Bacillus thuringiensis* var. israelensis against malaria mosquitoes in northwestern Burkina Faso. *Parasit Vectors*, 7, 371.
- Daubenspeck, J. M., Zeng, H., Chen, P., Dong, S., Steichen, C. T., Krishna, N. R., Pritchard, D. G. & Turnbough, C. L., Jr. 2004. Novel oligosaccharide side chains of the collagen-like region of BclA, the major glycoprotein of the *Bacillus anthracis* exosporium. *J Biol Chem*, 279, 30945-53.
- Dawes, I. W., Kay, D. & Mandelstam, J. 1969. Sporulation in *Bacillus subtilis*. Establishment of a time scale for the morphological events. *J Gen Microbiol*, 56, 171-9.
- Desrosier, J. P. & Lara, J. C. 1984. Synthesis of the exosporium during sporulation of *Bacillus cereus*. *Journal of General Microbiology*, 130, 935-940.
- Donovan, W. L., Zheng, B., Sabdman, K., & Losick, R. 1987. Genes encoding spore coat polypeptides from *Bacillus subtilis*. *J Mol Biol*, 196, 1-10.
- Driks, A. 1999. *Bacillus subtilis* spore coat. *Microbiology and Molecular Biology Reviews*, 63, 1-20.
- Driks, A. 2004. The *Bacillus* spore coat. *Phytopathology*, 94, 1249-51.
- Driks, A., Roels, S., Beall, B., Moran, C. P., Jr. & Losick, R. 1994. Subcellular localization of proteins involved in the assembly of the spore coat of *Bacillus subtilis*. *Genes Dev*, 8, 234-44.
- Drobniowski, F. A. 1993. *Bacillus cereus* and related species. *Clinical Microbiology Reviews*, 6, 324-338.
- Dubochet, J., Lepault, J., Freeman, R., Berriman, J. A. & Homo, J. C. 1982. Electron-microscopy of frozen water and aqueous-solutions. *Journal of Microscopy-Oxford*, 128, 219-237.
- Ebersold, H. R., Luthy, P., Cordier, J. L. & Muller, M. 1981. A freeze-substitution and freeze-fracture study of bacterial spore structures. *J Ultrastruct Res*, 76, 71-81.
- Ehling-Schulz, M., Fricker, M. & Scherer, S. 2004. *Bacillus cereus*, the causative agent of an emetic type of food-borne illness. *Mol Nutr Food Res*, 48, 479-87.
- Errington, J. 1993. *Bacillus subtilis* sporulation: regulation of gene expression and control of morphogenesis. *Microbiol Rev*, 57, 1-33.
- Errington, J. 2003. Regulation of endospore formation in *Bacillus subtilis*. *Nat Rev Microbiol*, 1, 117-26.
- Fairhead, H. & Setlow, P. 1992. Binding of DNA to alpha/beta-type small, acid-soluble proteins from spores of *Bacillus* or *Clostridium* species prevents formation of cytosine dimers, cytosine-thymine dimers, and bipyrimidine photoadducts after UV irradiation. *J Bacteriol*, 174, 2874-80.
- Fass, D. 2012. Disulfide bonding in protein biophysics. *Annu Rev Biophys*, 41, 63-79.
- Fazzini, M. M., Schuch, R. & Fischetti, V. A. 2010. A novel spore protein, ExsM, regulates formation of the exosporium in *Bacillus cereus* and *Bacillus anthracis* and affects spore size and shape. *J Bacteriol*, 192, 4012-21.
- Fouet, A. 2010. AtxA, a *Bacillus anthracis* global virulence regulator. *Res Microbiol*, 161, 735-42.
- Garcia-Patrone, M. & Tandecarz, J. S. 1995. A glycoprotein multimer from *Bacillus thuringiensis* sporangia: dissociation into subunits and sugar composition. *Mol Cell Biochem*, 145, 29-37.
- Gasteiger E., H. C., Gattiker A., Duvaud S., Wilkins M.R., Appel R.D., Bairoch A. 2005. *Protein Identification and Analysis Tools on the ExPASy Server*, Humana Press.
- Gerhardt, P. 1967. Cytology of *Bacillus anthracis*. *Fed Proc*, 26, 1504-17.
- Gerhardt, P. & Black, S. H. 1961. Permeability of bacterial spores. II. Molecular variables affecting solute permeation. *J Bacteriol*, 82, 750-60.
- Gerhardt, P. & Marquis, R. E. 1989. Spore thermoresistance mechanisms. *Regulation of Prokaryotic Development*, 43-63.
- Gerhardt, P., Pankratz, H. S. & Scherrer, R. 1976. Fine structure of the *Bacillus thuringiensis* spore. *Appl Environ Microbiol*, 32, 438-40.
- Gerhardt, P. & Ribí, E. 1964. Ultrastructure of the exosporium enveloping spores of *Bacillus cereus*. *J Bacteriol*, 88, 1774-89.
- Giorno, R., Bozue, J., Cote, C., Wenzel, T., Moody, K. S., Mallozzi, M., Ryan, M., Wang, R., Zielke, R., Maddock, J. R., Friedlander, A., Welkos, S. & Driks, A. 2007. Morphogenesis of the *Bacillus anthracis* spore. *J Bacteriol*, 189, 691-705.
- Giorno, R., Mallozzi, M., Bozue, J., Moody, K. S., Slack, A., Qiu, D., Wang, R., Friedlander, A., Welkos, S. & Driks, A. 2009. Localization and assembly of proteins comprising the outer structures of the *Bacillus anthracis* spore. *Microbiology*, 155, 1133-45.

- Gipson, B., Zeng, X. & Stahlberg, H. 2007a. 2dx\_merge: data management and merging for 2D crystal images. *J Struct Biol*, 160, 375-84.
- Gipson, B., Zeng, X., Zhang, Z. Y. & Stahlberg, H. 2007b. 2dx - user-friendly image processing for 2D crystals. *J Struct Biol*, 157, 64-72.
- Glaeser, R. M. 1971. Limitations to significant information in biological electron microscopy as a result of radiation damage. *J Ultrastruct Res*, 36, 466-82.
- Goldman, R. C. & Tipper, D. J. 1978. *Bacillus subtilis* spore coats: complexity and purification of a unique polypeptide component. *J Bacteriol*, 135, 1091-106.
- Gould, G. W., Stubbs, J. M. & King, W. L. 1970. Structure and composition of resistant layers in bacterial spore coats. *J Gen Microbiol*, 60, 347-55.
- Granum, P. E. 1994. *Bacillus cereus* and its toxins. *Soc Appl Bacteriol Symp Ser*, 23, 61S-66S.
- Granum, P. E. & Lund, T. 1997. *Bacillus cereus* and its food poisoning toxins. *FEMS Microbiol Lett*, 157, 223-8.
- Green, B. D., Battisti, L., Koehler, T. M., Thorne, C. B. & Ivins, B. E. 1985. Demonstration of a capsule plasmid in *Bacillus anthracis*. *Infect Immun*, 49, 291-7.
- Grigorieff, N. 2013. Direct detection pays off for electron cryo-microscopy. *Elife*, 2, e00573.
- Hachisuka, Y., Kojima, K. & Sato, T. 1966. Fine filaments on the outside of the exosporium of *Bacillus anthracis* spores. *J Bacteriol*, 91, 2382-4.
- Hall, C. E. 1955. Electron densitometry of stained virus particles. *J Biophys Biochem Cytol*, 1, 1-12.
- Han, C. S., Xie, G., Challacombe, J. F., Altherr, M. R., Bhotika, S. S., Brown, N., Bruce, D., Campbell, C. S., Campbell, M. L., Chen, J., Chertkov, O., Cleland, C., Dimitrijevic, M., Doggett, N. A., Fawcett, J. J., Glavina, T., Goodwin, L. A., Green, L. D., Hill, K. K., Hitchcock, P., Jackson, P. J., Keim, P., Kewalramani, A. R., Longmire, J., Lucas, S., Malfatti, S., Mcmurry, K., Meincke, L. J., Misra, M., Moseman, B. L., Mundt, M., Munk, A. C., Okinaka, R. T., Parson-Quintana, B., Reilly, L. P., Richardson, P., Robinson, D. L., Rubin, E., Saunders, E., Tapia, R., Tesmer, J. G., Thayer, N., Thompson, L. S., Tice, H., Ticknor, L. O., Wills, P. L., Brettin, T. S. & Gilna, P. 2006. Pathogenomic sequence analysis of *Bacillus cereus* and *Bacillus thuringiensis* isolates closely related to *Bacillus anthracis*. *J Bacteriol*, 188, 3382-90.
- Helgason, E., Okstad, O. A., Caugant, D. A., Johansen, H. A., Fouet, A., Mock, M., Hegna, I. & Kolsto, A. B. 2000. *Bacillus anthracis*, *Bacillus cereus*, and *Bacillus thuringiensis* - One species on the basis of genetic evidence. *Applied and Environmental Microbiology*, 66, 2627-2630.
- Henderson, R., Baldwin, J. M., Downing, K. H., Lepault, J. & Zemlin, F. 1986. Structure of purple membrane from *Halobacterium halobium* - Recording, measurement and evaluation of electron-micrographs at 3.5 Å resolution. *Ultramicroscopy*, 19, 147-178.
- Henderson, R. & Unwin, P. N. 1975. Three-dimensional model of purple membrane obtained by electron microscopy. *Nature*, 257, 28-32.
- Henriques, A. O. & Moran, C. P. 2007. Structure, assembly, and function of the spore surface layers. *Annual Review of Microbiology*, 61, 555-588.
- Henriques, A. O. & Moran, C. P., Jr. 2000. Structure and assembly of the bacterial endospore coat. *Methods*, 20, 95-110.
- Hilbert, D. W. & Piggot, P. J. 2004. Compartmentalization of gene expression during *Bacillus subtilis* spore formation. *Microbiology and Molecular Biology Reviews*, 68, 234-262.
- Hitchins, A. D., King, W. L. & Gould, G. W. 1966. Role of disulphide bonds in the resistance of *Bacillus cereus* spores to gamma irradiation and heat. *J Appl Bacteriol*, 29, 505-11.
- Hodgkiss, W., Ordal, Z. J. & Cann, D. C. 1967. The morphology and ultrastructure of the spore and exosporium of some *Clostridium* species. *J Gen Microbiol*, 47, 213-25.
- Hofte, H. & Whiteley, H. R. 1989. Insecticidal crystal proteins of *Bacillus thuringiensis*. *Microbiol Rev*, 53, 242-55.
- Holt, S. C. & Leadbetter, E. R. 1969. Comparative ultrastructure of selected aerobic spore-forming bacteria: a freeze-etching study. *Bacteriol Rev*, 33, 346-78.
- Holzwarth, G. & Doty, P. 1965. The ultraviolet circular dichroism of polypeptides. *J Am Chem Soc*, 87, 218-28.
- Huang, S. S., Chen, D., Pelczar, P. L., Vepachedu, V. R., Setlow, P. & Li, Y. Q. 2007. Levels of Ca<sup>2+</sup>-dipicolinic acid in individual *Bacillus* spores determined using microfluidic Raman tweezers. *J Bacteriol*, 189, 4681-7.

- Hudson, K. D., Corfe, B. M., Kemp, E. H., Feavers, I. M., Coote, P. J. & Moir, A. 2001. Localization of GerAA and GerAC germination proteins in the *Bacillus subtilis* spore. *J Bacteriol*, 183, 4317-22.
- Imamura, D., Kuwana, R., Takamatsu, H. & Watabe, K. 2010. Localization of proteins to different layers and regions of *Bacillus subtilis* spore coats. *J Bacteriol*, 192, 518-24.
- Imamura, D., Kuwana, R., Takamatsu, H. & Watabe, K. 2011. Proteins involved in formation of the outermost layer of *Bacillus subtilis* spores. *J Bacteriol*, 193, 4075-80.
- Inglesby, T. V., Henderson, D. A., Bartlett, J. G., Ascher, M. S., Eitzen, E., Friedlander, A. M., Hauer, J., Mcdade, J., Osterholm, M. T., O'toole, T., Parker, G., Perl, T. M., Russell, P. K., Tonat, K. & Biodefense, W. G. C. 1999. Anthrax as a biological weapon - Medical and public health management. *Jama-Journal of the American Medical Association*, 281, 1735-1745.
- Ivanova, N., Sorokin, A., Anderson, I., Galleron, N., Candelon, B., Kapatral, V., Bhattacharyya, A., Reznik, G., Mikhailova, N., Lapidus, A., Chu, L., Mazur, M., Goltsman, E., Larsen, N., D'souza, M., Walunas, T., Grechkin, Y., Pusch, G., Haselkorn, R., Fonstein, M., Ehrlich, S. D., Overbeek, R. & Kyrpides, N. 2003. Genome sequence of *Bacillus cereus* and comparative analysis with *Bacillus anthracis*. *Nature*, 423, 87-91.
- Jensen, G. B., Hansen, B. M., Eilenberg, J. & Mahillon, J. 2003. The hidden lifestyles of *Bacillus cereus* and relatives. *Environ Microbiol*, 5, 631-40.
- Jiang, S., Wan, Q., Krajcikova, D., Tang, J., Tzokov, S. B., Barak, I. and Bullough, P. A. 2015. Diverse supramolecular structures formed by self-assembling proteins of the *Bacillus subtilis* spore coat. *Mol. Micro.*, 97, 347-359.
- Johnson, M. J. 2004. The function of *ExsY* and *CotY*, two structural proteins of the *Bacillus cereus* exosporium. The University of Sheffield, UK.
- Johnson, M. J., Todd, S. J., Ball, D. A., Shepherd, A. M., Sylvestre, P. & Moir, A. 2006. ExsY and CotY are required for the correct assembly of the exosporium and spore coat of *Bacillus cereus*. *J Bacteriol*, 188, 7905-13.
- Kailas, L., Terry, C., Abbott, N., Taylor, R., Mullin, N., Tzokov, S. B., Todd, S. J., Wallace, B. A., Hobbs, J. K., Moir, A. & Bullough, P. A. 2011. Surface architecture of endospores of the *Bacillus cereus/anthracis/thuringiensis* family at the subnanometer scale. *Proceedings of the National Academy of Sciences of the United States of America*, 108, 16014-16019.
- Kay, D. & Warren, S. C. 1968. Sporulation in *Bacillus subtilis*. Morphological changes. *Biochem J*, 109, 819-24.
- Kennedy, M. J., Reader, S. L. & Swierczynski, L. M. 1994. Preservation records of microorganisms: evidence of the tenacity of life. *Microbiology*, 140 ( Pt 10), 2513-29.
- Kim, H., Hahn, M., Grabowski, P., Mcpherson, D. C., Otte, M. M., Wang, R., Ferguson, C. C., Eichenberger, P. & Driks, A. 2006. The *Bacillus subtilis* spore coat protein interaction network. *Mol Microbiol*, 59, 487-502.
- Klobutcher, L. A., Ragkousi, K. & Setlow, P. 2006. The *Bacillus subtilis* spore coat provides "eat resistance" during phagocytic predation by the protozoan *Tetrahymena thermophila*. *Proc Natl Acad Sci U S A*, 103, 165-70.
- Knaysi, G. & Hillier, J. 1949. Preliminary Observations on the Germination of the Endospore in *Bacillus megatherium* and the Structure of the Spore Coat. *Journal of Bacteriology*, 57, 23-29.
- Kobayashi, K., Ehrlich, S. D., Albertini, A., Amati, G., Andersen, K. K., Arnaud, M., Asai, K., Ashikaga, S., Aymerich, S., Bessieres, P., Boland, F., Brignell, S. C., Bron, S., Bunai, K., Chapuis, J., Christiansen, L. C., Danchin, A., Debarbouille, M., Dervyn, E., Deuerling, E., Devine, K., Devine, S. K., Dreesen, O., Errington, J., Fillinger, S., Foster, S. J., Fujita, Y., Galizzi, A., Gardan, R., Eschevins, C., Fukushima, T., Haga, K., Harwood, C. R., Hecker, M., Hosoya, D., Hullo, M. F., Kakeshita, H., Karamata, D., Kasahara, Y., Kawamura, F., Koga, K., Koski, P., Kuwana, R., Imamura, D., Ishimaru, M., Ishikawa, S., Ishio, I., Le Coq, D., Masson, A., Mauel, C., Meima, R., Mellado, R. P., Moir, A., Moriya, S., Nagakawa, E., Nanamiya, H., Nakai, S., Nygaard, P., Ogura, M., Ohanan, T., O'reilly, M., O'rourke, M., Pragai, Z., Pooley, H. M., Rapoport, G., Rawlins, J. P., Rivas, L. A., Rivolta, C., Sadaie, A., Sadaie, Y., Sarvas, M., Sato, T., Saxild, H. H., Scanlan, E., Schumann, W., Seegers, J. F., Sekiguchi, J., Sekowska, A., Seror, S. J., Simon, M., Stragier, P., Studer, R., Takamatsu, H., Tanaka, T., Takeuchi, M., Thomaidis, H. B., Vagner, V., Van Dijl, J. M., Watabe, K., Wipat, A., Yamamoto, H., Yamamoto, M., Yamamoto, Y., Yamane, K., Yata, K., Yoshida, K., Yoshikawa, H., Zuber, U. & Ogasawara, N. 2003. Essential *Bacillus subtilis* genes. *Proc Natl Acad Sci U S A*, 100, 4678-83.

- Kobayashi, K., Kumazawa, Y., Miwa, K. And Yamanaka, S. 1996.  $\epsilon$ -(glutamyl)lysine cross-links of spore coat proteins and transglutaminase activity in *Bacillus subtilis*. *FEMS Microbiol Lett* 144, 157–160.
- Koch, M. S., Ward, J. M., Levine, S. L., Baum, J. A., Vicini, J. L. & Hammond, B. G. 2015. The food and environmental safety of *Bt* crops. *Front Plant Sci*, 6, 283.
- Koch, R. 1876. Die Ätiologie der Milzbrand-Krankheit, begründet auf die Entwicklungsgeschichte des *Bacillus Anthracis*. *Beiträge zur Biologie der Pflanzen*, 2, 277-308.
- Koni, P. A. & Ellar, D. J. 1994. Biochemical characterization of *Bacillus thuringiensis* cytolytic delta-endotoxins. *Microbiology*, 140 ( Pt 8), 1869-80.
- Korza, G. & Setlow, P. 2013. Topology and accessibility of germination proteins in the *Bacillus subtilis* spore inner membrane. *J Bacteriol*, 195, 1484-91.
- Kozuka, S. & Tochikubo, K. 1985. Properties and origin of filamentous appendages on spores of *Bacillus cereus*. *Microbiol Immunol*, 29, 21-37.
- Krajcikova, D., Lukacova, M., Mullerova, D., Cutting, S. M. & Barak, I. 2009. Searching for protein-protein interactions within the *Bacillus subtilis* spore coat. *J Bacteriol*, 191, 3212-9.
- Kramer, J. M. G., R.J. 1989. *Bacillus cereus and other Bacillus species*, New York and Basel, Marcel Dekker.
- Kroos, L. & Yu, Y. T. 2000. Regulation of sigma factor activity during *Bacillus subtilis* development. *Curr Opin Microbiol*, 3, 553-60.
- Kunst, F., Ogasawara, N., Moszer, I., Albertini, A. M., Alloni, G., Azevedo, V., Bertero, M. G., Bessieres, P., Bolotin, A., Borchert, S., Borriss, R., Boursier, L., Brans, A., Braun, M., Brignell, S. C., Bron, S., Brouillet, S., Bruschi, C. V., Caldwell, B., Capuano, V., Carter, N. M., Choi, S. K., Cordani, J. J., Connerton, I. F., Cummings, N. J., Daniel, R. A., Denziot, F., Devine, K. M., Dusterhoft, A., Ehrlich, S. D., Emmerson, P. T., Entian, K. D., Errington, J., Fabret, C., Ferrari, E., Foulger, D., Fritz, C., Fujita, M., Fujita, Y., Fuma, S., Galizzi, A., Galleron, N., Ghim, S. Y., Glaser, P., Goffeau, A., Golightly, E. J., Grandi, G., Guiseppi, G., Guy, B. J., Haga, K., Haiech, J., Harwood, C. R., Henaut, A., Hilbert, H., Holsappel, S., Hosono, S., Hullo, M. F., Itaya, M., Jones, L., Joris, B., Karamata, D., Kasahara, Y., Klaerr-Blanchard, M., Klein, C., Kobayashi, Y., Koetter, P., Koningstein, G., Krogh, S., Kumano, M., Kurita, K., Lapidus, A., Lardinois, S., Lauber, J., Lazarevic, V., Lee, S. M., Levine, A., Liu, H., Masuda, S., Mauel, C., Medigue, C., Medina, N., Mellado, R. P., Mizuno, M., Moestl, D., Nakai, S., Noback, M., Noone, D., O'reilly, M., Ogawa, K., Ogiwara, A., Oudega, B., Park, S. H., Parro, V., Pohl, T. M., Portelle, D., Porwollik, S., Prescott, A. M., Presecan, E., Pujic, P., Purnelle, B., *et al.* 1997. The complete genome sequence of the gram-positive bacterium *Bacillus subtilis*. *Nature*, 390, 249-56.
- Laaberki, M. H. & Dworkin, J. 2008. Role of spore coat proteins in the resistance of *Bacillus subtilis* spores to *Caenorhabditis elegans* predation. *J Bacteriol*, 190, 6197-203.
- Lai, E. M., Phadke, N. D., Kachman, M. T., Giorno, R., Vazquez, S., Vazquez, J. A., Maddock, J. R. & Driks, A. 2003. Proteomic analysis of the spore coats of *Bacillus subtilis* and *Bacillus anthracis*. *J Bacteriol*, 185, 1443-54.
- Lechner, S., Mayr, R., Francis, K. P., Pruss, B. M., Kaplan, T., Wiessner-Gunkel, E., Stewart, G. S. & Scherer, S. 1998. *Bacillus weihenstephanensis* sp. nov. is a new psychrotolerant species of the *Bacillus cereus* group. *Int J Syst Bacteriol*, 48 Pt 4, 1373-82.
- Lees, J. G., Miles, A. J., Wien, F. & Wallace, B. A. 2006. A reference database for circular dichroism spectroscopy covering fold and secondary structure space. *Bioinformatics*, 22, 1955-62.
- Lees, J. G., Smith, B. R., Wien, F., Miles, A. J. & Wallace, B. A. 2004. CDtool - an integrated software package for circular dichroism spectroscopic data processing, analysis, and archiving. *Anal Biochem*, 332, 285-9.
- Lequette, Y., Garenaux, E., Combrouse, T., Thays, D. L. D., Ronse, A., Slomianny, C., Trivelli, X., Guerardel, Y. & Faille, C. 2011. Domains of BclA, the major surface glycoprotein of the *B. cereus* exosporium: glycosylation patterns and role in spore surface properties. *Biofouling*, 27, 751-761.
- Levin, P. A. & Losick, R. 1996. Transcription factor Spo0A switches the localization of the cell division protein FtsZ from a medial to a bipolar pattern in *Bacillus subtilis*. *Genes Dev*, 10, 478-88.
- Li, Y., Davis, A., Korza, G., Zhang, P., Li, Y. Q., Setlow, B., Setlow, P. & Hao, B. 2012. Role of a SpoVA protein in dipicolinic acid uptake into developing spores of *Bacillus subtilis*. *J Bacteriol*, 194, 1875-84.

- Little, S. & Driks, A. 2001. Functional analysis of the *Bacillus subtilis* morphogenetic spore coat protein CotE. *Mol Microbiol*, 42, 1107-20.
- Liu, H., Bergman, N. H., Thomason, B., Shallom, S., Hazen, A., Crossno, J., Rasko, D. A., Ravel, J., Read, T. D., Peterson, S. N., Yates, J., 3rd & Hanna, P. C. 2004. Formation and composition of the *Bacillus anthracis* endospore. *J Bacteriol*, 186, 164-78.
- Losick, R. & Stragier, P. 1992. Crisscross regulation of cell-type-specific gene expression during development in *B. subtilis*. *Nature*, 355, 601-4.
- Lund, B. M., Gee, J. M., King, N. R., Horne, R. W. & Harnden, J. M. 1978. Structure of Exosporium of a Pigmented *Clostridium*. *Journal of General Microbiology*, 105, 165-174.
- Lund, T. & Granum, P. E. 1997. Comparison of biological effect of the two different enterotoxin complexes isolated from three different strains of *Bacillus cereus*. *Microbiology*, 143 ( Pt 10), 3329-36.
- Mackey, B. M. & Morris, J. G. 1972. The exosporium of *Clostridium pasteurianum*. *J Gen Microbiol*, 73, 325-38.
- Mader, U., Schmeisky, A. G., Florez, L. A. & Stulke, J. 2012. SubtiWiki - a comprehensive community resource for the model organism *Bacillus subtilis*. *Nucleic Acids Res*, 40, D1278-87.
- Mallick, P., Boutz, D. R., Eisenberg, D. & Yeates, T. O. 2002. Genomic evidence that the intracellular proteins of archaeal microbes contain disulfide bonds. *Proc Natl Acad Sci U S A*, 99, 9679-84.
- Matz, L. L., Beaman, T. C. & Gerhardt, P. 1970. Chemical composition of exosporium from spores of *Bacillus cereus*. *J Bacteriol*, 101, 196-201.
- Mckenney, P. T., Driks, A., Eskandarian, H. A., Grabowski, P., Guberman, J., Wang, K. H., Gitai, Z. & Eichenberger, P. 2010. A distance-weighted interaction map reveals a previously uncharacterized layer of the *Bacillus subtilis* spore coat. *Curr Biol*, 20, 934-8.
- Mckenney, P. T. & Eichenberger, P. 2012. Dynamics of spore coat morphogenesis in *Bacillus subtilis*. *Mol Microbiol*, 83, 245-60.
- Mcperson, S. A., Li, M., Kearney, J. F. & Turnbough, C. L., Jr. 2010. ExsB, an unusually highly phosphorylated protein required for the stable attachment of the exosporium of *Bacillus anthracis*. *Mol Microbiol*, 76, 1527-38.
- Meador-Parton, J. & Popham, D. L. 2000. Structural analysis of *Bacillus subtilis* spore peptidoglycan during sporulation. *J Bacteriol*, 182, 4491-9.
- Mikesell, P., Ivins, B. E., Ristroph, J. D. & Dreier, T. M. 1983. Evidence for plasmid-mediated toxin production in *Bacillus anthracis*. *Infect Immun*, 39, 371-6.
- Miles, A. J., Whitmore, L. & Wallace, B. A. 2005. Spectral magnitude effects on the analyses of secondary structure from circular dichroism spectroscopic data. *Protein Sci*, 14, 368-74.
- Miyaguchi, K. 2014. Direct imaging electron microscopy (EM) methods in modern structural biology: overview and comparison with X-ray crystallography and single-particle cryo-EM reconstruction in the studies of large macromolecules. *Biol Cell*, 106, 323-45.
- Moberly, B. J., Shafa, F. & Gerhardt, P. 1966. Structural details of anthrax spores during stages of transformation into vegetative cells. *Journal of Bacteriology*, 92, 220-228.
- Mock, M. & Fouet, A. 2001. Anthrax. *Annual Review of Microbiology*, 55, 647-671.
- Moir, A., Corfe, B. M. & Behravan, J. 2002. Spore germination. *Cell Mol Life Sci*, 59, 403-9.
- Mortimer, P. R. & Mccann, G. 1974. Food-poisoning episodes associated with *Bacillus cereus* in fried rice. *Lancet*, 1, 1043-5.
- Nicholson, W. L., Fajardo-Cavazos, P., Rebeil, R., Slieman, T. A., Riesenman, P. J., Law, J. F. & Xue, Y. M. 2002. Bacterial endospores and their significance in stress resistance. *Antonie Van Leeuwenhoek International Journal of General and Molecular Microbiology*, 81, 27-32.
- Nicholson, W. L., Munakata, N., Horneck, G., Melosh, H. J. & Setlow, P. 2000. Resistance of *Bacillus* endospores to extreme terrestrial and extraterrestrial environments. *Microbiol Mol Biol Rev*, 64, 548-72.
- Nicolas, P., Mader, U., Dervyn, E., Rochat, T., Leduc, A., Pigeonneau, N., Bidnenko, E., Marchadier, E., Hoebeke, M., Aymerich, S., Becher, D., Bisicchia, P., Botella, E., Delumeau, O., Doherty, G., Denham, E. L., Fogg, M. J., Fromion, V., Goelzer, A., Hansen, A., Hartig, E., Harwood, C. R., Homuth, G., Jarmer, H., Jules, M., Klipp, E., Le Chat, L., Lecointe, F., Lewis, P., Liebermeister, W., March, A., Mars, R. A., Nannapaneni, P., Noone, D., Pohl, S., Rinn, B., Rugheimer, F., Sappa, P. K., Samson, F., Schaffer, M., Schwikowski, B., Steil, L., Stulke, J., Wiegert, T., Devine, K. M., Wilkinson, A. J., Van Dijl, J. M., Hecker, M., Volker, U., Bessieres, P. & Noirot, P. 2012. Condition-dependent transcriptome reveals high-level regulatory architecture in *Bacillus subtilis*. *Science*, 335, 1103-6.

- Nogales, E. & Scheres, S. H. 2015. Cryo-EM: A unique tool for the visualization of macromolecular complexity. *Mol Cell*, 58, 677-689.
- Ohye, D. F. & Murrell, W. G. 1973. Exosporium and spore coat formation in *Bacillus cereus* T. *J Bacteriol*, 115, 1179-90.
- Oliva, C., Turnbough, C. L., Jr. & Kearney, J. F. 2009. CD14-Mac-1 interactions in *Bacillus anthracis* spore internalization by macrophages. *Proc Natl Acad Sci U S A*, 106, 13957-62.
- Oliva, C. R., Swiecki, M. K., Griguer, C. E., Lisanby, M. W., Bullard, D. C., Turnbough, C. L., Jr. & Kearney, J. F. 2008. The integrin Mac-1 (CR3) mediates internalization and directs *Bacillus anthracis* spores into professional phagocytes. *Proc Natl Acad Sci U S A*, 105, 1261-6.
- Ozin, A. J., Henriques, A. O., Yi, H. & Moran, C. P., Jr. 2000. Morphogenetic proteins SpoVID and SafA form a complex during assembly of the *Bacillus subtilis* spore coat. *J Bacteriol*, 182, 1828-33.
- Paidhungat, M., Ragkousi, K. & Setlow, P. 2001. Genetic requirements for induction of germination of spores of *Bacillus subtilis* by Ca(2+)-dipicolinate. *J Bacteriol*, 183, 4886-93.
- Paidhungat, M. & Setlow, P. 2000. Role of ger proteins in nutrient and nonnutrient triggering of spore germination in *Bacillus subtilis*. *J Bacteriol*, 182, 2513-9.
- Paidhungat, M. & Setlow, P. 2001. Localization of a germinant receptor protein (GerBA) to the inner membrane of *Bacillus subtilis* spores. *J Bacteriol*, 183, 3982-90.
- Paidhungat, M. & Setlow, P. 2002. Spore germination and outgrowth. *Bacillus subtilis and its relatives: from genes to cells. American Society for Microbiology, Washington, DC*, 537-548.
- Palop, A., Raso, J., Pagan, R., Condon, S. & Sala, F. J. 1999. Influence of pH on heat resistance of spores of *Bacillus coagulans* in buffer and homogenized foods. *International Journal of Food Microbiology*, 46, 243-249.
- Pandey, N. K. & Aronson, A. I. 1979. Properties of the *Bacillus subtilis* spore coat. *J Bacteriol*, 137, 1208-18.
- Permpoonpattana, P., Phetcharaburanin, J., Mikelsone, A., Dembek, M., Tan, S., Brisson, M. C., La Ragione, R., Brisson, A. R., Fairweather, N., Hong, H. A. & Cutting, S. M. 2013. Functional characterization of *Clostridium difficile* spore coat proteins. *J Bacteriol*, 195, 1492-503.
- Pettersen, E. F., Goddard, T. D., Huang, C. C., Couch, G. S., Greenblatt, D. M., Meng, E. C. & Ferrin, T. E. 2004. UCSF Chimera - a visualization system for exploratory research and analysis. *J Comput Chem*, 25, 1605-12.
- Piggot, P. J. & Hilbert, D. W. 2004. Sporulation of *Bacillus subtilis*. *Current Opinion in Microbiology*, 7, 579-586.
- Pilo, P. & Frey, J. 2011. *Bacillus anthracis*: Molecular taxonomy, population genetics, phylogeny and patho-evolution. *Infection Genetics and Evolution*, 11, 1218-1224.
- Pizarro-Guajardo, M., Olguin-Araneda, V., Barra-Carrasco, J., Brito-Silva, C., Sarker, M. R. & Paredes-Sabja, D. 2014. Characterization of the collagen-like exosporium protein, BclA1, of *Clostridium difficile* spores. *Anaerobe*, 25, 18-30.
- Plomp, M., Carroll, A. M., Setlow, P. & Malkin, A. J. 2014. Architecture and assembly of the *Bacillus subtilis* spore coat. *PLoS One*, 9, e108560.
- Plomp, M., Leighton, T. J., Wheeler, K. E., Hill, H. D. & Malkin, A. J. 2007. *In vitro* high-resolution structural dynamics of single germinating bacterial spores. *Proc Natl Acad Sci U S A*, 104, 9644-9.
- Plomp, M., Leighton, T. J., Wheeler, K. E. & Malkin, A. J. 2005a. Architecture and high-resolution structure of *Bacillus thuringiensis* and *Bacillus cereus* spore coat surfaces. *Langmuir*, 21, 7892-8.
- Plomp, M., Leighton, T. J., Wheeler, K. E. & Malkin, A. J. 2005b. The high-resolution architecture and structural dynamics of *Bacillus* spores. *Biophys J*, 88, 603-8.
- Priest, F. G., Barker, M., Baillie, L. W. J., Holmes, E. C. & Maiden, M. C. J. 2004. Population structure and evolution of the *Bacillus cereus* group. *Journal of Bacteriology*, 186, 7959-7970.
- Ramamurthi, K. S., Clapham, K. R. & Losick, R. 2006. Peptide anchoring spore coat assembly to the outer forespore membrane in *Bacillus subtilis*. *Mol Microbiol*, 62, 1547-57.
- Rasko, D. A., Ravel, J., Okstad, O. A., Helgason, E., Cer, R. Z., Jiang, L., Shores, K. A., Fouts, D. E., Tourasse, N. J., Angiuoli, S. V., Kolonay, J., Nelson, W. C., Kolsto, A. B., Fraser, C. M. & Read, T. D. 2004. The genome sequence of *Bacillus cereus* ATCC 10987 reveals metabolic adaptations and a large plasmid related to *Bacillus anthracis* pXO1. *Nucleic Acids Res*, 32, 977-88.

- Read, T. D., Peterson, S. N., Tourasse, N., Baillie, L. W., Paulsen, I. T., Nelson, K. E., Tettelin, H., Fouts, D. E., Eisen, J. A., Gill, S. R., Holtzapple, E. K., Okstad, O. A., Helgason, E., Riilstone, J., Wu, M., Kolonay, J. F., Beanan, M. J., Dodson, R. J., Brinkac, L. M., Gwinn, M., Deboy, R. T., Madpu, R., Daugherty, S. C., Durkin, A. S., Haft, D. H., Nelson, W. C., Peterson, J. D., Pop, M., Khouri, H. M., Radune, D., Benton, J. L., Mahamoud, Y., Jiang, L., Hance, I. R., Weidman, J. F., Berry, K. J., Plaut, R. D., Wolf, A. M., Watkins, K. L., Nierman, W. C., Hazen, A., Cline, R., Redmond, C., Thwaite, J. E., White, O., Salzberg, S. L., Thomason, B., Friedlander, A. M., Koehler, T. M., Hanna, P. C., Kolsto, A. B. & Fraser, C. M. 2003. The genome sequence of *Bacillus anthracis* Ames and comparison to closely related bacteria. *Nature*, 423, 81-6.
- Redmond, C., Baillie, L. W., Hibbs, S., Moir, A. J. & Moir, A. 2004. Identification of proteins in the exosporium of *Bacillus anthracis*. *Microbiology*, 150, 355-63.
- Remsen, C. C. 1966. The fine structure of frozen-etched *Bacillus cereus* spores. *Arch Mikrobiol*, 54, 266-75.
- Rety, S., Salamitou, S., Garcia-Verdugo, I., Hulmes, D. J. S., Le Hegarat, F., Chaby, R. & Lewit-Bentley, A. 2005. The crystal structure of the *Bacillus anthracis* spore surface protein BclA shows remarkable similarity to mammalian proteins. *Journal of Biological Chemistry*, 280, 43073-43078.
- Riesenman, P. J. & Nicholson, W. L. 2000. Role of the spore coat layers in *Bacillus subtilis* spore resistance to hydrogen peroxide, artificial UV-C, UV-B, and solar UV radiation. *Appl Environ Microbiol*, 66, 620-626.
- Rodenburg, C. M., Mcpherson, S. A., Turnbough, C. L., Jr. & Dokland, T. 2014. Cryo-EM analysis of the organization of BclA and BxpB in the *Bacillus anthracis* exosporium. *J Struct Biol*, 186, 181-7.
- Ross, J. M. 1957. The pathogenesis of anthrax following the administration of spores by the respiratory route. *Journal of Pathology and Bacteriology*, 73, 485-8.
- Sanchez-Salas, J. L., Setlow, B., Zhang, P., Li, Y. Q. & Setlow, P. 2011. Maturation of released spores is necessary for acquisition of full spore heat resistance during *Bacillus subtilis* sporulation. *Appl Environ Microbiol*, 77, 6746-54.
- Scherrer, P. S. & Somerville, H. J. 1977. Membrane fractions from the outer layers of spores of *Bacillus thuringiensis* with toxicity to lepidopterous larvae. *Eur J Biochem*, 72, 479-90.
- Setlow, B., Melly, E. & Setlow, P. 2001. Properties of spores of *Bacillus subtilis* blocked at an intermediate stage in spore germination. *J Bacteriol*, 183, 4894-9.
- Setlow, B. & Setlow, P. 1995. Small, acid-soluble proteins bound to DNA protect *Bacillus subtilis* spores from killing by dry heat. *Appl Environ Microbiol*, 61, 2787-90.
- Setlow, P. 1995. Mechanisms for the prevention of damage to DNA in spores of *Bacillus* species. *Annu Rev Microbiol*, 49, 29-54.
- Setlow, P. 2003. Spore germination. *Curr Opin Microbiol*, 6, 550-6.
- Setlow, P. 2006. Spores of *Bacillus subtilis*: their resistance to and killing by radiation, heat and chemicals. *J Appl Microbiol*, 101, 514-25.
- Setlow, P. 2007. I will survive: DNA protection in bacterial spores. *Trends Microbiol*, 15, 172-80.
- Severson, K. M., Mallozzi, M., Bozue, J., Welkos, S. L., Cote, C. K., Knight, K. L. & Driks, A. 2009. Roles of the *Bacillus anthracis* spore protein ExsK in exosporium maturation and germination. *J Bacteriol*, 191, 7587-96.
- Shaw, P. J. & Hills, G. J. 1981. Tilted Specimen in the Electron-Microscope - a simple specimen holder and the calculation of tilt angles for crystalline specimens. *Micron*, 12, 279-282.
- Smirnova, T. A., Mikhailov, A. M., Tiurin, V. S. & Azizbekian, R. R. 1984. Ultrastructure of the bacterial spores and crystals of various *Bacillus thuringiensis* serotypes. *Mikrobiologiya*, 53, 455-62.
- Soberon, M., Pardo, L., Munoz-Garay, C., Sanchez, J., Gomez, I., Porta, H. & Bravo, A. 2010. Pore formation by Cry toxins. *Adv Exp Med Biol*, 677, 127-42.
- Somerville, H. J. & James, C. R. 1970. Association of the crystalline inclusion of *Bacillus thuringiensis* with the exosporium. *J Bacteriol*, 102, 580-3.
- Stahly, D. P., Dingman, D. W., Bulla, L. A., Jr. & Aronson, A. I. 1978. Possible origin and function of the parasporal crystal in *Bacillus thuringiensis*. *Biochem Biophys Res Commun*, 84, 581-8.
- Steichen, C., Chen, P., Kearney, J. F. & Turnbough, C. L., Jr. 2003. Identification of the immunodominant protein and other proteins of the *Bacillus anthracis* exosporium. *J Bacteriol*, 185, 1903-10.

- Steichen, C. T., Kearney, J. F. & Turnbough, C. L., Jr. 2005. Characterization of the exosporium basal layer protein BxpB of *Bacillus anthracis*. *J Bacteriol*, 187, 5868-76.
- Steichen, C. T., Kearney, J. F. & Turnbough, C. L., Jr. 2007. Non-uniform assembly of the *Bacillus anthracis* exosporium and a bottle cap model for spore germination and outgrowth. *Mol Microbiol*, 64, 359-67.
- Stewart, G. S., Johnstone, K., Hagelberg, E. & Ellar, D. J. 1981. Commitment of bacterial spores to germinate. A measure of the trigger reaction. *Biochem J*, 198, 101-6.
- Stragier, P. & Losick, R. 1996. Molecular genetics of sporulation in *Bacillus subtilis*. *Annu Rev Genet*, 30, 297-41.
- Sylvestre, P., Couture-Tosi, E. & Mock, M. 2002. A collagen-like surface glycoprotein is a structural component of the *Bacillus anthracis* exosporium. *Mol Microbiol*, 45, 169-78.
- Sylvestre, P., Couture-Tosi, E. & Mock, M. 2003. Polymorphism in the collagen-like region of the *Bacillus anthracis* BclA protein leads to variation in exosporium filament length. *J Bacteriol*, 185, 1555-63.
- Sylvestre, P., Couture-Tosi, E. & Mock, M. 2005. Contribution of ExsFA and ExsFB proteins to the localization of BclA on the spore surface and to the stability of the *Bacillus anthracis* exosporium. *J Bacteriol*, 187, 5122-8.
- Tan, L. & Turnbough, C. L., Jr. 2010. Sequence motifs and proteolytic cleavage of the collagen-like glycoprotein BclA required for its attachment to the exosporium of *Bacillus anthracis*. *J Bacteriol*, 192, 1259-68.
- Taylor, A. J. & Gilbert, R. J. 1975. *Bacillus cereus* food poisoning - provisional serotyping scheme. *Journal of Medical Microbiology*, 8, 543-550.
- Taylor, K. A. & Glaeser, R. M. 1974. Electron-diffraction of frozen, hydrated protein crystals. *Science*, 186, 1036-1037.
- Taylor, K. A. & Glaeser, R. M. 1976. Electron microscopy of frozen hydrated biological specimens. *J Ultrastruct Res*, 55, 448-56.
- Teleman, A. A., Graumann, P. L., Lin, D. C., Grossman, A. D. & Losick, R. 1998. Chromosome arrangement within a bacterium. *Curr Biol*, 8, 1102-9.
- Terry, C. 2010. *Assembly of the Bacillus Exosporium*. University of Sheffield, UK.
- Terry, C., Shepherd, A., Radford, D. S., Moir, A. & Bullough, P. A. 2011. YwdL in *Bacillus cereus*: Its Role in Germination and Exosporium Structure. *Plos One*, 6.
- Thomas, D. J., Morgan, J. A., Whipps, J. M. & Saunders, J. R. 2000. Plasmid transfer between the *Bacillus thuringiensis* subspecies kurstaki and tenebrionis in laboratory culture and soil and in lepidopteran and coleopteran larvae. *Appl Environ Microbiol*, 66, 118-24.
- Thompson, B. M., Hoelscher, B. C., Driks, A. & Stewart, G. C. 2011a. Localization and assembly of the novel exosporium protein BetA of *Bacillus anthracis*. *J Bacteriol*, 193, 5098-104.
- Thompson, B. M., Hoelscher, B. C., Driks, A. & Stewart, G. C. 2012. Assembly of the BclB glycoprotein into the exosporium and evidence for its role in the formation of the exosporium 'cap' structure in *Bacillus anthracis*. *Mol Microbiol*, 86, 1073-84.
- Thompson, B. M., Hsieh, H. Y., Spreng, K. A. & Stewart, G. C. 2011b. The co-dependence of BxpB/ExsFA and BclA for proper incorporation into the exosporium of *Bacillus anthracis*. *Mol Microbiol*, 79, 799-813.
- Thompson, B. M. & Stewart, G. C. 2008. Targeting of the BclA and BclB proteins to the *Bacillus anthracis* spore surface. *Mol Microbiol*, 70, 421-34.
- Thompson, B. M., Waller, L. N., Fox, K. F., Fox, A. & Stewart, G. C. 2007. The BclB glycoprotein of *Bacillus anthracis* is involved in exosporium integrity. *J Bacteriol*, 189, 6704-13.
- Todd, S. J., Moir, A. J., Johnson, M. J. & Moir, A. 2003. Genes of *Bacillus cereus* and *Bacillus anthracis* encoding proteins of the exosporium. *J Bacteriol*, 185, 3373-8.
- Tokieda, K., Morikawa, Y., Maeyama, K., Mori, K. & Ikeda, K. 1999. Clinical manifestations of *Bacillus cereus* meningitis in newborn infants. *J Paediatr Child Health*, 35, 582-4.
- Toth, E. A., Worby, C., Dixon, J. E., Goedken, E. R., Marqusee, S. & Yeates, T. O. 2000. The crystal structure of adenylosuccinate lyase from *Pyrobaculum aerophilum* reveals an intracellular protein with three disulfide bonds. *J Mol Biol*, 301, 433-50.
- Tourasse, N. J., Helgason, E., Klevan, A., Sylvestre, P., Moya, M., Haustant, M., Okstad, O. A., Fouet, A., Mock, M. & Kolsto, A. B. 2011. Extended and global phylogenetic view of the *Bacillus cereus* group population by combination of MLST, AFLP, and MLEE genotyping data. *Food Microbiology*, 28, 236-244.

- Uchida, I., Hornung, J. M., Thorne, C. B., Klimpel, K. R. & Leppla, S. H. 1993. Cloning and characterization of a gene whose product is a trans-activator of anthrax toxin synthesis. *J Bacteriol*, 175, 5329-38.
- Uchida, I., Sekizaki, T., Hashimoto, K. & Terakado, N. 1985. Association of the encapsulation of *Bacillus anthracis* with a 60 megadalton plasmid. *J Gen Microbiol*, 131, 363-7.
- Unwin, P. N. & Henderson, R. 1975. Molecular structure determination by electron microscopy of unstained crystalline specimens. *J Mol Biol*, 94, 425-40.
- Valpuesta, J. M., Carrascosa, J. L. & Henderson, R. 1994. Analysis of electron microscope images and electron diffraction patterns of thin crystals of phi 29 connectors in ice. *J Mol Biol*, 240, 281-7.
- Waller, L. N., Fox, N., Fox, K. F., Fox, A. & Price, R. L. 2004. Ruthenium red staining for ultrastructural visualization of a glycoprotein layer surrounding the spore of *Bacillus anthracis* and *Bacillus subtilis*. *J Microbiol Methods*, 58, 23-30.
- Waller, L. N., Stump, M. J., Fox, K. F., Harley, W. M., Fox, A., Stewart, G. C. & Shahgholi, M. 2005. Identification of a second collagen-like glycoprotein produced by *Bacillus anthracis* and demonstration of associated spore-specific sugars. *J Bacteriol*, 187, 4592-7.
- Wan, Q. 2013. *Structure and Assembly of Bacillus Spore Proteins*. University of Sheffield, UK.
- Wang, S., Setlow, P. & Li, Y. Q. 2015. Slow leakage of Ca-dipicolinic acid from individual *Bacillus* spores during initiation of spore germination. *J Bacteriol*, 197, 1095-103.
- Warth, A. D. & Strominger, J. L. 1972. Structure of the peptidoglycan from spores of *Bacillus subtilis*. *Biochemistry*, 11, 1389-96.
- Weaver, J., Kang, T. J., Raines, K. W., Cao, G. L., Hibbs, S., Tsai, P., Baillie, L., Rosen, G. M. & Cross, A. S. 2007. Protective role of *Bacillus anthracis* exosporium in macrophage-mediated killing by nitric oxide. *Infect Immun*, 75, 3894-901.
- Wehrli, E., Scherrer, P. & Kubler, O. 1980. The crystalline layers in spores of *Bacillus cereus* and *Bacillus thuringiensis* studied by freeze-etching and high resolution electron microscopy. *Eur J Cell Biol*, 20, 283-9.
- Weiner, Z. P. & Glomski, I. J. 2012. Updating perspectives on the initiation of *Bacillus anthracis* growth and dissemination through its host. *Infect Immun*, 80, 1626-33.
- Westers, L., Westers, H. & Quax, W. J. 2004. *Bacillus subtilis* as cell factory for pharmaceutical proteins: a biotechnological approach to optimize the host organism. *Biochim Biophys Acta*, 1694, 299-310.
- Wu, L. J. & Errington, J. 1994. *Bacillus subtilis* SpoIIIE protein required for DNA segregation during asymmetric cell division. *Science*, 264, 572-5.
- Wuytack, E. Y., Soons, J., Poschet, F. & Michiels, C. W. 2000. Comparative study of pressure- and nutrient-induced germination of *Bacillus subtilis* spores. *Appl Environ Microbiol*, 66, 257-61.
- Yasuda, Y., Kanda, K., Nishioka, S., Tanimoto, Y., Kato, C., Saito, A., Fukuchi, S., Nakanishi, Y. & Tochikubo, K. 1993. Regulation of L-alanine-initiated germination of *Bacillus subtilis* spores by alanine racemase. *Amino Acids*, 4, 89-99.
- Young, I. E. & Fitz-James, P. C. 1959a. Chemical and Morphological Studies of Bacterial Spore Formation : I. The Formation of Spores in *Bacillus cereus*. *J Biophys Biochem Cytol*, 6, 467-82.
- Young, I. E. & Fitz-James, P. C. 1959b. Chemical and morphological studies of bacterial spore formation. II. Spore and parasporal protein formation in *Bacillus cereus* var. alesti. *J Biophys Biochem Cytol*, 6, 483-98.
- Young, I. E. & James, P. C. 1962. Chemical and morphological studies of bacterial spore formation. IV. The development of spore refractility. *J Cell Biol*, 12, 115-33.
- Zaman, M. S., Goyal, A., Dubey, G. P., Gupta, P. K., Chandra, H., Das, T. K., Ganguli, M. & Singh, Y. 2005. Imaging and analysis of *Bacillus anthracis* spore germination. *Microsc Res Tech*, 66, 307-11.
- Zhang, J., Fitz-James, P. C. & Aronson, A. I. 1993. Cloning and characterization of a cluster of genes encoding polypeptides present in the insoluble fraction of the spore coat of *Bacillus subtilis*. *J Bacteriol*, 175, 3757-66.
- Zhang, J., Ichikawa, H., Halberg, R., Kroos, L. & Aronson, A. I. 1994. Regulation of the transcription of a cluster of *Bacillus subtilis* spore coat genes. *J Mol Biol*, 240, 405-15.
- Zheng, L. B., Donovan, W. P., Fitz-James, P. C. & Losick, R. 1988. Gene encoding a morphogenic protein required in the assembly of the outer coat of the *Bacillus subtilis* endospore. *Genes Dev*, 2, 1047-54.

## Publications

1. Jiang, S., Wan, Q., Krajcikova, D., Tang, J., Tzokov, S. B., Barak, I. and Bullough, P. A. (2015), Diverse supramolecular structures formed by self-assembling proteins of the *Bacillus subtilis* spore coat. *Molecular Microbiology*. **97**, 347-359.
2. Jiang *et al.*, **Manuscript in preparation**. Assembly of the core building blocks of the *Bacillus cereus/anthracis/thuringiensis* spore surface.
3. Jiang *et al.*, **Manuscript in preparation**. Exosporium architecture altered through mutations of *Bacillus cereus* surface proteins.

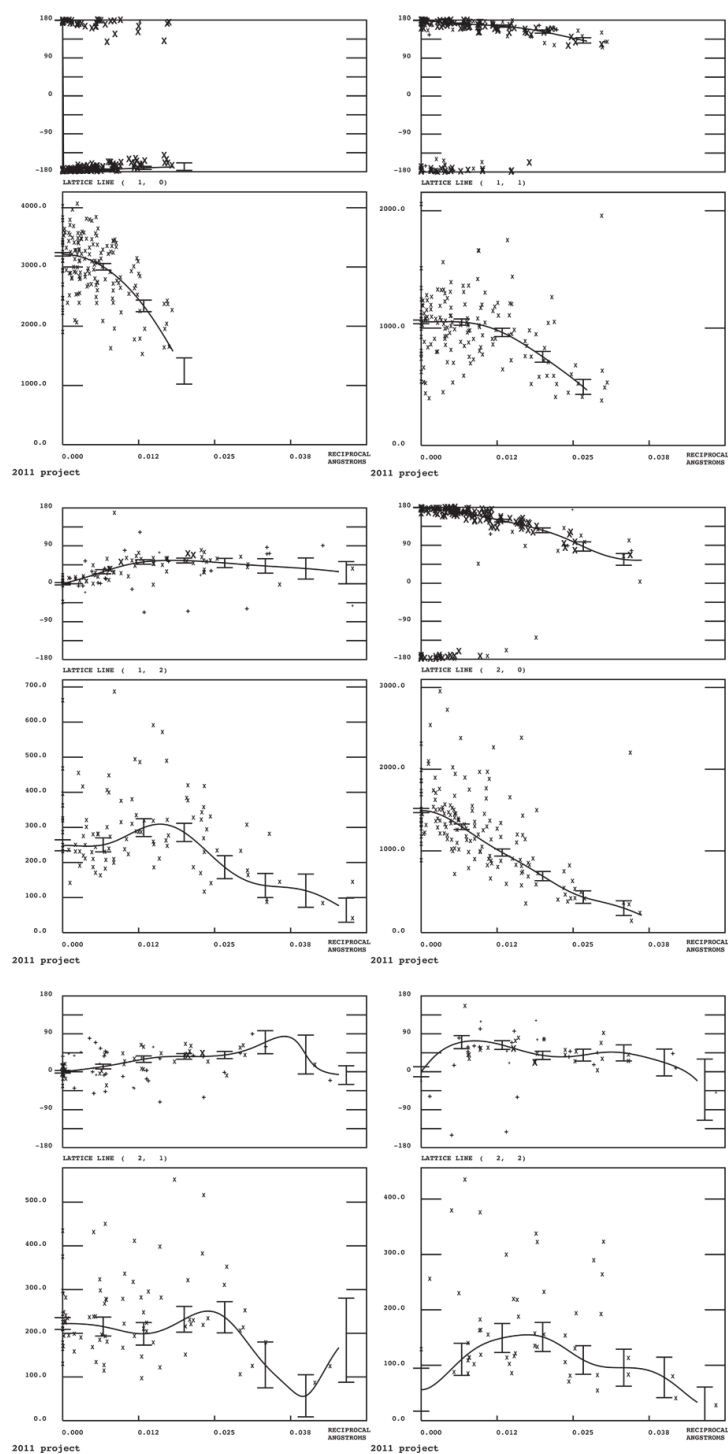
## Presentation of research

1. Poster Presenter, 6<sup>th</sup> European spores conference, Royal Holloway, University of London, 2014.
2. Poster Presenter, Bacillus ACT international anthrax conference, Victoria, Canada, 2013.

## Appendix

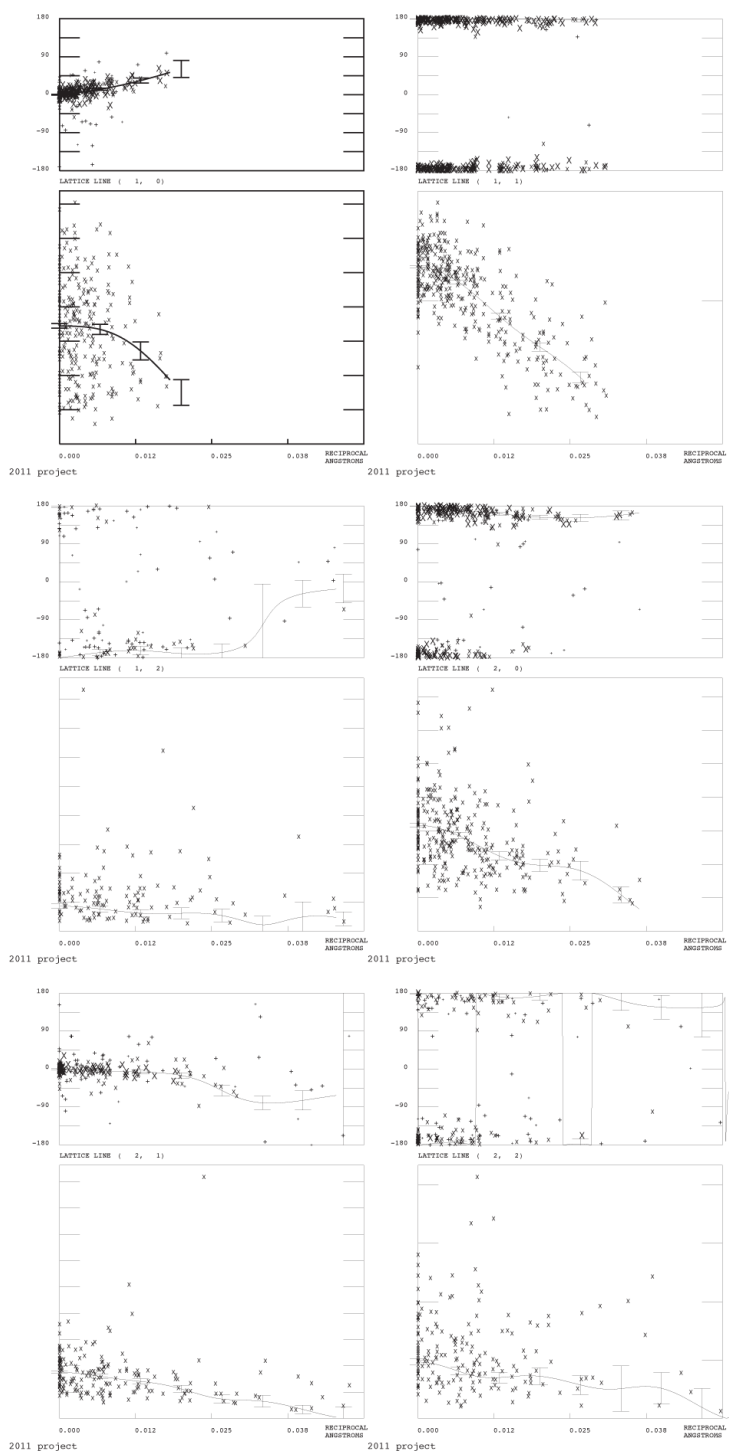
See following pages

**Appendix 3.1. Amplitude and phase variation along  $z^*$  for selected  $h, k$  values for *B. cereus* Form A exosporium crystals.  $p6$  symmetry was imposed.**



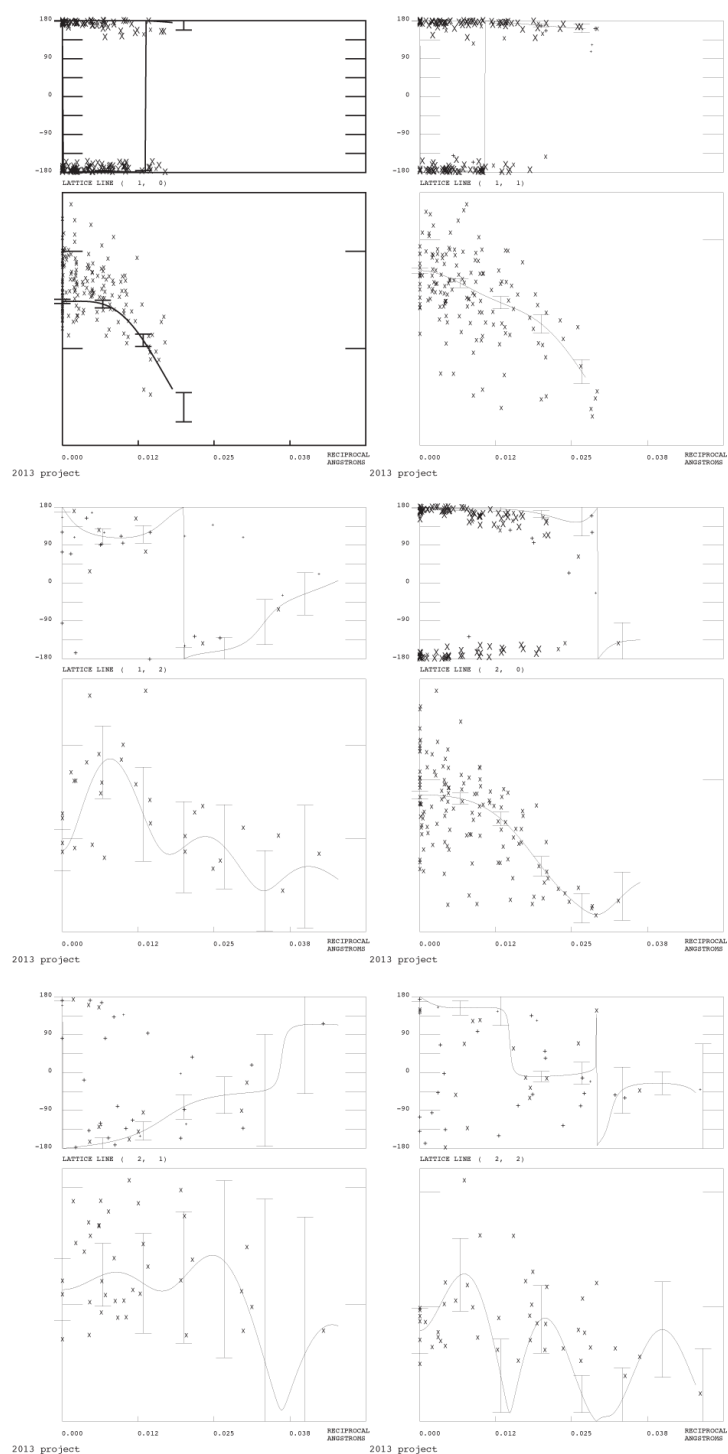
Lattice lines showing the phase variation along the  $z^*$  axis in  $^\circ$  (top panels) and amplitude variation in arbitrary units (lower panels). Horizontal axis displays distance from the origin of the lattice line. Standard error of fitted amplitude and phase values is represented in the error bars.

**Appendix 3.2. Amplitude and phase variation along  $z^*$  for selected  $h, k$  values for *B. cereus* Form B exosporium crystals.  $p6$  symmetry was imposed.**



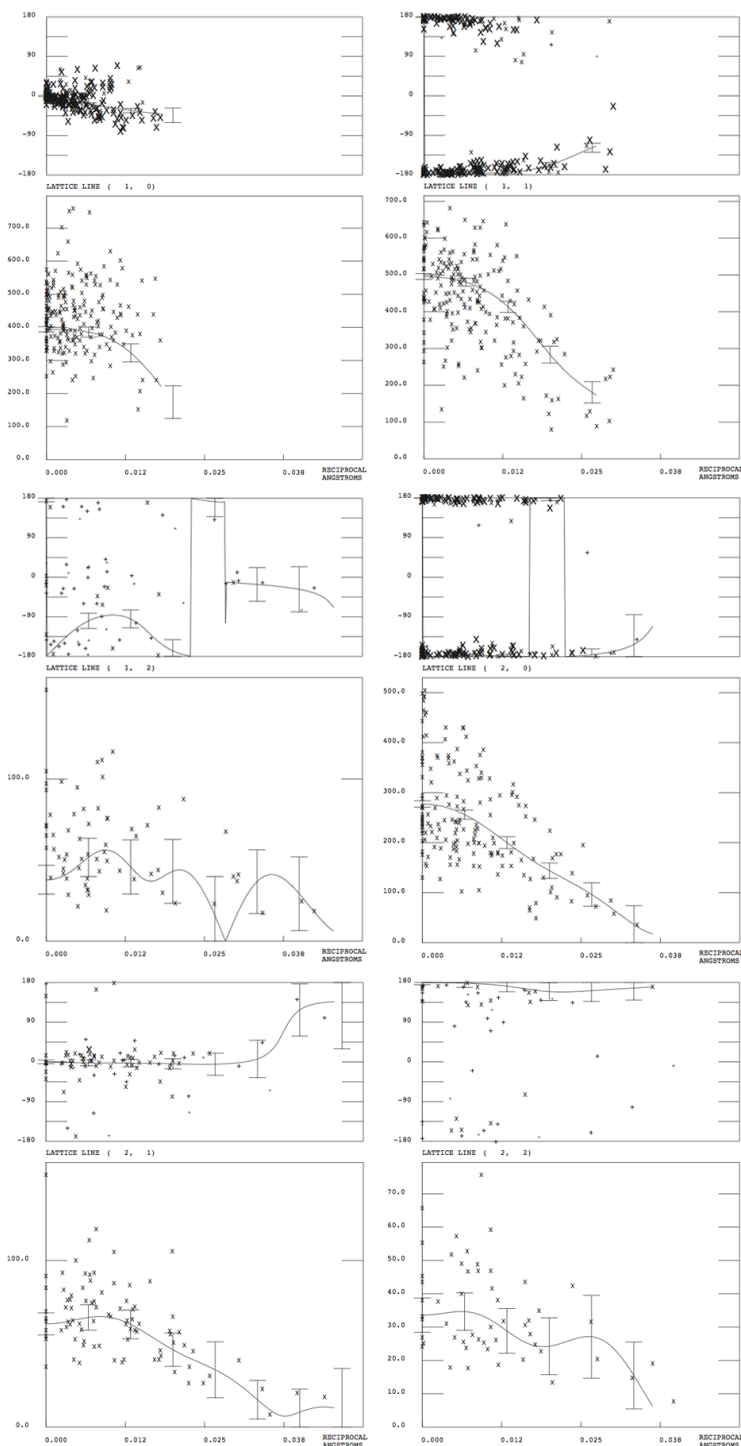
Lattice lines showing the phase variation along the  $z^*$  axis in  $^\circ$  (top panels) and amplitude variation in arbitrary units (lower panels). Horizontal axis displays distance from the origin of the lattice line. Standard error of fitted amplitude and phase values is represented in the error bars.

**Appendix 3.3. Amplitude and phase variation along  $z^*$  for selected  $h, k$  values for *B. cereus*  $\Delta$ exsFA exosporium crystals.  $p6$  symmetry was imposed.**



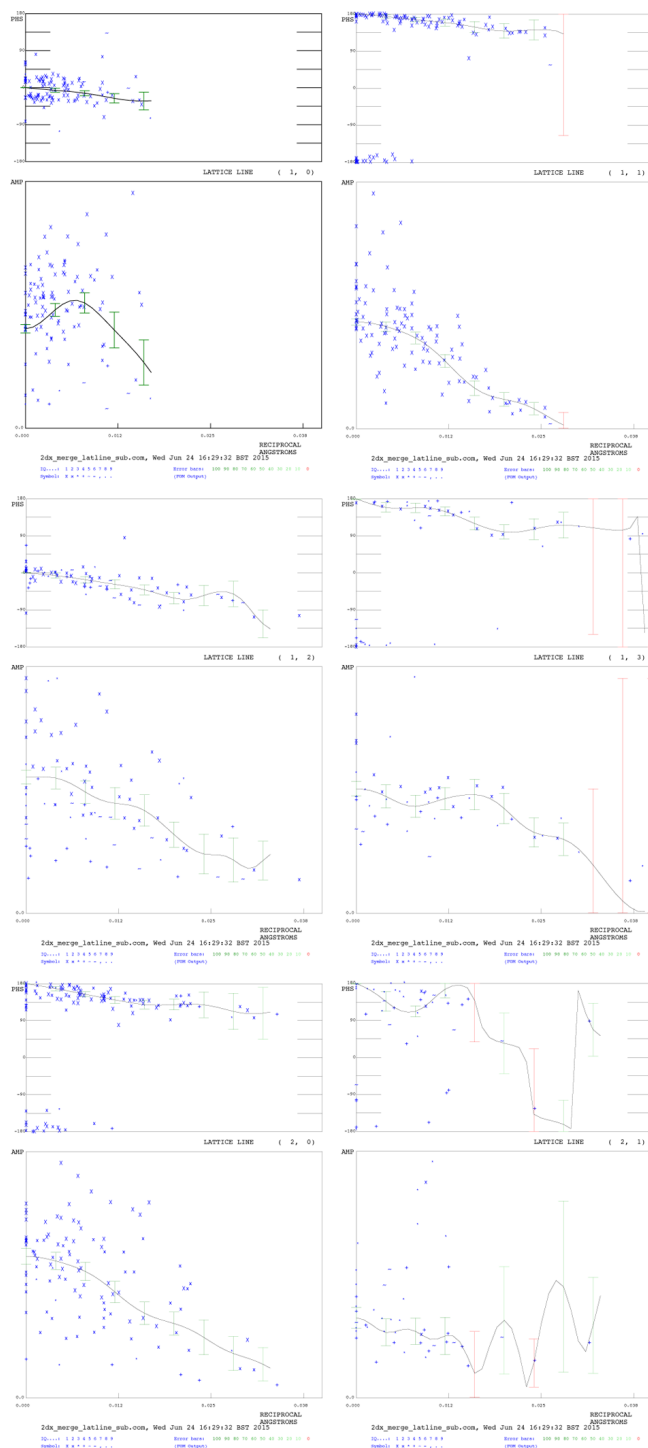
Lattice lines showing the phase variation along the  $z^*$  axis in  $^\circ$  (top panels) and amplitude variation in arbitrary units (lower panels). Horizontal axis displays distance from the origin of the lattice line. Standard error of fitted amplitude and phase values is represented in the error bars.

**Appendix 3.4. Amplitude and phase variation along  $z^*$  for selected  $h, k$  values for *B. cereus* Form A exosporium crystals.  $p6$  symmetry was imposed.**



Lattice lines showing the phase variation along the  $z^*$  axis in  $^\circ$  (top panels) and amplitude variation in arbitrary units (lower panels). Horizontal axis displays distance from the origin of the lattice line. Standard error of fitted amplitude and phase values is represented in the error bars.

**Supplementary Fig. 4.1. Amplitude and phase variation along  $z^*$  for selected  $h, k$  values for ExsY self-assembled crystals.  $p6$  symmetry was imposed.**



Lattice lines showing the phase variation along the  $z^*$  axis in  $^\circ$  (top panels) and amplitude variation in arbitrary units (lower panels). Horizontal axis displays distance from the origin of the lattice line. Standard error of fitted amplitude and phase values is represented in the error bars.

Supplementary Fig. 6.1. Amino acid sequence alignment of cysteine rich proteins CotZ, CotY from *B. subtilis* and ExsY from *B. cereus*.

```

CotZ MS--QKTS----SCVREAVENIEDLQNAVEEDCPTGCHSKLLSVS--HSL 42
CotY MSC-GKTHGRHENCVCDAVEKILAEQEAVEEQCPTGICYTNLLNPT--IAG 47
ExsY MSCNENKHHGSSSHCVVDVVKFINELQDCSTTTTCGSGCEIPFLGAHNTASV 50
      **          ** * * * * * * ** *

CotZ GDTVPPFAIFTSKSTPLVAFGNVG-ELDNGPCFNTVFFRVERVHG-SCATL 90
CotY KDTIPFLVFDKKGGLFSTFGNVGGFVDDMQCFESIFFRVEKLCD-CCATL 96
ExsY ANTRPFILYTKTGEPFEAFAPSA----SLTSCRSPIFRVESVDDDDSCAVL 96
      * **          *          ****      ** *

CotZ SLLIAFDEHKKHILDFTD----KDTVCEVFRLEKTNKYCIEVDLDCFCAINC 136
CotY SILRPVDVKGDTLSVCH----PCDP-DFFGLEKTDFCIEVDLGCFCAIQC 141
ExsY RVLTVVLGDSSPVPPGDDPICTFLAVPNARLISTTTCITVDLSCFCAIQC 146
      *          * * ** *** ***** *

CotZ LNPRLINRT-----HHH-- 148
CotY LSPVLVDRTSPHKDKKHHHNG 162
ExsY LRDVSIVK----- 154
      *

```

“\*” indicate conserved residues between CotZ, CotY and ExsY.